Estimation of In-situ Polymer Rheology by Simulation of Radial Flow Experiment

Master thesis in Petroleum Technology - Reservoir Chemistry

Tonje Nielsen

Centre for Integrated Petroleum Research
Department of Chemistry

University of Bergen

June 2017

Acknowledgement

First, I would like to express my gratitude towards Professor Arne Skauge for his valuable guidance, patience and his positive attitude throughout this year. The discussions with Arne have truly been insightful and helpful. The same gratitude goes to co-supervisors Iselin Cecilie Salmo and Nematollah Zamani for help in general and especially regarding reservoir modeling.

Furthermore, I would like to thank Centre for Integrated Petroleum Research and their staff for providing help, support and an office during my two years as a master student.

I would also like to thank my fellow students and friends at CIPR, Jørgen Gausdal Jacobsen and Lars Christian Kjær, for help and encouragement during long days, as well as both academic and social discussions.

Finally, I would like to thank my family and friends for all the support and understanding throughout my studies. Special thanks to Ole Sola for his patience and incredible support, as well as always being there for me.

Tonje Nielsen

Bergen, June 2017

Abstract

Most experiments about in-situ rheology of polymer flow in porous media presented in literature is executed on linear cores and hence, performed during steady state conditions where the pressure drop is constant over the entire core. In field applications, the differential pressure is under an unsteady state pressure regime where the flow velocities decrease with increasing radial distance from the well. The conditions experienced during field application is better replicated by performing experiments in radial cores, thus radial flow [1]. By executing polymer flooding in radial cores, a better estimation of the in-situ polymer rheology can be obtained and further, a better estimation of the injectivity. Furthermore, due to the viscoelastic behavior of synthetic polymers and the elongational flow caused by the porous media, the viscosity measurements obtained in viscometers deviates from the apparent in-situ polymer rheology. This consequently causes great uncertainties related to the performance of a polymer flood, which establishes the need to study in-situ polymer rheology.

The thesis is a simulation study carried out at the Centre for Integrated Petroleum Research (CIPR) and the objective was to estimate the in-situ polymer rheology by history matching experimental differential pressure and further study the influence of polymer rheology on injectivity. The base of the following simulation study was experimental data obtained by performing both waterflooding and polymer flooding in a radial Bentheimer disk. The estimation of the in-situ polymer rheology was obtained by both manual and automatic history matching.

Two simulators were used, STARS by CMG and MRST by SINTEF with an Ensemble Kalman Filter (EnKF) module developed by the University of Bergen. A sensitivity analysis performed in STARS investigated how altering various parameters and keywords in the script influenced the stabilized differential pressure and the results verified the script used for history matching manually in STARS. The results obtained by history matching in both simulators was consistent and only displayed minor deviations between the estimated output rheology.

The results displayed a dominant shear thickening behavior when subjected to high injection rates and is attributed to the viscoelastic nature of synthetic polymers. This is consistent with literature on both linear and radial cores. Both shear thickening and shear thinning were observed at lowered injection rates and although shear thinning is known to be observed in viscometers, the apparent shear thinning behavior in porous media is more widely discussed in literature. Furthermore, the in-situ polymer rheology appeared rate-dependent and the effect

was attributed to the viscoelastic nature of synthetic polymers which causes the apparent viscosity to depend on previous shear degradation. The degree of shear thickening and the estimated in-situ polymer rheology influences the injectivity and consequently the economics of the flooding project. An overestimated shear thickening, which is reported to be obtained in linear cores [1], consequently leads to an underestimated injectivity and an possible rejection of polymer flooding as an adequate EOR application. By estimating the in-situ rheology under similar pretenses as field conditions, this could possibly be avoided.

Nomenclature

Variables

A	area	[m^2]
a	radius of injection well	[m]
dP	differential pressure	[kPa]
dP/dr	pressure drop over radius r	[Pa/m]
dP/dx	pressure drop over distance x	[Pa/m]
dP/dt	pressure drop over time, t	[Pa/s]
dV/dr	the rate of deformation, shear rate	[s^{-1}]
E_A	areal sweep efficiency	[-]
E_D	microscopic displacement efficiency	[-]
E_R	expected recovery factor	[-]
E_V	vertical sweep efficiency	[-]
E_{vol}	volumetric displacement efficiency	[-]
F	force	[N], [$kgms^{-2}$]
f	fractional flow	[-]
G	modulus of a solid body	[Pa]
h	thickness of the core	[m], [cm]
I	injectivity	[$m^3/Pa \cdot s$]
K	power law constant	[-]
K	absolute permeability	[m^2], [D]
k_i	effective permeability	[m^2]
k_{ri}	relative permeability	[-]
k_r^0	endpoint relative permeability	[-]
M	mobility ratio	[-]
M^0	endpoint mobility ratio	[-]
M_n	number average weight	[Da]
M_w	average molecular weight	[Da]
N	standard oil originally in place	[m^3]
N_{Deb}	Deborah number	[-]
N_P	oil produced	[m^3]
n	power law exponent	[-]
n_x	amount of substance x	[mole]

m	mass	[kg]
P	pressure	[Pa], [bar]
P_r	external boundary pressure	[Pa]
P_w	internal bottomhole flowing pressure	[Pa]
Q	injection rate	[m^3/s]
r_w	well radius	[m]
r	radius of the core	[m]
r	radial position	[m]
R_F	resistance factor	[-]
R_{RF}	residual resistance factor	[-]
R^2	Root-mean-square	[-]
S	Skin factor	[-]
S	saturation	[-]
u	Darcy velocity	[m/s]
u (r)	Darcy velocity as a function of radius	[m/s]
t_D	dimensionless time	[-]
V	volume	[m^3]
v	velocity	[m/s]
V_b	bulk volume	[m^3]
V_p	pore volume	[m^3]
V_{pa}	total pore volume	[m^3]
V_i	pore volume occupied by fluid i	[m^3]
x_i	mole fraction of substance i	[-]
x_D	dimensionless position	[-]
α	constant related to pore geometry	[-]
Δ	difference	[-]
η	apparent viscosity	[cP]
$\eta(\dot{\gamma})$	apparent viscosity	[cP]
γ	strain	[-]
γ_{eff}	effective shear rate	[s^{-1}]
$\dot{\gamma}$	shear rate	[s^{-1}]
λ	time constant	[s]
λ_i	mobility of fluid i	[$m^2/Pa\cdot s$]
λ^0	endpoint mobility	[$m^2/Pa\cdot s$]

μ	viscosity	[mPas], [cP]
φ	porosity	[-]
ρ	density	[kg/m^3]
Γ	retention level	[µg/g]
Γ_m	retention	[lb/AF]
τ	shear stress	[Pa]
τ_E	characteristic period of elongation	[s]
τ_r	relaxation time	[s]

Subscripts

A	Areal
abs	Absolute
b	bulk
D	Microscopic
eff	Effective
g	Gas
i	Component
max	maximum shear thickening
o	Oil
pa	Pore Volume
pol	polymer
r	relative
res	residual
R	Recovery
tot	total
v	Vertical
vol	volumetric
w	water
wp	Brine mobility after displacing all mobile polymer
0	zero shear rate
∞	infinite shear rate

Abbreviations

2D	Two-dimensional
3D	Three-dimensional
BT	Breakthrough
CMG	Computer Modelling Group
CIPR	Center for Integrated Petroleum Research
EnKF	Ensemble Kalman Filter
EOR	Enhanced oil recovery
HPAM	Hydrolyzed polyacrylamide
IPV	Inaccessible pore volume
IOR	Improved oil recovery
NSC	Norwegian Continental Shelf
MATLAB	Matrix laboratory
MBE	material balance error
MRST	MATLAB Reservoir Simulation Toolbox
MWD	molecular weight distribution
OOIP	Original oil in place
PAM	Polyacrylamide
PDI	Polydispersity index
ppm	Parts per million (mass)
STARS	Steam, Thermal and Advanced Process Reservoir Simulator
STOOIP	Standard oil originally in place
UiB	University of Bergen

STARS KEYWORDS

ADMAXT	maximum adsorption capacity	[lbmol/ft^3], [gmol/cm^3]
ADRT	residual adsorption level	[lbmol/ft^3], [gmol/cm^3]
ADSTABLE	table of adsorption	[molfrac] vs [gmol/cm^3]
adt	adsorption	[lbmol/ft^3], [gmol/cm^3]
AVISC	viscosity	[cP]
cpt	composition, mole fraction	[molfrac]
CMM	molecular weight	[kg/gmol]
DTMAX	maximum time step allowed	[day], [min]
PORFT	accessible pore volume	[frac]
RRFT	residual resistance factor	[-]
SHEARTAB	Darcy velocity vs viscosity	[cm/min] vs [cP]

Table of Contents

List of Figures

List of tables

1 Introduction

In 2015, the primary global energy consumption only increased by 1 %, which is 0,9 % below the 10-year average of 1,9 %. Although this, together with the 2009 recession, was the lowest global growth since 1998, oil still remains the dominant energy source and accounts for almost one third of the global energy consumption [2]. The high global demand for oil requires a continuous oil production and to maintain or increase the global oil supply, one need to invest in enhanced oil recovery (EOR) techniques, as primary and secondary recovery methods result in a lower production of oil [3].

Reservoirs recovered by pressure depletion will typically only recovery 10 % of the oil volume available, while waterflooding, which works as a pressure support, can increases the volume of oil recovered and has a typical recovery factor of 35 % [4]. An further increase of the recovery factor can be accomplished by application of enhanced oil recovery techniques, as for example: chemical flooding, CO_2-injection or thermal treatment by injection of steam [3]. By applying EOR techniques it is possible to increase the recovery factor by 5-30 % [5]

Most of the large fields were discovered decades ago and have reached their peak of production years ago. More recent discovered fields are often smaller and more challenging to both find and produce [3], which have led to an increased interest and attention in enhanced oil recovery technology. Chemical flooding involves injection of chemicals and one of the mature methods is polymer flooding, which has been applied for more than 40 years [5]. Adding polymer to the injection water leads to an increase in the injected fluid viscosity, which further alters and decreases the mobility ratio between the displacing and displaced fluid, consequently resulting in a more stable front and displacement. This is usually applied when the oil viscosity is high or when the reservoir is heterogeneous [6].

When water is injected in a reservoir, it chooses the path with the least resistance, i.e. the path with the lowest pressure, which usually is the layer of the highest permeability. If the oil is highly viscous, fingers of water will form due to the high mobility of the injective water, causing large areas to be unswept and a large volume of bypassed oil. Increasing the viscosity of the injected fluid will result in less viscous fingering, a reduced mobility and more stable displacement, consequently an increased oil production [5].

Synthetic polymers are more frequently applied in enhanced oil recovery processes, compared to biopolymers [7]. This due to their relatively low cost, good viscosifying property and well-known characteristic. However, the existing polymer technology has its limitations in term of retention, degradation and polymer rheology [5]. Synthetic polymers and their viscoelastic nature causes a great uncertainty in their rheological behavior as it appears to deviate from bulk measurements and in-situ measurement. The viscoelastic effect causes increased viscosity with increased velocities. The velocities are highest near the injection-well, causing the synthetic polymer solution to reach its highest viscosity and consequently affect the injection pressure and the injectivity of the well. The in-situ rheological behavior at lower flow velocities is a widely discussed theme as well, and appears not to be completely resolved. Polymer in-situ behavior, although applied in the field for over 40 years, is an uncertain science and there is still much to learn.

The objective of this thesis is to estimate the polymer in-situ rheology by performing history matches and further study polymer injectivity. The thesis consists of 12 chapters in total when including appendix and references. Chapter 2 presents the general reservoir concepts and properties, which is essential background information needed to understand the results. Chapter 3 is an introduction to polymer rheology and polymer properties, which provides necessary information to support the discussion of the results. Chapter 4 is a literature study of previous laboratory and modelling research. In chapter 5 there is a short review of both reservoir simulators, as well as a sensitivity analysis performed in STARS. The sensitivity analysis investigated how changing different parameters and keywords in the script, effected the stabilized differential pressure. Chapter 6 presents the experimental data used for history matching and chapter 7 is the results and discussion chapter. This chapter presents the history matches obtained in both reservoir simulators and the corresponding permeability and polymer rheology used to obtain these matches. The results obtained from both simulators was very consistent when compared to each other, and only demonstrated minor deviations. The chapter also includes a short discussion of how polymer rheology affects the injectivity. Chapter 8 and 9 is the conclusion and further recommended work.

2 Theory

Pressure depletion is the primary oil recovery method and uses the natural energy of the reservoir as a drive to produce oil. This recovery method has a low oil recovery due to development of solution gas caused by a rapid decrease in the reservoir pressure. A secondary oil recovery method is therefore applied. Waterflooding, which is low cost and high efficiency, helps maintain the reservoir pressure hence preventing solution gas from developing and increasing the oil recovery [6].

The expected recovery factor, E_R, is defined as:

$$E_R = \frac{N_P}{N} = E_D \cdot E_{Vol} = E_D \cdot E_A \cdot E_V \tag{2.1}$$

where:

Oil produced, N_p

Standard oil originally in place (STOOIP), N

The microscopic displacement efficiency, $E_D = \frac{volume\ oil\ displaced}{volume\ oil\ contacted}$

The volumetric displacement efficiency, $E_{vol} = \frac{volume\ oil\ contacted}{volume\ oil\ in\ place}$

The areal sweep efficiency, $E_A = \frac{Area\ contacted\ by\ water}{Total\ area}$

The vertical sweep efficiency, $E_V = \frac{Cross{-}scetional\ area\ contacted\ by\ water}{Total\ cross{-}section\ area}$ [8].

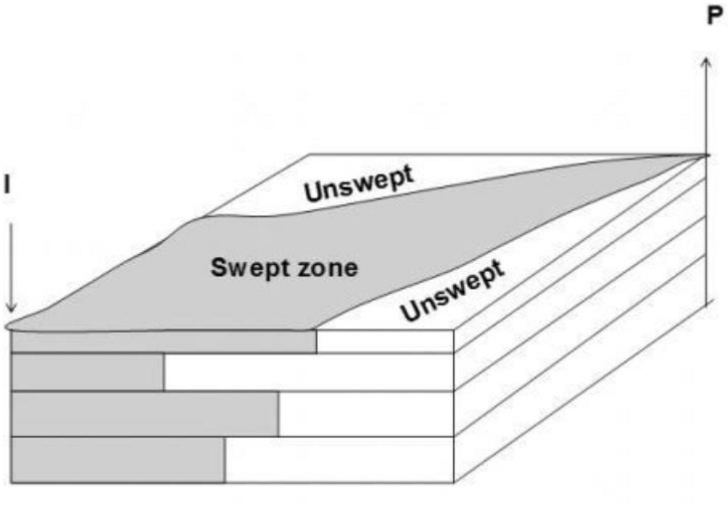

Figure (2.1). Sweep efficiency schematic. The picture is taken from Skauge and Skarestad, 2014, p. 95 [8].

Waterflooding, compared to pressure depletion results in a better recovery, but large volumes of oil is still left behind due to capillary forces, an unfavorable mobility ratio between water and oil or reservoir heterogeneities causes large areas left unswept, illustrated in Figure (2.1). Therefore, it is often necessary to perform a tertiary recovery method to enhance the oil recovery [6]. Enhanced oil recovery (EOR) is defined as oil recovery by injection of materials that normally is not present in the reservoir and is a subcategory of the broader term, IOR, which refers to any practice that improves the oil recovery [9].

The main objective of EOR methods is to increase the volumetric (macroscopic) sweep efficiency and enhance the displacement (microscopic) efficiency, which results in a lower residual oil saturation and a higher oil recovery [6]. Polymer flooding is a mature EOR method and is known to increase the macroscopic sweep efficiency by increasing the viscosity of the injected fluid and consequently alter and improve the mobility ratio between displacing and displaced fluid. This apparent increase in viscosity is attributed to the viscoelastic behavior of synthetic polymers and in recent times there has some discussion whether this viscoelastic effect also can improve the microscopic efficiency [10].

For a better understanding of the mechanisms behind EOR, it is necessary to view the fundamental petrophysical and the fluid properties governing the recovery process.

2.1 Petrophysical properties

2.1.1 Porosity

Porosity is a dimensionless parameter and defined as the rock's capacity to store fluids in the void of the rock, unoccupied by grain or cement. The total void in a rock sample is referred to as the absolute porosity, φ_{abs}, and is defined as the total pore volume in the rock sample, V_{pa}, divided by the bulk volume, V_b [6]:

$$\varphi_{abs} = \frac{V_{pa}}{V_b} \tag{2.2}$$

The absolute porosity relates to the connectivity of the pores in the rock sample and consists of two contributions, φ_{eff} and φ_{res}. The effective porosity, φ_{eff}, describes the connective pores that can maintain a fluid flow, while φ_{res}, the residual porosity, represents the pores that are isolated from the rest of the network and are not connected [11].

$$\varphi_{abs} = \varphi_{eff} + \varphi_{res} \tag{2.3}$$

The effective porosity will depend on several factors; type of rock, grain size, packing and contents of clay mineral and sedimentation [6], which also are factors that controls the permeability [12].

2.1.2 Permeability

2.1.2.1 Absolute permeability

The permeability of a porous media, as a reservoir rock, is a parameter that describes how easily a fluid can flow through a rock sample with interconnected pores [12]. Absolute permeability, by definition, is a rock property, given that the rock sample is completely saturated and only one fluid is flowing through the media. Darcy's law for a linear, horizontal, steady-state flow of an incompressible fluid defines the absolute permeability [6]:

$$q = -A\frac{K}{\mu}\frac{dP}{dx} \tag{2.4}$$

Where A is the cross-sectional area of the media, K is the absolute permeability, μ is the viscosity of the fluid and dp/dx is the pressure gradient. The right-hand term is negative as it represents the negative pressure gradient in the direction of the flow, as illustrated in figure (2.2). Permeability is often represented with the unit darcy (D) or millidarcy (mD) [6].

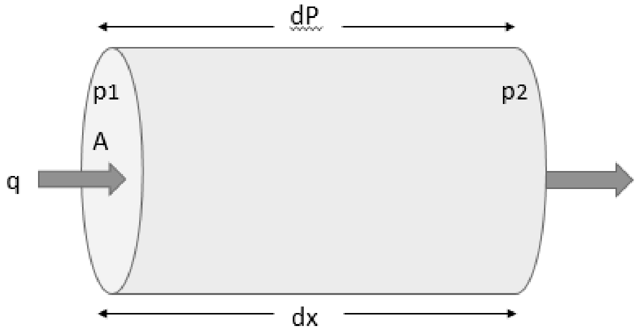

Figure (2.2). Illustration of Darcy's law in a linear model.

In this thesis, the experimental polymer floods were performed in a radial geometry and Darcy's law will therefore be modified to some extent. Figure (2.3) illustrates the fluid flow in the radial model.

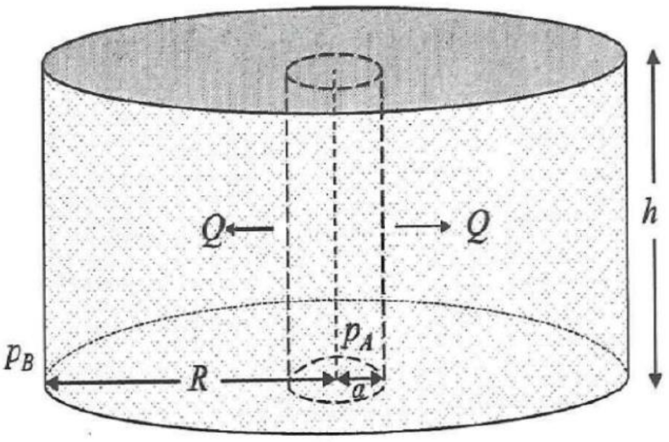

Figure (2.3). Radial flow in a cylindrical model. The figure taken from Lien, 2011, p.44 [13].

The pressure drop between the reservoir pressure, P_r, and the well pressure, P_w, drives a radial flow from the center, located at the radius r_w, to the reservoir, located at the radius r_e. In some distance r, between $r_w<r<r_e$, there is a horizontal fluid flow, Q, flowing towards the production well through the cross-section $A = 2\pi rh$. By inserting these variables into equation (2.4) and integrating, we get Darcy's law for radial flow, equation (2.7):

$$Q = -\frac{KA}{\mu}\frac{dP}{dx} = -\frac{2\pi hK}{\mu} r\frac{dP}{dr} \tag{2.5}$$

$$Q\int_{r}^{r_w}\frac{dr}{r} = -\frac{2\pi hK}{\mu}\int_{P_r}^{P_w} dP \tag{2.6}$$

$$P_r = P_w + \frac{\mu Q}{2\pi hK}\ln(\frac{r_w}{r}) \tag{2.7}$$

Where:

P_r – the outlet pressure

P_w - the pressure at the injection well

μ - the viscosity

Q - the injection rate

h - the thickness of the core

K is the absolute permeability

r_w - the radius of the injection well

r - the location of some pressure point at a distance r from the center of the disk.

The equation is used to calculate permeability at different radiuses between the innermost radius, r_w, and the outermost radius, r_e, from the measured pressure drop during a waterflood in a radial disk [13].

2.1.2.2 Relative permeability

In the case of more than one fluid present in the rock sample, each fluid will have its own effective permeability, k_i, which describes how the fluids flow relative to each other [6]. The relationship between the effective permeability to the fluid i, and the absolute permeability to the porous media, is defined as the relative permeability, k_{ri}, by following equation:

$$k_{ri} = \frac{k_i}{K} \tag{2.8}$$

This parameter will depend on both the porous media and the saturations, S_i, to the phases present in the porous media [14].

2.3 Saturation

The pore volume in a rock sample or reservoir, V_p, will be occupied by volumes of water, oil and gas, denoted respectively; V_w, V_o, V_g or in more general terms, by the fluid i, with volume V_i. From this, one can define the saturation of the fluid, S_i, which describes the fraction of the pore volume that is occupied by the phase i [6].

$$S_i = \frac{V_i}{V_p} \tag{2.9}$$

Where

$$S_w + S_o + S_g = 1 \tag{2.10}$$

During production, several factors causes entrapment of reservoir fluids and the fraction of oil that is not produced and left behind in the reservoir is referred to as residual oil saturation, S_{or} [6].

2.2 Fluid properties

2.2.1 Viscosity

Viscosity, μ, defines a fluids internal resistance to flow and indicates the thickness of the fluid. By dividing a fluid into layers, illustrated in Figure (2.4), it is possible to define the shear stress, τ, working between two layers of a fluid as:

$$\tau = \frac{F}{A} \tag{2.11}$$

Where F is the force and A is the area.

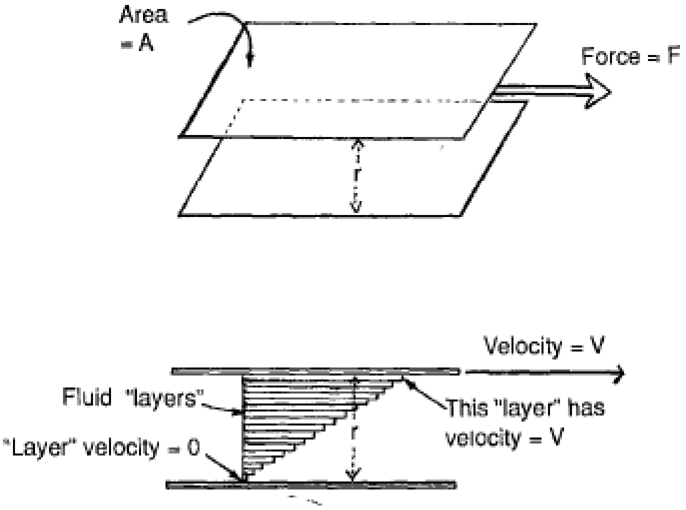

Figure (2.4). Illustration of simple shear flow. Taken from Sorbie, 1991, p.38 [7].

It is found experimentally that the velocity gradient between the fluid layers are linear in many cases and for a large class of fluids the force is found to be:

$$F \propto \frac{AV}{r} \tag{2.12}$$

Where A is the area, r is the distance between the lower and upper surface and V is the velocity of the upper surface. V/r is the velocity gradient.

$$\tau \propto (\frac{dV}{dr}) \tag{2.13}$$

Where (dV/dr) is the rate of deformation and is known as the shear rate.

Based on these relations, one can define viscosity by Newton's relation:

$$\tau = -\mu\left(\frac{dV}{dr}\right) = \mu\dot{\gamma} \tag{2.14}$$

Where τ is the shear stress and $\dot{\gamma}$ is the shear rate [7]. The unit for viscosity used in this thesis is centipoise, which is equivalent to [6]:

$$1000 \text{ cP} = 1 \text{ Pa} \cdot \text{s} = 1 \frac{N \cdot s}{m^2}$$

2.2.2 Mobility ratio

The mobility of a fluid i, λ_i, is the ratio between the effective permeability to the fluid to the fluid viscosity:

$$\lambda_i = \frac{k_i}{\mu_i} \tag{2.15}$$

The mobility ratio is the ratio between the mobility of the displacing fluid and the mobility of the displaced fluid. In case of a waterflood, the mobility ratio will be defined as [15]:

$$M = \frac{\lambda_w}{\lambda_o} = \frac{k_{rw}}{\mu_w} \cdot \frac{\mu_o}{k_{ro}} \tag{2.16}$$

The endpoint mobility, M^0, given by equation (2.17), has a significant effect on the shape of the fraction flow curve and has an important role in the displacement efficiency during a waterflood as it describes the stability of the displacement. This is illustrated in Figure (2.5) [8].

$$M^0 = \frac{\lambda_w}{\lambda_o} = \frac{k_{rw}^0}{k_{ro}^0} \cdot \frac{\mu_o}{\mu_w} \tag{2.17}$$

$$f_w = \frac{\lambda_w}{\lambda_w + \lambda_p} = \frac{1}{1 + 1/M} \tag{2.18}$$

Where f_w is the fractional flow of water.

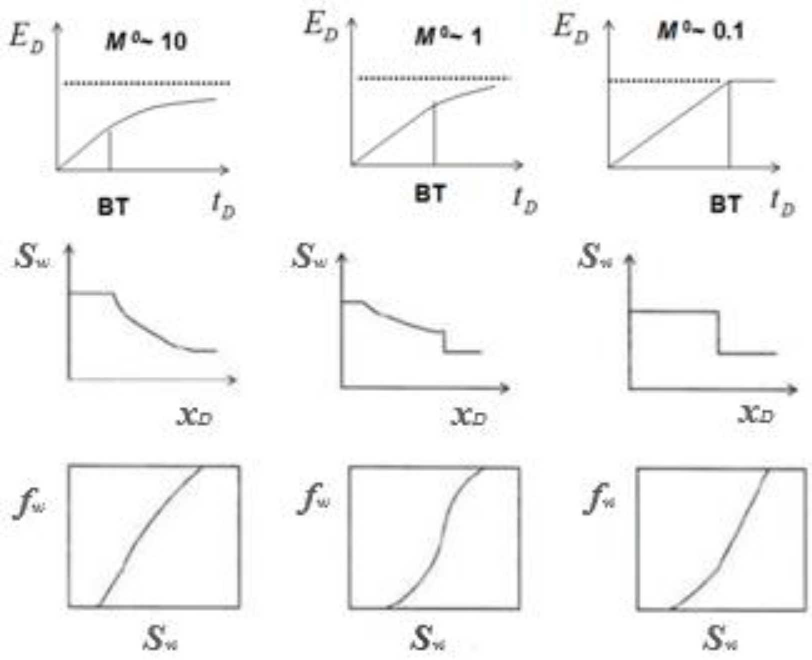

Figure (2.5). The effect of endpoint mobility ratio on the displacement efficiency. E_D - microscopic displacement efficiency, t_D – dimensionless time, S_w – water saturation, x_D – dimensionless position and f_w – the fractional flow of water. The figure is from an modified combination of Skauge and Skarestad, 2014, p.92 [8].

The left side of Figure (2.5) illustrates a high endpoint mobility ratio ($M^0 > 1$) and the fractional flow curve is said to be spreading, which results in an early water breakthrough (BT) and consequently shows a long tail production of oil due to viscous instabilities [8]. This is well known for displacement processes where the fluid displacing has a lower viscosity than the fluid being displaced, as the displacement process between water and viscous oil [7]. The front of the displacement becomes unstable leading to development of viscous fingers penetrating the fluid that is being displaced. The viscous instabilities starts when the end point mobility ratio is greater than unity and the effect becomes more pronounced as the value of M^0 increases [16]. This is not a favorable displacement as it results in a lower production of oil, an increased production of the injected fluid and a poor areal sweep efficiency, illustrated in Figure (2.6). In heterogeneous reservoirs, the effect is more pronounced due to high permeable channels [7].

The endpoint mobility ratio can become more favorable by decreasing the viscosity of oil, increasing the viscosity of water or by reducing the relative permeability to water, seen from equation (2.17) [8]. By adding polymer to the injective fluid, the water viscosity increases and alters both the mobility ratio and the fractional flow curve.

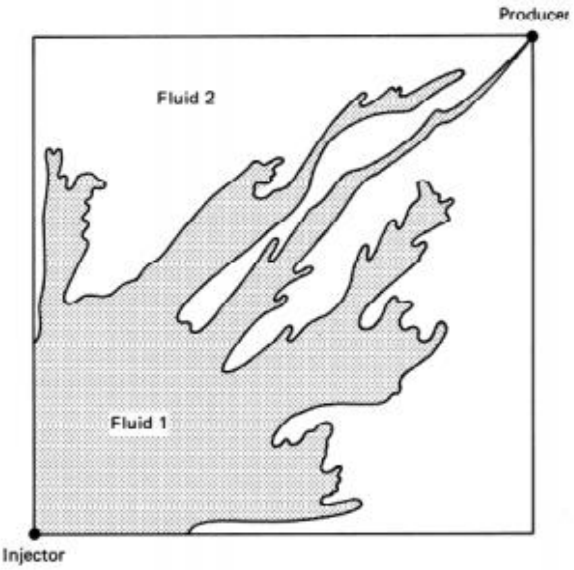

Figure (2.6). Viscous fingering at a $M^0 = 17$. The picture is taken from Lake, 2014, p. 224 [9].

The middle of Figure (2.5) shows the situation that arises when the mobility ratio is equal to unity and the corresponding sharpening and spreading, S-shaped fractional flow curve. An S-shaped curve generates several S_W-values for the same position which is a nonphysical phenomenon and is eliminated by invoking formation of shocks [8]. Furthermore, the right-hand side of Figure (2.5) illustrates that an endpoint mobility ratio less than unity results in a more favorable, piston-like displacement and the fraction flow curve is defined as a sharpening wave. The viscous instabilities are not present thus leading to a later water breakthrough, a smaller tail production and an increased sweep efficiency, illustrated in Figure (2.7) [8].

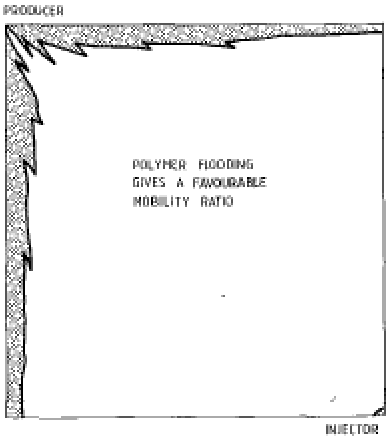

Figure (2.7). The improvement of areal sweep caused by polymer flooding, $M^0 \leq 1$. The picture is taken from Sorbie, 1991, p. 248 [7].

A previous study at CIPR by Skauge et al. (2012) reported that waterflooding of heavy oil at non-waterwet state developed fingers in the early part of the waterflooding and that the fingers varied with mobility ratio. Higher oil viscosities resulted in shaper fingers and a continuous water injection led to fusing of established fingers to development of channels [17]. Furthermore, Skauge et al. (2014) investigated how a modest change in mobility ratio caused by a tertiary polymer injection impacts the oil recovery and stated that even the lowest oil viscosities showed initial viscous fingering. The water fingers collapsed into wider channels and pockets of unswept oil was left behind after the waterflooding. They further stated that polymer flooding was remarkably efficient, even at high adverse mobility ratios [18].

Altering the mobility ratio from unfavorable to a more desirable value by adding polymer to the injected fluid and the mechanisms behind this apparent increase in the solution viscosity is further discussed in the upcoming chapters.

2.2.3 Flow regimes

Flow regimes can be divided into three categories; the transient period, semi-steady state and steady state. Due to the objectives of this thesis, only the first and the third category will be discussed.

The transient period corresponds to the pressure change that occurs in the reservoir when the production starts. As the production begins, the pressure in the well drops and causes pressure disturbances throughout the reservoir. By definition, the transient period is the transition where the pressure disturbances that starts in the well-bore region reaches the outer boundary of the reservoir. This will be a function of both time and radial position.

$$\frac{dp}{dt} = f(r,t) \tag{2.19}$$

Where p is the pressure, t is the time and r is the radial position.

As the pressure disturbances reaches the outer rim, the pressure will either fall as there are no injection of water to maintain the pressure and it reaches a semi-steady state or water will be injected to maintain the pressure and the reservoir reaches a steady state. In a steady state the pressure will be independent of time and radial position [14]:

$$\frac{dp}{dt} = 0 \tag{2.20}$$

3 Polymers

Polymer flooding is classified as an EOR method and involves adding polymer to the injection water to increase the viscosity of water as well as reducing the relative permeability to water. The result of this is a more favorable mobility ratio between oil and water, which in turn leads to improved volumetric sweep efficiency and accelerates the oil recovery [6]. The aim of polymer flooding is not to target the irreducible oil saturation ca, but to decrease the saturation of the remaining oil in the reservoir by producing the oil bypassed by the waterflood due to reservoir heterogeneities or unfavorable mobility ratios [7]. In general, a polymer flood will only be economical if the water mobility is high, the reservoir heterogeneities is high or a combination of both [9]. On the Norwegian continental shelf, most oils are light which make reservoir heterogeneities the target of polymer flooding [8].

The most commonly used polymers is the synthetic polymer hydrolyzed polyacrylamide, HPAM, and the biopolymer produced in microbial processes, Xanthan [8]. In this thesis, the polymer will be a synthetic polymer, biopolymers are therefore not further discussed. The following chapters gives a short introduction to synthetic polymers and their properties.

3.1 HPAM

3.1.1 Molecular structure

The chemical structure and the molecular conformation for a polymer is the basis for several physical properties of a polymer and is therefore important to consider. Flow behavior, adsorption, retention, thermal and shear stability, which will be discussed later in this chapter, are all linked back to the molecular structure of the polymer.

HPAM is a synthetic randomly coiled, straight-chained polymer constituted of acrylamide monomers that are hydrolyzed to some degree, as illustrated in Figure (3.1) [7]. The polymer is partially hydrolyzed to prevent adsorption by converting some of the amide groups to carboxyl groups and consequently giving the backbones of the polymer a negative charge [19]. The degree of hydrolysis, which is the fraction of amide groups hydrolyzed, affects the solubility, salinity sensitivity, retention and viscosity [16]. If the degree of hydrolysis is too small, the polymer will not be soluble in water, but if the degree of hydrolysis is too high, the polymers properties will be too sensitive to salinity and hardness. The normal degree of hydrolysis lies between 30 to 35% [9].

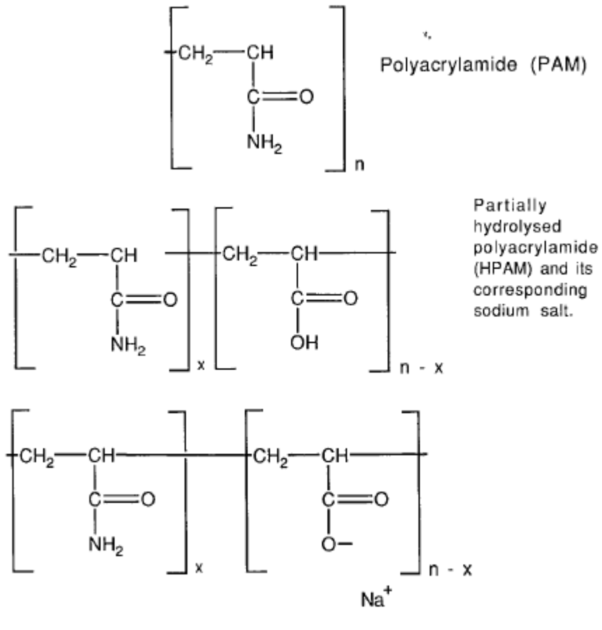

Figure (3.1). The primary chain of polyacrylamide and HPAM. The figure is taken from Sorbie, 1991, p. 20 [7].

HPAM is a polyelectrolyte, which causes it to interact with ions when in polymer solution. Because of its flexibility and lack of a rigid structure, it responds sharply to the ionic strength of the solution and this causes the hydrodynamic size of the polymer to change, as illustrated in Figure (3.2) [7].

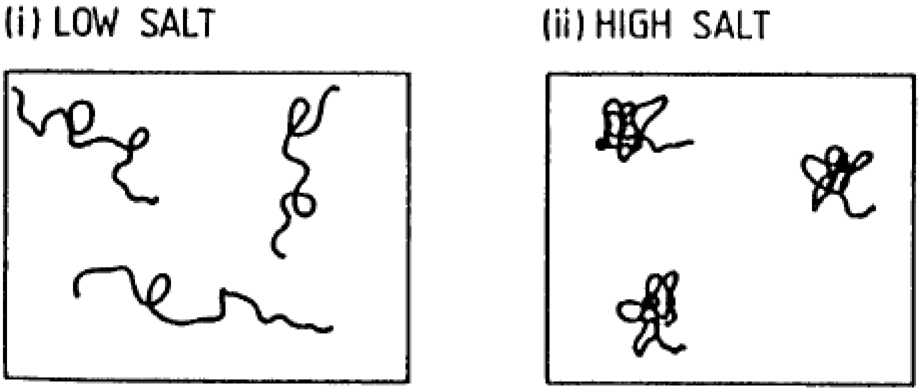

Figure (3.2). How the salinity of the solution affects the polymer. The figure is taken from Sorbie, 1991, p. 21 [7].

As the figure schematically illustrates, on the left-hand side, the solution has a low salinity and the negative charged groups on the backbone of the polymer repulse each other and causes the polymer to stretch, which increases the solutions viscosity. At higher salinities, illustrated on the right hand side, the polymer coil itself because of shielded, decreased repulsive forces and the viscosity of the solution decreases [19].

3.1.2 Molecular weight and molecular weight distribution

Synthetic polymers can be produced by polymerization of acrylamide monomers or copolymerization and depending on the extent of the polymerization, the average molecular weights rage from 0,5 to 30 million Daltons. For EOR application the weight average molecular weight, M_w, is normally between 1 to 10 million Daltons. All polymerization products results in a wide molecular weight distribution (MWD) and thereby a broad polydispersity index (PDI) [16]. Due to the broad distribution of species of different molecular weight and the difficulty to obtain them, the product specifications of synthetic polymers is usually given as an average molecular weight based on weight average or number average, M_n [7].

3.2 Rheology

Rheology is the study of the deformation and flow of matter [20]. Polymers, because of their rheological properties in dilute solutions, are of interest for EOR applications [16]. The relationship between shear stress, τ, and shear rate, $\dot{\gamma}$, divides fluids in two rheological groups; Newtonian and non-Newtonian [21].

3.2.1 Newtonian and non-Newtonian fluids

A Newtonian fluid follows a linear relationship between shear stress and shear rate, given previously by equation (2.14), where the proportionality constant is the solution viscosity, μ, which is independent of the shear rate. This is typical behavior for water, gases or polymers at low shear rates [8].

A non-Newtonian fluid has a shear rate dependent viscosity and consequently follows a non-linear relationship:

$$\tau = -\eta\left(\frac{dV}{dr}\right) = \eta(\dot{\gamma})\dot{\gamma} \tag{3.1}$$

Where $\eta(\dot{\gamma})$ is the apparent viscosity and is shear rate dependent [7].

Based on equation (2.14) and (3.1), it is clear that the viscosity can either be constant (Newtonian) or shear rate dependent (non-Newtonian), which results in several types of relationships between shear stress and shear rate, illustrated in Figure (3.3). This applies for a laminar flow through a capillary, referred to as a simple shear flow or the bulk rheology of the polymer.

A Newtonian fluid follows a linear slope and the steepness of the slope indicates how viscous the fluid is.

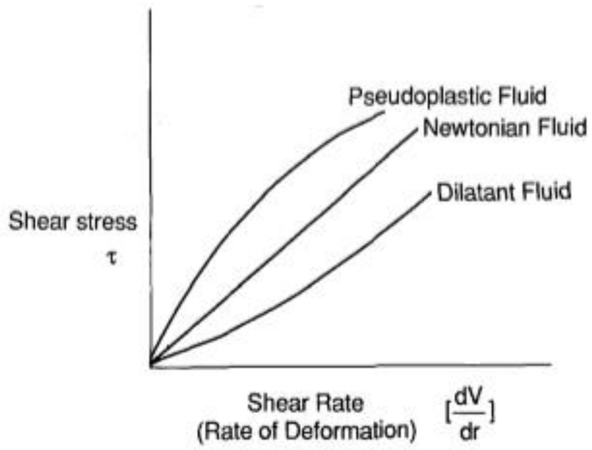

Figure (3.3). The different rheological behavior of polymeric fluids. The figure is modified and from Sorbie, 1991, p. 52 [7].

Dilitant fluids are shear thickening, meaning that the apparent viscosity increases with increasing shear rate. Pseudoplastic fluids are shear thinning, meaning that the apparent viscosity of the fluid decreases as the shear rate increases. This usually applies for dilute polymer solutions [7]. The shear thinning effect is caused by the polymer molecules aligning with the shear field, which reduces the internal friction and the interactions between the polymers. This can be expressed by the power law model:

$$\eta(\dot{\gamma}) = \mathrm{K}\,\dot{\gamma}^{(n-1)} \tag{3.2}$$

Where K is the power law constant and n is a power law exponent indicating the behavior regime of the polymer [16]. If n = 1, the fluid is Newtonian and the power law constant is the constant viscosity. If n ≤ 1, the fluid will be shear thinning. As previously mentioned, dilute polymer solutions are known to be Newtonian at low shear rates. Based on this, the power law model is not suitable for low and high shear rates, as it only describes the shear thinning region [7]. The Carreau model describes the complete rheological behavior of a shear thinning fluid, illustrated in Figure (3.4):

$$\eta(\dot{\gamma}) = \eta_\infty + (\eta_0 - \eta_\infty)[1 + (\lambda\dot{\gamma})^2]^{(n-1)/2} \tag{3.3}$$

Where λ is a time constant and n is the same as the power law constant [7].

At low rates, the fluid behaves Newtonian, as the apparent viscosity is constant. This region is classified as the lower Newtonian plateau and the viscosity in this region is denoted η_0, the zero shear rate viscosity.

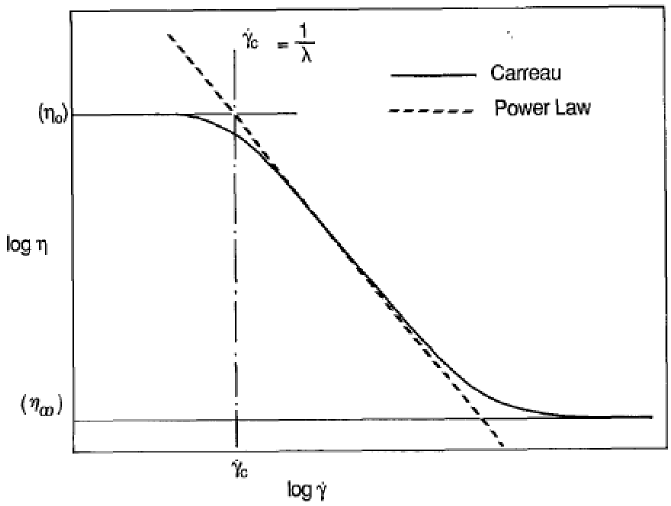

Figure (3.4). Apparent viscosity versus shear rate. The figure is from Sorbie, 1991, p. 56 [7].

As the shear rate increases, the fluid enters the shear thinning region. The critical shear rate, $\dot{\gamma}_c$, is the shear rate at the onset of shear thinning. At higher shear rates, there is a new transition to a new Newtonian plateau, known as the upper Newtonian region with a viscosity denoted as η_∞, infinite shear rate viscosity. The infinite shear rate viscosity usually equals the solutions viscosity and in the case of water as the solute, it will be equal to 1cP [16].

Synthetic polymer solutions are known to show a pseudoplastic behavior in viscometers, but their rheological behavior in a porous media, known as in-situ rheology, will differ from their bulk rheology due to the more complex structures in the media and the presence of both shear and extensional stress [22]. The effect of the shear thickening behavior at higher flow rates in a porous media has been referred to as both "pseudodilatant" and "viscoelastic" and can be explained by the viscoelastic nature of synthetic polymers and the extensional flow caused by the media [23].

3.2.2 Viscoelasticity

Polymer fluids are known to be viscoelastic, which means that their behavior lies in between the elastic behavior of a solid and the viscous behavior of a liquid. Similar as how the viscosity was defined by equation (2.14), as the ratio of shear stress to shear rate, the modulus, G, of a solid body, can be described by the rate of shear stress to strain, γ:

$$\tau = G\gamma \tag{3.4}$$

Viscosity is a characteristic of a liquid and reflects the relative motion of the molecules. When a liquid is subjected to stress, it flows and energy will be dissipated by friction. Elasticity is a characteristic of a solid and reflects storage of energy. When subjected to strain, the solid deforms as the molecules adapt to a non-equilibrium distribution of conformations. A polymer chain will stretch or align with flow direction as long as the strain is applied. When the molecules are left by themselves, they will relax and their relative motion through the surrounding fluid will dissipate stored energy. Relaxation time describes the time it takes for a polymer to go from a non-equilibrium state to an equilibrium state [24].

In a porous media, there are several contractions and expansions due to the variations in pore size and geometry [7]. Synthetic polymers have a flexible coil formation in solutions and when flowing through a porous media from pore to pore, it will deform, and the molecules will elongate and align with the direction of the flow. If the average flow time from one constriction (pore throat) to another is large enough relative for the polymer to relax back to its equilibrium state, it remains pseudoplastic and shear thinning. At high flow rates the transient time between the constrictions will be in the same order as the polymers relaxation time, causing the polymer to stay elongated and increasing the solutions apparent viscosity [19].

By extending Figure (3.4), the complete rheological behavior for a synthetic polymer in a porous media is illustrated in Figure (3.5):

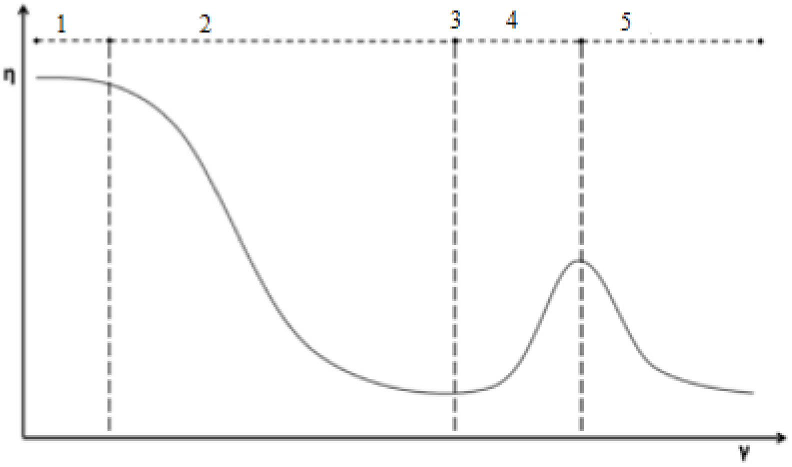

Figure (3.5). The complete rheological behavior of a synthetic polymer. The picture is modified and the original is taken from Skauge et al., 2016, p.2 [1].

Figure (3.5) illustrates the five distinct regions of the rheology behavior to a synthetic polymer. Shortly summarized:

1. The lower Newtonian plateau. Viscosity is independent of shear rate.
2. Shear-thinning region.
3. The upper Newtonian plateau.
4. Shear thickening due to extensional flow
5. Viscosity decreases due to mechanical degradation, which is elaborated later [1].

The onset of viscoelastic behavior, i.e. shear thickening, is defined by the dimensionless Deborah number:

$$N_{Deb} = \frac{\tau_r}{\tau_E} = \tau_r \cdot \dot{\gamma} \tag{3.5}$$

Where τ_r is the relaxation time for a polymer molecule and τ_E is the characteristic period for elongation and contraction as the polymer flows through a series of contractions and expansions, $\dot{\gamma}$ is the effective shear rate [25].

A large Deborah number results in a viscoelastic behavior due to the low characteristic period value, while a small Deborah number results in a Newtonian behavior, as the characteristic period is longer and not the same magnitude as the relaxation time of the polymer [26].

As neither of the previously mentioned equations, Power law model and Carreau, includes both shear thinning and shear thickening, it is necessary to introduce a third equation, developed by Delshad et al in 2008, referred to as the extended Carreau equation:

$$\eta(\dot{\gamma}) = \eta_\infty + (\eta_0 - \eta_\infty)[1 + (\lambda\dot{\gamma})^\alpha]^{(n-1)/\alpha} + \eta_{\max}[1 - \exp(-(\lambda_2\tau_r\dot{\gamma})^{n_2-1})] \tag{3.6}$$

Where $\eta(\dot{\gamma})$ is the apparent viscosity, η_∞ is the infinite shear rate viscosity and is usually 1cP, η_0 is the zero shear rate viscosity, λ, λ_2, n and n_2 is polymer specific empirical constants, $\eta_{\max}$ an empirical constant, τ_r is the relaxation time for the polymer molecule and γ_{eff} is the effective shear rate. α is generally equal to 2. The left hand side of the equation represents the shear thinning behavior, while the right hand side represents the shear thickening behavior [25].

Due to the available information and the values listed above, this thesis uses a modified version of the extended Carreau equation:

$$\eta(\dot{\gamma}) = \eta_\infty + (\eta_0 - \eta_\infty)[1 + (\lambda_1\dot{\gamma})^2]^{(n_1-1)/2} + \eta_{\max}[1 - \exp(-(\lambda_2\dot{\gamma})^{n_2-1})] \tag{3.7}$$

Where most of the parameters are the same as listed above, but with a small change where $\eta_{\max}$ is maximum shear thickening viscosity and λ_2 includes the polymers relaxation time [27]. Although this equation considers both the shear thinning and shear thickening behavior of a viscoelastic fluid, it does not include the possible mechanical degradation which might occur at high shear rates, illustrated by region 5 in Figure (3.5).

The effective shear rate, $\dot{\gamma}$, is proportional to the flow rate, Q, and based on a capillary bundle model it can be determined as following:

$$\dot{\gamma} = \alpha\frac{4u}{\sqrt{8\phi K}} \tag{3.8}$$

α is a constant related to pore geometry and type of porous media, ϕ is the porosity of the rock, K is the permeability and u is the Darcy velocity. For a bundle of capillaries α = 1, while for consolidated sand it varies between 1,4 to 14 [6].

In a radial geometry, the Darcy velocity is defined as:

$$u(r) = \frac{Q}{A} = \frac{Q}{2\pi r h} \tag{3.9}$$

Where Q is the injection rate, A is the cross-sectional area, and h is the thickness of the radial core. The thickness of the core is constant, while the Darcy velocity depends on the distance from well, r. As the fluid flow propagates towards the outer boundary of the disk, the velocity decreases as the r increases [1].

3.3 Polymer stability

The most important property of a polymer is that when added in small concentrations, it will increase the solutions viscosity significantly by several orders of magnitude. For a polymer to be useful during a flooding, it needs to be stable at reservoir conditions. Polymers degrade at certain conditions and it is therefore essential to know its stability [16]. Polymer degradation can be divided into three categories: chemical degradation, mechanical degradation and biological degradation. Biological degradation may occur for both synthetic and biopolymers, but as the problem is more common for biopolymers [7], this will not be further discussed as the polymer used in this thesis is synthetic. Due to the objective of this thesis the focus will be on mechanical degradation and chemical degradation.

3.3.1 Mechanical degradation

Mechanical degradation refers to the process that breaks down the polymer molecule as result of high flow rates. This applies for regions near the well-bore where there are high mechanical stresses on the macromolecule. Little mechanical degradation occurs within the reservoir as the velocity of the flow rapidly falls off with increased distance from the well [9].

By definition, mechanical stability refers to the molecules ability to withstand high stress. Mechanical degradation breaks the large macromolecules apart into smaller fragments and reduces the average molecular weight and thereby the solution viscosity [7]. The main factor effecting mechanical degradation is the flexibility and structure of the molecule, which make synthetic polymers more susceptible to mechanical degradation [16].

The mechanical degradation of synthetic polymers occurs at high flow rates, longer flow distances or in low permeability media due to small average pore throat diameter and increased stress. Large molecules may experience a higher rate of chain rupture due to their resistance to flow and thereby experiencing larger shear stress [19].

Seright (1983) found that mechanical degradation has a characteristic “entrance pressure drop” when synthetic polymer solutions is injected into a porous media. The magnitude of the entrance pressure drop indicated the degree of mechanical degradation. The greater the pressure drop, the more degradation [28]. The polymers tendency to mechanical degrade can be reduced by partially pre-shearing the polymer solution before injection [9].

3.3.2 Chemical degradation

Chemical degradation refers to the breakdown of polymer molecules due to short-term attacks by contaminants, like oxygen, or long-term attacks on the backbone of the molecule through extended hydrolysis.

The presence of oxygen leads to oxidative degradation of synthetic polymers and the degradation rate increases with increasing temperature. As the concentration of oxygen increases the viscosity of the solution decreases [19]. The contamination attack of oxygen can be minimized by reducing the content of oxygen in the brine by adding oxidative scavengers, but this is not typically applied in field operations [16].

The thermal stability of polymers need to be considered. At some temperature, the polymers will thermally crack, but since the reservoir temperature usually is below this limit, it is not a concern. As the polymers residence time in a reservoir is long, even slow reactions need to be considered. At exceedingly high and extremely low pH, combined with high temperatures, synthetic polymers will experience a further degree of hydrolysis, which destroys the already selected extent of hydrolysis and causes an increased sensitivity to the brine hardness and a decrease in the solutions viscosity [9].

The effect of monovalent ions, referred to as synthetic polymers sensitivity to salinity have been discussed previously. Shortly summarized monovalent ions causes a decrease in viscosity due to reduced repulsions between the carboxylate groups and thereby a reduction in the hydrodynamic volume. The hardness of the brine refers to the presence of multivalent ions and the effect is more complex [19]. At low reservoir temperatures, the synthetic polymer solution is stable in the presence of multivalent ions, but at elevated temperatures the presence of multivalent ions causes a stability problem. As the degree of hydrolysis increases, the solubility of the polymer decreases as the multivalent ions screens the negative charges of the backbone more effectively [16]. This can cause precipitation [19].

3.4 Polymer retention

As previously mentioned, partially hydrolyzing a synthetic polymer reduces the degree of adsorption, but it does not eliminate the issue. All polymers traveling through a permeable media experience polymer retention to some degree, depending on the polymers average molecular weight, flow rate, temperature, the rock composition, permeability, brine salinity and hardness. Polymer retention primarily occur due to adsorption on the surface of solid, referred to as polymer adsorption, but it can also occur due to mechanical entrapment in small pores or be caused by a sudden increases in flow rates after a steady-state polymer injection, referred to as hydrodynamic retention, but this mechanism appears to be reversible and less severe [16]. The two latter mechanisms of retention is related and all three are illustrated in Figure (3.6) [7].

Polymer adsorption, which is the primary retention mechanism, is due to the interaction between the solid surface and the polymer molecules. The interactions binds the polymer molecules to the surface and removes them from the bulk solution [19], causing the concentration and thereby the viscosity of the polymer solution to decrease. The larger the surface area, the higher levels of adsorption will occur [7].

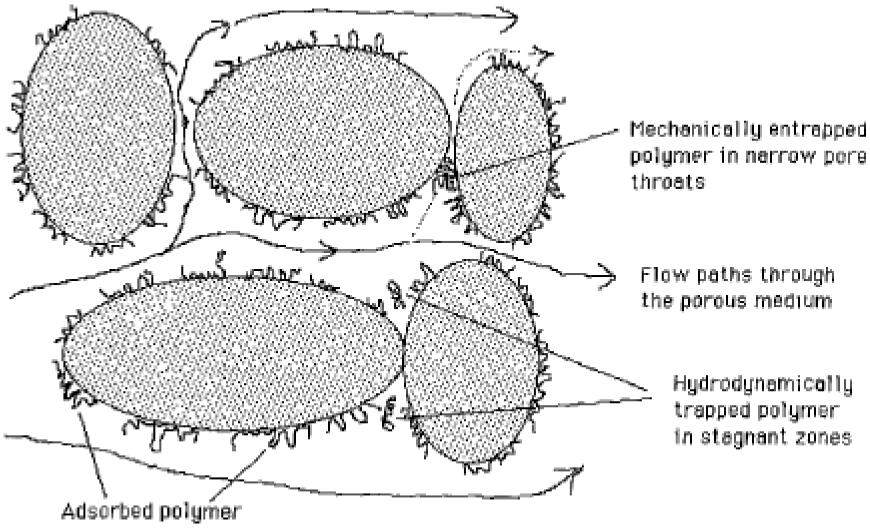

Figure (3.6). Diagram of polymer retention mechanisms in porous media. Picture is taken from Sorbie, 1991, p. 129 [7].

Mechanical entrapment only occurs in a porous media and can be viewed as a filtration mechanism. The constrictions in the porous media can be small relative to the large polymer molecules and thereby preventing them to pass and mechanically traps the polymer molecules. As the polymer solution often has an unknown size distribution and the molecular weight is given as an average of the wide range of average sizes, no general relationship has been developed between polymer mechanical entrapment and the medias broad pore size distribution [16].

Hydrodynamic retention only occurs in porous media as well. Maerker (1973) found that synthetic polymer (and biopolymer) solutions lose more molecules at higher flow rates by determining the residual resistance factor after studying several injections with a decreasing constant pressure drop. He concluded that this happened through interactions between the polymers and the porous rock and concluded that these interactions was somewhat reversible [29].

Due to the difficulties of measuring the three retention mechanisms, the loss of polymer during a flooding is referred to as retention without differentiating between the mechanisms [19]. Retention causes loss of polymer and consequently reduces the mobility control effect and the efficiency of the polymer flood [9]. One of the key factors determining which type of polymer that will be used during a polymer flood is the retention due to the economic viability [7]. The desirable level of polymer retention is below 20 $\mu g/cm^3$ [9].

3.4.1 Consequences of polymer retention

A consequence of polymer retention is the inaccessible pore volume (IPV). The average size of the polymer molecules is larger than the water molecules and due to mechanically entrapment, the polymers cannot flow through all the pores contacted by water. The fraction of pores not contacted by polymer is referred to as inaccessible pore volume and has been observed for all types of polymers [16]. The inaccessible pore volume becomes more pronounced as the average molecular weight increases and the characteristic pore size decreases [9].

Polymer retention causes reduction in the permeability of the rock and depends on polymer type, pore-size distribution and the average polymer size compared to the size of the pores to the porous media [16]. The permeability reduction causes reduced mobility and increased viscosity, which results in an offset between bulk rheology measured in viscometers and viscosity-shear-rate data derived from flow experiments. An indicator of the polymers total mobility lowering contribution is the resistance factor, R_F, which is the ratio of the injectivity to brine to the injectivity of a single-phase polymer flow under same conditions. It can also be expressed in the terms of the invers ratio of pressure drops during constant flow rate experiments and is often used to express the apparent viscosity of the polymer [9].

$$R_F = \frac{\lambda_w}{\lambda_p} = \frac{dP_{polymer}}{dP_{brine}} \tag{3.10}$$

Where

λ_w – the mobility to brine

λ_p – the mobility to polymer

The permanence of the permeability reduction is described by the residual resistance factor, R_{RF}, and can be determined by measuring the permeability to brine before and after a polymer flood. It can be described in terms of the ratio of the initial brine mobility, λ_w, to the brine mobility after displacing all the mobile polymers, λ_{wp} [9], [16].

$$R_{RF} = \frac{\lambda_w}{\lambda_{wp}} \tag{3.11}$$

At high salinities or hardness the permeability reduction is decreased due to reasons explained above [16].

3.5 Injectivity

The injectivity, I, of a well can be thought of as the opportunity to flow a desired volume of polymer solution into a reservoir each day and is defined as:

$$I = \frac{q}{\Delta P} \tag{3.12}$$

Where q is injection rate and ΔP is injection pressure drop [28], [30]. If combining equation (3.12) with Darcy's equation for radial flow, equation (2.7), the injectivity of a one-phase Newtonian flow through a radial porous media is defined as:

$$I = \frac{q}{\Delta P} = \frac{2\pi h K}{\mu \ln(\frac{r_w}{r})} \tag{3.13}$$

where h is the thickness of the radial core, K is the absolute permeability, μ is the viscosity of the fluid, r_w is the radius of the well and r is the radius of the core.

Maintaining an adequate injectivity during a polymer flood is a well-known issue, together with polymer stability and salinity and is important to consider for several reasons [9]. The economics of a polymer project is directly affected by the possible rate the polymer solution can be injected, as it controls the propagation of the polymer front and the arrival of the oil bank [31]. However, the injectivity is constrained by the fracturing pressure of the formation and high injection rates and consequently high injection pressures, can cause the formation to fracture near the well. Fracturing and fracture growth, especially in layered reservoirs, has an significant influence on the oil recovery and sweep efficiency as fracture growth in one layer can cause the other layers to remain unswept [32]. Furthermore, possible cleanup jobs performed on an injection well due to polymer or polymer-microgel plugging, which decreases the injectivity of the well, also influences the economics of the project [31]

Directly from equation (3.12) it is clear that mechanisms that increases the pressure drop contributes to decreasing the injectivity of the well [30]. Shear thickening is therefore a less favorable mechanism near the wellbore and shear thinning is a desirable property as the polymer solution can be injected without the same level of additional pressure drop in the wellbore region at higher rates. Shear thickening is a desirable property in the rest of the reservoir as it more effectively displaces the unswept (bypassed) oil from zones of lower permeability and has a high apparent viscosity in high permeable zones due to higher velocities. Consequently a shear thinning behavior would perform weaker in displacing bypassed oil as the apparent viscosity in the high permeable zones could be lower than the one in low permeability zones, due to increased velocity in high permeable zones [25].

Increased average polymer molecular weight as well as polymer retention and mechanically degradation is also known to affect the injectivity of a well [30]. An increased polymer molecular weight results in a larger molecular coil and higher viscosities, and when adsorbed or retained, consequently leads to an increased permeability reduction. A lowered permeability causes an increased pressure drop and thereby reduces the injectivity. Mechanically degradation breaks the polymer apart thus reducing the viscoelastic effect and the apparent viscosity. A decreased solution viscosity results in a lower differential pressure and an improved injectivity. However, mechanical degradation influences the viscosifying extent of the polymer solution and consequently results in a reduced solution viscosity and a less favorable mobility, which could further influence the volumetric sweep efficiency [31]. Polymer plugging is also a well-known cause of reduced injectivity and is due to ineffective polymer hydration or debris in the polymer solution [33]. If the polymer solution is derived from dry polymer, the powder needs to be uniformly wetted and hydrated and if not dispersed and mixed properly, lumps of polymer powder remain in the solution. Depending of the size of these lumps, an external or internal filter cake will form and reduce the injectivity. Further, large molecular weight species and microgels will be filtered by the porous media and result in a reduced injectivity [31].

Depending of the cause of the injectivity decline, several measures can be performed to overcome the reduced injectivity, as reducing the injection rate or reduce the polymer concentration if the injectivity decline is caused by polymer rheology [31].

4 Previous laboratory studies

In 1964, Pye reported that water-soluble polymers containing polyacrylamide exhibited an unusual and interesting property, which was later known as viscoelastic behavior i.e. shear thickening, and their viscosity measured in formation differed from the values found in a viscometer. He defined the term resistance factor, R, on the basis of the ratio of the brine mobility to the polymer solution mobility, under the assumption that the permeability was constant and there were no permanent permeability loss resulting from the polymer flow. An increase in resistance factor was observed at high rates and thought to be related to the rock properties [34].

In the following years, numerous studies were performed to examine polyacrylamide behavior in porous media and a general agreement of the viscoelastic behavior of synthetic polymers in porous media was stated. Smith (1970) reported that the polymer solution mobility decreased with increased flow rate [35], Jennings et al. (1971) found that the complex flow behavior of viscoelastic fluids could result in large flow resistances at high flow rates in porous media [36] and Hirasaki and Pope (1974), Chauveteau (1981), and others, reported that the shear thickening effect could be explained by the coil-stretch transition of macromolecules in elongational parts of the flow [37], [38]. This confirmed Pye's theory of how the increase in resistance factor was related to rock properties.

Comprehensive studies regarding mechanical degradation of synthetic polymer was performed as well. Maerker (1975) investigated the cause of mechanical degradation in dilute polymer solutions and reported that mechanical degradation was caused by large viscoelastic normal stresses generated primarily by elongation flow fields and became more severe with larger fluxes. This is due to the flexible nature of synthetic polymers [39]. This has also been confirmed in recent time by Zaitoun et al. (2012), who found that mechanically degradation occurs mainly when the macromolecule is fully stretched, which happens at high velocities and near the wellbore where viscous friction is high. They also concluded that acrylamide polymers are very sensitive for mechanical degradation due to their flexible nature and that hydrolyzed polyacrylamides sensitivity to degradation increases with molecular weight and salinity [40].

In 1983, Seright reported that polyacrylamide solutions mechanically degrade at high fluxes when injected into porous medium and this effect could be seen by an entrance pressure drop. This entrance pressure drop was observed to be equal to zero at low fluxes. He further defined the injectivity model and stated that polymer solution injectivity increases at higher injection rates due to severe mechanical degradation and the following entrance pressure drop [28].

Another topic of discussion in literature is whether synthetic polymers in porous media exhibits a pseudoplastic (i.e. shear thinning) behavior at low velocities, an apparent Newtonian plateau at moderate velocities and a pseudodilatant (i.e. shear thickening) at higher velocities, or if it is only shear thickening at high velocities and is approaching a Newtonian plateau at lower velocities.

Delshad et al. (2008) developed an apparent viscosity model that accounts for both shear-thinning and shear-thickening behavior for polymer solutions in porous media, which was tested by history matching and reported as a good fit and thereby reporting both shear-thinning and shear-thickening behavior of HPAM solutions in porous media [25]. This is also confirmed by several authors, including Skauge et al. (2016) who found that radial polymer flow demonstrates both shear thinning and shear thickening behavior [1].

Seright et al. (2009) examined injectivity characteristics of EOR polymers and observed that at low to moderate fluxes, HPAM solutions behaved Newtonian, while a pseudodilatant behavior was observed at moderate to high fluxes. They found no evidence of pseudoplastic behavior and proposed that this type of behavior was an experimental artifact originating from either less accurate pressure transducers, forming of an internal or external filter cake due to mirogels or high molecular weight species preventing the flow to propagate or that the temperature was not controlled [33]. However, in 2010, Seright et al. stated that shear thinning could be observed in porous media if:

1. Fresh HPAM solutions was injected in short cores with sufficiently low permeability. The effect was attributed to high molecular weight species and was found to be reduced by either exposing the solution for high flux before injection or pass the solution through rock at low flux.
2. HPAM solutions with a sufficiently low salinity and/or sufficiently high polymer concentration at moderate to low fluxes.

The shear thinning effect was found to be small compared to the level of shear thickening [41].

The onset of shear thickening behavior is an important topic as well, and Heemskerk [1984] reported that the viscoelastic properties of polymer solutions in porous medium became reflected by a shear thickening behavior beyond a critical shear rate [42].

More recent studies at CIPR, Skauge et al. (2016), found that the onset of shear thickening increases with injection rate in radial flow. Further, higher rates experience a longer shear thickening region and reaches an apparent Newtonian plateau further away from the injection well compared to lower rates [1]. The onset of extensional flow (shear thickening) has also been correlated to rock properties by Zamani et al. (2015) who found the onset of shear thickening to depend on rock type, its tortuosity and permeability, as well as the polymer properties. They attributed the variating onset to the polymer memory effect and stated that the onset in one single rock sample will vary at different points in the porous media thus vary for various injection rates [27]. Skauge et al. (2015) further suggested that the slope of shear thickening might be an inherent rock property and related to permeability, pore size distribution and tortuosity as the slope of shear thickening appeared to be independent of polymer molecular weight and brine salinity [43].

5 Simulation models

In this thesis two simulation tools were used for history matching; STARS by Computer Modelling Group and MRST (MATLAB) by SINTEF. STARS was used to perform the manual history matching, while MRST was utilized for automatic history matching using EnKF. The following subchapters will have a short introduction of both, together with the core model used in each simulator and a sensitivity analysis performed in STARS.

5.1 STARS by CMG

Stars is a product of Computer Modeling Group Ltd. (CMG) and is an advanced process reservoir simulator, which includes chemical flooding, dual porosity and permeability, flexible grids and more. It uses a wide range of grid and porosity models in both field and laboratory scale and the grid systems can be either Cartesian, of variable depth/thickness or cylindrical. The latter is used in this thesis.

Here, STARS is used to history match flooding experiments, both for waterflooding and polymer flooding on laboratory scale. The results from the simulations in STARS was utilized by the feature “Results 3D”, which lets you view the changes in the grids when a property changes with time [44]. In this thesis, the focus was on both the pressure and the apparent viscosity. To ensure that the flooding has gone through the whole disk, it was necessary to observe the viscosity development with time in “Results 3D”. To plot the pressure against the radius of the disk, the output pressure data was extracted and matched towards the experimental pressure data. Since STARS calculates the absolute pressure and not the pressure drop over the disk, the atmospheric pressure was subtracted from the pressure output of the simulations, taken from the feature “graph viewer”. As the output pressure in STARS is given in kPa and the experimental data is given in mbar, was the differential pressure from STARS converted from kPa to mbar.

In the following subchapters, there will be a review of STARS and the focused variables used when manually history matching waterflooding and polymer flooding, as well as a sensitivity analysis.

5.1.1 STARS – Core model

The core model used in STARS is based on the core used in the experiment, shown in chapter 6, and is a radial disk with a thickness of 3,11cm and a radius of 15cm. The properties of the rock are presented in Table 6.1. The disk consists of one grid in J and K-direction and is divided into 148 grids in I-direction. 147 grids have a grid size of 0,1cm, while the last grid (nr.148) represents the outer boundary and has a grid size of 0,3cm and a very high permeability and porosity. The permeability of the 147 grids is considered to be isotropic. The radius of the injection well is 0,3cm and the producer is located in a radial path, 15cm away from the injection well.

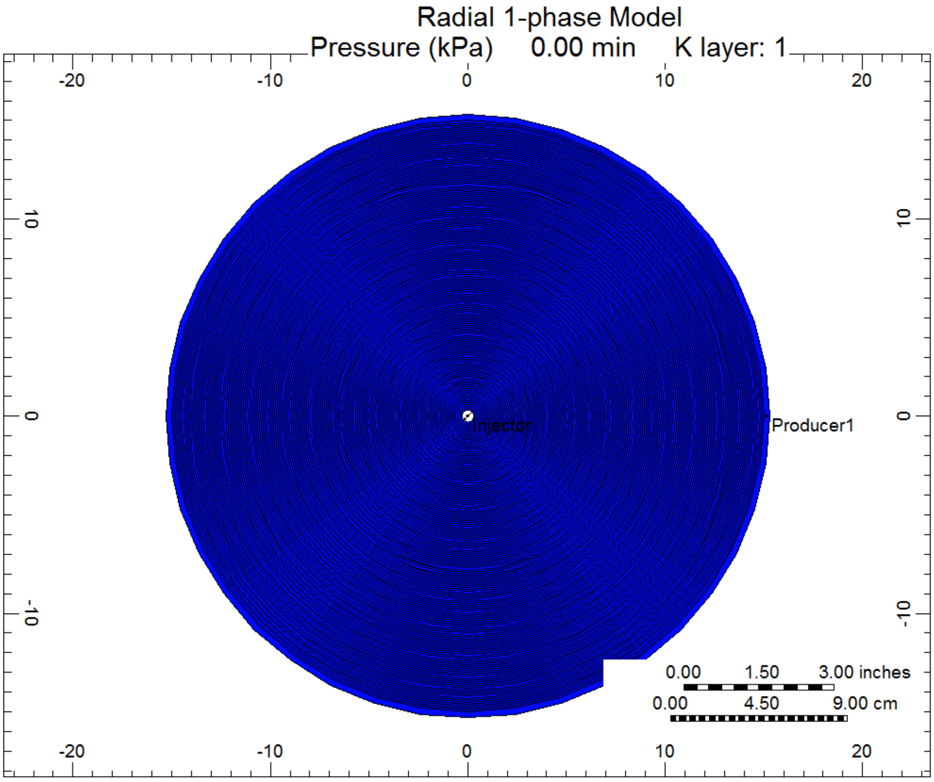

Figure (5.1). The core model used for the sensitivity analysis and the core scale history matching viewed in areal I-J 2D view.

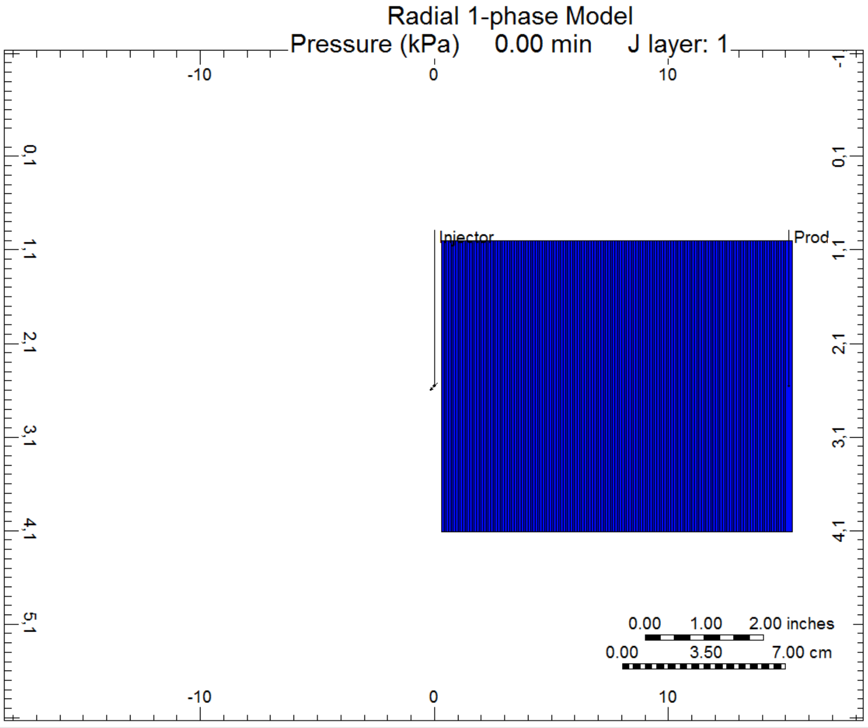

Figure (5.2). The core model used for sensitivity analysis and history matching on core scale, viewed in areal I-K 2D view.

5.1.2 STARS – Waterflooding

As previously mentioned, the experiments used for history matching is performed on a radial disk. This is specified in the script by the keyword GRID and RADIAL. The main objective of simulating a waterflood is to determine the absolute permeability of the core and it is the only tuning parameter when history matching a waterflood, as it is the only free variable in the Darcy equation for radial flow. This is specified by the keyword PERMI, when assumed that the permeability isotropic, i.e. the same in J, K and I direction.

5.1.3 STARS – Polymer flooding

Similar to the history matching of waterflooding, there is only one tuning parameter in history matching of a polymer flood. As the permeability is determined from the waterflood, the viscosity of the polymer is the only free variable in Darcy's equation for radial flow, hence the only tuning parameter. In STARS, the viscosity is specified by the keywords AVISC and SHEARTAB. However, there are several keywords which need to be considered when simulating a polymer flooding, due to the polymer properties described in chapter 3.

ADRT
ADSTABLE
ADMAXT
AVISC
CMM
DTMAX
PORFT
RRFT
SHEARTAB

ADRT is the residual adsorption level. This parameter is ranging from completely reversible (0) to completely irreversible (the value of *ADMAXT*). *ADMAXT* represents the maximum adsorption capacity of the rock and must be a positive value. When *ADMAXT* equals 0, there is no adsorption. *ADSTABLE* is a table of adsorption (*adt*) versus composition (*cpt*) and denotes the composition dependence. The absorption (*adt*) is the adsorbed moles per unit of pore volume at composition *cpt* and *cpt* is the mole fraction of the phase from which the adsorbing components composition dependence will be taken. *adt* and *cpt* has to increase by more than 1e-10 [44]. In this thesis, *cpt* refers to the mole fraction of polymer in water.

PORFT is the accessible pore volume and has an allowed range from 0, meaning that there is no fraction of available pore volume, to 1, meaning that every pore is available. *RRFT* is the residual resistance factor for the adsorbing component, which must be greater or equal to the default, which is 1.

CMM assigns molecular weights and consequently affects the mole fraction of the polymer, *cpt*. *SHEARTAB* specifies the non-Newtonian viscosity in a table with Darcy velocity versus viscosity and has a maximum allowed number of 40 table rows. AVISC is the viscosity and when BVISC equals 0, the viscosity is temperature independent. DTMAX is the maximum time step allowed and has a range to 10^{20} days. [44]. The unit of each parameter is listed in the nomenclature.

5.1.4 Sensitivity analysis in STARS

The following sensitivity analysis is executed to verify the script used in the history matches executed manually in STARS. This is performed to measure the sensitivity of the parameters and their influence on the simulation results. As the history matches performed in this thesis is based on differential pressure, the sensitivity analysis will examine how the following parameters and keywords, which were introduced in chapter 3 and 5.1.3, influence the differential pressure; molecular weight, viscosity, residual resistance factor, adsorption, reversible and irreversible adsorption, inaccessible pore volume, time steps and grid size. The parameters effect on viscosity will not be examined as the viscosity is defined in the shear tab and is a set value.

The base case used for the following sensitivity analysis is a history match of a polymer flooding with an injection rate of 10ml/min. The differential pressure data used for history matching and this sensitivity analysis is presented in Table 6.4. The core model used was described previously in chapter 5.1.1.

The sensitivity analysis is performed in lab scale, in grid block 76,1,1, which is located 7,6cm out in the porous media. Each simulation is run long enough to ensure that the properties and the pressure is stabilized.

5.1.4.1 The effect of grid size

When chemicals used in EOR propagates through a porous medium, they are influenced by the tortuous paths and the heterogeneities of the media [44]. This can cause smearing of the spatial gradients of saturation or concentration and a less piston-like displacement due to distribution of the polymer over a larger area. The effect can be reduced by lowering time steps and/or increasing the grid resolution by decreasing the grid size and thereby creating a sharper front [45].

As the permeability in the simulations performed in chapter 7 is divided into three regions, changing the grid size consequently would result in an altered permeability field which would affect the value of the output differential pressure. Due to this effect, the sensitivity analysis of the grid size was performed with a homogenous permeability equal to 2360mD, to avoid an altered permeability and a thereby an altered pressure response.

The sensitivity analysis is performed in block 76,1,1, given that the grid size = 0,1cm. When increasing the grid size, the block number will be changed together with the pressure response, and will therefore not level off at the exact same value. The deviation between the values is not considered significant and is ± 0,5mbar.

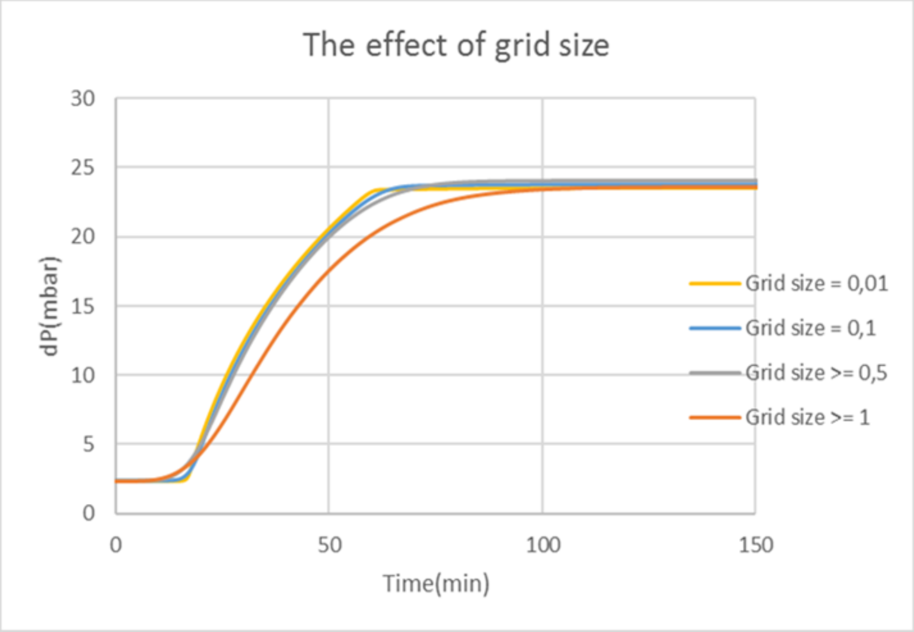

Figure (5.3). The effect of grid size on differential pressure.

Figure (5.3) illustrates how the pressure stabilizes slower with increasing grid size. A grid size ≥ 0,5 deviates slightly from the grid sizes of lower values, but not significantly. Due to the measurements of the core, a homogenous grid size is easier to work with when defining the model and the permeability in the script. As grid size = 0,1 and 0,01 shows no noticeable difference in differential pressure response and achieves an adequate grid resolution to prevent smearing of the front, a grid size of 0,1 is considered sufficient when history matching and does not influence the stabilized differential pressure value.

5.1.4.2 The effect of time steps (DTMAX)

DTMAXT is the maximum allowed time step, which on lab scale is measured in minutes. The DTMAX values tested was: 0,01, 0,1, 1 and 10.

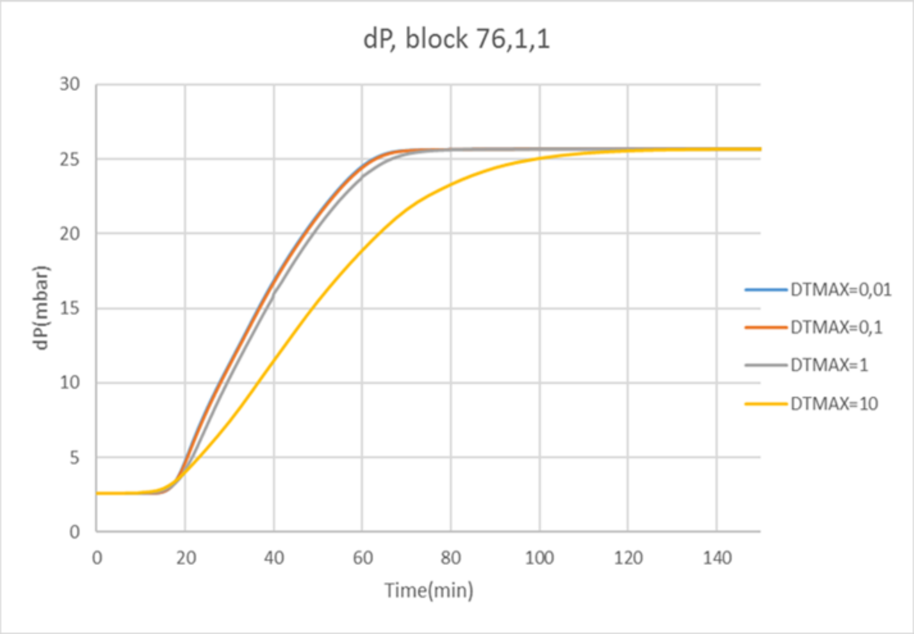

Figure (5.4). The effect of DTMAX on the differential pressure in block 76,1,1.

Figure (5.4) demonstrates how an increase in DTMAX causes a slower stabilization of the differential pressure. DTMAX=10 illustrates numerical dispersion, but the effect appears to diminish when DTMAX < 1. The simulations performed in chapter 7 is carried out with DTMAX=0,01, however DTMAX=0,1 would be considered sufficient as there is no noticeable difference in the stabilization of the differential pressure values between DTMAX=0,01 and 0,1.

5.1.4.3 The effect of viscosity (SHEARTAB)

The viscosity, which is the most important property when determining the efficiency of a polymer flood, is the only parameter that is being altered during the differential pressure history matches of polymer flooding. As the main objective of this thesis is to estimate the in-situ polymer rheology, it is therefore a critical value to consider during the sensitivity analysis. It is important that the keyword SHEARTAB follow the values stated in the script and that the differential pressure response follows accordingly. Simulations was run with shear tabs which had an increase of +50% and decrease of -50% of the base case shear tab apparent viscosity, shown in the figures below.

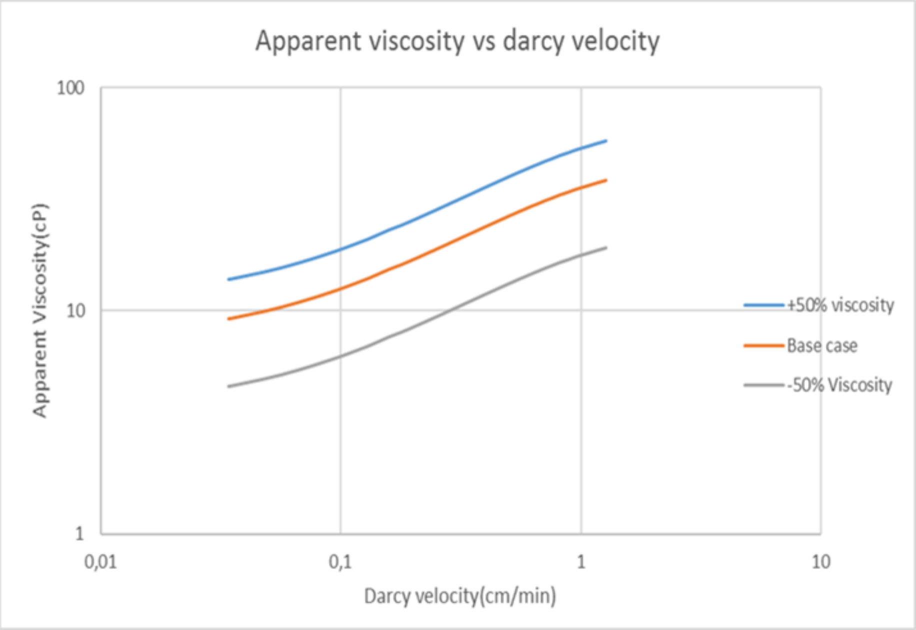

Figure (5.5). Sensitivity of SHEARTAB.

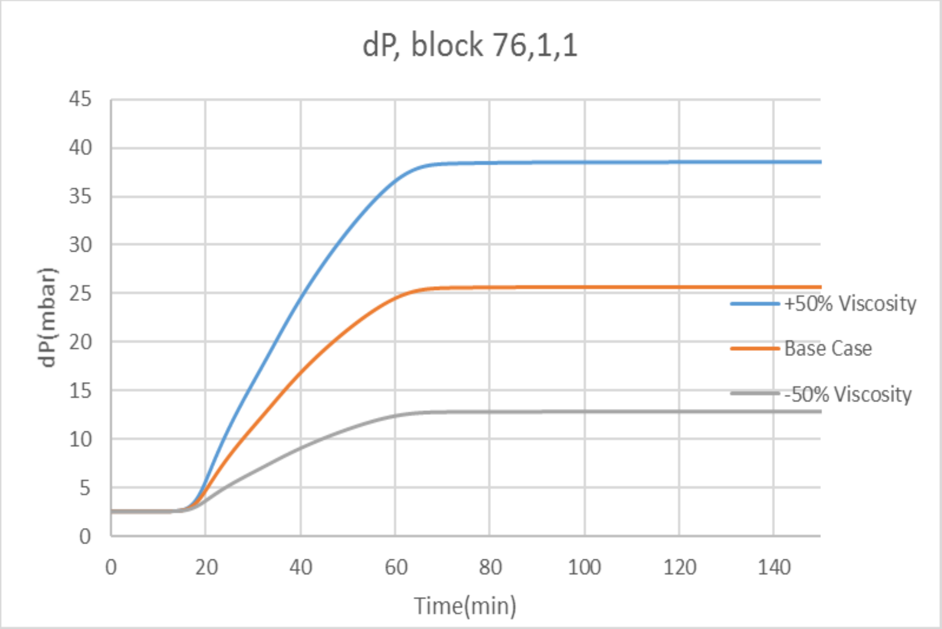

Figure (5.6). The effect of the apparent viscosity on the differential pressure.

Figure (5.5) and Figure (5.6) illustrates how an increased apparent viscosity of +50% of the base case leads to an increase in differential pressure by 50%, as expected as the viscosity is proportional to the differential pressure by Darcy’s equation of radial flow.

5.1.4.4 The effect of molecular weight (CMM)

The molecular weight of the polymer is given as 18 million Daltons and is used to calculate both the mole fraction and the adsorption. Adsorption is considered as the primary retention mechanism and was calculated by (5.1), taken from [7], p. 128.

$$\Gamma_m = x2{,}7194\rho_R \; lb/AF \tag{5.1}$$

Where Γ_m is the retention in mass of polymer per unit volume of rock, x = the adsorption level in mass polymer pr unit mass of solid, Γ and ρ_R is the bulk formation density, assumed to be equal to 2,65g/cm^3. Lb/AF is pound per acre feet and was converted to g/cm^3 [7]. The unit used in STARS is mol/cm^3 and the retention value was therefore divided by molecular weight.

Consequently, when using a molecular weight equal to 18 million Dalton, the adsorption level (adt) resulted in a value below the allowed range. By scaling the molecular weight and thereby scaling the mole fraction and the adsorption level, a more satisfying value was obtained. However, the effect of scaling the molecular weight, mole fraction and adsorption should be examined.

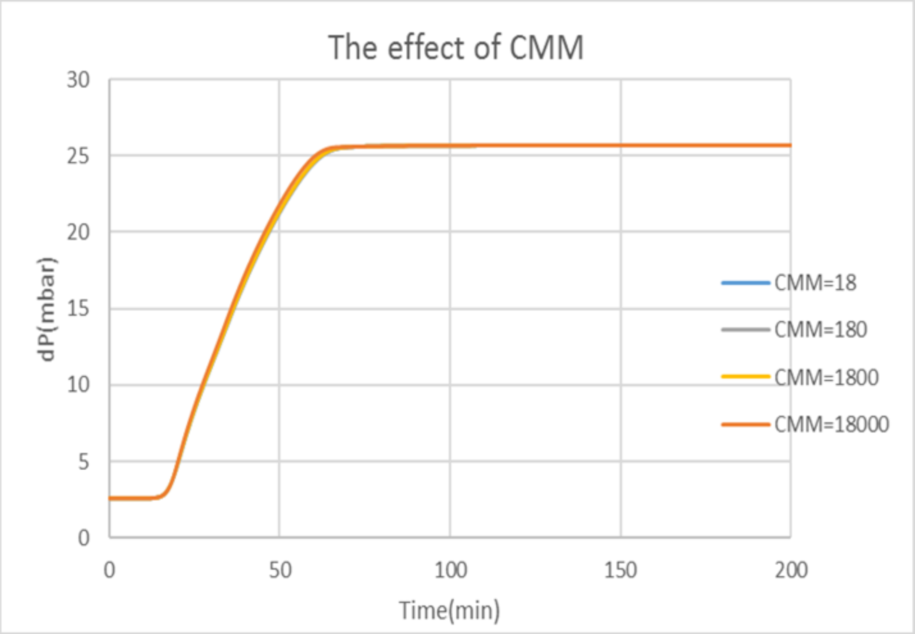

Figure (5.7). The effect of scaling molecular weight (CMM) on differential pressure.

By only changing CMM in the script, it appears that scaling the molecular weight from the original value of 18 million Daltons, which equals 18000kg/mole, to 18kg/mole, has no effect on the differential pressure, illustrated in Figure (5.7). Although this have no effect on the differential pressure, it does influence the material balance error, MBE, which ideally should be as low as possible. The material balance error which occurred by only scaling the CMM in the script is shown in Table 5.1.

Table 5.1. The effect of only scaling CMM in the script and the corresponding material balance error.

CMM (kg/gmole)	cpt	MBE (%)
18	$1,0008 \cdot 10^{-6}$	0,295
180	$1,0008 \cdot 10^{-6}$	0,339
1800	$1,0008 \cdot 10^{-6}$	0,755
18000	$1,0008 \cdot 10^{-6}$	3,643

Altering the molecular weight alone and not the corresponding mole fraction will result in an increased material balance error and has no true meaning as these two are directly related. Thus, the following will examine the effect of altering both the molecular weight and the corresponding mole fraction, cpt. The mole fraction is converted from the polymer solution concentration (ppm) by following equation:

$$Concentration\ (weight\ \%) = \frac{n_p}{n_w} \cdot \frac{M_p}{M_w} \tag{5.2}$$

Where n_p is mole polymer, n_w is the mole water, M_w and M_p is the molecular mass of water and polymer, respectively.

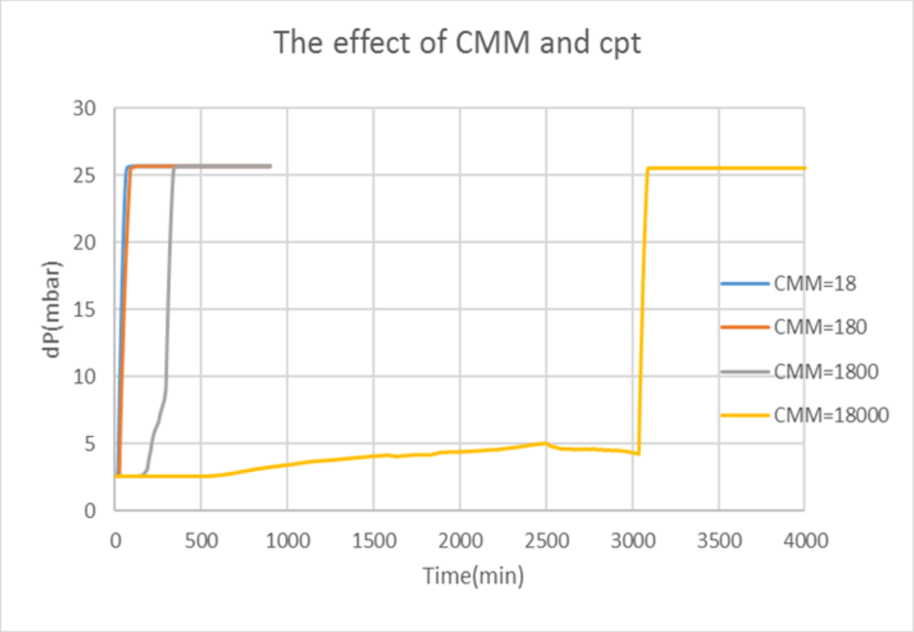

Figure (5.8). The effect of scaling both CMM and cpt on the differential pressure.

Figure (5.8) is supposed to demonstrate how the scaling of both CMM and cpt effect the differential pressure, however, the figure demonstrates more the effect of adsorption. When scaling both the molecular weight and the mole fraction, but not the corresponding adsorption, the mole fraction becomes closer to the order of the adsorption thus it require more time to reach a stabilized differential pressure as the front of polymer is highly adsorbed and propagates slower through the media. This is better illustrated under the discussion of ADMAXT, in chapter 5.1.4.7. The material balance error occurring when scaling both CMM and cpt is listed in Table 5.2.

Table 5.2. The effect of changing both CMM and cpt and their corresponding material balance error.

CMM (kg/gmole)	cpt	MBE (%)
18	$1{,}0008 \cdot 10^{-6}$	0,295
180	$1{,}0008 \cdot 10^{-7}$	16,57
1800	$1{,}0008 \cdot 10^{-8}$	42,25
18000	$1{,}0008 \cdot 10^{-9}$	33,37

The material balance error increases with increased molecular weight and corresponding decreasing mole fraction, shown in Table 5.2. This can be an artifact of the unscaled adsorption, but since the adsorption cannot be scaled with the molecular weight due to the limit of 1e-10, it is difficult to determine comprehensiveness of this artifact. However, the discussion has shown that scaling the molecular weight by a factor of 1000 can be justified as it reduces the material balance error and does not affect the stabilized differential pressure value.

5.1.4.5 The effect of adsorption (ADSTABLE)

ADSTABLE is the composition dependence which is specified by a table of adsorption. The composition, cpt, is given in mole fraction and has an allowed range from 0 to 1. The molecular weight of the polymer is 18MDa and as the adsorption (adt) of the polymer must increase by at least 1e-10, the molecular weight of the polymer was scaled down from $18 \cdot 10^{6}$g/mole to 18000g/mole as a larger molecular weight consequently resulted in an adsorption below the allowed value and in a higher material balance error, as explained in the previous subchapter [44].

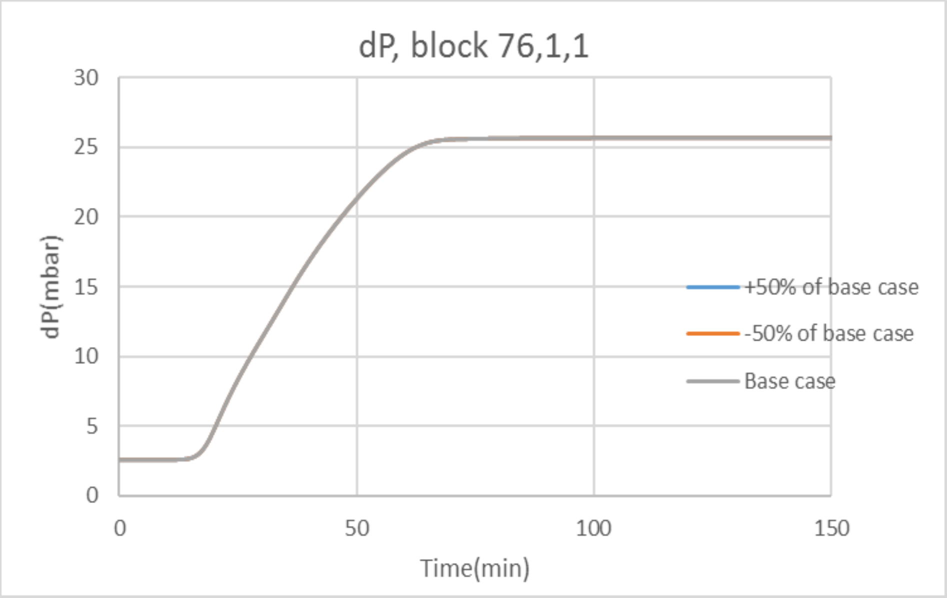

Figure (5.9). The effect of ADSTABLE (adt) on the differential pressure in block 76,1,1.

The figure above illustrates the effect of changing the adsorption in ADSTABLE to - 50% of the base case and + 50% of the base case adsorption. This appears to have no effect on the stabilized differential pressure value or the time it uses to reach a stable differential pressure. Altering adt does not affect the material balance error, listed in Table 5.3.

Table 5.3. The material balance error when changing the adsorption, adt.

adt	MBE (%)
+50% of base case	0,295
Base case	0,295
-50% base case	0,295

Shortly summarized: changing the adt has no effect on the time or value of the stabilization of the differential pressure and does not influence the material balance error.

5.1.4.6 The effect of reversible and irreversible adsorption (ADRT)

As the simulations is run as a single injection and not as a sequence, it is expected that changing the keyword ADRT and thereby the reversibility of the adsorption will show no effect on the differential pressure. Adsorption causes permeability reductions which can be discovered by a second water flooding, for example by running a sequence of polymer and water injections and observing the permeability reductions by an increase in the differential pressure.

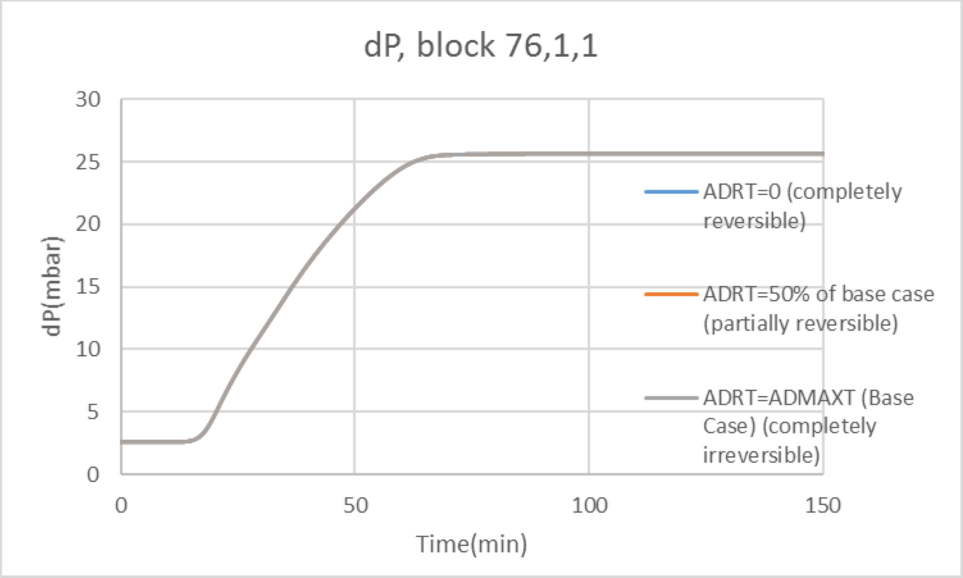

Figure (5.10). The effect of reversible and irreversible adsorption, ADRT.

Table 5.4. How the value of ADRT affect the material balance error.

ADRT	MBE (%)
Completely irreversible	0,295
Partially reversible	0,295
Completely reversible	0,295

However, as illustrated in Figure (5.10) and listed in Table 5.4, changing the reversibility of the adsorption has no influence on the stabilization of the differential pressure nor the material balance error as the simulation is run as a single injection.

5.1.4.7 The effect of the maximum adsorption capacity (ADMAXT)

ADMAXT is the maximum adsorption capacity of the rock. When ADMAXT=0, no adsorption occurs.

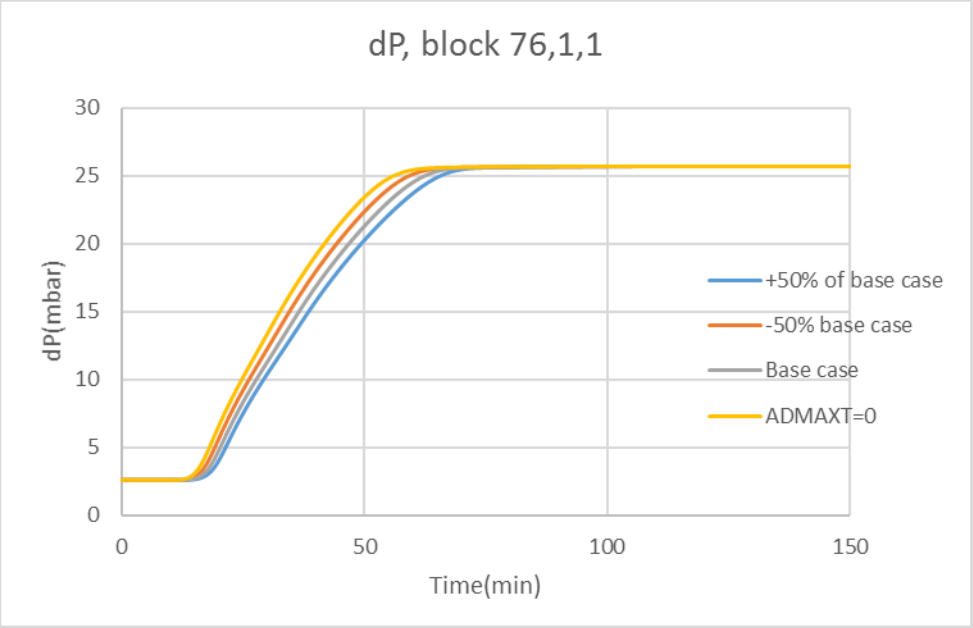

Figure (5.11). The effect of ADMAXT on differential pressure in block 76,1,1.

Figure (5.11) demonstrates how an increased adsorption causes a slower stabilization of the differential pressure due to the slower propagation through the porous media, caused by the continuously adsorption and thereby the need of injection more polymer solution. Consequently, zero adsorption shows a more rapid stabilization of the differential pressure. The amount of absorption appears to influence the material balance error, shown in Table 5.5.

Table 5.5. How changing the value of ADMAXT affect the material balance error.

ADMAXT	MBE (%)
+50% of base case	0,4167
Base case	0,2948
-50% base case	0,158
0	0,0034

As neither the keyword ADSTABLE or ADRT displayed an influence on the stabilization of the differential pressure or the material balance error, it appears that the keyword ADMAXT controls the degree of adsorption. However, it has no influence on the value of the stabilized pressure, only the time of stabilization and the material balance error is considered as sufficiently low.

5.1.4.8 The effect of accessible pore volume (PORFT)

The assumption in the history matching performed in chapter 7 is that all pores are accessible, ergo PORFT=1. PORFT is the fraction of the pores available, meaning that when PORFT=0,9, 10% of the pores are inaccessible.

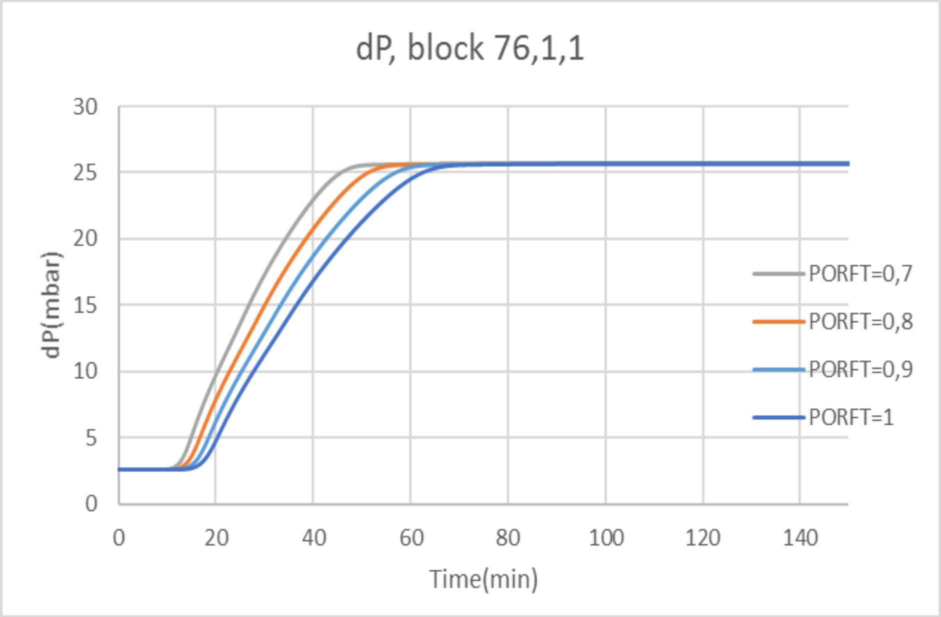

Figure (5.12). The effect of PORFT on differential pressure.

The fraction of pore volume available influences the time of stabilization of the differential pressure and when the fraction of pore volume available decreases, the differential pressure stabilizes faster, shown in Figure (5.12). As the polymer flow travels to a smaller pore volume it reaches equilibrium earlier. The value of PORTF only displays minor effects on the material balance error, which is listed in Table 5.6.

Table 5.6. How the fraction of inaccessible pore volume affect the material balance error.

PORFT	MBE (%)
0,7	0,399
0,8	0,357
0,9	0,323
1	0,295

Shortly summarized: the value of PORFT only influences the time of stabilization.

5.1.4.9 The effect of the residual resistance factor (RRFT)

The residual resistance factor, R_{RF}, indicates the permanence of the permeability reduction caused by the polymers. It must be greater or equal to 1 and is defined:

$$R_{RF} = \frac{\lambda_w}{\lambda_{wp}} \tag{5.3}$$

where λ_w is the mobility of the water before performing a polymer flood and λ_{wp} is the mobility of the waterflooding after displacing all the mobile polymer retained after the polymer flooding.

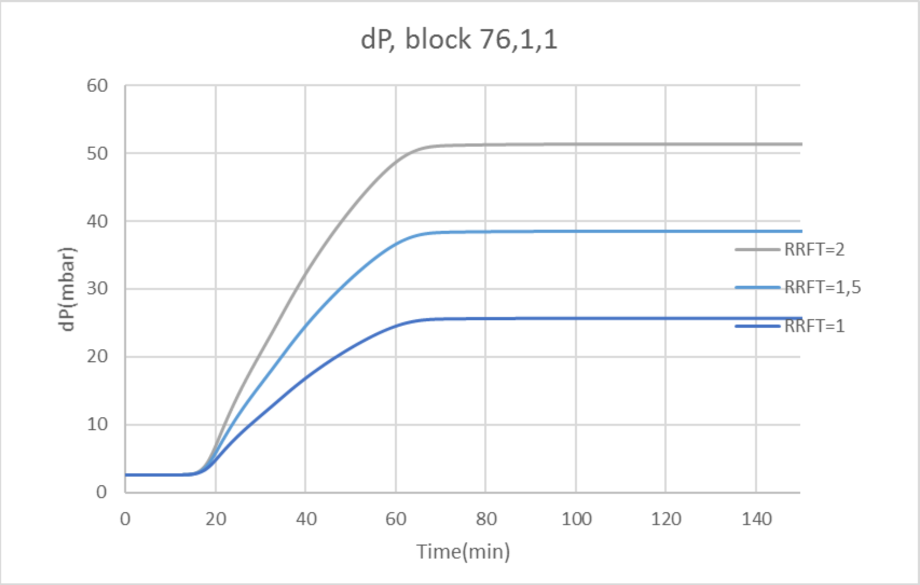

Figure (5.13). The effect of RRFT on the differential pressure.

Figure (5.13) illustrates how the the differential pressure increases when the value of the RRFT increases. This is an expected behavior and is a direct effect of equation (5.3), which also can be written as:

$$R_{RF} = \frac{\Delta P_2}{\Delta P_1} = \frac{\mu_2 Q_2 / K_2}{\mu_1 Q_1 / K_1} = \frac{K_1}{K_2} \qquad (5.4)$$

where K_1 is the absolute permeability of the rock during the first waterflooding, K_2 is the effective permeability after the polymer flooding determined by a second waterflooding, μ_w and μ_{wp} is the water viscosity in the first and the second waterflooding, respectively, and ΔP_1 and ΔP_2 is the differential pressure in the first and second waterflooding, respectively. Equation (5.4) assumes that μ_w and μ_{wp} have the same value and the injection rate is the same in both waterfloodings.

Followed by equation (5.4), an increase in RRFT will result in a decrease in the effective permeability after the polymer flooding, hence an increase in the differential pressure. Doubling the RRFT value from the base case value equal to 1, consequently results in doubling of the differential pressure as the permeability has been reduced to half the value of its original base case value.

The polymer flooding history matches performed in chapter 7 uses a constant permeability field determined by the waterflooding performed before any polymers had traveled through the porous media. Since no secondary waterflooding was performed, there is no information of the possible permeability reduction happening when flooding with a high average molecular weight polymer solution and the RRFT is therefore equal to 1. However, if any permeability reduction occurs in the polymer flooding, this is taken to account by the apparent viscosity, as it is the only tuning parameter. It is therefore possible that the apparent viscosity might be overestimated to reach an adequate differential pressure, which might be increased due to permeability reduction. Since no experimental information about this factor was given, it is considered sufficient to set this keyword equal to 1.

5.1.4.10 Summary of the sensitivity analysis

The numerical dispersion effect diminished with an increased grid solution obtained by decreasing the time steps and the grid size. The simulations in chapter 7 is performed with DTMAX=0,01 and grid size equal to 0,1cm as the grid resolution is sufficiently minimizing the smearing of the front. The keyword SHEARTAB follows the input data in the script and the differential pressure follows accordingly. Scaling the molecular weight and the corresponding mole fraction by a factor of 1000, does not affect the stabilized differential pressure value and resulted in the smallest material balance error. The keyword ADMAXT seems to control the adsorption as the keywords adt and ADRT had no effect on the stabilization of the differential pressure.

The assumption in the simulations in chapter 7 is that the flow is steady-state. Although the pressure is transient, as it varies with position, it is stable after some time and can therefore be numerically considered as steady-state. The polymer properties are not changing over time and are constant when they have stabilized, shown in the sensitivity analysis above.

5.2 MRST

MATLAB is developed by The MathWorks and stands for matrix laboratory. Some of its typical uses include modeling, simulation and data analysis [46]. In this thesis, we use MATLAB Reservoir Simulation Toolbox (MRST) developed by SINTEF, which is an open-source code that aims to support research on modeling, simulation of flow in porous media and contains a wide variety of mathematical models. It consists of a core module that gives basic data structures and since it does not contain flow equations and solvers, it is necessary with add-on modules [47]. The Ensemble Kalman Filter (EnKF) is a workflow tool and an add-on module for MRST, which is developed by the University of Bergen (UiB) and the add-on module utilized in this thesis. EnKF was first introduced in 1994 by Evensen and is an approximating filtering method which has been widely used for history matching of reservoir data [48]. The tool operates by continuous iterations which compares output simulation values with the input experimental data. However, the tool is quite comprehensive and the following will just be a short summary of the approach used in this thesis.

5.2.1 MRST - Waterflooding

Similar to the simulations performed in STARS, the injection rate and the rock properties are stated in the script and the only tuning parameter is the permeability. An analysis of the absolute permeability in the core, performed in chapter 7.1, led to the assumption that the permeability of the core was heterogenous as a homogenous permeability resulted in poor history matches. Furthermore, the disk was divided into three regions and the automatically history matching of waterflooding is thereby governed by five parameters;

- K_1 – the permeability in region 1
- K_2 – the permeability in region 2
- K_3 – the Permeability in region 3
- r_1 – the outer boundary of region 1
- r_3 – the inner boundary of region 3

A description of the core model used in MRST is shown in Figure (5.14). Region 1 is illustrated on the left side of the figure as the blue area near the wellbore and stretches from the outer boundary of the wellbore to the simulated r_1 value determined by the history matches. r_1 and r_3 is given as a fraction of the radius and their corresponding permeability is K_1 and K_3, given in mD. Region 3 is the light blue area illustrated on the right-hand side of Figure (5.14) and the rest of the core, the red area, corresponds to region 2.

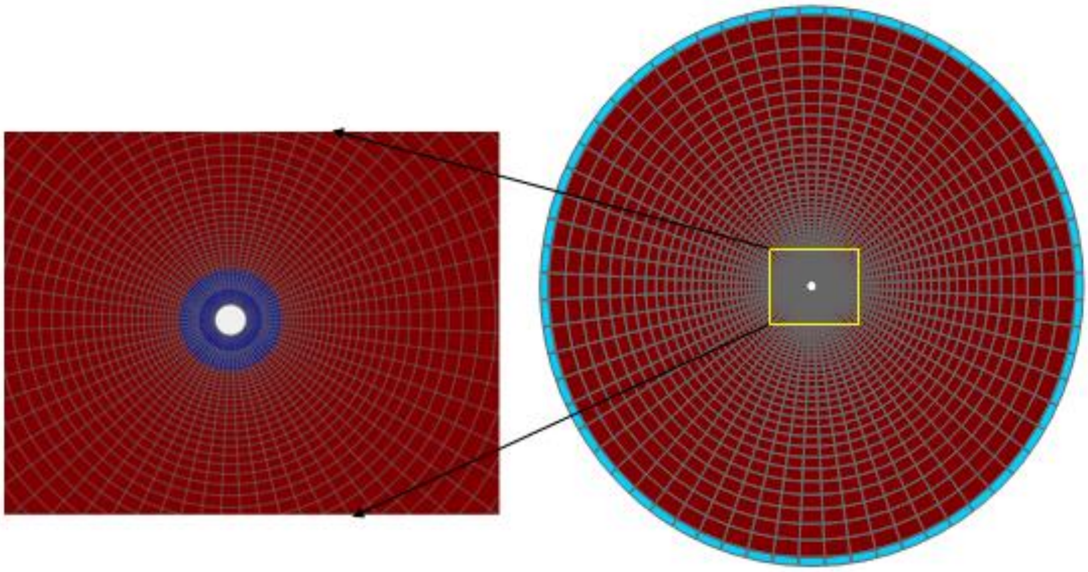

Figure (5.14). Illustration of the core model used in MRST.

By defining a range for each variable and stating the number of ensemble members, iterations and the experimental error, the EnKF numerically simulates the best match within the range of the variables stated in the script. This is better explained by a simple example:

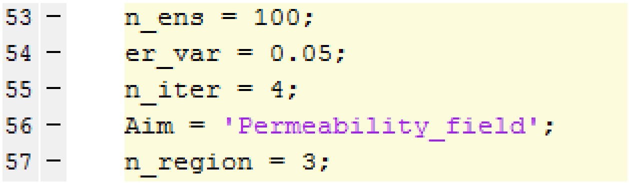

```
n_ens = 100;
er_var = 0.05;
n_iter = 4;
Aim = 'Permeability_field';
n_region = 3;
```

Figure (5.15). A section of the code used in MRST.

The input parameters shown in Figure (5.15) is:

- n_ens – the number of ensembles performed for each iteration. If equal 100, it means that for each iteration, it picks 100 values within the specified range. The recommended value is 100 and the higher the number, the more accurate it is.

- er_var – the experimental error. Describes how trustworthy the experimental data is. The recommended value is between 5-20% and the higher the value, the more freedom the code has.

- Aim – this can either be “Permeability_field” or “in_situ_rheology” and depends on the aim for the simulation. For history matching of a waterflood is the aim “permeability_field” and for polymer flooding, the aim is “in_situ_rheology”.

- n_region – how many permeability regions the disk is divided into.

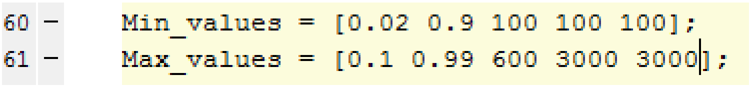

```
Min_values = [0.02 0.9 100 100 100];
Max_values = [0.1 0.99 600 3000 3000];
```

Figure (5.16). Another section of the code. The range of the variables.

Waterflooding aims to find the permeability field which results in the best history match. Figure (5.16) illustrates the range of each parameter in the following order: r_1, r_3, K_1, K_2 and K_3. The top line is minimum value and the bottom line is the maximum value of the range. These might be changed if the first run does not result in an acceptable history match. The bigger the range, the more freedom the code has. The experimental pressure data used for the history match is included in the code as a text file.

After the simulation is finished, MRST gives out three plots; one differential pressure graph, one distribution chart and one for the iterations performed. As the two first are of importance, these are illustrated below for a history match performed for q=5ml/min.

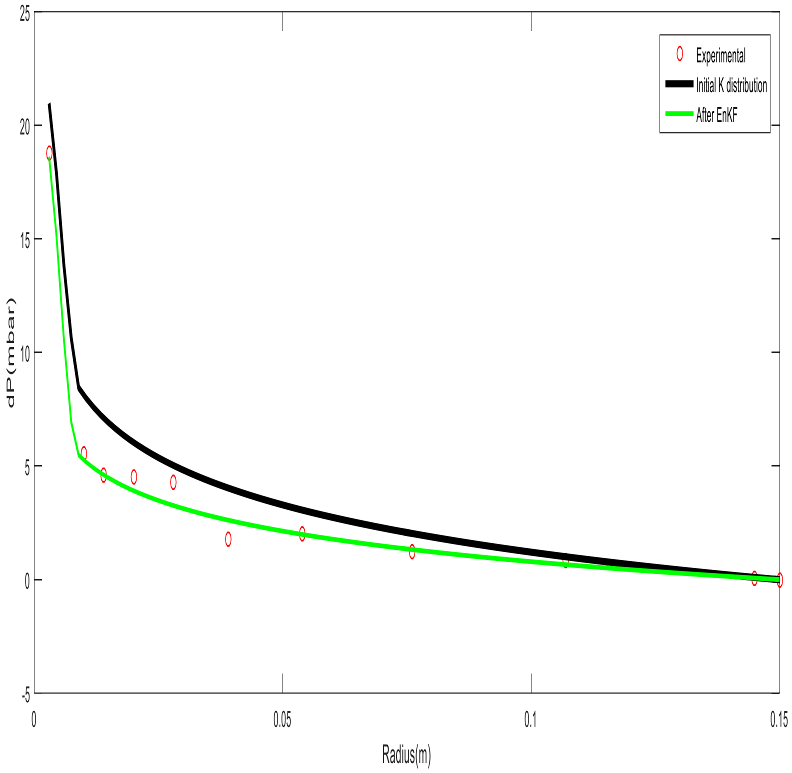

Figure (5.17). Output pressure curve from MRST. Differential pressure versus radius. Red dots – experimental points, black line – Initial K distribution and the green line – after EnKF is ran.

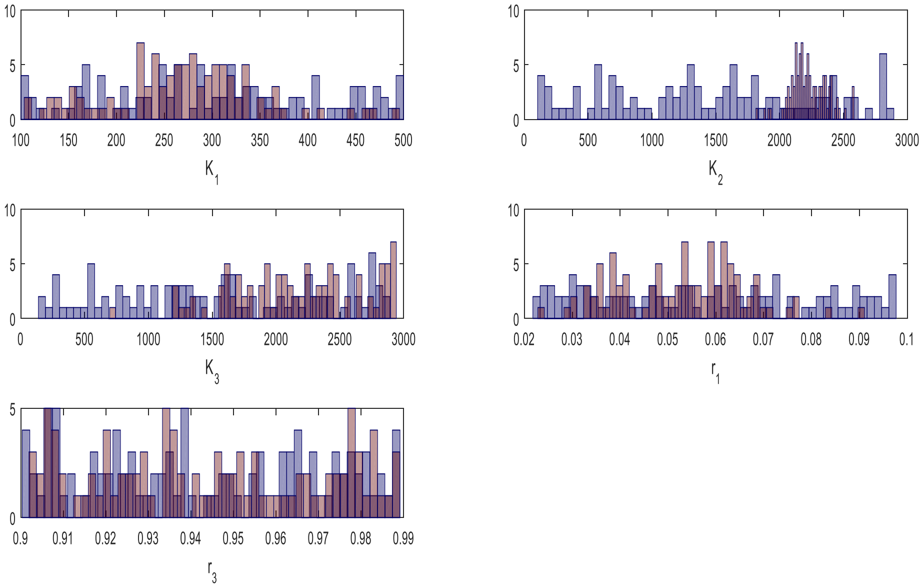

Figure (5.18). The output distribution chart from MRST. Top left hand-side and downwards: K_1, K_3 and r_3. Top right-hand side and downwards: K_2 and r_1.

The distribution chart in Figure (5.18) indicates the distribution of the parameters within the stated range in the script, plotted along the x-axis. The light blue area is the initial values chosen and the average of these initial values and their corresponding pressure match is the "initial K-distribution", shown as a black curve in the differential pressure plot in Figure (5.17). The purple area demonstrates the new hundred values found after the EnKF run and their frequency distribution fraction, stated on the y-axis. A further analysis of Figure (5.18) indicates which parameters are definite, restricted or indefinite:

- K_2 can be considered as a definite parameter as it demonstrates a high frequency within a narrow, defined range.
- K_3 can be considered as a restricted parameter as its frequency distribution is over a larger range and is not as pronounced as K_2.
- r_3 is an indefinite parameter and carries a large uncertainty as its frequency distribution stretches over the whole range of initial values.

The output from MRST is the average of the new values, given as $K_{1\text{ new avg}}$, $K_{2\text{ new avg}}$, $K_{3\text{ new avg}}$, $r_{1\text{ new avg}}$ and $r_{3\text{ new avg}}$ and their corresponding differential pressure match is the labeled "After EnKF", shown as a green curve in Figure (5.17).

5.2.2 MRST – Polymer flooding

The approach for the polymer flooding resembles the previously described approach for the waterflooding. The main difference is the aim: "in_situ_rheology", a specified permeability field and instead of five parameters, there are now six. The code is using the extended Carreau equation (5.5) and the six parameters are listed below:

$$\eta(\dot{\gamma}) = \eta_\infty + (\eta_0 - \eta_\infty)[1 + (\lambda_1\dot{\gamma})^2]^{(n_1-1)/2} + \eta_{\max}[1 - \exp(-(\lambda_2\dot{\gamma})^{n_2-1})] \tag{5.5}$$

Where:

- $\eta(\dot{\gamma})$ – the apparent viscosity
- η_∞ - the infinite shear rate viscosity, equal to 1cP
- η_0 – zero shear rate viscosity
- η_{max} – maximum shear thickening viscosity
- λ_1 – polymer specific empirical constant with an unknown range

- λ_2 – polymer specific empirical constant that includes the polymer relaxation time. The range is unknown, although $\lambda_1 > \lambda_2$.
- n_1- polymer specific empirical constants, should be below 1 and represents the shear thinning behavior of the polymer
- n_2 – polymer specific empirical constant, and should be more than 1 and describes the shear thickening behavior of the polymer. Above 2,5 it is unstable and can lead to numerical errors [25], [27].

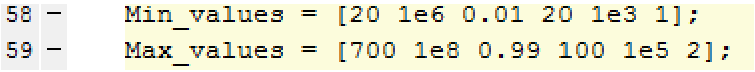

```
Min_values = [20 1e6 0.01 20 1e3 1];
Max_values = [700 1e8 0.99 100 1e5 2];
```

Figure (5.19). Section of the code. The range of the parameters used in in_situ_rheology.

Figure (5.19) illustrates the range of the parameters in the following order: η_0, λ_1, n_1, η_{max}, λ_2 and n_2. The output from MRST is given in four different plots; one differential pressure plot, one distribution chart, one iteration plot and one plot of the rheological behavior of the polymer determined for the specific injection rate. As both the differential pressure plot and the distribution chart was explained in chapter 5.2.1, only the plot of the rheological behavior is shown in this subchapter.

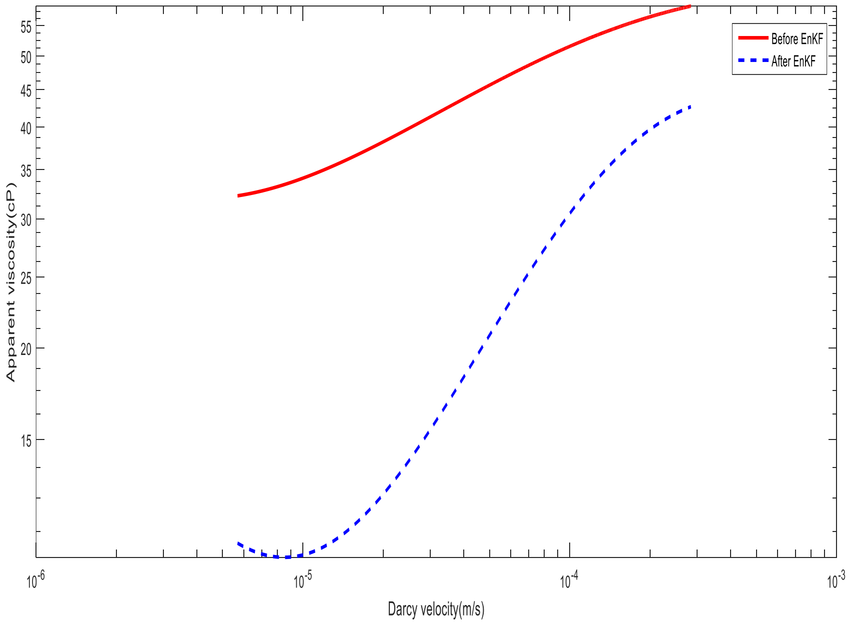

Figure (5.20). The output MRST plot of the apparent viscosity vs. Darcy velocity.

The apparent viscosity curve given by MRST follows equation (5.5). The red curve represents the viscosity before EnKF and the blue curve represents the apparent viscosity estimated by EnKF. The y-axis is the apparent viscosity, given in cP, and the x-axis is the Darcy velocity, given in m/s.

6 Experimental data

Laboratory studies was performed on a radial Bentheimer rock that had a porosity of ~ 24 %, a diameter of 30cm and a height of 3,11cm. The permeability of the disk was not stated in the given experimental dataset, however Bentheimer rocks are known to have a homogenous permeability and usually equals 2,6D [1]. The core properties of the rock material used in this study is listed in Table 6.1.

The disk had 11 pressure ports, when including the pressure ports located at the inner boundary by the injection well and the outer boundary, at the outer rim of the disk. Figure (6.1) illustrates the disk as well as listing the various locations of the pressure ports drilled in the disk.

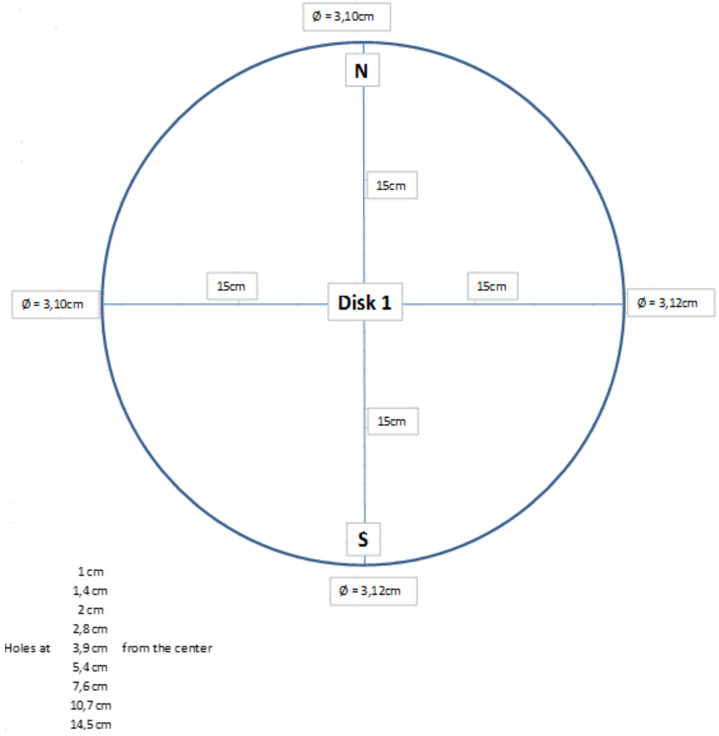

Figure (6.1). Core used in experiment.

Experimental absolute pressures for both waterflooding and polymer flooding of various rates was given and the corrected differential pressures for the floodings is listed in subchapter 5.1 and 5.2. The polymer injected was HPAM at a concentration of 1000ppm and an average molecular weight of 18 million Dalton. Before injecting the polymer, it was pre-filtered at a rate of 1ml/min through a Swagelok filter (60μm) located between the piston cylinder and the core, illustrated in Figure (6.2).

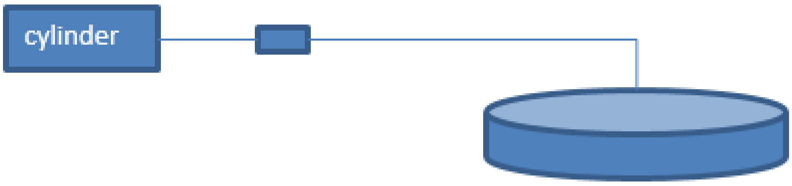

Figure (6.2). Experimental set-up.

Table 6.1. Core properties

			Radial core model
Diameter	D	[cm]	30
Radius	R	[cm]	15
Thickness	H	[cm]	3,11
Bulk Volume	V_b	[cm^3]	2197,22
Pore Volume	V_p	[ml]	525,21
Porosity	Φ	[frac.]	0,239

6.1 Waterflooding

The experiment performed the waterflooding at different, increasing rates:

- 5ml/min
- 10ml/min
- 15ml/min
- 20ml/min
- 30ml/min
- 40ml/min

The corresponding pressure drop at the locations of the pressure ports is presented in Table 6.2. The given experimental pressure data was not back-pressure corrected, thus it was necessary to subtract the outer boundary pressure from the stated pressure values.

Table 6.2. Corrected differential pressure (mbar) for the waterflooding of different rates (ml/min).

q	dP_{rw}	$dP_{r=1}$	$dP_{r=1,4}$	$dP_{r=2}$	$dP_{r=2,8}$	$dP_{r=3,9}$	$dP_{r=5,4}$	$dP_{r=7,6}$	$dP_{r=10,7}$	$dP_{r=14,5}$	$dP_{r=15}$
5	18,77	5,57	4,59	4,50	4,25	1,80	1,99	1,26	0,82	0,04	0
10	30,64	10,85	8,06	7,18	7,28	4,63	3,97	2,65	1,59	-0,44	0
15	44,05	15,63	12,51	10,83	9,57	5,97	5,78	4,20	2,35	-0,54	0
20	57,71	17,43	18,14	13,77	12,40	8,78	7,56	5,06	3,01	0,41	0
30	82,56	28,81	24,70	20,58	19,12	13,49	11,31	8,20	4,26	0,20	0
40	100,08	39,19	32,82	27,12	25,39	19,97	14,83	10,72	5,66	1,27	0

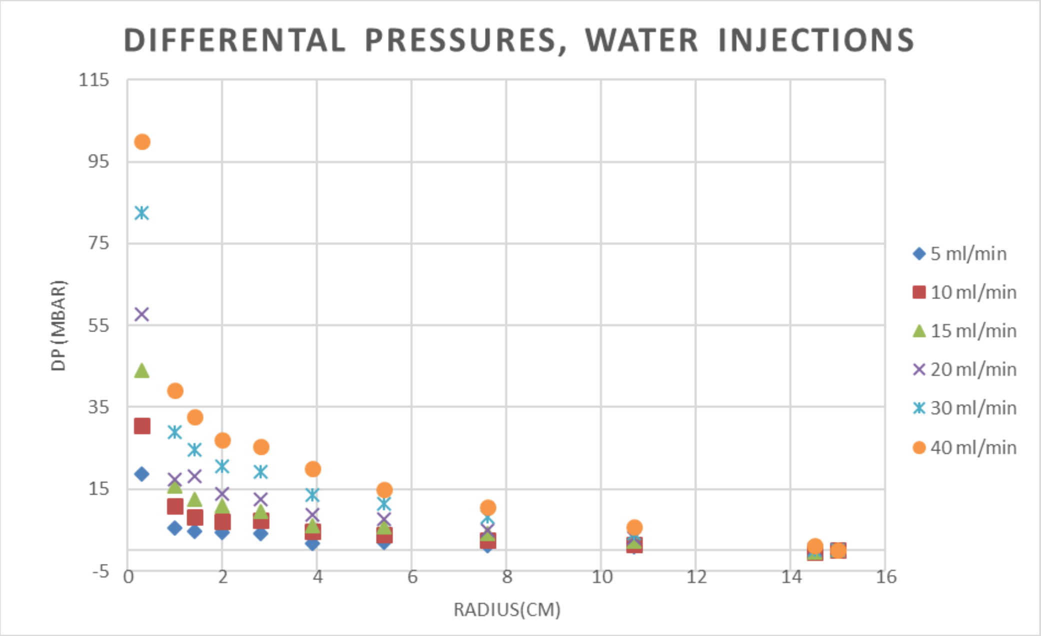

Figure (6.3). The corrected pressures from table (6.2). Differential pressure, dP(mbar), versus radius (cm).

Both Table 6.2 and Figure (6.3) illustrates that there are some differential pressures below zero and these are considered as deviations, as they probably are an experimental artifact caused by the uncertainties of the pressure transducers and the correction of the back-pressure. Lower injection rates and thus low differential pressures carries a greater uncertainty due to the uncertainty of the pressure transducer, depending on their set maximum range.

6.2 Polymer flooding

Polymer flooding is performed in radial disks to better study the in-situ rheology experienced in field applications as the velocities decreases with increased radial distance from the injection well and consequently goes through an unsteady pressure regime. Linear cores do not display this behavior and injection performed in linear cores are at steady state conditions, hence results in a different rheological behavior and is known to display an severe degree of shear thickening [1]. By studying radial flow, a better insight to the conditions experienced in field applications can be obtained.

The polymer flooding was performed by a total of 10 injections rates, where eight of them were increasing in rate from 0,5ml/min to 20ml/min. After the 20ml/min, the injection rate was lowered to 8ml/min and lowered again to 1ml/min.

The experimental pressure values were not corrected for the back pressure, and the pressure measured at the outer boundary of the core was therefore subtracted from the experimental values. The corrected pressure values used for history matching is shown in Table 6.4

Table 6.3. Polymer properties

	Type of polymer	Concentration(ppm)	Average Molecular Weight (Da)	Adsorption, Γ(μg/g)
Radial I	HPAM	1000	18 million	50

Table 6.4. Corrected differential pressure (mbar) for polymer flooding of different rates (ml/min)

q (ml/min)	**dP_{rw}**	**$dP_{r=1}$**	**$dP_{r=1,4}$**	**$dP_{r=2}$**	**$dP_{r=2,8}$**	**$dP_{r=3,9}$**	**$dP_{r=5,4}$**	**$dP_{r=7,6}$**	**$dP_{r=10,7}$**	**$dP_{r=14,5}$**	**$dP_{r=15}$**
0,5	37,49	4,93	3,21	3,37	2,93	1,74	2,34	2,38	2,15	1,73	0
3	217,62	23,48	17,57	19,19	12,95	10,93	9,73	10,03	6,89	5,31	0
5	389,92	48,95	35,70	35,39	25,83	20,35	16,82	13,97	9,49	7,02	0
8	672,19	110,97	75,74	66,06	51,17	38,34	30,16	22,26	14,07	8,85	0
10	894,53	169,26	112,11	92,58	72,13	53,18	40,78	30,26	19,46	12,39	0
12	1087,68	223,43	148,36	114,46	88,47	66,05	49,83	37,12	23,21	14,24	0
16	1494,75	363,01	247,39	183,88	145,14	106,93	81,35	57,40	35,38	20,58	0
20	1928,06	504,59	346,79	253,28	199,28	148,22	111,69	78,71	47,84	26,62	0
8	541,97	119,93	90,27	78,39	66,17	51,89	40,38	27,65	16,16	7,35	0
1	22,47	9,76	7,36	7,42	7,12	3,65	4,06	2,35	1,49	1,35	0

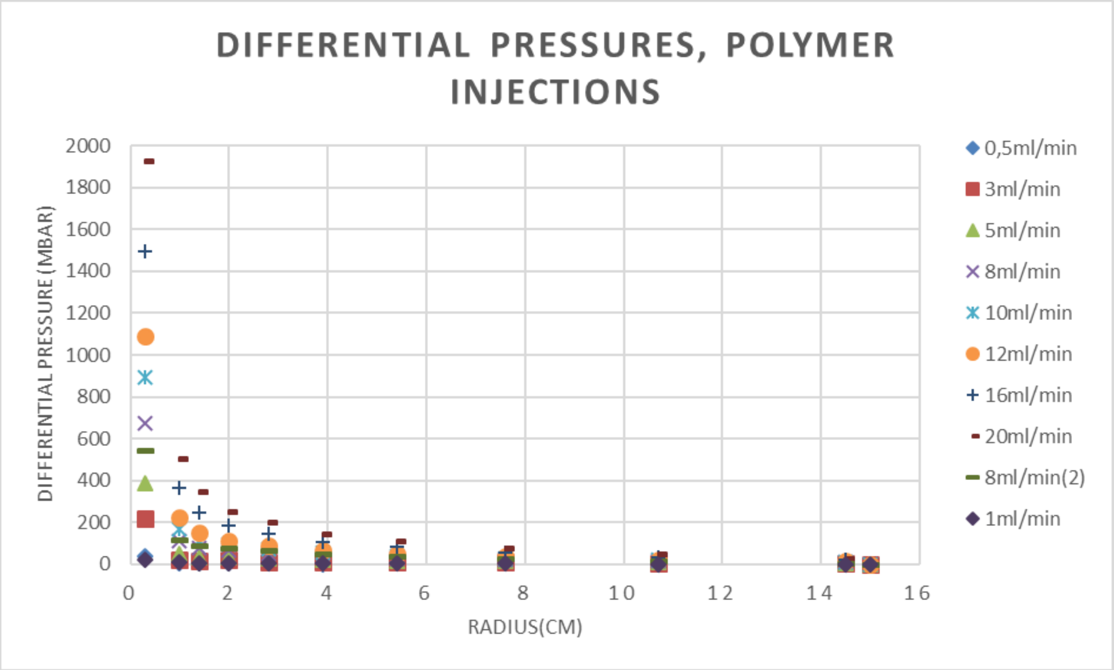

Figure (6.4). The corrected pressures from table (6.4). Differential pressure, dP (mbar), versus the increasing radius (cm).

Since the measured pressure values for the polymer flood is higher than the ones measured during the waterflood, the values do not experience the same issue with negative pressures at the rim as the waterflooding. However, the lowest rates with the lowest differential pressures does, as previously stated, carry a greater uncertainty compared to the higher injection rates.

The resistance factor, R_F, was reported and is presented in Figure (6.5). These experimental RF values are calculated by using equation (3.10). Based on the differential pressure values measured for each injection rate for water, corresponding differential pressure values for the injection rates used during the polymer flood, were calculated for water and thereby a calculated RF was stated in the experimental dataset. As these values were calculated based on experimental differential pressure values and will be referred to as the experimental apparent viscosity.

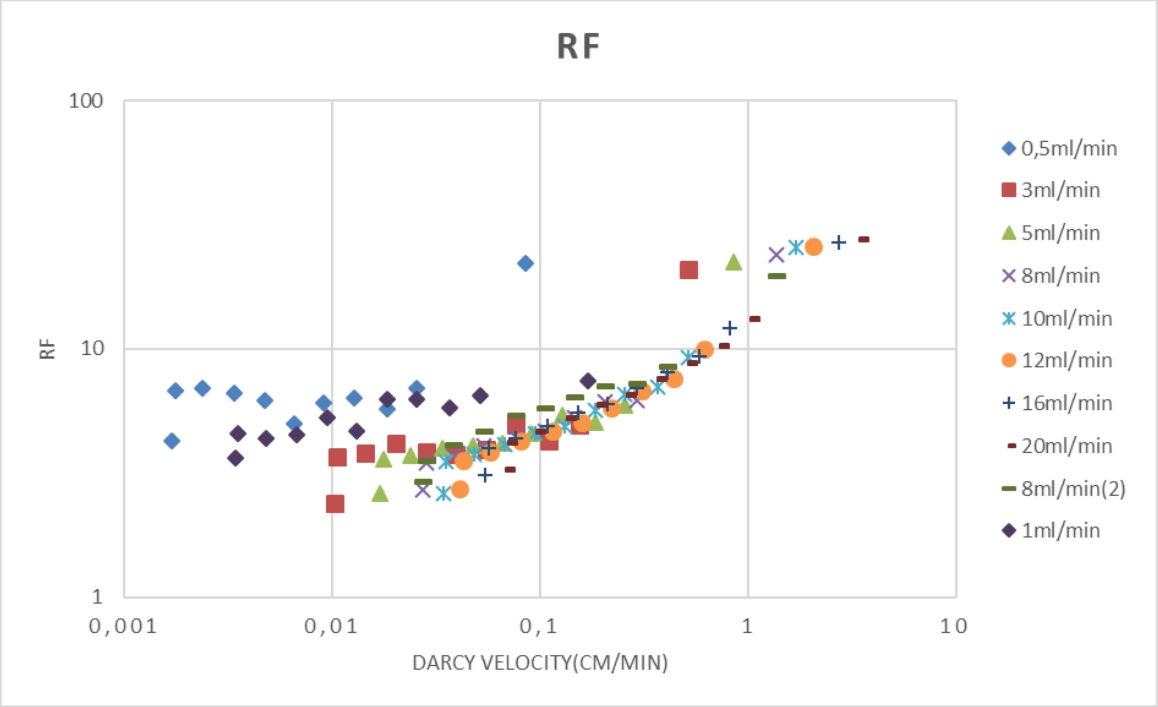

Figure (6.5). Resistance factor, R_F, versus Darcy velocity (cm/min)

The experimental data shows a general shear thickening trend. The injection rates denoted 8ml/min (2) and 1ml/min was performed after the flooding had reached its highest rate and do not follow the same distinct trends as the others. This might be due to altered rock permeability or the uncertainties in the pressure transducer. There will be a closer discussion of these values in chapter 7.

7 Results and discussion

7.1 Waterflooding

The main objective of a waterflooding is to establish the absolute permeability of the core. This is done by running a waterflood of different rates and matching them towards their corresponding experimental differential pressures. The history matching is based on Darcy's equation for radial flow [1]:

$$P_r = P_w + \left[\frac{\mu Q}{2\pi h K}\right] \ln(\frac{r_w}{r}) \tag{7.1}$$

Where:

P_r - the pressure at the location r
P_w - the pressure at the injection well
μ - the viscosity
Q - the injection rate
h - the thickness of the core
K is the absolute permeability
r_w - the radius of the injection well
r is the location of some pressure point at a distance r from the center of the disk.

The only free variable in equation (7.1) is the permeability and is therefore the only tuning parameter when history matching the waterflood. As the absolute permeability is inverse proportional to the pressure drop over the core, history matching the differential pressure gives an indication if the input permeability is too low or too high. If the simulated differential pressure is too high compared to the experimental differential pressures, it indicates that the input permeability might be too low and needs to increase to decrease the pressure drop.

Both STARS and MRST was used to simulate waterflooding to establish the permeability field of the core for further use in the polymer flooding. In the following subchapters, results from both STARS and MRST will be presented and discussed.

7.1.1 STARS – Waterflooding

The absolute permeability of the rock can be determined analytically based on the experimental pressures listed in Table 6.2. The analytical solution can be used as a starting point when history matching the permeability. The following subchapters will include simulation results from an analytically determined absolute permeability, as well as manually and automatically history matches and their corresponding absolute permeability.

7.1.1.1 Analytically determined permeability

Analytically, the absolute permeability can be determined by equation (7.1). The equation involves a logarithmic term of the radius; thus, the pressure is expected to follow a logarithmic trend when plotting absolute pressure versus the logarithmic radius.

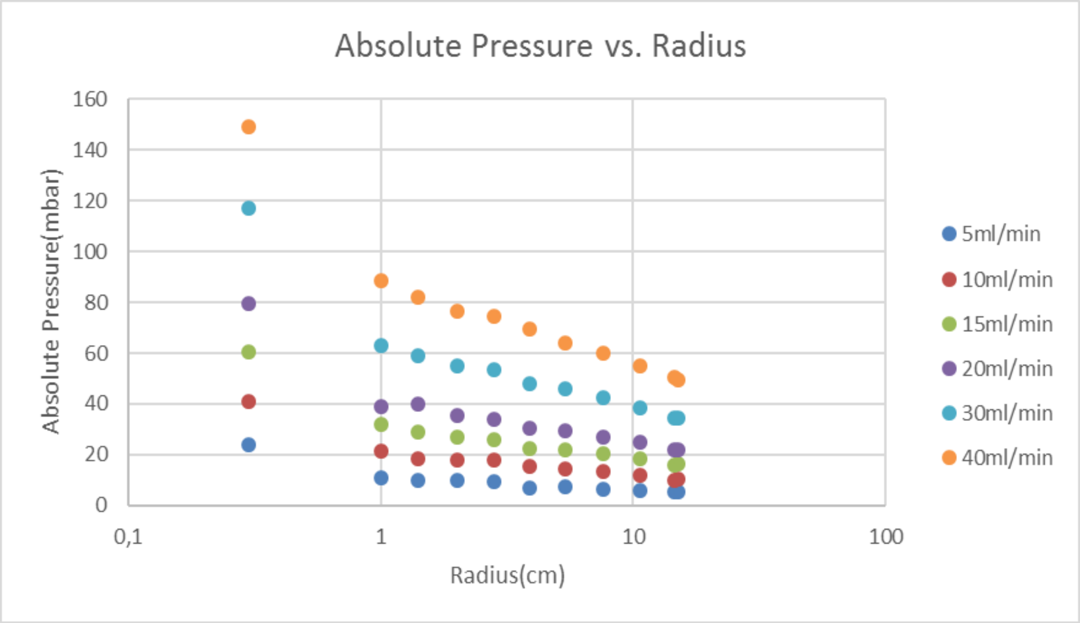

Figure (7.1). Waterflooding. Absolute pressure versus radius for each injection rate.

Figure (7.1) shows how the experimentally measured pressure point does not follow a logarithmic trend and displays high pressures in the near-well bore region causing the curve to be non-linear. By excluding the pressures measured in the near well-bore region, which might be influenced by near-well effects, a more linear logarithmic trend can be obtained.

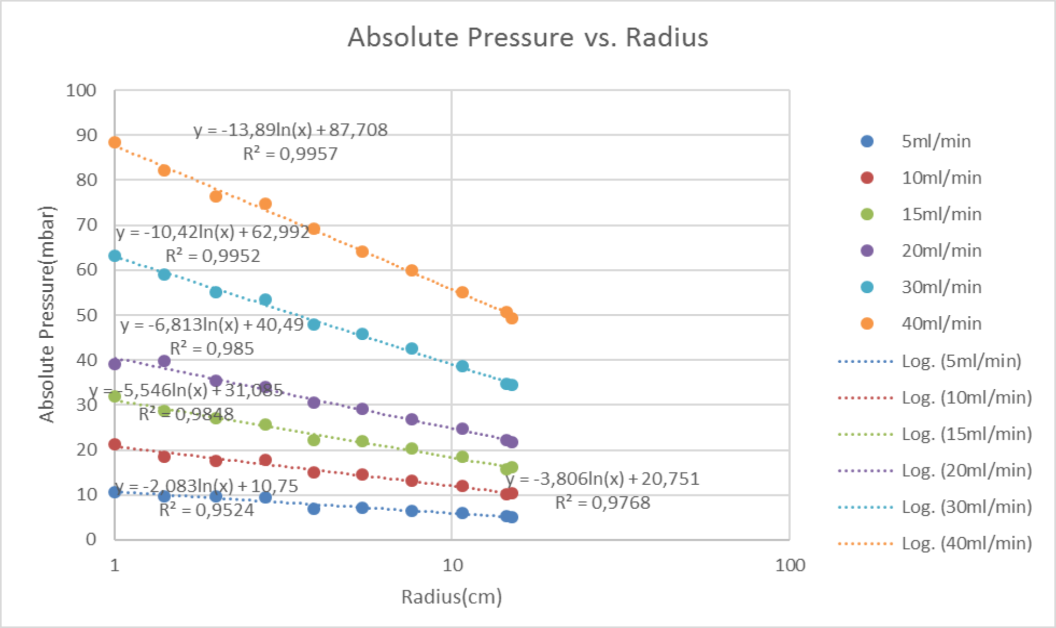

Figure (7.2). Absolute pressure versus radius for the waterflooding performed experimentally.

Figure (7.2) states the near linear trend obtained by excluding the pressure measurements near the well and their following logarithmic trendline. The logarithmic trend line can be written as:

$$P_r = a \cdot \ln(r) + b \tag{7.2}$$

Where r is the radius, P_r is the pressure measured at the specific radius and a and b are constants found from the equation of the logarithmic trendline, listed in Table 7.1.

Table 7.1. Logarithmic trendline function for each injection rate and their corresponding R^2-function.

q (ml/min)	a	B	R^2
5	-2,083	10,75	0,952
10	-3,806	20,751	0,977
15	-5,546	31,085	0,985
20	-6,813	40,49	0,985
30	-10,42	62,992	0,995
40	-13,89	87,708	0,996

The R^2-function indicates how accurate the trendline fit the data, given by equation (7.3), and the closer the value is to 1, the more accurate is the fit.

$$R^2 = \frac{[\sum_i (x_i - \bar{x})(y_i - \bar{y})]^2}{\sum_i (x_i - \bar{x})^2 \sum_i (y_i - \bar{y})^2} \tag{7.3}$$

Shown in Table 7.1, the accuracy of the R^2-fuction increases with increasing injection rates, as expected since the uncertainty of the pressure transducers decrease with increased rate.

By inserting equation (7.1) into (7.2), the absolute permeability for each injection rate can be determined. These are listed in Table 7.2 and plotted in Figure (7.3).

Table 7.2. The absolute permeability for each injection rate determined analytically.

q (ml/min)	5	10	15	20	30	40	Average K (D)
K (D)	2,09	2,28	2,35	2,51	2,47	2,46	2,36

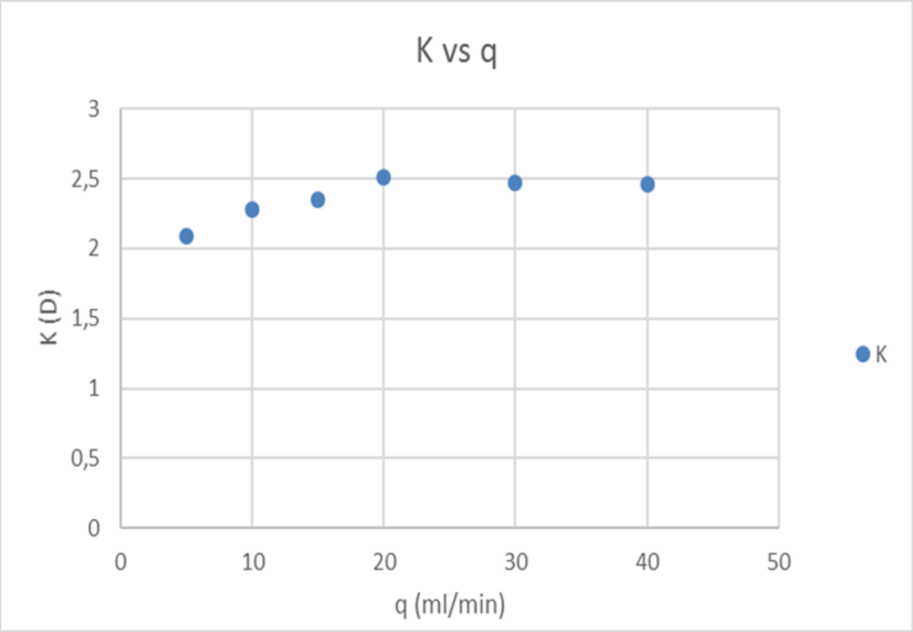

Figure (7.3). Analytical determined permeability for each injection rate

Figure (7.3) illustrates how the absolute permeability behaves nearly rate-independent, although the permeability analytically determined for the lowest injection rate deviates slightly from the others and displays a lower permeability. The pressure at this injection rate is low and the uncertainties is higher due to the uncertainties of the pressure transducers, which also is reflected by the R^2-function, and can therefore be considered as a deviation.

Under the assumption that the permeability is flowrate independent, each injection rate was history matched with the average permeability stated in Table 7.2. The results are presented below for some of the rates, while the others can be found in appendix A.

5ml/min

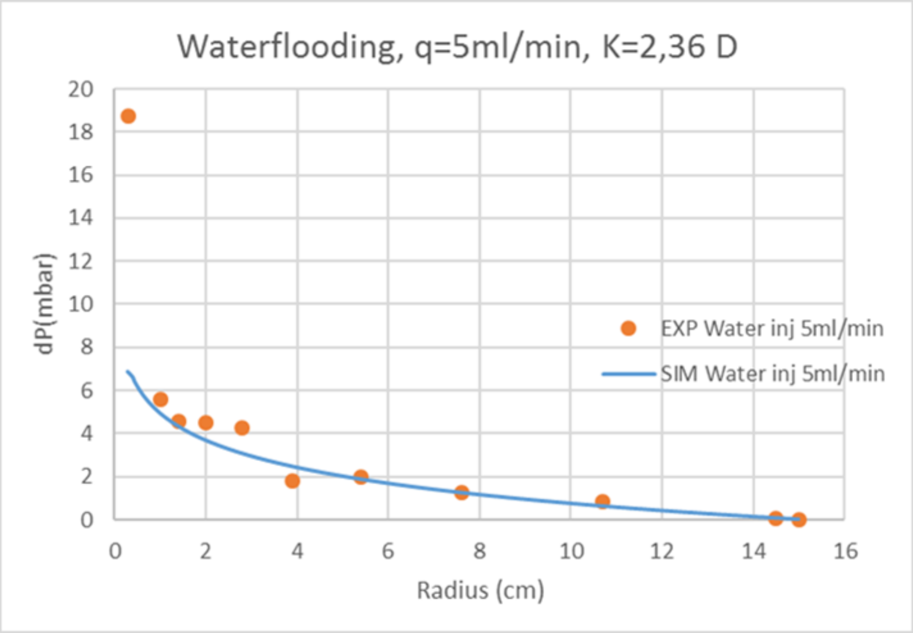

Figure (7.4). History match for q=5ml/min with an average analytical determined permeability, K=2,36 D.

The average permeability gives an adequate fit in the middle of the core, but deviates from the experimental pressure points in both the near-well region and 4cm out in the porous media and is thereby considered as a poor fit. The differential pressure is too low throughout larger portions of the core, which indicates that the permeability should be lowered to increase the differential pressure, as found and stated in Table 7.2.

30ml/min

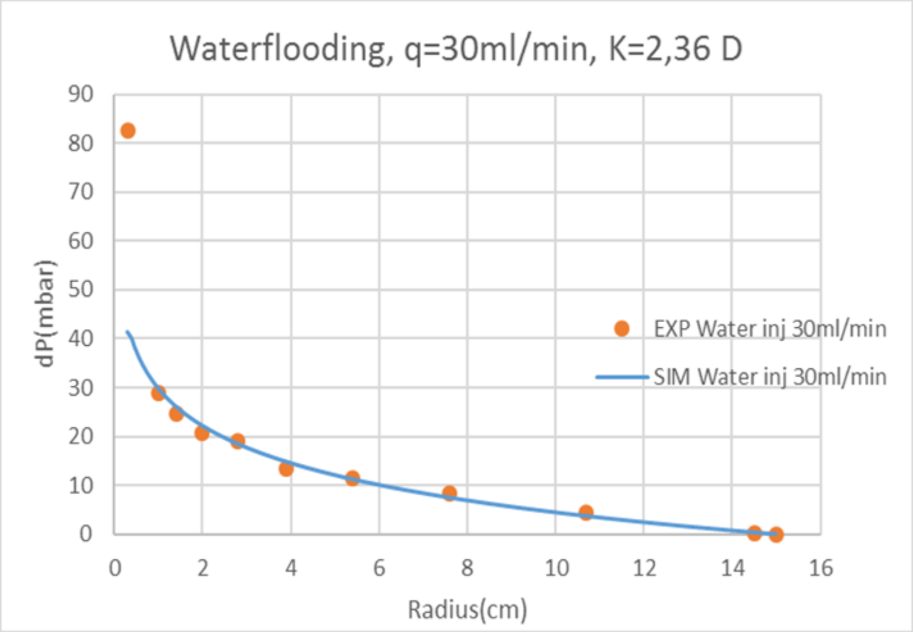

Figure (7.5). History match for q=30ml/min with an average analytical determined permeability, K=2,36 D.

By comparing of Figure (7.4), Figure (7.5) and other corresponding figures found in appendix A, the average permeability determined analytically gives a good average match and improves with increasing rates. Furthermore, the history matches display the same trend through most of them; the well-bore differential pressure is not adequately high and the differential pressure from the middle and throughout the core is too low.

7.1.1.2 Homogenous permeability

A homogenous permeability is when the permeability is uniform across the core and there are no preferential pathways for the flow [49]. By giving the model a constant, isotropic and homogenous permeability, it is possible to get a more specific indication of the absolute permeability of the rock. This is illustrated in Figure (7.6).

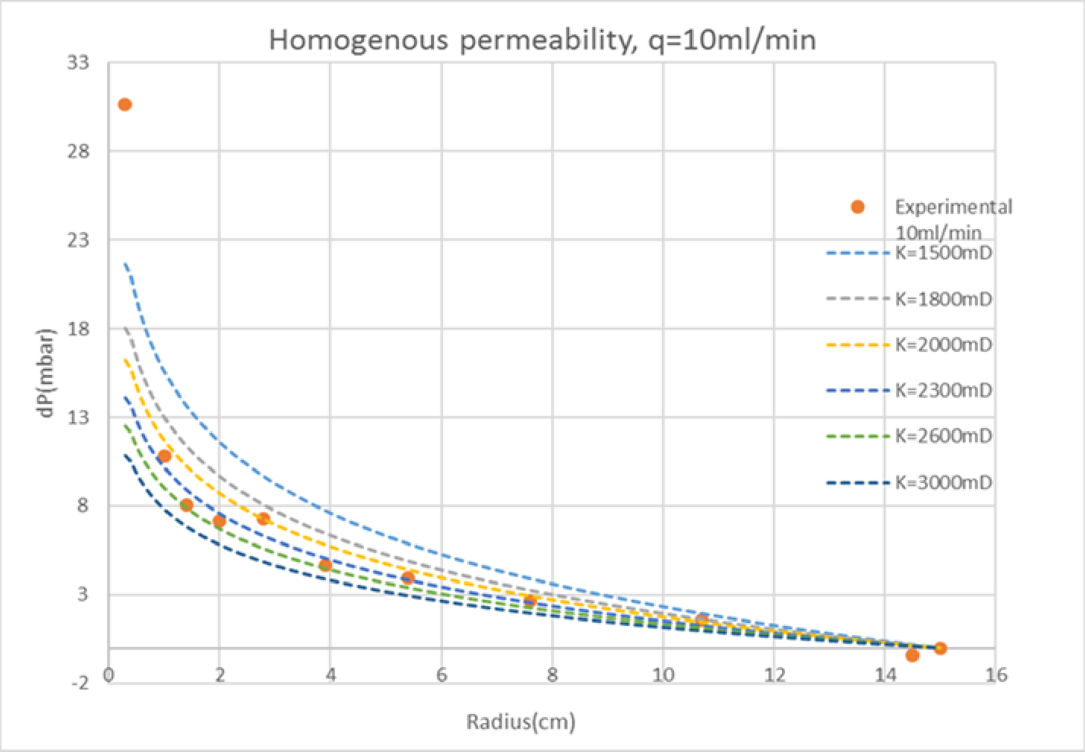

Figure (7.6). dP (mbar) versus radius (cm) for q=10ml/min waterflooding with various homogenous permeability

The orange dots in Figure (7.6) represents the experimental differential pressure values for a waterflood performed with q=10ml/min. The legends in the figure is the simulated output differential pressure when utilizing various homogenous permeability and these are discussed below.

1. K=1500mD – the differential pressure over most of the core is too high, except from the near wellbore area where it is too low, thus indicating that the permeability should be increased everywhere but in the near wellbore area, where it should be lowered to achieve an adequate pressure drop. Based on this and the results from the analytical determined permeability, it is possible to predict that the absolute permeability of the core not is homogenous.

   The following legends will have an increasing permeability and the pressure drop in the well-bore region will not be adequate for either of them and are therefore not further mentioned.

2. K=1800mD - the same issue as (1).

3. K=2000mD – this permeability demonstrates a better history match than previously discussed legends, but does not follow the same trend as the experimental points. From 1cm to 8cm, it overestimates the differential pressure and from 9cm to 15cm it results in a good match.

4. K=2300mD – this is close to the previously discussed analytically determined permeability and results in an acceptable average history match as it follows the trend of the experimental points.

5. K=2600mD – this permeability results in a good match from 1cm to 5cm, but the differential pressure is too low throughout the rest of the core, indicating that the permeability should be lower in the outer portion of the core.

6. K=3000mD – The differential pressure is too low throughout the whole core.

Based on the analysis of the homogenous permeabilities in Figure (7.6), together with the analysis of the analytical determined permeability, the homogenous permeability does not result in an acceptable history match, hence the following assumption; the core is heterogenous and consists of three regions. One region in the area close to the injection well, another region near the outlet of the core and a third region in-between these two. In the following discussion, the area close to the injection well is referred to as region 1, the area near the outlet of the core is referred to as region 3 and the area between these two is referred to as region 2.

7.1.1.3 Heterogeneous permeability

The previously performed analysis clearly indicated that the permeability in the near wellbore region should be low to achieve an adequate pressure drop. Although the analysis gave a good indicator of the value of the permeability of each region, the issue now is to estimate the size of the regions and their actual corresponding permeability. Each rate was history matched towards their experimental differential pressure in Table 6.2 and the results will be presented in this subchapter and appendix A.

5ml/min

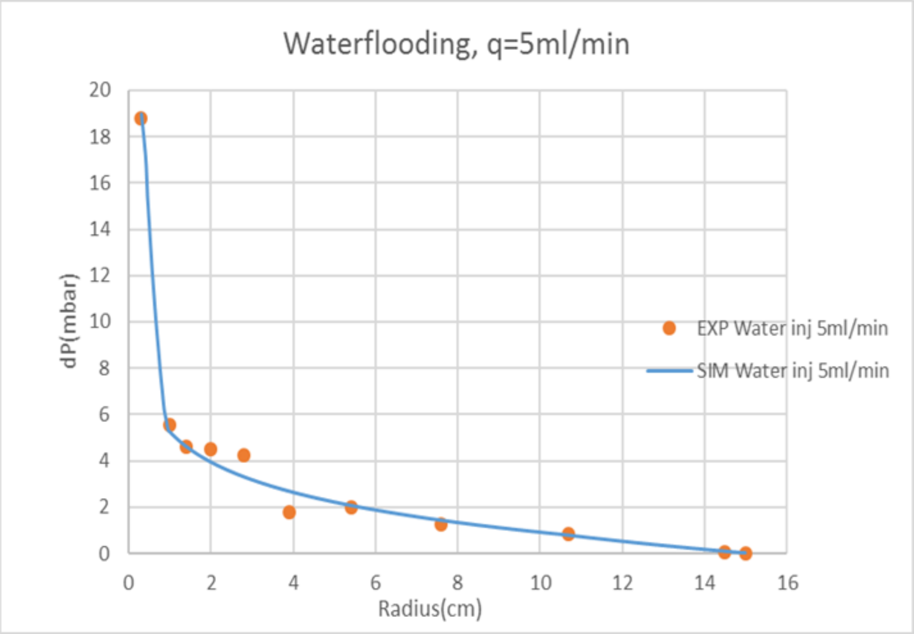

Figure (7.7). History match of the waterflooding with q = 5ml/min. Distance from well(cm) versus pressure drop, dP (mbar).

The previously discussed trend of the pressure transducers increased uncertainty with decreasing rates due to low pressures, is pronounced in Figure (7.7), where several experimental differential pressure points, illustrated by the orange dots, can be classified as outliers. The points located at 2, 2,8 and 3,9cm deviates from the other as they do not follow the same decreasing pressure drop trend and is therefore not considered when history matching the waterflooding of q=5ml/min. The match was obtained with the permeability field presented in Table 7.3.

10ml/min

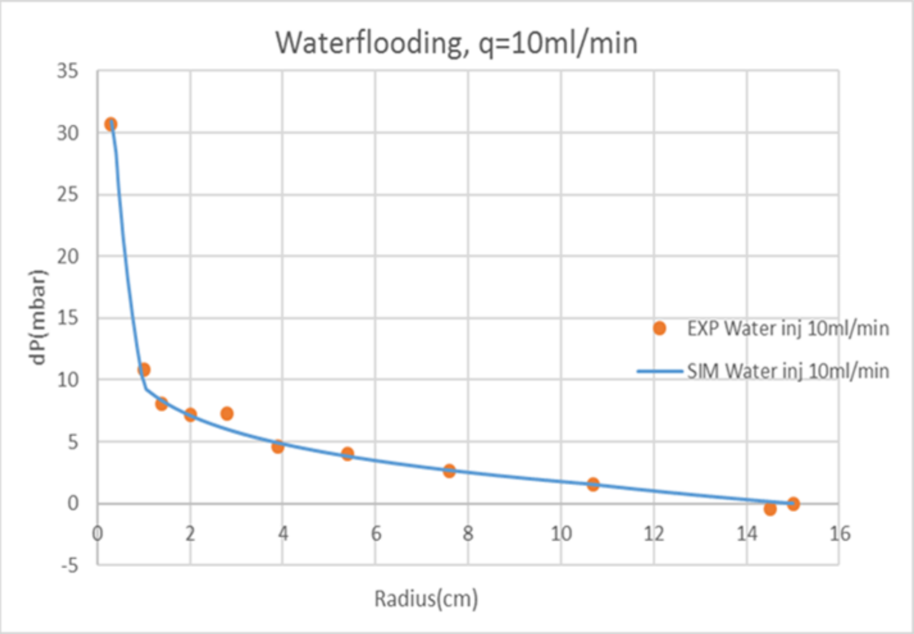

Figure (7.8). History match of a waterflooding with q = 10ml/min. Radius versus pressure drop.

The differential pressure increases and the number of experimental outliers decrease, demonstrated by comparison of Figure (7.7) and Figure (7.8). The experimental point located at 2,8cm is considered a deviation as it displays an apparent increase in differential pressure, together with the point located at 14,5cm which has a negative value. The history match was obtained with the permeability field presented in Table 7.3.

The previously analysis of a homogenous permeability stated that a permeability of 2600mD resulted in a poor history match from 5cm and throughout the core. However, due to the resulting pressure build-up caused by the lowered permeability of region 3, a permeability of 2600mD in region 2 results in a good match. Table 7.3 summarizes the history matched permeability field for each injection rate.

Table 7.3. The manually simulated permeability fields for waterflooding of different rates

	Permeability field		
q (ml/min)	**Region 1**	**Region 2**	**Region 3**
5	6*300	97*2300	44*1900
10	7*420	96*2600	44*1900
15	7*445	96*2600	44*1900
20	7*460	96*2700	44*1900
30	7*495	96*2700	44*1900
40	7*565	96*2700	44*1900

Table 7.3 lists the history matched permeability field for each rate in the waterflooding. The near wellbore region, referred to as region 1, have a significant lower permeability, compared to the other regions, which is due to the additional pressure drop experienced in the well region. The additional pressure drop in this region can be an effect of the location of the pressure transduces. If the pressure transducer is located in the center of the well, it will experience high pressure caused by the direct impact of the injected fluid or, if located at the rim of the well, it will experience higher pressure due to the resistance of the fluid as it enters the porous media.

This localized additional pressure drop can also be attributed to wellbore damage causing a significantly reduced permeability close to the injection well and is known as the skin effect. The additional pressure drop can be referred to as Δp_{skin} and the region with the altered permeability is known as the skin zone [15]. The additional pressure drop is defined as:

$$\Delta p_{skin} = \frac{\mu Q}{2\pi K h} S \tag{7.4}$$

where μ is the viscosity, Q is the injection rate, K is the absolute permeability, h is the height and S is the mechanical skin factor, which is an dimensionless constant and can be positive or negative depending on whether the permeability near the well is decreasing or increasing [14]. The skin factor can be numerically corrected for in the script in STARS, however, for a more detailed analysis of the altered zone, this possible effect is corrected for by a lowered permeability in the region near the wellbore. This applies for the simulations performed for both the water and polymer flooding. From Table 7.3, it appears that the altered permeability zone in the near well-bore region stretches from outer rim of the injection well to 0,6-0,7cm out in the porous media.

The permeability in the near wellbore region demonstrates a rate-dependent trend and increases with increasing rate. One could therefore argue that the skin effect behaves rate-dependently, although this is known to be a gas-related artifact and is due to non-Darcy, i.e. turbulent flow [15], which is not valid for this case. Since the skin factor appears to decrease with increased injection rate, the well damage could be caused by microfractures that seems to open at higher injection rates, hence increasing the permeability and reduce the skin factor.

The rock properties are expected to be constant and rate-independent, thus one constant permeability field of the rock was chosen due to its consistency, simplicity and based on the analytical determination of the permeability, the permeability field appeared flowrate independent. The permeability field determined from the waterflooding will be further used in the simulations of the polymer flooding and as most of the polymer flooding rates is close to q=10ml/min, the permeability field history matched for the waterflooding of q=10ml/min was chosen. The following figures illustrates how choosing one constant, rate-independent permeability field consequently affects the history matches of the waterflooding of varying rates.

5ml/min

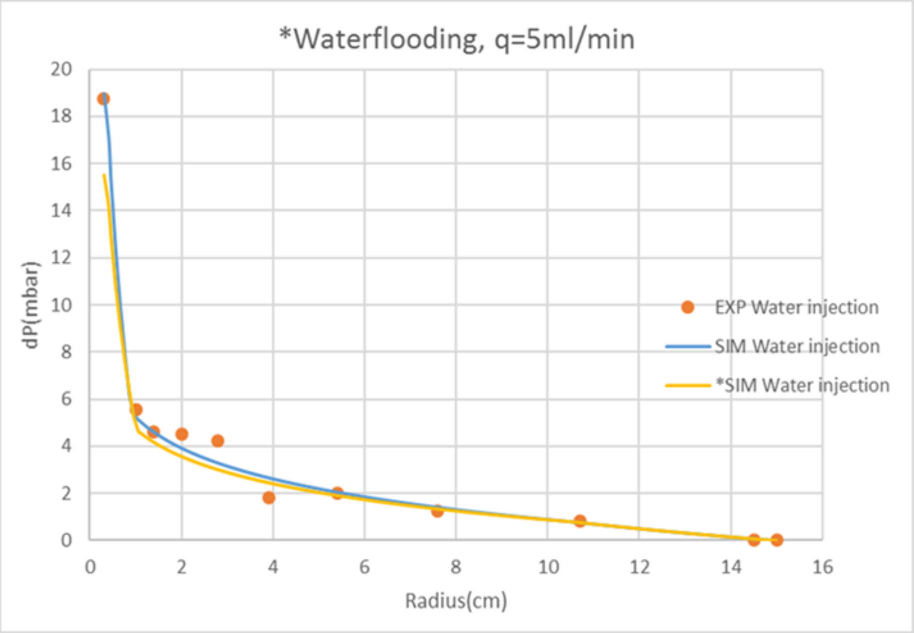

Figure (7.9). History match of a water injection, q = 5ml/min with the permeability field history matched for q=10ml/min.

The blue curve is the simulated differential pressure when using the history matched permeability field of q=5ml/min. The yellow curve represents the simulated differential pressure when using the history matched permeability field of q=10ml/min waterflooding, both presented in Table 7.3. The same color code will be used throughout the chapter.

Figure (7.9) illustrates how the two permeability fields history matched for q=10ml/min and 5ml/min differs from each other in both region 1 and 2. The history matched obtained when using the fitted permeability field of q=10ml/min is slightly poorer near the injection well and 4 cm out in the porous media when compared to the match obtained when using the permeability field of q=5ml/min. However, the difference in differential pressure in the near wellbore area is the more pronounced deviation between them, hence the deciding factor. The difference is ~3,5mbar, which not is considered a significant deviation.

20ml/min

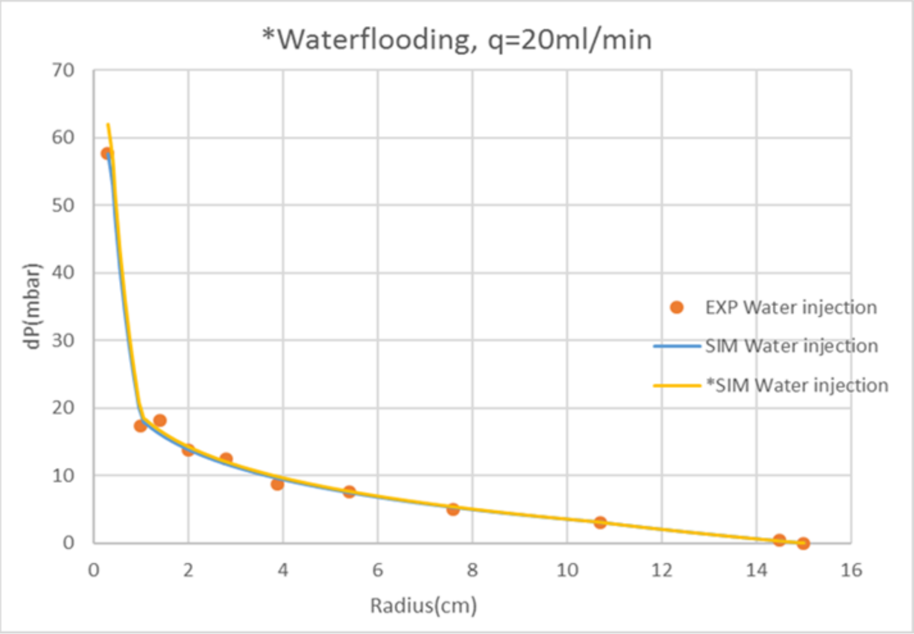

Figure (7.10). History match of a water injection with q = 20ml/min with the permeability field history matched for q=10ml/min.

The difference between the two permeability fields determined for q=10ml/min and 20ml/min is small, thus the history match of the waterflooding with q=20ml/min when using the fitted permeability of q=10ml/min, still qualifies as a good match as illustrated in Figure (7.10). Since these two fields mainly differs from each other in region 1, the effect is more pronounced in this region. Furthermore, the difference between the differential pressure obtained in the near wellbore area when using these two permeability fields is ~4,5mbar and not considered prominent.

The same procedure was performed for the remaining waterflooding rates, q = 15ml/min, 30ml/min and 40ml/min and their history matches can be found in appendix A. Table 7.4 schematically summarizes the differences in the differential pressure in the wellbore region obtained when using the history matched permeability field determined specific for each rate and when using the history matched permeability of q=10ml/min.

Table 7.4. Simulated pressure drop by the injection well in STARS. dP – when using the permeability fitted for q = 10ml/min, dP* - when using the permeability fitted for each injection rate, presented in table 7.3.

q (ml/min)	**dP (mbar)**	**dP* (mbar)**	**Difference (mbar)**
5	15,49	18,97	-3,48
15	46,46	44,65	+1,81
20	61,95	57,63	+4,32
30	92,93	82,27	+10,66
40	123,90	100,64	+23,26

In table 7.4 the following notation is used: dP represent the simulated differential pressure in region 1 when using the permeability history matched for q=10ml/min and dP* is the simulated differential pressure in region 1 obtained by using the permeability history matched specific for each injection rate. The apparent rate-dependent permeability trend shown in Table 7.3, demonstrated an increased permeability with increased rate. Consequently, the differential pressure deviations increase with rate as the history matched permeability of q=10ml/min is lower in region 1, compared to the ones history matched for higher rates. The same effect is shown for the lowest rate as the permeability found for q=5ml/min is lower than the one determined for q=10ml/min, hence using the permeability of q=10ml/min results in an underestimated pressure drop in the wellbore region for q=5ml/min, which is shown in Figure (7.4).

The differences in differential pressure obtained in the wellbore region appears to be within range of an acceptable history match as the pressure transducers uncertainty minimum value is 10mbar, when assuming 1% uncertainty of maximum range. Consequently, the permeability field determined for q=10ml/min will be further used in the polymer flooding performed in chapter 7.2. However, as the permeability field is invers proportional with the differential pressure and the apparent viscosity is proportional with the differential pressure, the choice of a constant, rate-independent permeability will further affect the output polymer rheology. The extent of this effect will be examined and discussed in chapter 7.2.

7.1.1.4 Injectivity

As previously mentioned in chapter 3, it is possible to calculate the injectivity by using (3.12):

$$I = \frac{q}{\Delta P} \tag{7.5}$$

Where I is the injectivity, q is the injection rate and ΔP is the pressure drop in the injection well.

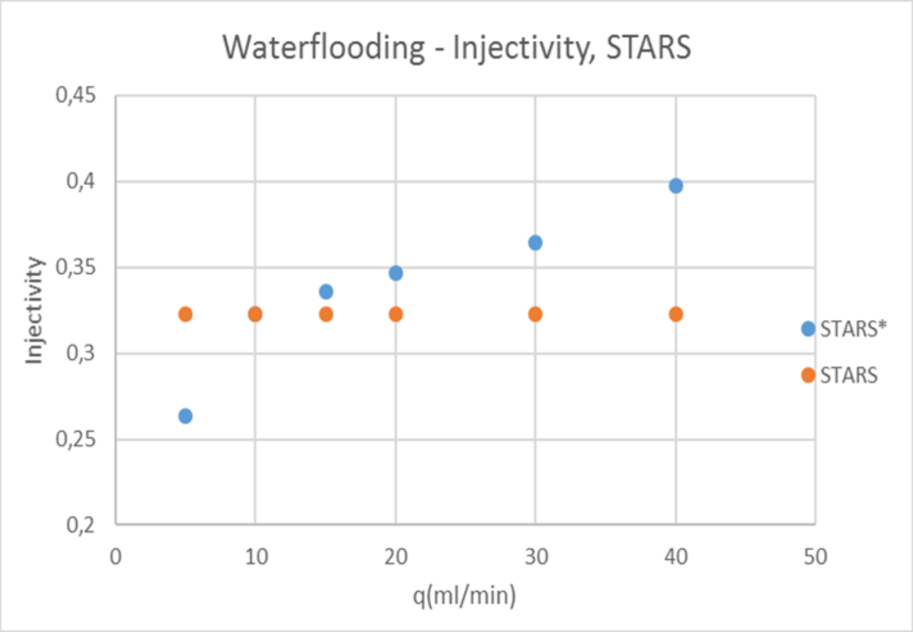

Figure (7.11). The injectivity of the simulated waterflooding in STARS. STARS* - the injectivity calculated from the simulated differential pressure drop history matched for each injection rate when using their own corresponding permeability and STARS - the calculated injectivity when using the history matched permeability of q=10ml/min for each injection rate.

Figure (7.11) demonstrates how the injectivity of the waterflooding increases with injection rate, which is illustrated by the blue dotted curve marked STARS*. These values are obtained from the history matches performed with rate-dependent permeabilities, where each injection rate has its own history matched permeability. The orange dotted curve is the calculated injectivity when using the history matched permeability of q=10ml/min for each injection rate and the corresponding differential pressure listed in Table 7.4. Using one, constant rate-independent permeability affects the injectivity of the waterflooding, causing it to become rate-independent instead of increasing with rate. However, as water is a Newtonian fluid with a constant and rate-independent viscosity, it follows from Darcy's equation that the injectivity for water is, in fact, rate-independent. This further supports the decision of using a constant, rate-independent permeability.

7.1.2 MRST - Waterflooding

The basic procedure used for obtaining history matches in MRST has been explained in chapter 5. The following subchapter will present the results and compare it to the history matches and the permeability fields determined manually in STARS. As the automatic history matches are similar to the manual, only one history match will be presented and the others can be found in appendix A.

10ml/min

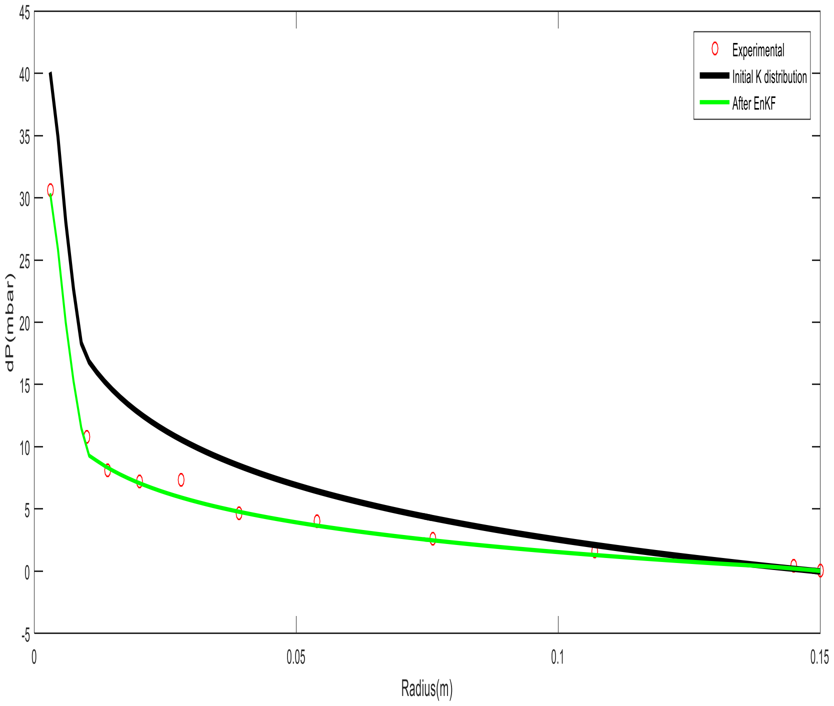

Figure (7.12). Automatically history match found in MRST, for waterflooding where q=10ml/min. Red dots is the experimental pressure point, the black line is the "initial K-distribution" and the green line is the pressure match found after EnKF run.

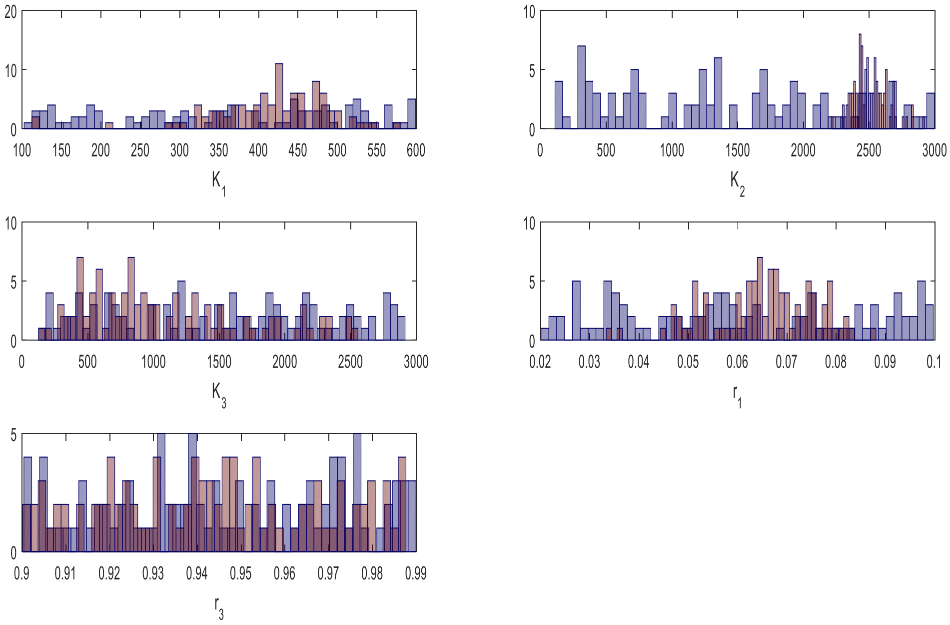

Figure (7.13). Distribution chart for q=10ml/min.

By comparison of the history matches obtained with STARS and MRST, MRST appears to classify the same experimental differential pressure points as deviations as previously discussed in chapter 7.1.1. A summary of the automatic determined permeability field for each injection rate can be found in Table 7.5.

Table 7.5. The average, automatically simulated permeability fields and their corresponding regions for waterflooding of varying rates.

	Output				
q (ml/min)	K_{1avg} (mD)	K_{2avg} (mD)	K_{3avg} (mD)	r_{1avg} (cm)	r_{3avg} (cm)
5	268,99	2225,8	2166,6	0,79	0,83
10	416,14	2507,8	1086,6	0,98	0,84
15	433,21	2643,8	1082,3	0,96	0,96
20	318,49	2567,1	1250,2	0,69	0,82
30	384,57	2465,4	2269	0,75	0,75
40	464,59	2597,8	959,12	0,80	0,85

When comparing Table 7.5 with Table 7.3, the history matched permeability field obtained in MRST does not follow the same apparent permeability trend as the fields determined manually in STARS. The permeability in region 1 increased with increasing rate, however MRST displays a more random behavior. However, both the manual and the automatic history matches demonstrate a lower permeability in region 1, when compared to the other regions and the permeability reduction in the near wellbore region is assumed to be confirmed as both simulators display the same reduced permeability trend. The permeability for region 2 obtained in MRST is similar to the one determined in STARS and they vary within the same range. The permeability in region 3 is rate-independent and constant in the manual history matches, while it varies within a large range in the automatic history matches.

The size of region 1 varies between 0,1-0,7cm in the automatic history matches, while it was determined to be between 0,6-0,7cm in the manual history matches. As the input range of r_3 set to find a region which not was larger than 10% of the radius of the disk, the size of region 3 is significantly smaller in the automatic matches, causing region 2 to be larger than the one determined manually. In STARS the size of region 3 was determined to be 4,4cm, while it varied between 0,75-0,96cm in MRST. As the area of region 3 is small and the differential pressure values at the outer rim of the disk is low, they carry a great uncertainty which might explain why the permeability of region 3 varies between 959-2269 mD for the various injection rates in the automatic history matches.

Under the assumption that the permeability field is flowrate independent, one constant permeability field was chosen for further use in the polymer flooding. By switching the aim in MRST to “Check_permeability”, the consequences of using a rate-independent permeability field was examined for every injection rate. For an easier comparison between the results from STARS and MRST, the permeability field obtained for q=10ml/min was examined. As the procedure is the same as previously performed in STARS, only one plot will be shown and the rest can be found in appendix A. The consequences of using a rate-independent permeability field in the automatic history matches of the waterflooding is summarized in Table 7.6.

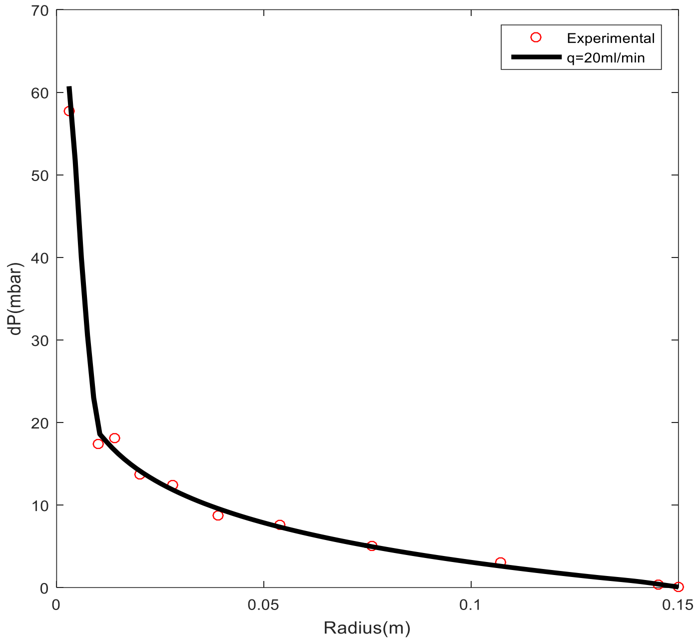

Figure (7.14). Automatic history match of a waterflooding with q=20ml/min, when using the history matched permeability field from q=10ml/min.

As the permeability in region 1, history matched for q=10ml/min, was higher than the permeability obtained for q=20ml/min, it was not expected that the differential pressure in this region would be higher when utilizing the permeability field obtained for q=10ml/min when performing a history match for q=20ml/min. This effect is attributed the lower permeability in region 2 and 3 of the permeability field of q=10ml/min, which causes a pressure build-up from the rim and consequently a higher differential pressure in region 1. However, the difference in the near wellbore differential pressure between the two permeability fields is +3,7mbar, which is not significant and the history match still qualifies as a good match.

Table 7.6. The simulated differential pressure by the injection well, in MRST dP – when using the permeability fitted for q=10ml/min, dP* - when using the permeability field for each injection rate, presented in table 7.5.

q(ml/min)	dP(mbar)	dP*(mbar)	Difference(mbar)
5	15,18	18,62	-3,44
15	45,55	44,05	+1,5
20	60,73	57,03	+3,7
30	91,09	81,4	+9,69
40	121,5	99,53	+21,97

By comparing Table 7.4 and Table 7.6 it appears that the consequence of using a rate-independent permeability results in similar deviations for the manually and the automatic history matches. The manual determined and the automatic history matched permeability deviates in the size of the regions but are somewhat similar in value. Consequently, causing the same rate-independent effect on the injectivity, shown in Figure (7.15).

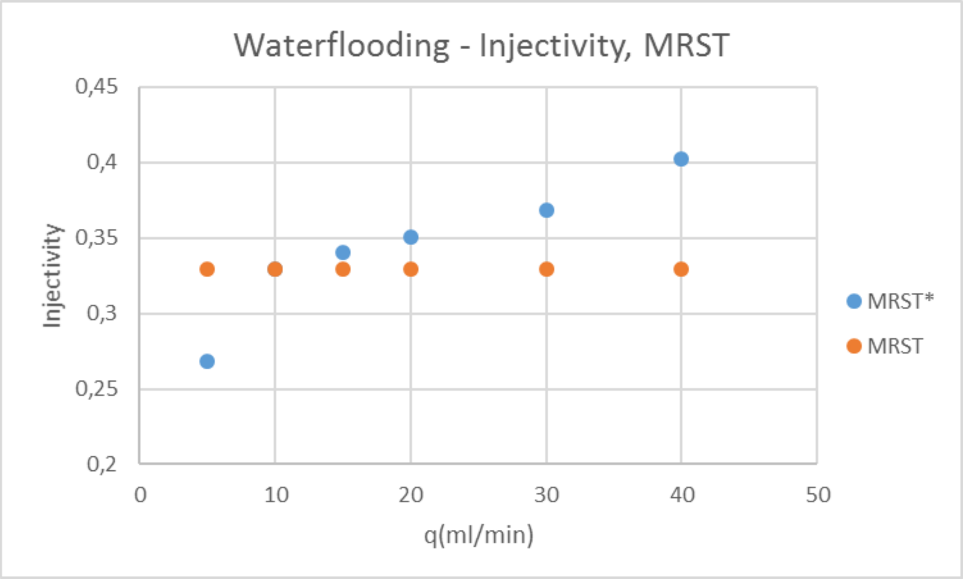

Figure (7.15). The injectivity of the simulated waterflooding in MRST. MRST* - the injectivity calculated from the simulated differential pressure drop history matched for each injection rate when using their own corresponding permeability and MRST – the calculated injectivity when using the history matched permeability field of q=10ml/min for each rate.

Table 7.7. The permeability fields used further in the manual simulations performed in STARS and the automatic simulations performed in MRST.

	r_1 (cm)	r_3 (cm)	K_1 (mD)	K_2 (mD)	K_3 (mD)
STARS	0,7	4,4	420	2600	1900
MRST	0,98	0,84	416	2508	1089

Table 7.7 lists the permeability field used in STARS and in MRST during the following history match of the polymer flooding. As they showed the same range of deviation under the examination of using a rate-independent permeability field when history matching the waterflood and the difference between them is not significant, it is assumed the application of different permeability fields in the simulators not will cause large deviations between them in the rheology output. However, this assumption will be further examined in chapter 7.2.

7.2 Polymer flooding

History matching of polymer flooding is performed to estimate the in-situ rheology of the polymer. The permeability of the rock has previously been determined from the waterflooding, thus the only tuning parameter is the viscosity which is the only free variable in Darcy’s law of radial flow. As the apparent viscosity is proportional with the differential pressure, the differential pressure match with the experimental differential pressures indicates whether the apparent viscosity input is too low or too high.

The following subchapter includes both manual history matches performed in STARS and automatic history matches obtained in MRST, based on the experimental data presented in chapter 6. Their corresponding rheology curves and the difference between the them will be discussed, as well as the rate-independent permeability influence on the rheology.

7.2.1 STARS – Polymer flooding

The experimental differential pressures used for history matching is listed in Table 6.4, and as previously stated, the tuning parameter during history matching in STARS is the keyword SHEARTAB and the corresponding AVISC. The rheology curves are the output viscosity data from STARS and the following figures will illustrate both the obtained differential pressure history match and the corresponding rheology curve. As there are several injection rates, hence many graphs, only a few will be presented in this chapter while the rest can be found in appendix A.

7.2.1.1 STARS – Individual history matches for polymer flooding of different rates

20ml/min

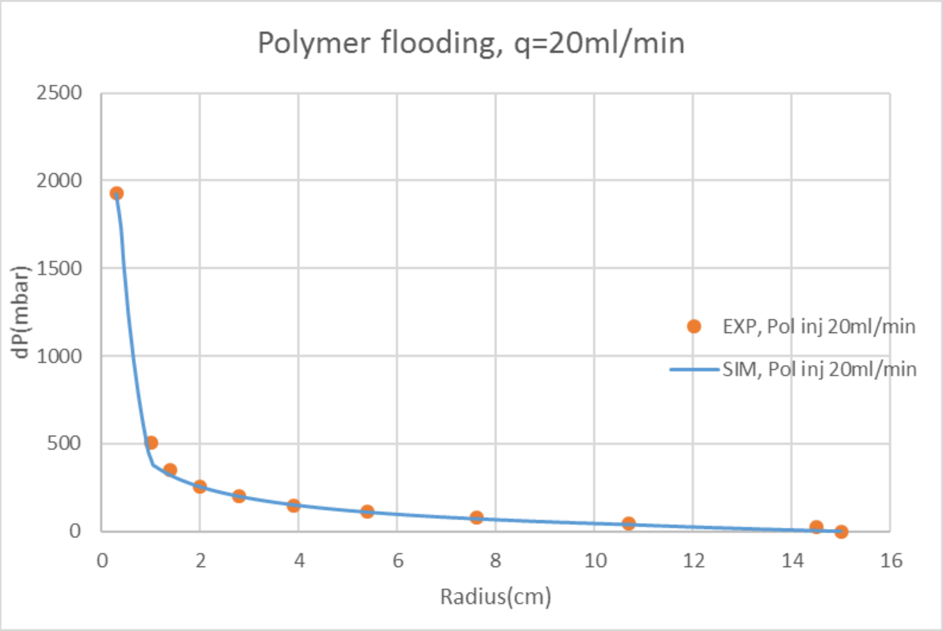

Figure (7.16). History match of a polymer flooding, q=20ml/min.

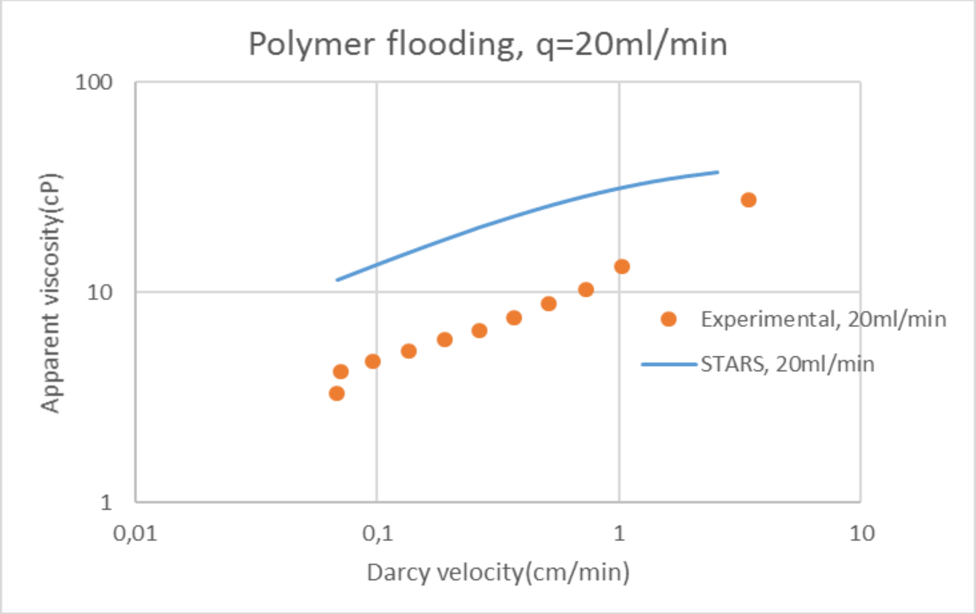

Figure (7.17). Viscosity output data from STARS and the calculated R_F from the experimental data for q=20ml/min.

The history match shown in Figure (7.16) was obtained with the apparent viscosity illustrated in Figure (7.17). The manually simulated apparent viscosity is higher than the calculated R_F, which is expected as the experimentally calculated R_F does not consider the development of the pressure and the function behavior of the whole curve, which the simulations does. Although they deviate from each other in value, they do display the same rheological behavior, except at the lowest Darcy velocity where the experimental apparent viscosity experience some form of rime effect. They both illustrate a shear thickening behavior where the apparent viscosity increases with increased velocity, although the simulated viscosity has a less steep slope of shear thickening.

Shear thickening is expected from literature as several authors have reported a shear thickening viscosity at moderate to high velocities [33], [37]. This effect is attributed to the viscoelastic behavior of synthetic polymers and is expected in the near wellbore region where the velocities are high and the characteristic relaxation time of the polymer is longer than the transit time between the successive constrictions. This is known to effect the injectivity of the well as it results in an increased apparent viscosity, hence an increased differential pressure and lowered injectivity [28].

8ml/min

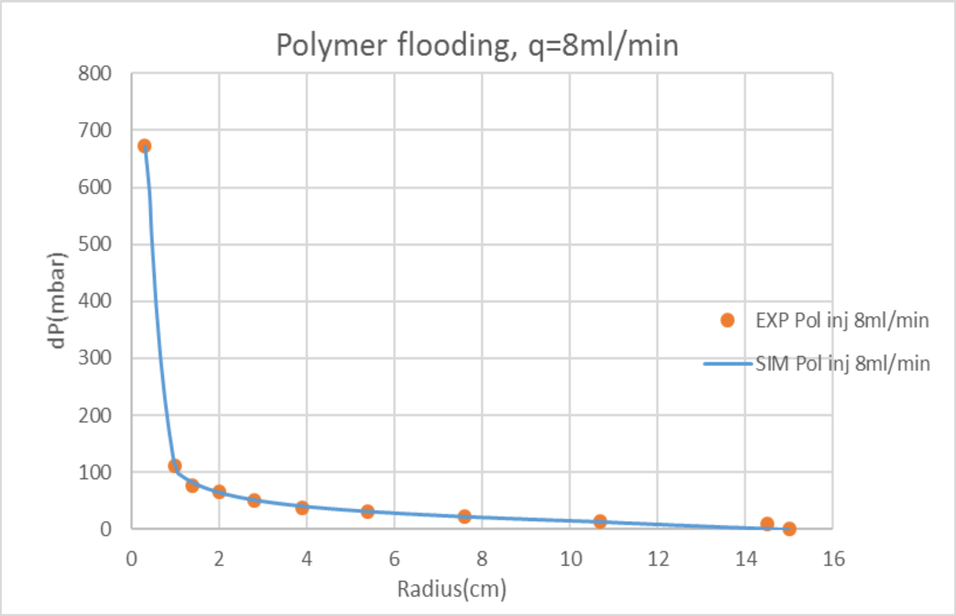

Figure (7.18). History match of a polymer flooding, q=8ml/min.

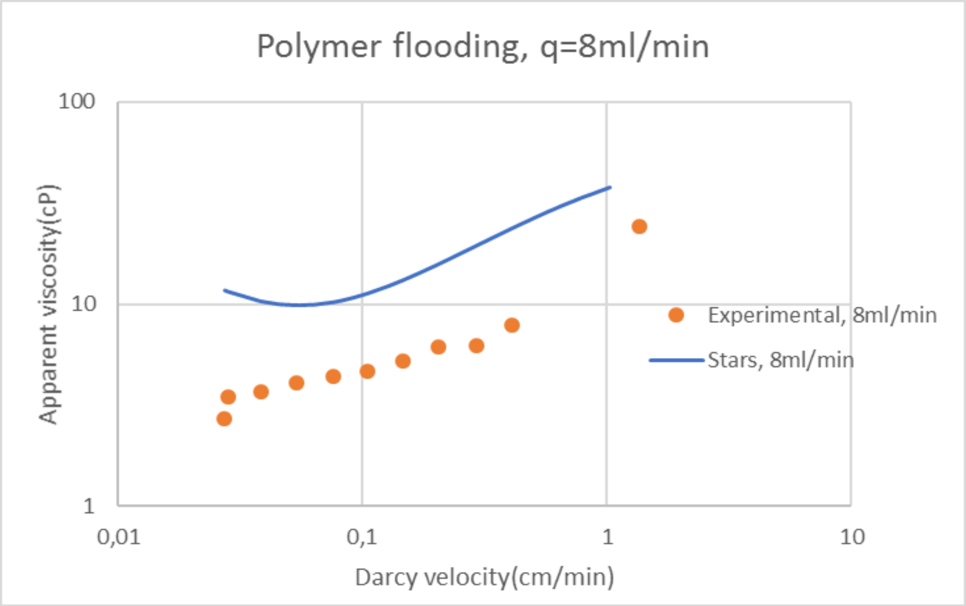

Figure (7.19). Viscosity output data from STARS and the calculated R_F from the experimental data for q=8ml/min.

The rheology of the polymer displays a change in behavior as it reaches lower velocities and demonstrates both a shear thinning and a shear thickening behavior. The shear thinning is due to the increased transit time between the successive constrictions causing it to be higher than the characteristic relaxation time of the polymer, thus the polymer reaches its equilibrium state between each constriction and aligns with the flow field.

Compared to Figure (7.17), the shear thickening slope is both steeper and shorter at a lower injection rate, illustrated in Figure (7.19). The steepness of the shear thickening slope might be an effect of using a rate-independent permeability field. As the permeability in the wellbore area originally decreased with decreasing injection rate, this effect is possibly not sufficiently accounted for when using the constant, rate-independent permeability and consequently results in an overestimated, steep shear thickening behavior to achieve an adequate differential pressure in the wellbore area. The shortness of the slope is due to a lowered injection rate which achieve lower velocities and consequently a change in the polymer behavior.

The simulated apparent viscosity and the experimental RF does deviate from each other in value, but follow a similar shear thickening slope. However, the experimental values demonstrate an apparent Newtonian behavior when reaching lower velocities, while the simulated rheology displays a shear thinning behavior.

Shear thinning has been reported by several authors, previously mentioned in the literature study in chapter 4, and is caused by the polymer molecules alignment with the flow field causing reduced interaction between them. This is known to happen at low velocities and low shear rates and are often observed in viscometers. Seright et al. (2010) reported an apparent shear thinning behavior, but stated that it could be minimized or removed by mechanically degrade the polymer before injection [41]. Skauge et al. (2016) reported shear thinning in radial core flood and speculated that polymers are degraded to a less extent in radial floods, compared to linear floods of the same velocities [1]. The shear thinning behavior can thereby be a consequence of the absence of mechanical degradation, an experimental artifact due to the uncertainties of the pressure transducers or a consequence of an apparent increase in the differential pressure due to mechanical entrapment of large molecule species [41].

3ml/min

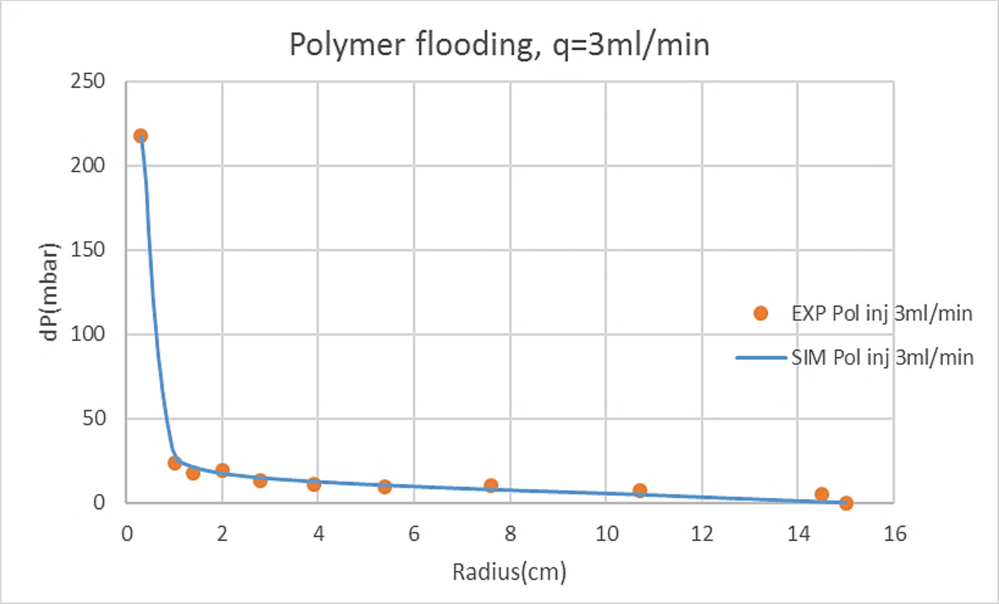

Figure (7.20). History match of a polymer flooding, q=3ml/min.

When comparing the experimental differential values in fFigure (7.16), Figure (7.*18*) and Figure (7.*20*), the two latter displays a less steep slope of pressure drop from the middle to the rim of the core. The experimental differential values appear to level of, which might be an indication of shear thinning as it can be seen as a relative increase in the pressure at lower rates and longer distances away from the well [1]. The trend is more pronounced at lower rates, shown in Figure

(7.20), which also displays an increasing shear thinning behavior by comparison of Figure (7.19) and Figure (7.21). It is possible that the observation of the differential pressure leveling of is caused by a smaller differential pressure range causing it to be more pronounced at lower rates. However, the apparent leveling off effect can also be attributed to the uncertainties of the pressure transducers, which is known to have carry a larger uncertainty at lower injection rates and differential pressures.

The following discussion assumes that the shear thinning behavior is correct and not an experimental artifact, as the differential pressures are considered sufficient and the polymer was pre-filtered, which would prevent the entrapment of large molecules and an apparent increase in differential pressure [41].

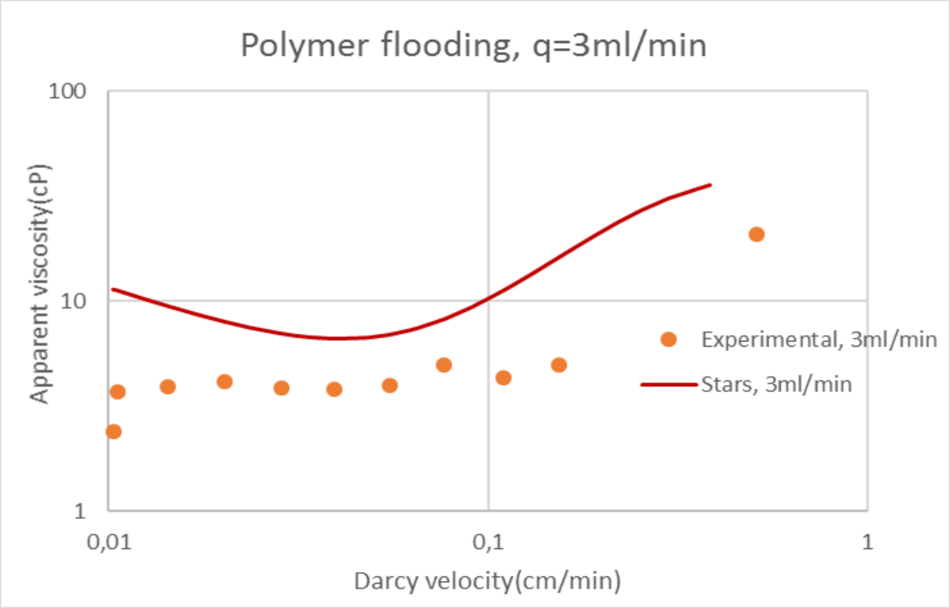

Figure (7.21). The viscosity output data from STARS and the calculated R_F from the experimental data, for q=3ml/min.

The shear thinning trend continues as the polymer reaches lower Darcy velocities, which is expected as the transit time between each constriction becomes longer. The calculated R_F values and the simulated rheology displayed in Figure (7.21) illustrates a similar shear thickening slope, but deviates from each other in behavior when reaching lower Darcy velocities, as previously observed. The experimental values level off to an apparent upper Newtonian plateau, while the simulated rheology exhibits a shear thinning behavior. A lowered injection rate causes lower Darcy velocities in the porous media and consequently a more pronounced shear thinning behavior.

The output velocity and viscosity data from STARS does not include the Darcy velocity equal to the injection rate, as seen in Figure (7.17), Figure (7.*19*) and Figure (7.*21*). This assumed to be a modelling error. Further, the simulated apparent viscosity is found to be higher than the experimental R_F and as an average, they deviate from each other by a factor of 2,8.

7.2.1.2 The complete rheology obtained from the manual simulations in STARS

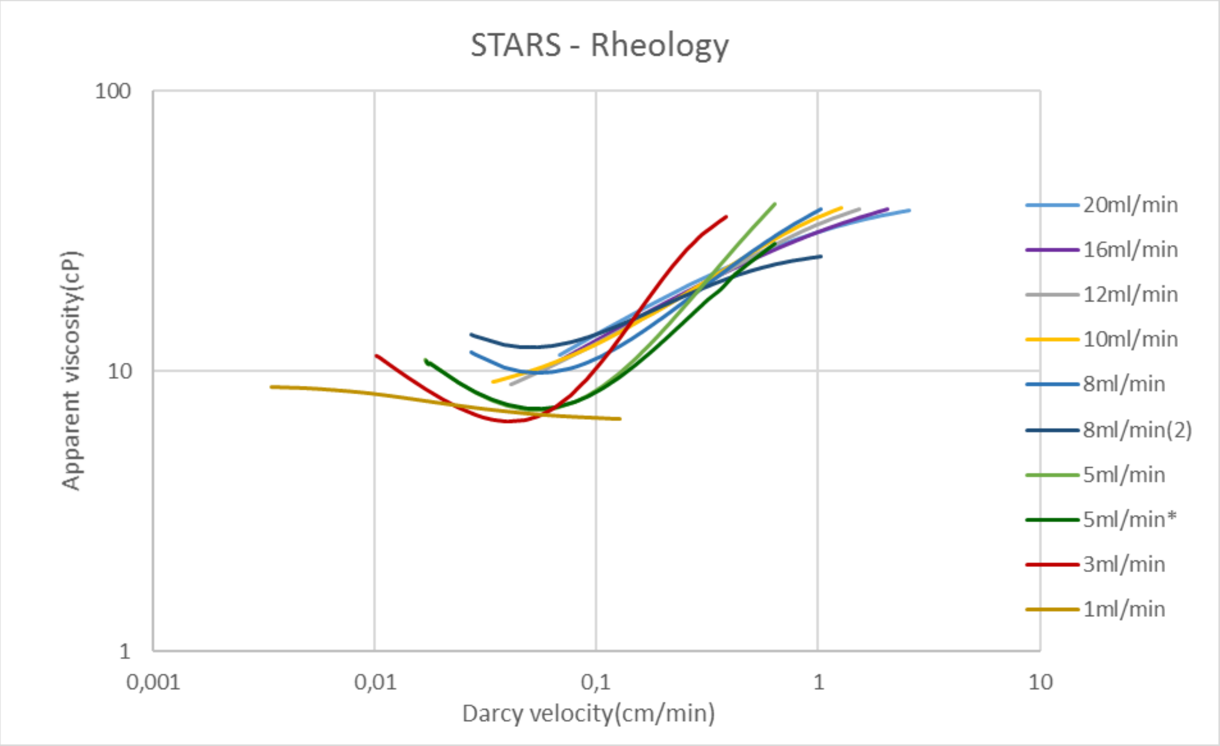

Figure (7.22). The complete manually determined rheology of the synthetic polymer.

Figure (7.22) shows the complete rheology behavior of the synthetic polymer and is the result of the manual history matches of the polymer flooding performed in STARS. The figure will be closely examined in the following discussion.

The rheology determined for each injection rate does not overlap and most of the rates does not act as an extension of each other, which might would have been expected as they overlap in Darcy velocity. Figure (7.22) illustrates that each Darcy velocity has several corresponding apparent viscosity values and demonstrates a rate-dependent rheology. This rate-dependent rheology can be attributed to the time-dependent properties of polymer solutions and the memory effect caused by the viscoelastic nature of synthetic polymers. The behavior of the polymer will depend on the shear history and previously deformations, thus the rheology curve obtained by various injection rates will not result in the same apparent viscosity and behavior as various injection rates consequently results in different flow rates and ultimately, a different shear history [50]. As these effects are complex and involve aspects which is beyond this thesis, this will not be further elaborated and it is considered adequate to state that the viscosity is, as shown, rate-dependent.

High to moderate injection rates displays a shear thickening behavior and appears as an extension of each other, better illustrated in Figure (7.23). They do not follow the exact same slope of shear thickening, which might be an effect of the constant, rate-independent permeability field chosen or a result of a non-identical shear degradation. The effect of a rate-independent permeability will be discussed later. The viscosity at the highest Darcy velocity for each injection rate is similar and is ~37-38cP.

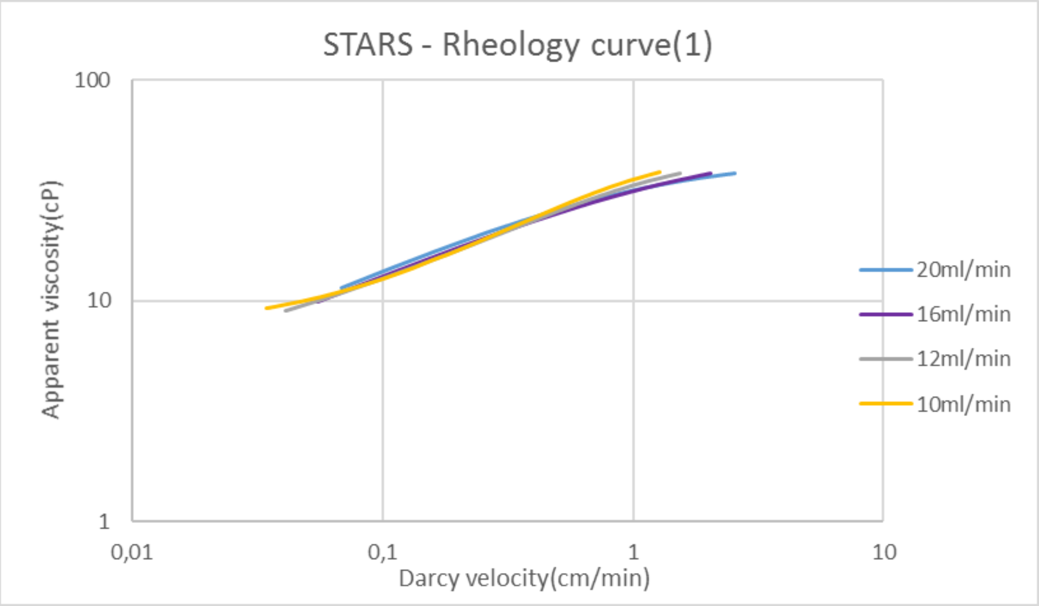

Figure (7.23). The rheology manually determined for q= 20, 16, 12 and 10ml/min.

By comparison of Figure (3.5) and Figure (7.23), there is no sign of mechanical degradation as the manually determined rheology does not display a decrease in apparent viscosity when reaching the highest Darcy velocities and lower flow rates exhibits an apparent shear thinning behavior, which according to Seright et al. (2010) would not a appear if the polymer was mechanically degraded [41]. However, the extended Carreau equation does not consider the possible mechanical degradation which might occur at high injection rates and consequently, using the equation will lead to no apparent signs of mechanical degradation. Assuming that there is no mechanical degradation as the rheology displays shear thinning, the high differential pressure drop in the near wellbore region can thereby only be a result of the increased solution viscosity when adding polymer and is dominated by the viscoelastic behavior of the polymer near the wellbore at high velocities [28].

Seen from Figure (7.22), higher rates have a longer shear thickening region, compared to lower rates which displays both a shear thinning and a shear thickening behavior. This is better illustrated in Figure (7.24), which shows how the onset of shear thickening is shifted towards lower Darcy velocities with lower injection rates.

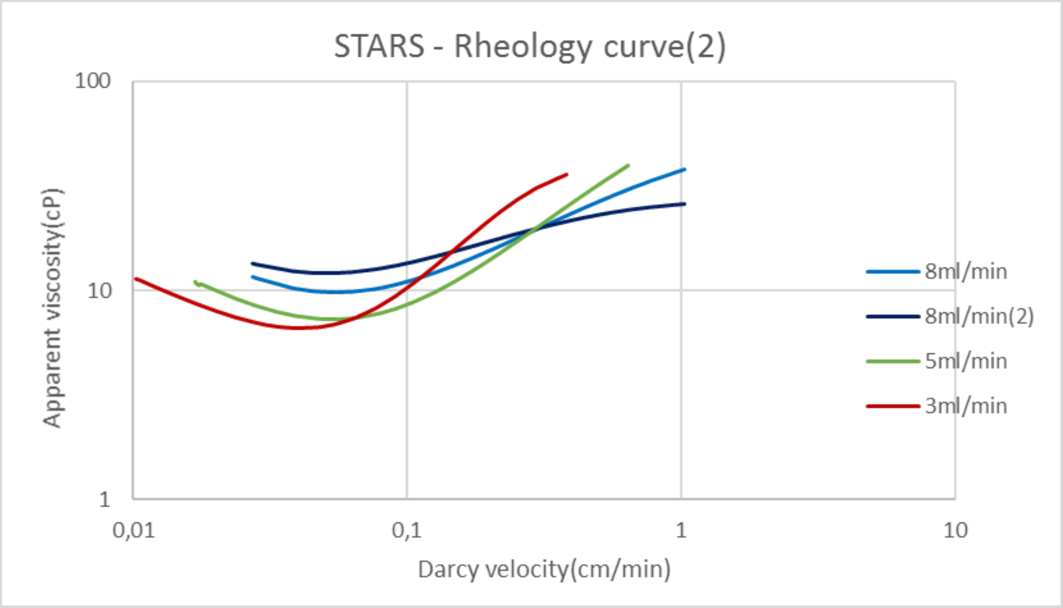

Figure (7.24). The apparent viscosity manually determined for q=8,5, 3ml/min and 8ml/min(2).

Higher injection rates cause the polymer molecules to deviate from their equilibrium state and the deviation increases with increasing injection rate as higher injection rates causes increased shear degradation. Consequently, the polymer will need a longer distance and more time to return to its equilibrium state [1].

Since the higher rates experiences a longer shear thickening region, lower rates will experience a shorter shear thickening region and thereby reach an apparent upper Newtonian plateau closer to the injection well due to the smaller degree of shear degradation [1]. Seen from Table 7.8, the onset of shear thickening occurs closer to the injection well with decreasing rate, which is consistent with literature as Skauge et al. (2016) observed that the onset of shear thickening shifted to decreasing Darcy velocities for decreasing injections rates [1]. This is better illustrated in Figure (7.25).

Table 7.8. The onset of shear thickening determined by manual simulation in STARS.

	Onset of shear thickening	
q(ml/min)	**Darcy velocity(cm/min)**	**Distance from well(cm)**
0,5	23,41E-03	1,09
3	39,93E-03	3,85
5	51,70E-03	4,95
8	53,88E-03	7,60
8(2)	53,53E-03	7,65

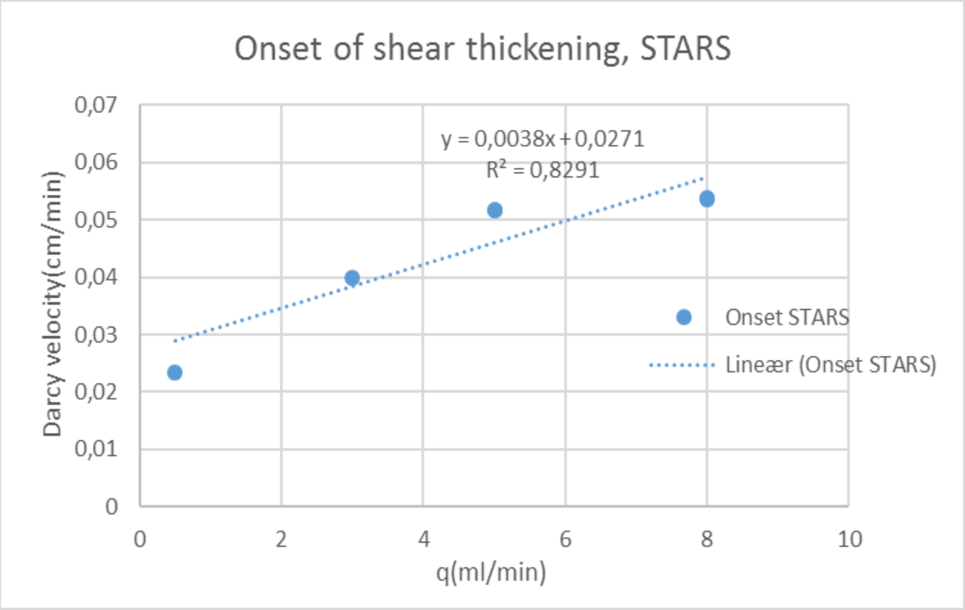

Figure (7.25). The onset of shear thickening, manually simulated in STARS.

The expected upper Newtonian plateau from literature, illustrated in Figure (3.5), appears very short, if not non-existing in Figure (7.24) and behaves more as a short transition zone between the shear thinning and shear thickening behavior, caused by the transition from shear to elongational flow. The apparent minimum value at intermediate flow velocities demonstrates the region where shear flow governs the process and the elongational flow diminishes [50]. However, this short upper Newtonian plateau is consistent with data for linear flow presented in literature by Chauveteau (1981) [38], Delshad et al. (2008) [25] and Heemskerk (1984) [42], where the viscosity exhibit a minimum value at intermediate velocities [41]. Skauge et al. (2016) reported a longer apparent Newtonian plateau for radial flow [1]. Furthermore, the apparent minimum viscosity value is shifted for each rate, which might indicate that the polymer has not reached its equilibrium state and not fully stabilized due to the shear degradation.

Further observations of Figure (7.24) is how the slope of shear thickening increases with decreasing rate. The shorter shear thickening region with decreasing rate has previously been discussed and attributed to a less severe shear degradation, however the steepness of the slope of shear thickening might be an artifact of using a constant, rate-independent permeability instead of the previously discovered rate-dependent permeability field.

The slope of shear thinning is approximately similar for each injection rate, except for the second 8ml/min injection, which was performed after a 20ml/min injection and is referred to as 8ml/min(2). This injection deviates from the others in differential pressure and consequently, rheology. The following subchapters examine both the effect of the rate-independent permeability field as well as the deviating behavior of the 8ml/min(2) injection.

7.2.1.3 The deviating behavior of q=8ml/min(2) and 1ml/min

The shear thickening slope of q=8ml/min(2) is not as steep as the other, it reaches a lower intermediate minimum viscosity value and exhibit less shear thinning, as shown in both Figure (7.24) and Figure (7.26).

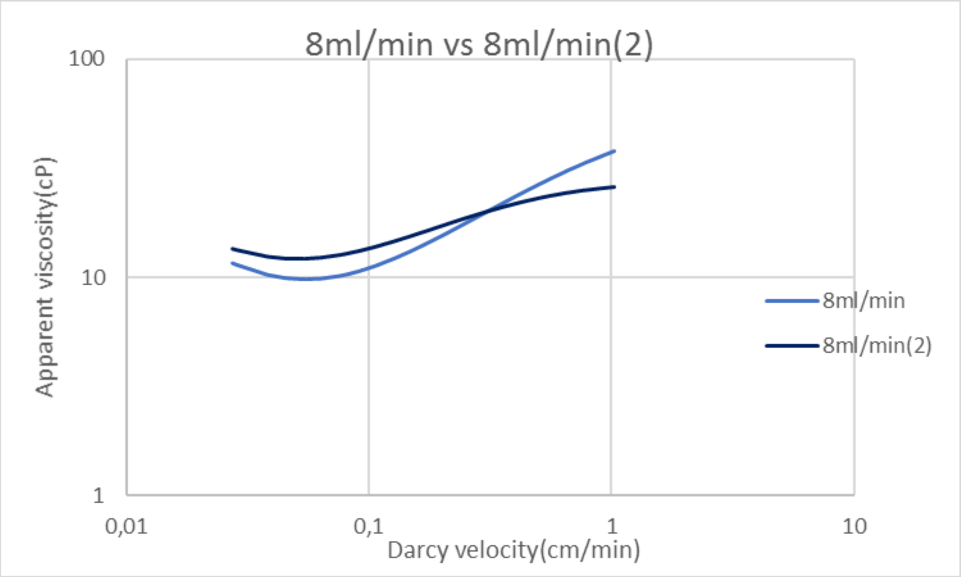

Figure (7.26). The difference between the simulated apparent viscosity of q=8ml/min and 8ml/min(2).

One reason for this deviation in rheological behavior could be mechanical degradation, which causes the polymer molecular to break and results in a significantly reduces apparent viscosity at the high Darcy velocities and furthermore, a minimized shear thinning effect, as reported by Seright et al. (2010) [41]. In addition, Seright et al. (1983) reported that mechanical degradation improved the injectivity of the well due to the decrease in apparent viscosity and an following decrease in differential pressure [28], which further supports the theory of mechanical degradation of q=8ml/min(2), shown in Figure (7.27).

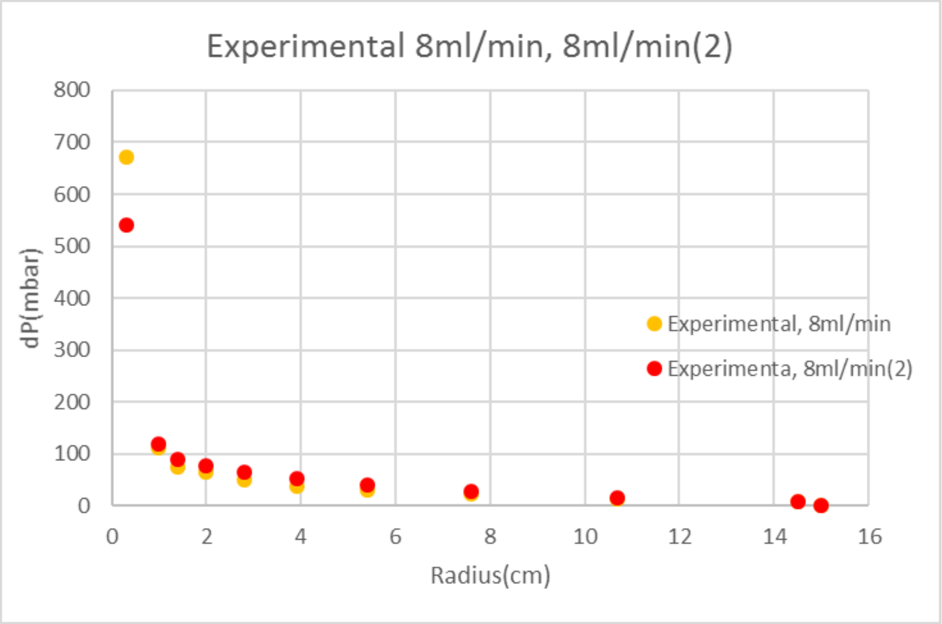

Figure (7.27). The difference in experimental differential pressure between 8ml/min and 8ml/min(2).

However, there is one problem with this assumption. Mechanical degradation occurs when the polymer is subjected to high shear rates, which happens at high flow rates and there was no sign of mechanical degradation at the previously higher injection rates, but this could be due to the use of the extended Carreau equation which does not consider mechanical degradation.

Another possibility is that the permeability in the porous media has been altered. Straining, which is blocking of pores by single molecules, reduces the permeability and is known to increase with increased rate. As q=8ml/min(2) follows the highest performed injection rate during the polymer flood, it is possible that the permeability has been reduced which consequently results in an increased differential pressure. Figure (7.27) illustrates an increase in differential between 1 and 8cm out in the core which further supports the assumption, as large molecule species are known not to propagate far out in the porous media [41]. As the polymer flooding is performed with a constant permeability, the decreased permeability and following increase in differential pressure is thereby accounted for by an increase in apparent viscosity and a higher intermediate viscosity value. However, this does not explain the lowered differential pressure in the wellbore area and the following reduced apparent viscosity at high flow rates.

Furthermore, since the rheology curves is obtained by history matching differential pressure, the deviation between the two injection rates could also be an experimental artifact caused by the pressure transducers, combined with the uncertainty from the simulated permeability field.

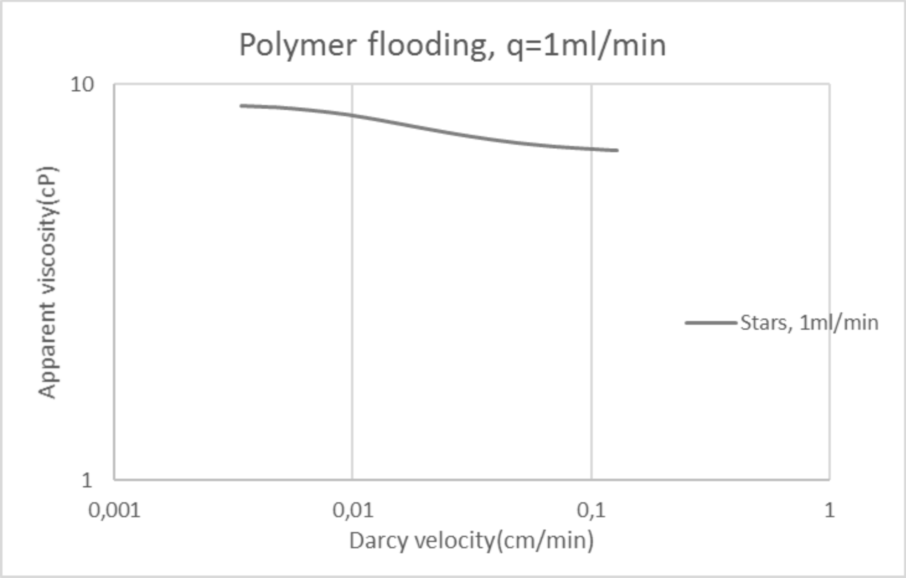

Figure (7.28). The simulated rheology curve for q=1ml/min.

The same discussion also applies for q=1ml/min as it deviates from the other rates in both differential pressure and hence, rheology, illustrated in Figure (7.28). As it only displays a shear thinning behavior and a lower differential pressure than q=0,5ml/min, listed in Table 6.4, it supports the theory of mechanical degradation. However, this is not possible to confirm and is not expected at such low rates.

7.2.1.4 The effect of the rate-independent permeability field

In chapter 7.1, the history matching of the waterflooding demonstrated a rate-dependent permeability, however, as the rock properties is not expected to change, one constant rate-independent permeability was chosen to use for the further history matching of the polymer flood. As the absolute permeability is invers proportional and the viscosity is proportional to the differential pressure, the choice of permeability will furthermore influence the apparent viscosity and the rheology output from the differential pressure history matches for each injection rate.

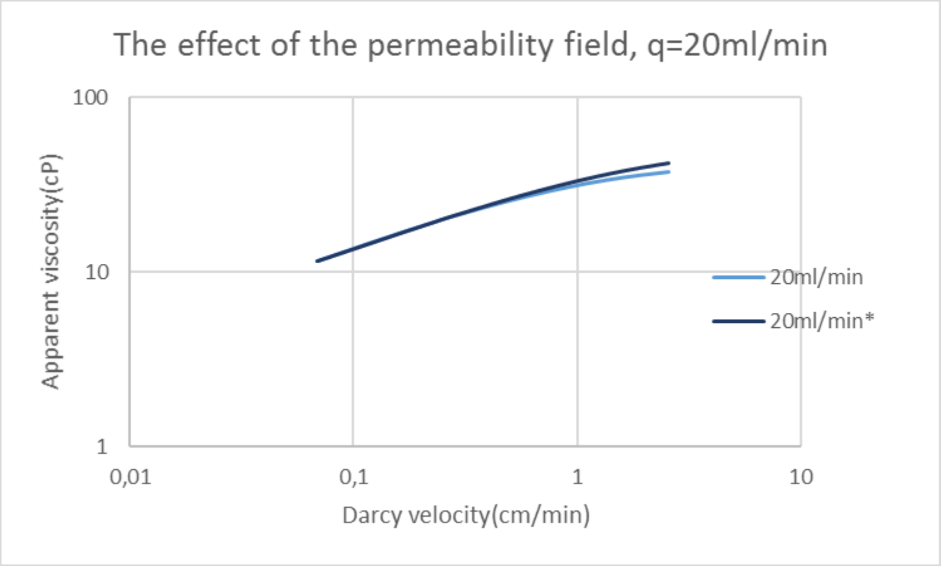

Figure (7.29). The apparent viscosity for q=20ml/min when using the permeability found for q=10ml/min and the apparent viscosity for q=20ml/min when using the permeability found for q=20ml/min, marked with *.

Figure (7.29) shows the rheology obtained from history matching with the rate-independent permeability, illustrated by the light blue curve, and the rheology obtained when using the individual rate-dependent permeability history matched for q=20ml/min, illustrated by the dark blue curve. Both permeability fields are listed in Table 7.3 and only differ from each other in region 1, hence the rheology output is only affected in the near wellbore area represented by high Darcy velocities. The difference between the two permeability fields is 40 mD, thus the rheology output is not significantly influenced at high injection rates.

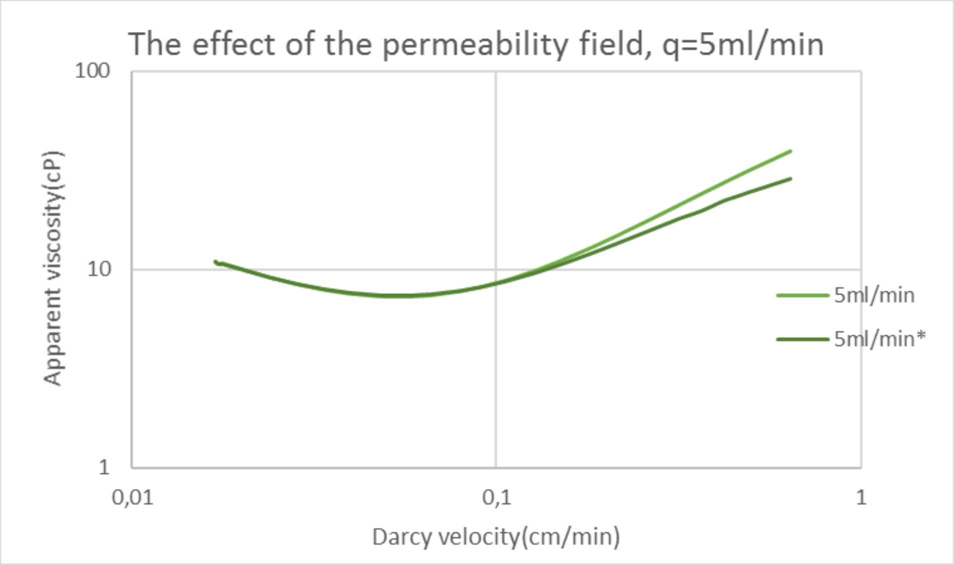

Figure (7.30). The apparent viscosity for q=5ml/min when using the permeability field found for q=10ml/min and the apparent viscosity simulated for 5ml/min when using the permeability found for q=10ml/min, marked with *.

Figure (7.30) shows how choosing the rate-independent permeability for further use in the polymer flooding influences the simulated rheology obtained for the lower injection rates. The light green curve is the rheology obtained by using the rate-independent permeability, while the dark green curve is the rheology obtained by using the history matched permeability of q=5ml/min. The permeability fields, listed in Table 7.3, deviate from each other in both region 1 and 2 and consequently effects the rheology to a greater extent than previously observed. The slope of shear thickening is steeper when using the rate-independent permeability due to the higher permeability in region 1. Hence, to achieve an adequate differential pressure response, the apparent viscosity and the slope of shear thickening increases. However, the onset of shear thickening appears to not be influenced by using a rate-independent permeability.

The difference between the two simulated rheology curves is noticeable and one might argue that the consequences of using the constant and rate-independent permeability field instead of the implied rate-dependent permeability caused by an apparent skin effect, results in an overestimated shear thickening behavior for lower injection rates.

7.2.1.5 Injectivity

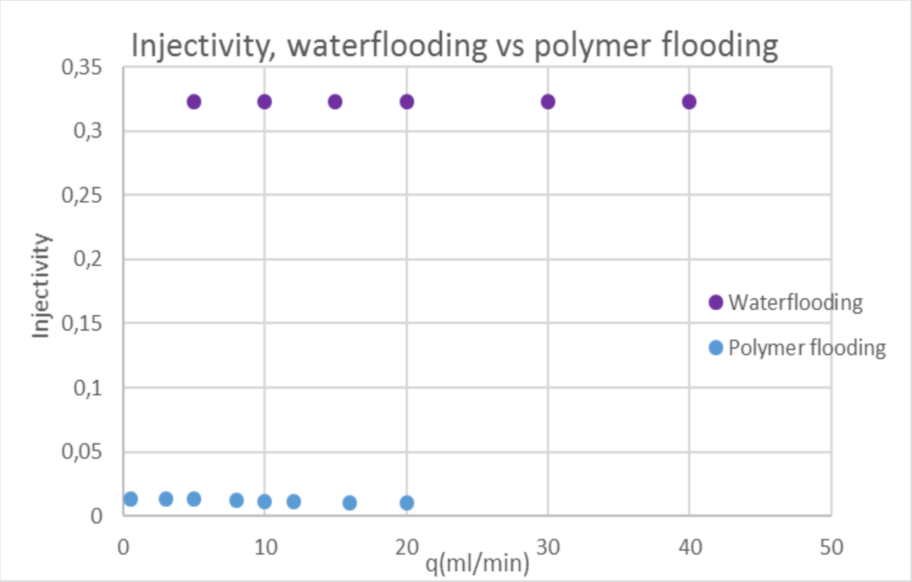

Figure (7.31). The calculated injectivity of the waterflooding and the polymer flooding, performed in STARS.

As previously mention, it is expected that the injectivity of a polymer flood is significantly lower than the injectivity of a waterflood due to the increased apparent viscosity caused by the viscoelastic nature of the synthetic polymer. This is consistent with Figure (7.31), which shows that the injectivity values of the polymer flood is more than one order lower than the values obtained for the waterflood. However, Figure (7.31) poorly illustrates the injectivity development of the polymer flooding due to the value difference between the injectivity of the waterflood and the injectivity of the polymer flood. The polymer flood injectivity is better illustrated in Figure (7.32).

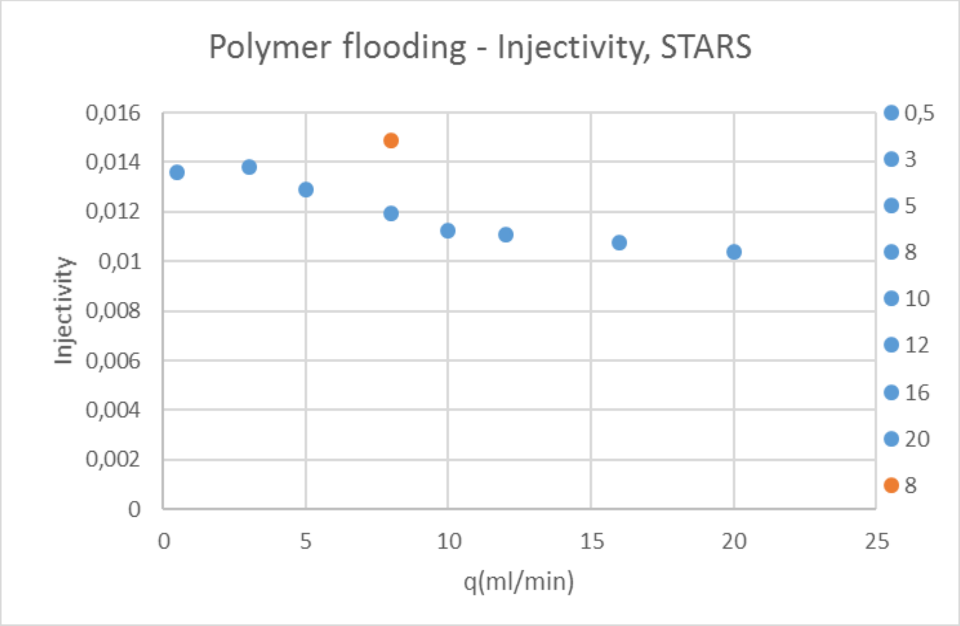

Figure (7.32). The calculated injectivity for the polymer flooding based on the simulated differential pressure in the injection well, performed in STARS.

The injectivity of a polymer flood is also known to decrease with increased injection rate due to the synthetic polymers shear thickening behavior which causes an increasing apparent viscosity with increasing injection rates and consequently, a drastic increase in differential pressure. Figure (7.32) is consistent with this and illustrates a steadily decreasing injectivity with increasing injection rates. The highest obtained injectivity appears to be when q=3ml/min, as the orange dot in Figure (7.32) is q=8ml/min(2) and is considered a deviation, since the cause of the deviating differential pressure and rheology is not to be determined and the rate carries great uncertainty. This also applies for q=1ml/min, which resulted in an injectivity too high to include due to the poor illustration of the injectivity of the other injection rates. However, mechanical degradation is known to increase the injectivity of a polymer flood and the increased injectivity of q=8ml/min(2) and 1ml/min supports the argument.

7.2.2 MRST – Polymer flooding

The history matches are based on the same experimental data as the previously subchapter and is performed to examine the difference between the manual estimated rheology from STARS and the automatic obtained rheology in MRST. Due to the objective, the differential pressure history matches obtained in MRST can be found in appendix A. The execution of the following was introduced in chapter 5 and the rheology curves are obtained by the extended Carreau equation and the six parameters: λ_1, λ_2, n_1, n_2, η_0 and η_{max}.

7.2.2.1 STARS vs MRST

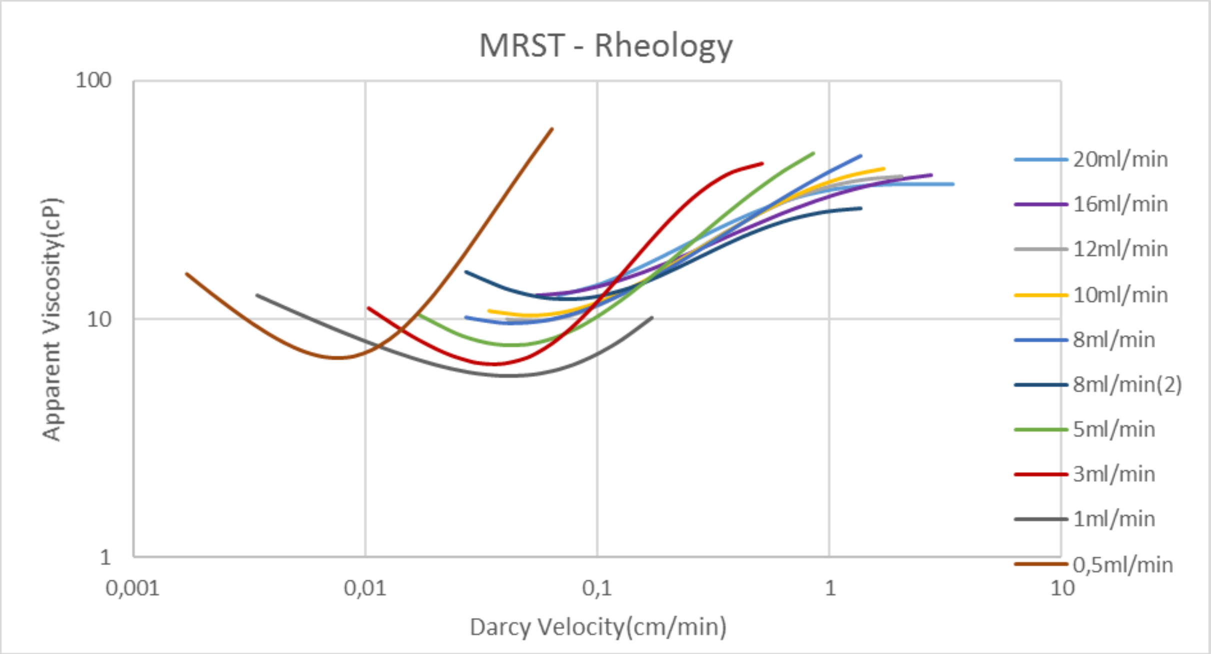

Figure (7.33). The complete rheology curve obtained from MRST.

Figure (7.33) shows the complete rheology curve obtained by the automatic simulations performed in MRST. By comparison with figure (7.22), the manual and automatic obtained rheology appears similar, although MRST demonstrates a greater degree of consistency between high to intermediate injection rates. They both displays a rate-dependent rheology, a shear thickening and shear thinning behavior, an increased shear thickening slope with decreasing injection rates, a shorter shear thickening region with decreasing injection rates and a shifted onset of shear thickening with decreasing injection rates. Although they are exceedingly similar, there are some differences between them.

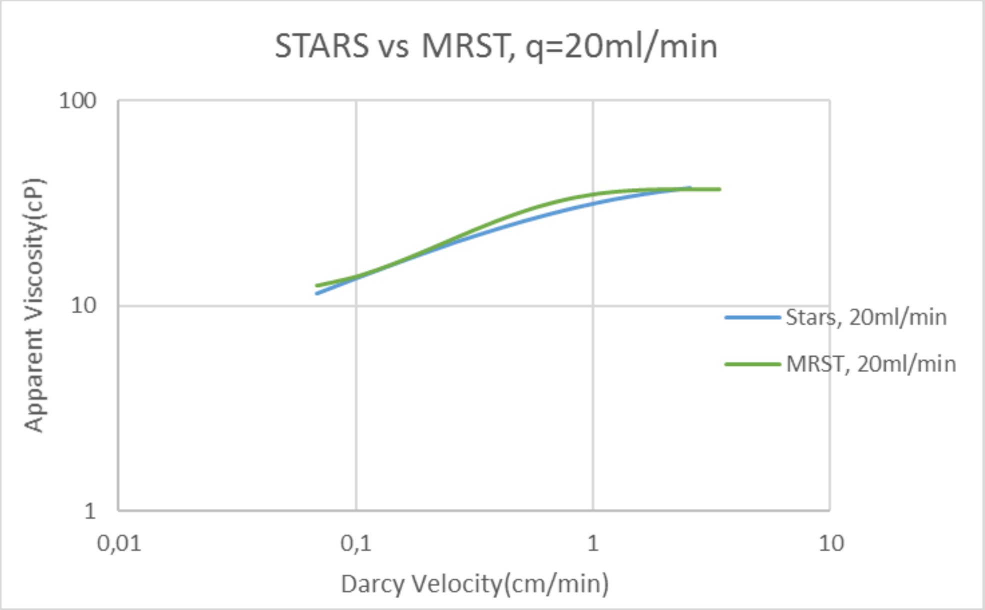

Figure (7.34). STARS vs MRST rheology, q=20ml/min.

Figure (7.34) illustrates the difference between the rheology curve obtained by manual and automatic simulations and represents the difference between the higher injection rates of the polymer flooding. They do not deviate much in value, though the automatic rheology demonstrates a slightly different behavior. The slope of shear thickening is less steep and the apparent viscosity appear to level of at higher Darcy velocities and reaches an apparent plateau. The apparent plateau is similar to the plateau illustrated in Figure (3.5) and a further increase in velocity might cause mechanical degradation. However, this is only speculation as the manual simulations did not display the same apparent plateau, although the slope of shear thickening did decrease with increased injection rate.

The manually obtained rheology continues it slope of shear thickening when reaching lower Darcy velocities and displays a longer shear thickening region, while the automatic displays a gradual decrease in the shear thickening slope and appears to reach an apparent Newtonian plateau at lower injection rates. This is better illustrated in Figure (7.35), which represent the difference between the automatic and manual rheology at intermediate injection rates.

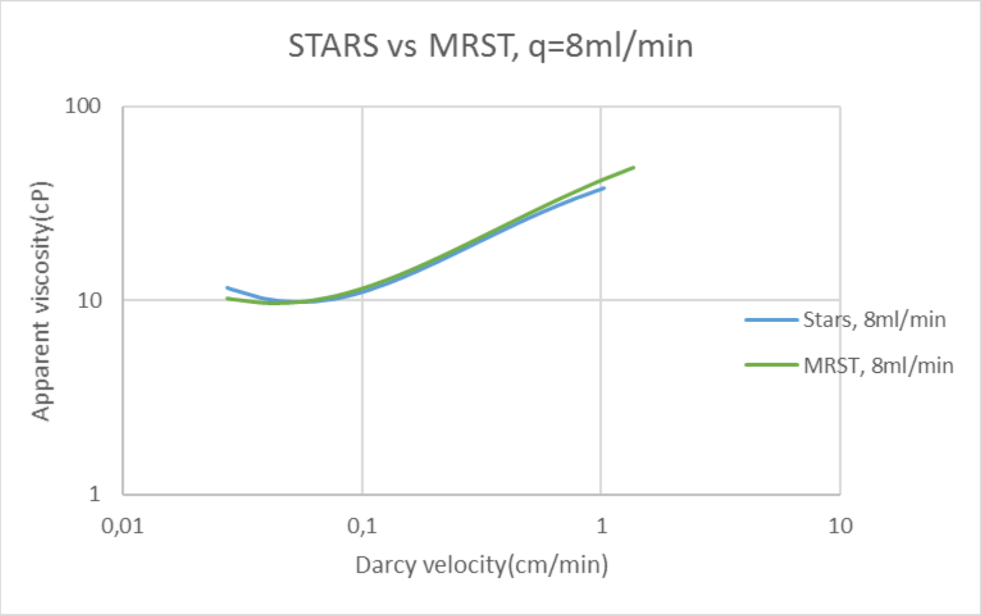

Figure (7.35). STARS vs MRST rheology, q=8ml/min.

Figure (7.35) illustrates how the automatic obtained rheology displays a more distinct apparent upper Newtonian plateau, compared to the previously discussed transition zone in the manual estimated rheology. Compared to literature on radial flow, this apparent Newtonian plateau is not as long as expected [1]. However, this convergence towards an apparent upper Newtonian plateau diminished with decreasing injection rate and consequently behaves more as a transition zone as demonstrated in the manually obtained rheology. This is better illustrated in Figure (7.36).

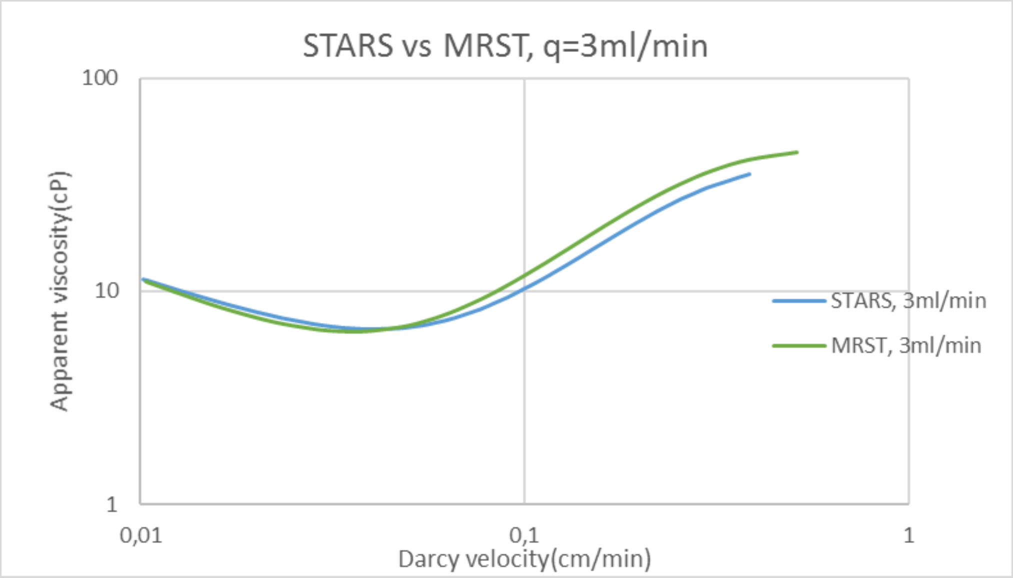

Figure (7.36). STARS vs MRST rheology, q=3ml/min.

The difference in apparent viscosity between the manual and automatic obtained rheology increases with decreasing injection rate, as demonstrated in Figure (7.36). However, their rheological behavior is similar and the difference between them is the slope of shear thickening and an apparent shift in the onset of shear thickening. The shift in the onset of shear thickening is more pronounced at lower injection rates, but as STARS seemed to struggle with pressure stabilization at lower rates combined with the fact that lower rates carries a greater degree of uncertainty, the q=0,5ml/min rheology is not presented.

It was previously stated when discussing the manual simulations that high to intermediate injection rates did not display a shear thinning behavior and only behaved shear thickening. However, MRST displays a shear thickening and shear thinning behavior at intermediate to low injection rates, shown in Figure (7.37).

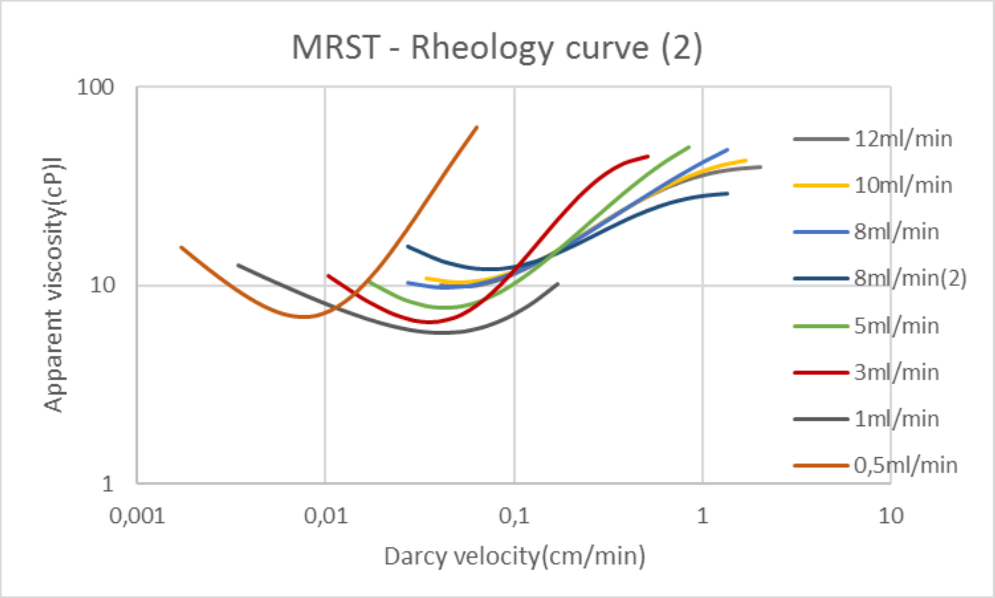

Figure (7.37). The injections rates which demonstrate both shear thickening and shear thinning in MRST.

Although MRST display an apparent shear thinning at higher Darcy velocities, the onset of shear thickening is shifted to lower Darcy velocities and occurs further away from the injection well, when compared to the onset of shear thickening estimated manually in STARS. This is easier observed by comparing of Table 7.8 and Table 7.9 and illustrated by Figure (7.39).

Table 7.9. The onset of shear thickening from automatic simulations in MRST.

Onset of shear thickening		
q(ml/min)	**Darcy velocity(cm/min)**	**Distance from well(cm)**
0,5	7,31E-03	3,50
1	42,65E-03	1,20
3	34,12E-03	4,50
5	39,37E-03	6,50
8	45,49E-03	9,00
8(2)	75,82E-03	5,40
10	47,83E-03	10,70
12	57,39E-03	10,70

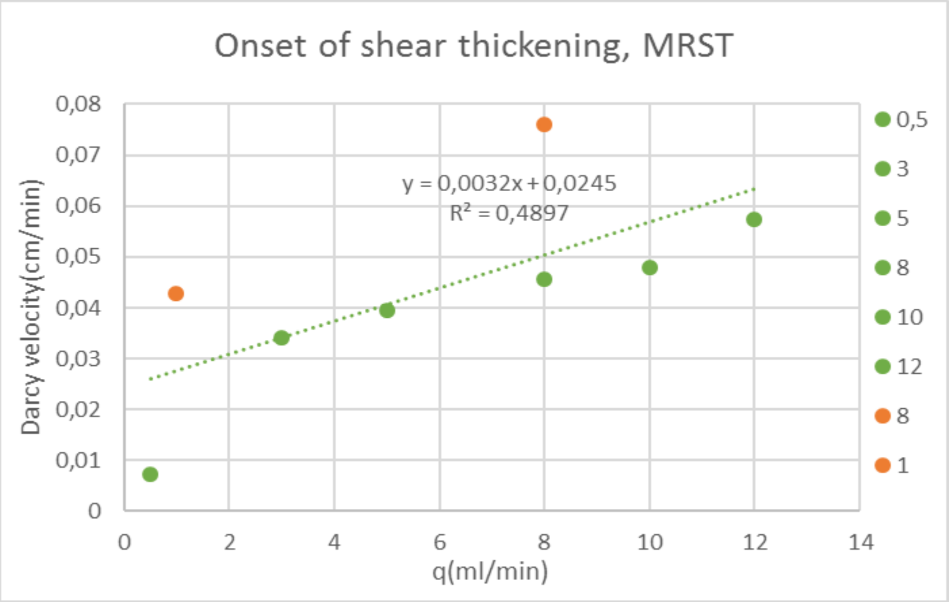

Figure (7.38). The onset of shear thickening found in MRST.

If classifying the q=8ml/min(2) and 1ml/min as deviations, the rheology obtained in MRST displays the same trend as the manual history matches; the onset of shear thickening decreases with decreasing rate and occurs closer to the well with decreasing rates.

In Figure (7.39) the onset of shear thickening obtained in STARS and MRST for q=0,5ml/min has been ignored as it has a high uncertainty and influences the customization of the function.

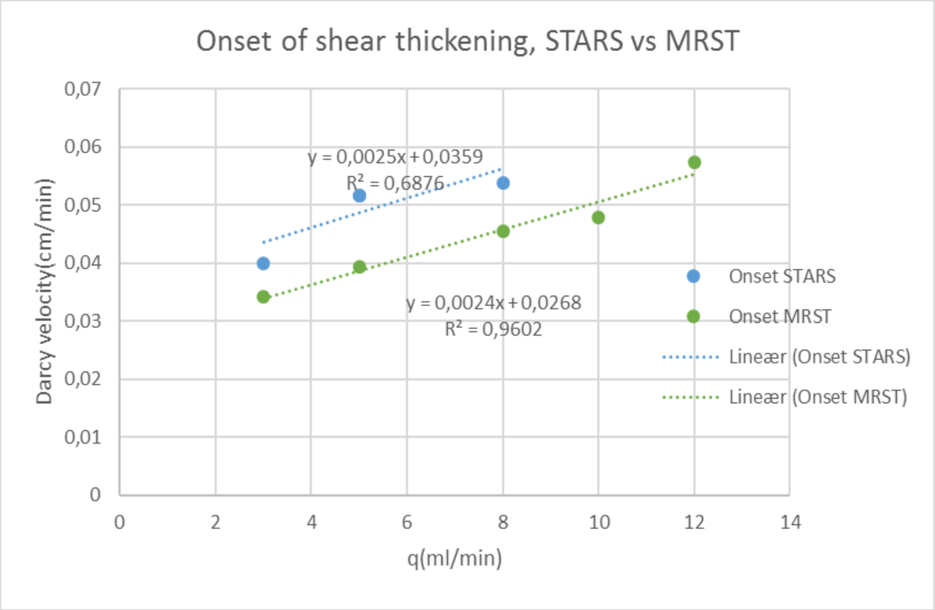

Figure (7.39). The onset of shear thickening, STARS vs MRST.

Figure (7.39) illustrates the onset of shear thickening obtained in STARS and MRST and demonstrates a parallel shift between the two. They follow a very similar slope of shear thickening but deviate from each other in value as STARS demonstrates an onset of shear thickening at higher Darcy velocities and consequently, an onset which occur closer to the injection well, shown in Figure (7.40).

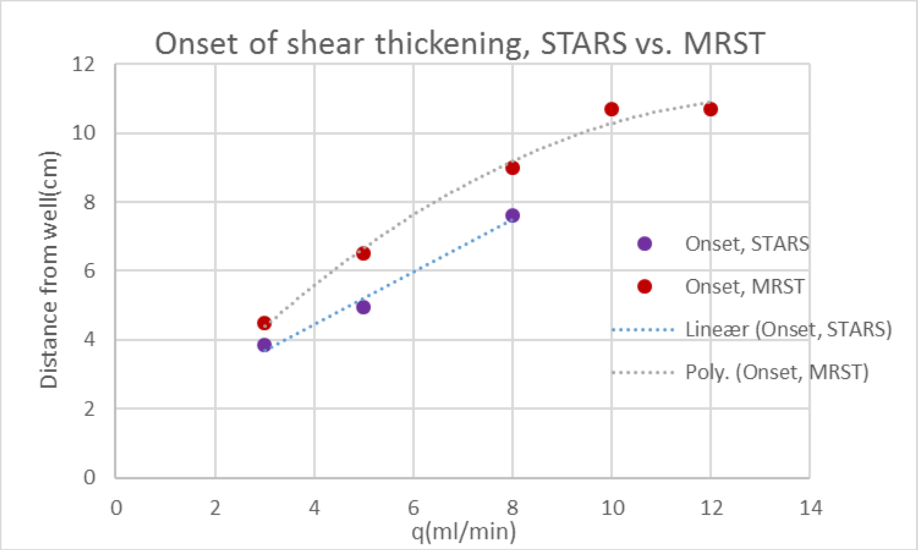

Figure (7.40). Illustration of how the onset of shear thickening occurs closer to the injection well with decreasing injection rates.

The onset obtained from MRST appears to converge to a plateau at high injection rates and demonstrates flowrate independency beyond q=10ml/min, however there is insufficient data to support this apparent trend. As the onset of shear thickening obtained in STARS only includes three rates, it includes a higher uncertainty due to fewer points. Further, the deviations between the onset of shear thickening estimated in STARS and MRST is minor, of a small order and based on their similar rheological output data for most of the rates, can be ignored.

7.2.2.2 The deviating behavior of q=8ml/min(2) and 1ml/min

The deviating behavior of q=8ml/min(2) and 1ml/min was previously considered during the discussion of the manual simulations and as the automatic simulations is based on the same experimental differential pressures, it is expected that it demonstrates a similar deviating trend.

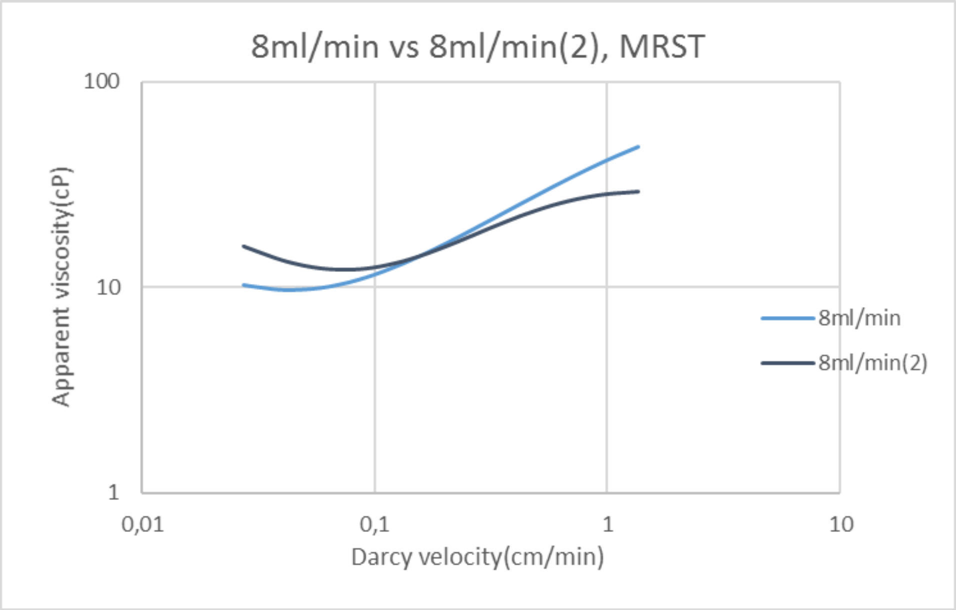

Figure (7.41). The difference between the simulated apparent viscosity of q=8ml/min and 8ml/min(2) in MRST.

Figure (7.41) demonstrates similar deviating behavior as discussed previously; a decreased apparent viscosity at high flow rates and a higher minimum intermediate viscosity value. However, MRST displays an increase in shear thinning behavior which opposes the argument of mechanical degradation which is known to minimize shear thinning behavior of the synthetic polymer [41]. This apparent increase shear thinning behavior is also displayed for q=1ml/min, showed in Figure (7.42).

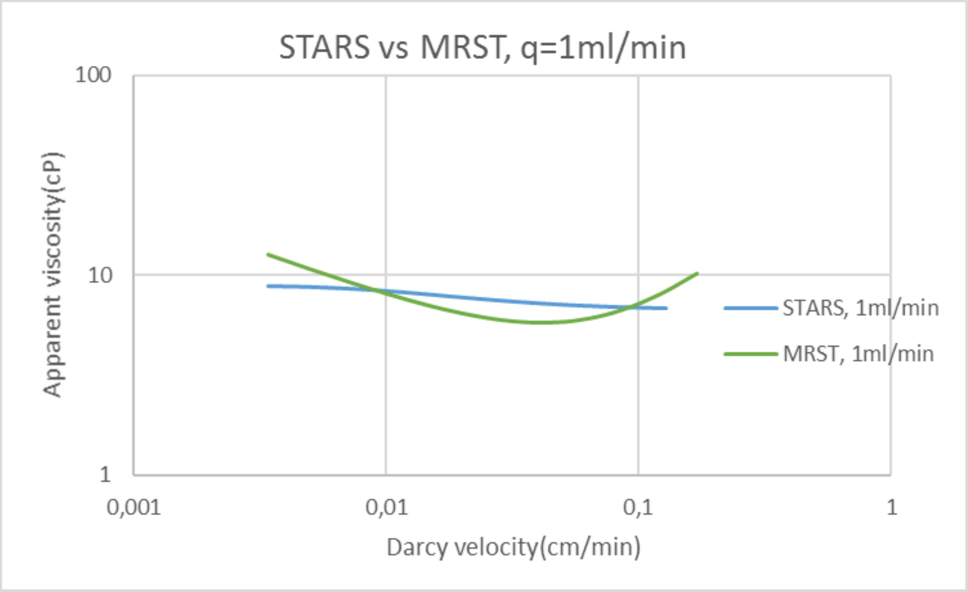

Figure (7.42). STARS vs MRST rheology, q=1ml/min.

Figure (7.42) illustrates the deviating behavior between STARS and MRST at q=1ml/min. While STARS displayed a slightly shear thinning and almost an apparent Newtonian behavior, MRST displays both shear thickening and shear thinning. However, as this is a low rate and consequently low differential pressures, the results include a high degree of uncertainty.

The results from MRST deviates from the results obtained in STARS and it is therefore hard to establish an accurate behavior and hence, the possible cause of the altered behavior of the polymer flooding performed after q=20ml/min. It is therefore considered adequate to state that the behavior deviates from the other injection rates. The deviations could possibly be caused by mechanical degradation, straining, permeability reductions or the uncertainty of the pressure transducers combined with the uncertainties of the simulated permeability, as discussed previously, however this is not possible to establish and the manual and automatic simulations did not display the same deviating trend.

7.2.2.3 The effect of rate-independent permeability field

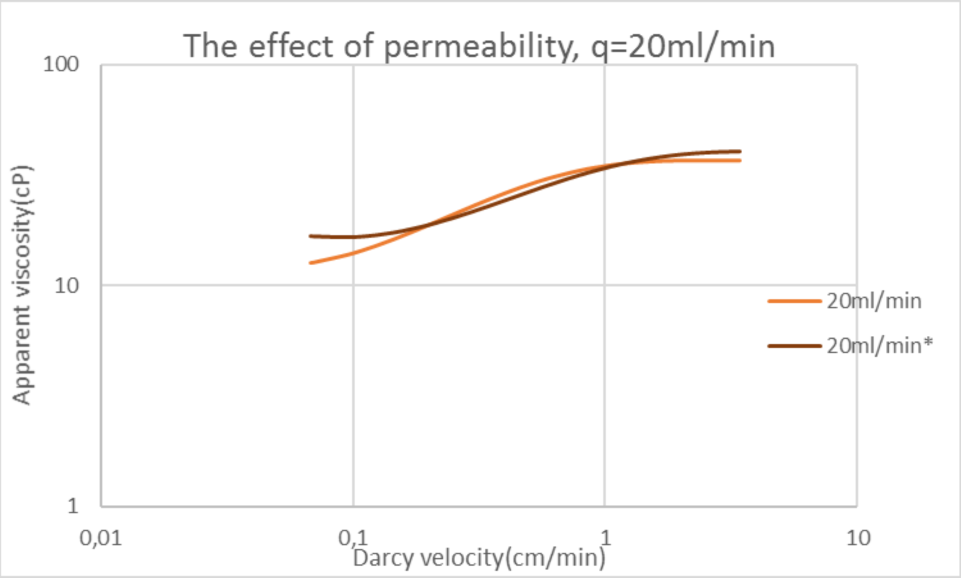

Figure (7.43). The apparent viscosity for q=20ml/min when using the permeability history matched for q=10ml/min and the apparent viscosity for q=20ml/min when using the permeability determined for q=20ml/min, marked with *, performed in MRST.

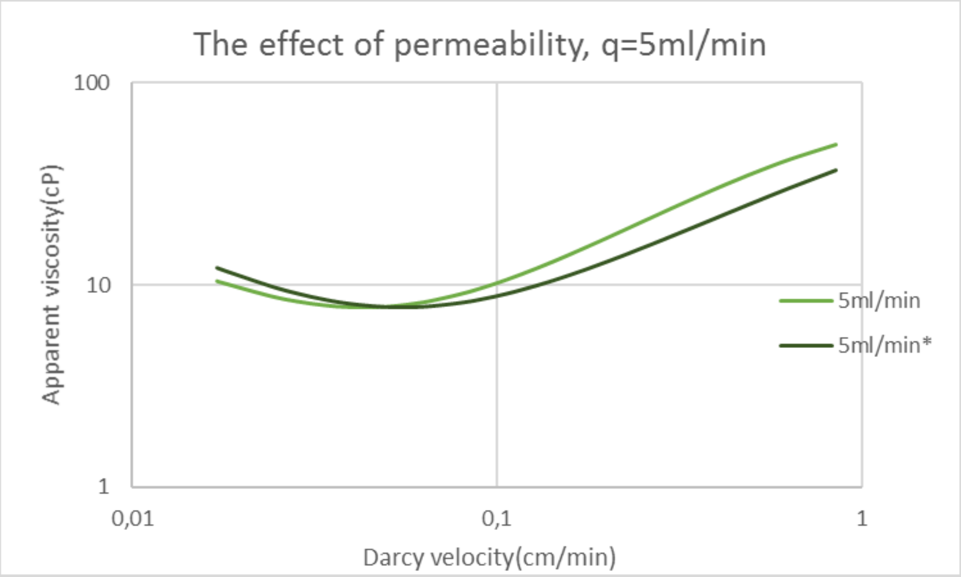

Figure (7.44). The apparent viscosity for q=5ml/min when using the permeability history matched for q=10ml/min and the apparent viscosity for q=5ml/min when using the permeability determined for q=5ml/min, marked with*, performed in MRST.

MRST did not the display the same rate-dependent permeability trend in the wellbore area as STARS and the permeability fields obtained by the automatic simulations of the waterflooding illustrated a more random behavior. Examining the effect of using the chosen rate-independent permeability in MRST consequently does not demonstrate an identical influence on the rheology as previously observed in the manual simulations, however, it does show a similar trend.

Figure (7.43) illustrates the influence of a rate-independent permeability at high injection rates. As the rate-independent permeability differed from the history matched permeability of q=20ml/min in both region 1 and 3, the rheology consequently differs from each other in these regions. This pronounced in region 3, where the rate-independent permeability was lower, hence the apparent viscosities obtained when using the rate-dependent permeability increased to achieve an adequate differential pressure.

The rate-independent permeability has a larger influence on lower injection rates, which is evident when comparing Figure (7.43) and Figure (7.44). This is consistent with the previously findings in the manual simulations and the rate-independent permeability causes an overestimated shear thickening behavior at low injection rates. As the permeability fields obtained by automatic history matching, listed in Table 7.5, varies more from each other than the ones obtained manually, the effect of a rate-independent permeability became more prominent in MRST.

7.2.2.3 Injectivity

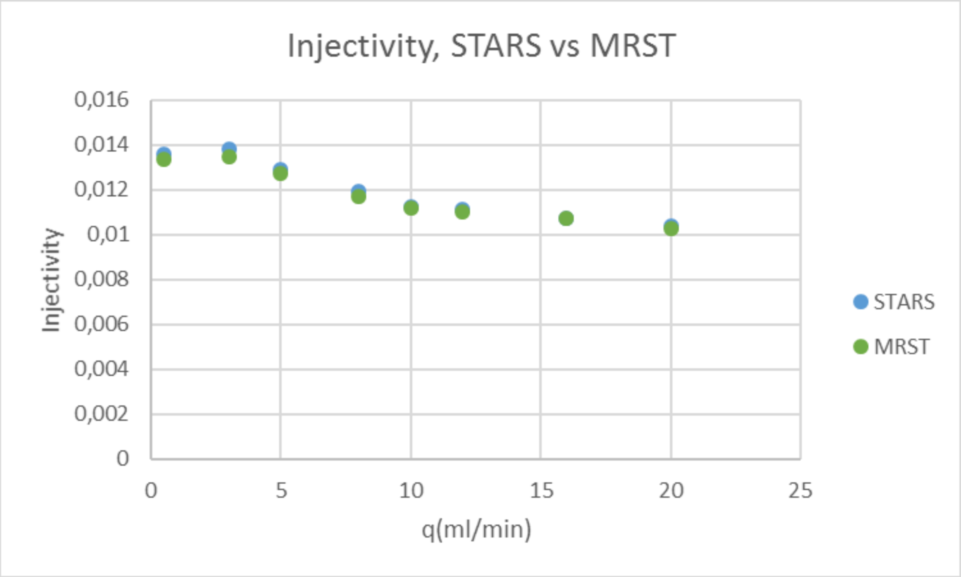

Figure (7.45). The calculated injectivity for polymer flooding based on the simulated differential pressure in the injection well, in both STARS and MRST.

As the same experimental pressure data is used when history matching in both STARS and MRST, they display the same injectivity and the same trend. The minor deviation between them is illustrated in Figure (7.45) is caused by slightly different obtained differential pressure values during the history matches.

7.3 The effect of polymer rheology on injectivity

The previous subchapters demonstrated how both STARS and MRST displayed the approximately same polymer rheology. As the injectivity is strongly influenced by polymer rheology, the following chapter will examine the extent of polymer rheology and the viscoelastic nature of synthetic polymer influence on the expected injectivity. The following simulations is performed manually in STARS and utilizes the same core model as previously described in chapter 5.

Injectivity is defined by equation (7.5) and during the previously performed history matches, it was a constant as the performed history matches was based on injection rate and an experimentally measured differential pressure. However, the following is not an history match, but an attempt to illustrate how the polymer rheology influences the injectivity.

By performing minor alterations in the script used for the manual history matching, it is possible to set a constant bottom hole pressure, instead of a constant injection rate. Thereby it is possible to determine the highest obtainable injection rate when applying a specific polymer rheology. This is done by utilizing the history matched polymer rheology, presented in the previous subchapter and the constant bottom hole pressure was chosen to be within the differential pressure range of the experimental data and is set equal to 1000mbar.

As the previously obtained polymer rheology corresponds to specific Darcy velocities due to a specific injection rate, the curves had to be extended to both increased and decreased Darcy velocities. The extension of the rheology curve was due to the difficulty of predicting which Darcy velocity range a constant bottom hole pressure equal to 1000mbar would operate within, as it depends on the viscoelastic nature of the polymer.

The rheology curves in Figure (7.46) are based on the polymer rheology obtained in the manual simulations in STARS. The purple curve displays an only shear thickening behavior and is an extended version of q=16ml/min, while the two curves referred to as “shear thickening + shear thinning (1)” and “shear thickening + shear thinning (2)” are created by an expansion of q=5ml/min and q=5ml/min*, respectively. The yellow curve, which only displays a shear thinning behavior, is purely empirical and is designed by changing the variables in the extended Carreau equation, as the previous history matches did not demonstrate a purely shear thinning rheology.

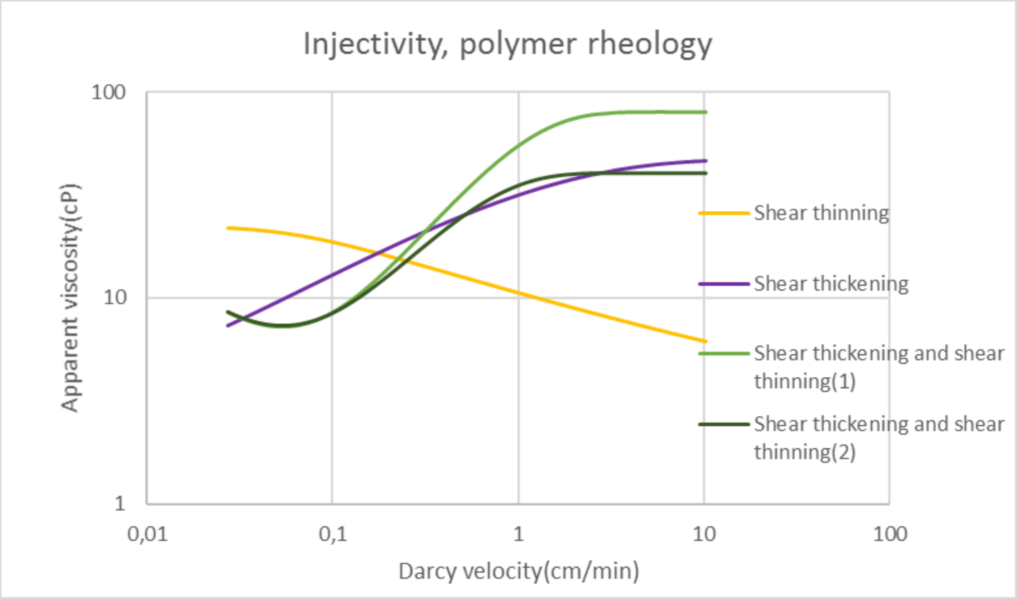

Figure (7.46). The input apparent viscosities and corresponding Darcy velocities in SHEARTAB in STARS.

Figure (7.46) illustrates the input apparent viscosities and their corresponding Darcy velocities used in the simulations in STARS which aimed to find the highest possible injection rate when setting the constant bottom hole pressure equal to 1000mbar and using a specific polymer rheology. However, as the polymer rheology influences the injectivity of the well, it is expected that a shear thinning behavior results in a possible higher injection rate due to the low apparent viscosity and consequently achives higher Darcy velocities in the porous media. This is better illustrated in Figure (7.47), which illustrates the apparent viscosity output data obtained from the simulations in STARS.

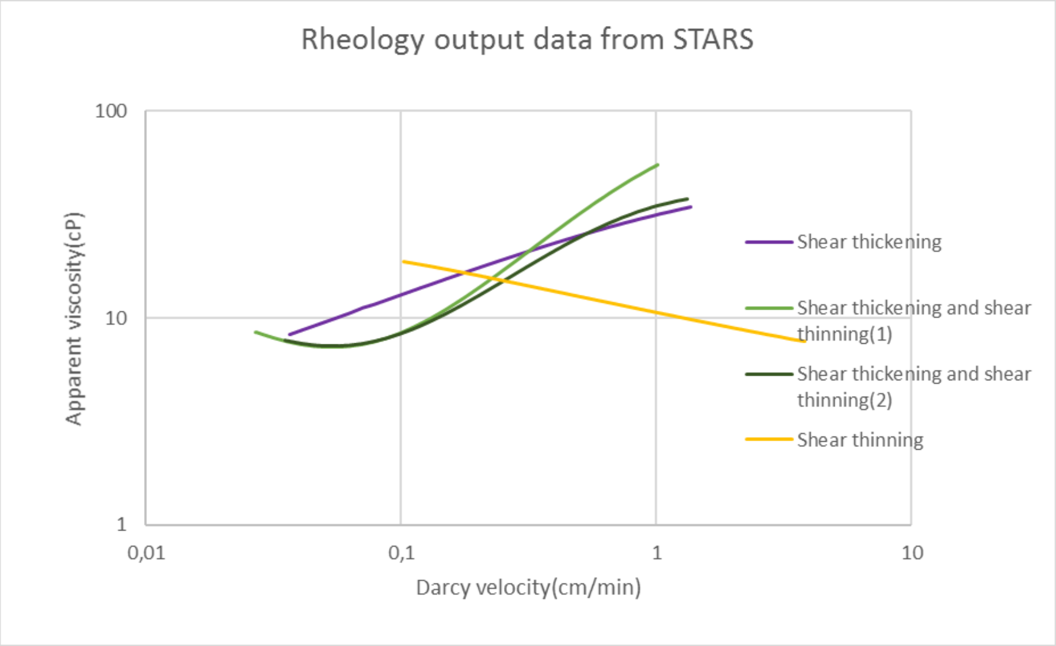

Figure (7.47). The output apparent viscosity data from the examination of the polymer rheology influence on injectivity.

Figure (7.47) clearly demonstrates that a shear thinning behavior can be injected with a higher injection rate as it displays higher Darcy velocities, compared to the Darcy velocities obtained when the polymer has a shear thickening behavior.

As previously stated the choice of using a rate-independent permeability field did cause an overestimated degree of shear thickening, shown in Figure (7.30). To illustrate the effect of this on the injectivity, both rheology curves was used to examine the effect of a shear thickening and a shear thinning behavior on the injectivity.

The effect of Newtonian fluids, as water and glycerol, was also tested. The water viscosity was set to 1cP and the glycerol viscosity was set to 101,5cP. The effect of polymer behavior and the viscosity of Newtonian fluids is shown in Figure (7.47) and in Table 7.10. The water injectivity was significantly higher than the injectivity calculated for polymer and glycerol, which is why it is not plotted in Figure (7.48), as it caused a poor illustration of the other injectivities.

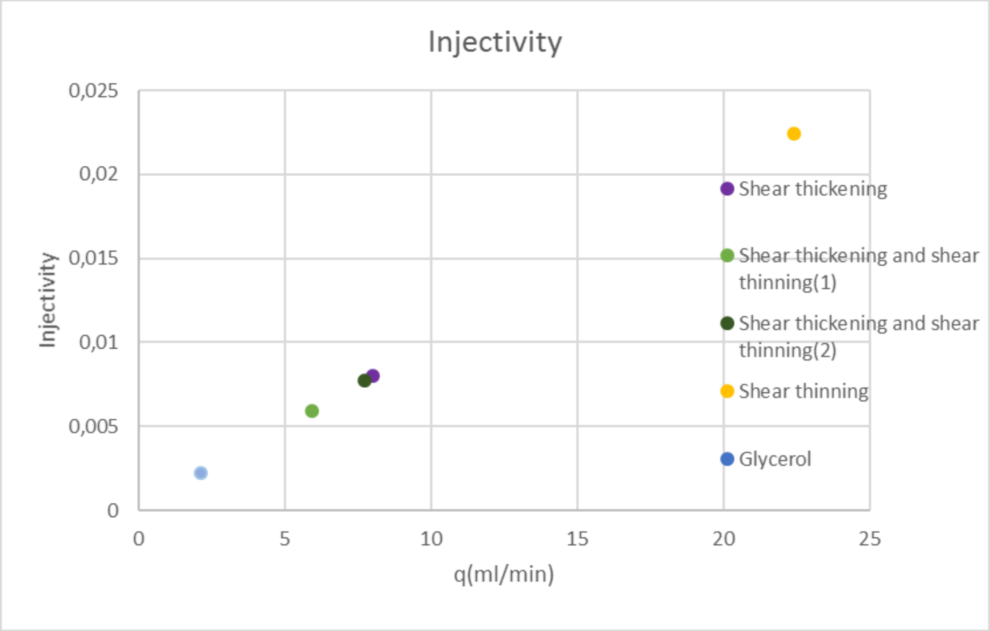

Figure (7.48). The injectivity obtained by non-Newtonian polymer rheology and Newtonian, viscous fluid.

Table 7.10. The injectivity and injection rates obtained by non-Newtonian polymer rheology and Newtonian fluids.

	Shear thickening	**Shear thickening + shear thinning (1)**	**Shear thickening + shear thinning (2)**	**Shear thinning**	**Water**	**Glycerol**
q(ml/min)	8,02	5,92	7,73	22,40	219,63	2,16
BHP(mbar)	1000	1000	1000	1000	1000	1000
Injectivity	0,008	0,006	0,008	0,022	0,219	0,002

Water display the best injectivity, which is expected from both literature and the previously discussion which compared water injectivity with polymer injectivity. As water has a low viscosity and Newtonian behavior, consequently it can be injected at higher injection rates without the additional pressure drop caused by the viscoelastic character when injecting a non-Newtonian synthetic polymer solution. Although water displays the best injectivity, it is also known to not result in the best recovery factor due to reservoir heterogeneities and viscous fingering.

A polymer solution displaying only a shear thinning behavior results in the second best injectivity. This is due to its low viscosity in the wellbore area and the lack of viscoelastic behavior. Even though the polymer solution can be injected at high rates without too much additional pressure drop and the displacement efficiency might be better than the one obtained during a waterflooding, the displacement is not as efficient. As the flow velocity in high-permeable zones would be higher than the one in low-permeable zones, the displacement efficiency in the high-permeable zones would be low due to the low apparent viscosity of the polymer solution when behaving shear thinning [25].

The choice of using a rate-independent permeability did cause an increased shear thickening slope for low injection rates, which results in an overestimated apparent viscosity and a lowered injectivity, illustrated by the green curve in Figure (7.47) and the green point in Figure (7.48). This is caused by the high viscosity at high flow rates in the wellbore area, causing an additional pressure drop due to the steep viscoelastic effect. When using a less steep shear thickening slope and a lower apparent viscosity, it results in an increased injectivity as pressure in the well-bore region is lower, compared to a steeper shear thickening slope and a higher apparent viscosity. A shear thickening behavior in the well region is not desired as it causes high injection pressure and a low injectivity it consequently must be injected at lower rates, as shown in Table 7.10. Although the shear thickening of polymers is not desirable in the well-bore region due to the lowered injectivity, it is desirable throughout the rest of the reservoir as it results in a better displacement efficiency [25].

The viscosity of the injected fluid controls the pressure drop in the well, which is why the Newtonian fluid, glycerol, demonstrates the poorest injectivity, as it, in this case, has the highest viscosity. On a field scale or at higher injection rates, the polymer solution would be subjected to higher flow velocities and shear rates which would lead to an increased apparent viscosity, probably higher than the viscosity of glycerol, and furthermore demonstrate a poorer injectivity than glycerol.

7.4 Summary of the results

The experimental differential pressure obtained by the waterflooding was used to simulate and estimate the absolute permeability of the radial core. The only tuning parameter in the simulations of the waterflood was the absolute permeability.

An ordinary Bentheimer rock usually has a homogenous permeability ~ 2,6D and the first attempt to estimate the absolute permeability of the rock was consequently by an analytical function derived from Darcy's law of radial flow. The analytical estimated permeability of 2,36D results in a good average fit when history matching the waterflood, however the differential pressure in the near-well region was inadequate, which indicated a lowered permeability in this region to achieve an adequate pressure drop in the well region. A further analysis of a homogenous permeability resulted in the same indication. The experimental data appeared to display an heterogenous permeability and the absolute permeability of the disk was consequently divided into three regions; one region near the wellbore, one region at the outer boundary of the disk and another region in-between.

Each rate was manually history matched in STARS and automatically history matched in MRST. The both displayed a trend of a low permeability in the region near the injection well and the trend was attributed to either the location of the pressure transducers or an apparent skin effect. Furthermore, the permeability appeared to be rate-dependent as the history matches of each rate resulted in various permeability fields. The permeability in the near-well region appeared to increase with increasing injection rate, however, this trend was more pronounced in the manual simulation and the automatic simulations resulted in a more random behavior which ranged between 270-470mD. The permeability estimated for the automatic simulations in the outer region of the core also appeared random and ranged between 970mD and 2270mD. However, the large range of this region was attributed to the low differential pressure and consequently, a high uncertainty of the pressure transducers.

As the rock permeability as expected to be constant and rate-independent, a further examination was performed to study how an heterogenous and rate-independent permeability would influence the history matches of the waterflooding of varying rates. However, both the manual and the automatic history matches displayed an assumed insignificant influence which led to further use of heterogenous rate-independent permeability. These are listed in Table 7.3, and although the permeability field estimated for further use in STARS and MRST deviates from each other in size of the regions, they do display a similar value in each region, which was further assumed not to cause great deviations between the output polymer rheology obtained during the history matching of the polymer flood in STARS and MRST. By utilizing a rate-independent permeability this consequently led to an rate-independent injectivity, which is, by Darcy’s equation of radial flow, correct.

Polymer rheology during radial flow is influenced by a decreasing Darcy velocity with increasing radial distance from the well, as experienced during field applications. As synthetic polymer solutions demonstrate a viscoelastic behavior in porous media, this consequently results in a deviation in behavior between the rheology obtained by viscometers and the in-situ rheology in porous media. Hence, an estimation of the in-situ polymer rheology is of great importance. The experimental differential pressure obtained by the polymer flood was used to simulate and estimate the apparent in-situ rheology of the synthetic polymer. As the permeability was estimated by the history matching of the waterflood, the only tuning parameter was the apparent viscosity. Both manual simulation in STARS and automatic simulation in MRST was performed to estimate the in-situ polymer rheology and the results were exceedingly similar, although there were some minor deviations between them.

The degree of shear thickening is influenced by the injection rate, as larger injection rates causes the successive time between each constriction to be of the same order as the characteristic relaxation time of the polymer and consequently results in a shear thickening behavior due to elongation flow. Further, high injection rates cause a higher degree of shear degradation, causing the polymer to need both more time and longer distances to reach an equilibrium state. This was observed in both the manual and automatic history matches, as high injection rates demonstrated a long shear thickening behavior and did not reach an expected apparent upper Newtonian plateau at intermediate flow velocities. This was further shown to influence the injectivity, as a high degree of shear thickening causes high differential pressure and furthermore, a decreased injectivity. Mechanical degradation was not observed at the high injection rates; however, this is possibly due to the use of the extended Carreau equation which does not consider mechanical degradation.

Lower injection rates displayed a shorter shear thickening region as it experiences less shear degradation. This was consistent in the estimated in-situ polymer rheology results from both simulators. Furthermore, the slope of shear thickening was found to display an increased slope with decreasing injection rates. This was attributed to the heterogenous rate-independent permeability chosen from the history matching of the waterflood, as it possibly did not adequately account for the lowered permeability estimated in the near-well region with lower injection rates. This was examined in both simulators and the results were consistent; the rate-independent permeability field had insignificant influence on the output rheology estimated for high injection rates, but appeared to cause an overestimated shear thickening behavior at lower injection rates. This consequently affects the prediction of the injectivity, as an overestimated shear thickening behavior consequently results in a further underestimated injectivity, due to the overestimated pressure drop caused by the increased apparent viscosity.

Results from both STARS and MRST showed a shear thickening and shear thinning behavior when injected with intermediate to low injection rates. MRST demonstrated a shear thinning behavior at higher injection rates, compared to STARS and furthermore an apparent upper Newtonian plateau at intermediate injection rates, whereas STARS displayed more of a transition zone. However, this apparent Newtonian plateau diminished when lowering the injection rates.

As lower injection rates reach lower Darcy velocities in the porous media, the successive time between each constriction increases, allowing the polymer to reach it equilibrium state between each constriction and furthermore display a shear thinning behavior. Synthetic polymers are known to demonstrate a shear thinning behavior in viscometers, however, the shear thinning behavior is porous media is a debated issue and although this behavior has been reported in literature by some authors [1, 25], others has attributed shear thinning behavior in porous media to experimental artifacts as entrapment of large molecular species and insufficient pressure transducers [33, 41].

The onset of shear thickening was found to shift towards lower Darcy velocities at lower injection rates, consequently approaching closer to the injection well. This apparent trend was estimated by both simulators, although they deviated slightly from each other in value as the automatic history matches displayed a somewhat higher onset velocity value. The deviations were considered minimal and insignificant as they were of low order.

Furthermore, an illustration on how Newtonian fluids and the polymer rheology influences the injectivity was shown. This was performed by running manual simulations in STARS with a constant bottom hole pressure to illustrate the highest possible injection rate when utilizing a specific polymer rheology. This clearly illustrated that a shear thinning behavior results in the best injectivity and that an increased slope of shear thickening consequently reduces the injectivity due to the increased differential pressure.

8 Conclusion

Simulation of in-situ polymer rheology in a radial core was performed to estimate the in-situ polymer rheology of synthetic polymers and the estimated polymer rheology influence on injectivity. The base of the simulation study is an experiment of waterflooding and polymer flooding executed in a radial model, which represent the decreasing velocity with increasing radial distance from the injection well as experienced field applications. The simulation study was performed by using two simulators, where manual history matching was performed in STARS and automatic history matching was performed in MRST combined with an EnKF module. The results obtained by both manual and automatic history matching was consistent and only displayed minor deviations.

The analysis of the rock permeability resulted in the assumption of a heterogenous permeability, although Bentheimer rocks are known to be homogenous. Both simulators displayed a rate-dependent permeability, however, a rate-independent permeability was considered more probable as the rocks properties are not expected to change. A permeability reduction in the well-bore region was demonstrated by both simulators and attributed to either the location of the pressure transducers or an apparent skin effect. The rate-independent permeability was found to influence the slope of shear thickening of lower injection rates and further cause an overestimation of shear thickening.

The synthetic polymers displayed a shear thickening behavior at every injection rate which is agreement with literature and is due to the viscoelastic nature of synthetic polymers. The period of a shear thickening behavior was found to vary with rate and was attributed the extent of shear degradation which increases with increased velocities and consequently causes the polymers to need both longer time and distances to reach an equilibrium state when injected with higher rates. A shear thickening behavior is consistent with literature on polymer solutions in porous media, however, most of the existing literature involves linear cores, and only a few authors have reported experiments or numerical simulations of radial core experiments, which better imitate the flow regime obtained during field applications.

Further, lower injection rates displayed a shear thinning behavior when reaching lower Darcy velocities. Although this is a discussed phenomenon in porous media, the experimental artifacts attributed to causing an apparent shear thinning was assumed not to apply for this experiment as the polymer solution was pre-filtered before injection and the differential pressure was assumed to be sufficient [33, 41]. Furthermore, shear thinning in radial flow has been reported in literature [1, 25].

Both simulators displayed a shifted onset of shear thickening towards a decreasing Darcy velocity with decreasing injection rates, which has been reported in literature by Skauge et al. (2016). Further, a deviating behavior of the injection rates performed after q=20ml/min was observed. The cause of the deviation was not established and possible causes as mechanical degradation, straining and permeability reduction was purposed.

Injectivity is influenced by in-situ polymer rheology and viscoelastic nature of synthetic polymers causes a decreased injectivity due to increased differential pressure. However, a shear thickening behavior is favorable throughout the rest of the reservoir due to increased sweep efficiency. The viscosity of synthetic polymer solutions measured in viscometers deviates from in-situ polymer rheology due to viscoelastic nature and elongational flow experienced in porous media. Furthermore, linear core flooding is performed under steady state conditions and displays a severe degree of shear thickening which could cause an underestimated injectivity [1]. Radial core flooding better demonstrates the in-situ rheology experienced in field applications. Consequently, the origin of the rheological data influences the estimated injectivity, the economics of polymer flooding projects and determines if polymer flooding should be considered as applicable EOR technique for specific fields. In order to best estimate the economic prospects and performance of polymer flooding in field applications, it is important to model the injectivity as correct as possible. Radial flow is considered the best approach to obtain data describing in-situ polymer rheology for further modeling of injectivity.

9 Further work

So far only few experiments on synthetic polymer solutions in radial flow have been performed and reported in literature. For a further study of the in-situ polymer rheology of polymer solutions in radial flow, it is necessary with numerous experiments performed in radial cores which should, among other things, research various polymers types, different concentration and molecular weight species. Radial performed experiments would potentially lead to a better estimation of the well injectivity. Additionally, simulations of these experiments by history matching could provide an increased understanding of in-situ polymer rheology.

Further, analysis of molecular weight distributions, MWD, obtained by various rates should be performed, as this would give insight of the possible mechanisms experienced in the radial core. Mechanical degradation could be observed by an apparent wider MWD as the high molecular weight species would be broken to smaller fragments. Straining in the porous media would result in a narrower MWD due to the loss of large molecular weight species retained in the media.

The injection rates used in the base experiment and the simulations is lower than the ones utilized in field applications. As in-situ polymer rheology has been illustrated a rate-dependent behavior, further work should consequently investigate the in-situ polymer rheology experienced in field by examination of real field injection rates for a better estimation of both in-situ polymer rheology and injectivity.

10 References

1. Skauge, T., et al., *Radial and Linear Polymer Flow - Influence on Injectivity*, in *SPE Improved Oil Recovery Confrence*. 2016, Society of Petroleum Engineers: Tulsa, Oklahoma, USA.
2. BP.com/statisticalreview. *BP Statistical Review of World Energy June 2016*. 2016 June 2016 [cited 2017 20.05]; Available from: http://www.bp.com/content/dam/bp/pdf/energy-economics/statistical-review-2016/bp-statistical-review-of-world-energy-2016-full-report.pdf.
3. Miller, R.G. and S.R. Sorrell, *The future of oil supply*. Philosophical Transactions of the Royal Society A: Mathematical, Physical & Engineering Sciences 2013. **372**.
4. BP. *Improving the oil recovery factor*. 2013 1.10.2013 [cited 2017 20.05]; Available from: http://www.bp.com/en/global/corporate/bp-magazine/innovations/the-recovery-factor.html.
5. Abidin, A.Z., T. Puspasari, and W.A. Nugroho, *Polymers for Enhanced Oil Recovery Technology*, in *Procedia Chemistry*. 2012, Elsevier Ltd. p. 11-16.
6. Zolotukhin, A.B. and J.-R. Ursin, *Introduction to Petroleum Reservoir Engineering*. 2000, Kristiansand: Høyskoleforlaget AS - Norwegian Academic Press.
7. Sorbie, K.S., *Polymer-Improved Oil Recovery*. 1991, Glasgow, London: Blackie and Son Ltd.
8. Skauge, A. and M. Skarestad, *PTEK213 - Reservoarteknikk II*. 2014, Bergen: University of Bergen.
9. Lake, L.W., *Fundamentals of Enhanced Oil Recovery*. 2014: Society of Petroleum Engineers.
10. Zamani, N., et al., *Pore Scale Modelling of Polymer Flow*, in *EAGE 17th European Symposium on Improved Oil Recovery*. 2013: St. Petersburg, Russia.
11. Lien, J.R., M. Jakobsen, and A. Skauge, *PTEK100 - Introduksjon til petroleums- og prosessteknologi* 2007, Bergen: University of Bergen.
12. Gluyas, J. and R. Swarbrick, *Petroleum Geoscience*. 2004, Oxford, UK: Blackwell Science Ltd.
13. Lien, J.R., *PTEK211 - Grunnleggende reservoarfysikk (Kjerneanalyse og logging)*. 2004, Bergen: University of Bergen.
14. Lien, J.R., *PTEK212 - Reservoarteknikk I*. 2014, Bergen: University of Bergen.

15. Ahmed, T., *Reservoir Engineering Hanbook*. 2010, Amsterdam: Elsevier.

16. Willhite, P.G. and D.W. Green, *Enhanced Oil Recovery*. 1997, Richardson, TX: Society of Petroleum Engineers.

17. Skauge, A., et al., *2-D Visualisation of Unstable Waterflood and Polymer Flood for Displacement of Heavy Oil*, in *Eighteenth SPE Improved Oil Recovery Symposium*. 2012, Society of Petroleum Engineers: Tulsa, Oklahoma, USA.

18. Skauge, T., et al., *Polymer Flood at Adverse Mobility Ratio in 2D Flow by X-ray Visualization* in *SPE EOR Conference at Oil and Gas Asia*. 2014, Society of Petroleum Engineers: Muscat, Oman.

19. Sheng, J.J., *Modern Chemical Enhanced Oil Recovery - Theory and Practice*. 2011, Amsterdam, London, Oxford, Singapore: Elsevier Inc

20. Engineers, S.o.P. *Glossary:Rheology*. 2013 13 September 2013 [cited 2017 3. January]; Available from: http://petrowiki.org/Glossary:Rheology.

21. McCabe, W.L., J.C. Smith, and P. Harriot, *Unit Operations of Chemical Engineering*. 2005, New York: McGraw Hill Companies.

22. Chauveteau, G., *Fundamental Criteria in Polymer Flow Through Porous Media and Their Importance in the Performance Differences of Mobility-Control Buffers*, in *Water-Soluble Polymers*. 1986, American Chemical Society. p. 227-267.

23. Wever, D.A.Z., F. Picchioni, and A.A. Broekhuis, *Polymer for enhanced oil recovery: A paradigm for structure-property relationships in aqueous solution*, in *Progress in Polymer Science*. 2011, Elsevier Ltd. p. 1558-1628.

24. Hiemenz, P.C. and T.P. Lodge, *Polymer Chemistry: Second Edition*. 2007, London, New York: CRC Press.

25. Delshad, M., et al., *Mechanisitic Interpretation and Utilization of Viscoelastic Behavior of Polymer Solutions for Improved Polymer-Flood Efficiency*, in *2008 SPE/DOE Improved Oil Recovery Symposium*. 2008, Society of Petroleum Engineers: Tulsa, Oklahoma, USA.

26. Reiner, M., *The Deborah Number*, in *Physics Today*. 1964, AIP Publishing LLC.

27. Zamani, N., et al., *Effect of porous media properties on the onset of polymer extensional viscosity*, in *Journal of Petroleum Science and Engineering*. 2015, Elsevier. p. 483-495.

28. Seright, R.S., *The Effects of Mechanical Degradation and Viscoelastic Behavior on Injectivity of Polyacrylamide Solutions.* SPE Journal, 1983: p. 475-485.

29. Maerker, J.M., *Dependence of Polymer Retention on Flow Rate.* Journal of Petroleum Technology, 1973: p. 1307-1308.

30. Lake, L.W. and E.D. Holstein, *Petroleum Engineering Handbook.* Vol. V. 2006, Richardson, TX: Society of Petroleum Engineers

31. Glasbergen, G., et al., *Injectivity Loss in Polymer Floods: Causes, Preventions and Mitigations*, in *SPE Kuwait Oil & Gas Show*. 2015, Society of Petroleum Engineers: Mishref, Kuwait. p. 15.

32. Lee, K., C. Huh, and M.M. Sharma, *Impact of Fractures Growth on Well Injectivity and Reservoir Sweep during Waterflood and Chemical EOR Processes*. 2011, Society of Petroleum Engineers. p. 1-15.

33. Seright, R.S., M. Seheult, and T. Talashek, *Injectivity Characteristics of EOR Polymers.* SPE Reservoir Evaluation & Engineering, 2009. **12**(05): p. 783-792.

34. Pye, D.J., *Improved Secondary Recovery by Control of Water Mobility.* Journal of Petroleum Technology, 1964: p. 911-916.

35. Smith, F.W., *The Bahvior of Partially Hydrolyzed Polyacrylamide Solutions in Porous Media.* Journal of Petroleum Technology, 1970. **22**(02): p. 148-156.

36. Jennings, R.R., J.H. Rogers, and T.J. West, *Factors Influencing Mobility Control By Polymer Solutions.* Journal of Petroleum Technology, 1971. **23**(03): p. 391-401.

37. Hirasaki, G.J. and G.A. Pope, *Analysis of Factors Influencing Mobility and Adsorption in the Flow of Polymer Solution Through Porous Media.* Society of Petroleum Engineers Journal, 1974. **14**(04): p. 337-346.

38. Chauveteau, G., *Molecular Interpretation of Several Different Properties of Flow of Coiled Polymer Solutions Through Porous Media in Oil Recovery Conditions*, in *56th Annual Fall Technical Conference and Exhibition* 1981, Society of Petroleum Engineers of AIME: San Antonia, Texas. p. 1-13.

39. Maerker, J.M., *Shear Degradation of Partially Hydrolyzed Polyacrylamide Solutions.* Society of Petroleum Engineers Journal, 1975. **15**(04): p. 311-321.

40. Zaitoun, A., et al., *Shear Stability of EOR Polymers.* SPE Journal, 2012. **17**(02): p. 335-339.

41. Seright, R.S., et al., *New Insights into Polymer Rheology in Porous Media.* SPE Journal, 2010. **16**(01): p. 35-42.

42. Heemskerk, J., et al., *Quantification of Viscoelastic Effects of Polyacrylamide*, in *SPE/DOE Fourth Symposium on Enhanced Oil Recovery*. 1984, Society of Petroleum Engineers of AIME: Tulsa, Oklahoma. p. 223-228.

43. Skauge, T., O.A. Kvilhaug, and A. Skauge, *Influence of Polymer Structural Conformation and Phase Behaviour on In-situ Viscosity*, in *IOR 2015 - 18th European Symposium on Improved Oil Recovery*. 2015: Dresden, Germany.
44. Computer Modelling Group, L., *STARS User Guide - Advanced Process & Thermal Reservoir Simulations*. 2016, CMG: Calgary, Alberta.
45. Fanchi, J.R., *Principles of Applied Reservoir Simulation - Third Edition*. 2006, Amsterdam, London, Singapore, New York: Elsevier Inc.
46. Mathwork, T., *MATLAB - The Language of Technical Computing. Getting Started With matlab.* . 2005, The Mathworks.
47. Lie, K.A., *An Introduction to Reservoir Simulation Using Matlab. User Guide for the Matlab Reservoir Simulation Toolbox (MRST).* 2016, Oslo: SINTEF ICT, Department of Applied Mathematics.
48. Katzfuss, M., J.R. Stroud, and C.K. Wikle, *Understanding the Ensemble Kalman Filter.* The American Statistician, 2016. **70**(04): p. 350-357.
49. Baker, O.R., Yarranton, W.H., Jensen, L.J., *Practical Reservoir Engineering and Characterization*. 2015, Waltham, MA, USA: Elsevier Inc.
50. Sochi, T., *Non-Newtonian flow in porous media*, in *Polymer*. 2010, Elsevier London. p. 5007-5023.

A. Appendix A

A.1 STARS – Waterflooding

A.1.1 Analytically determined permeability

10ml/min

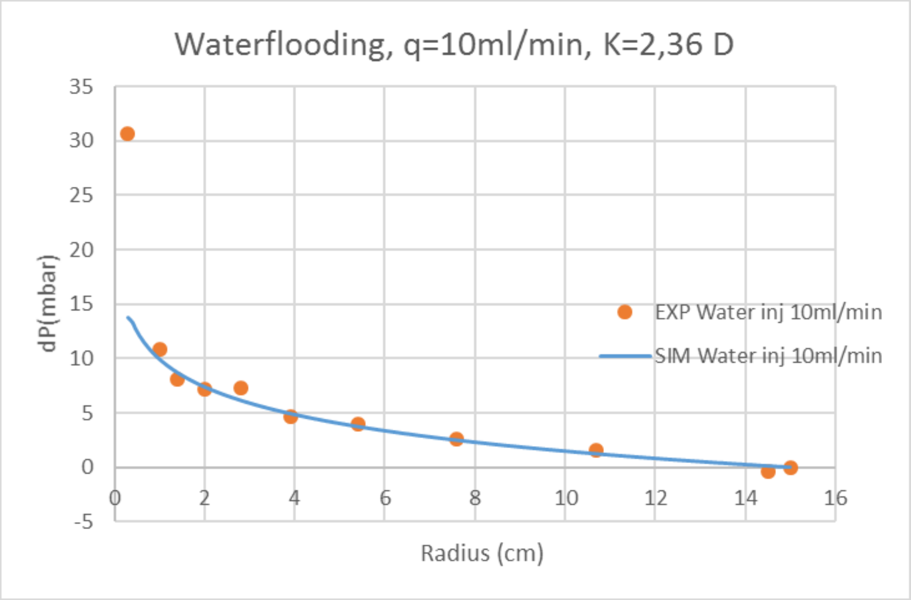

Figure (A.1). History match for q=10ml/min with an average analytical determined permeability, K=2,36D.

15ml/min

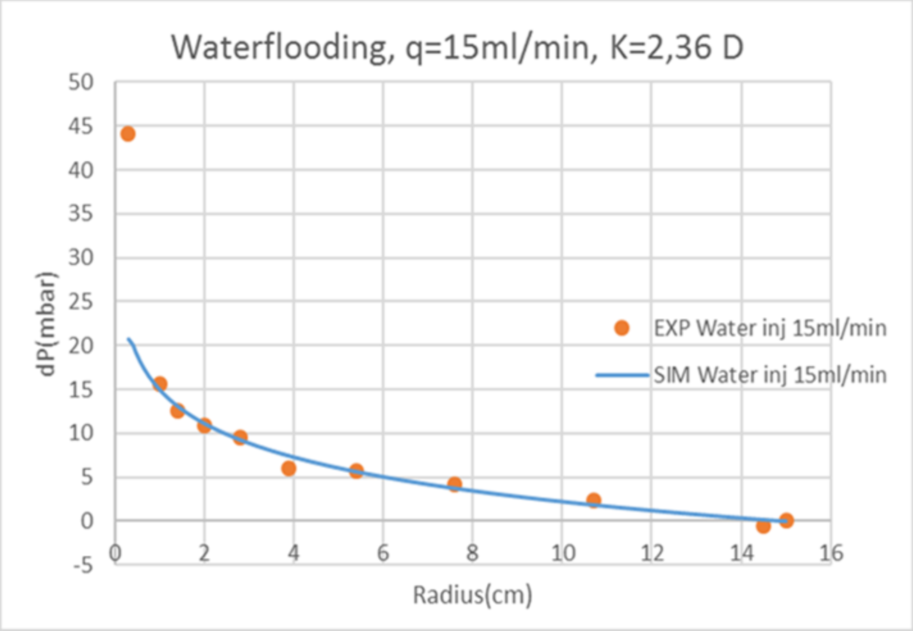

Figure (A.2). History match for q=15ml/min with an average analytical determined permeability, K=2,36D.

20ml/min

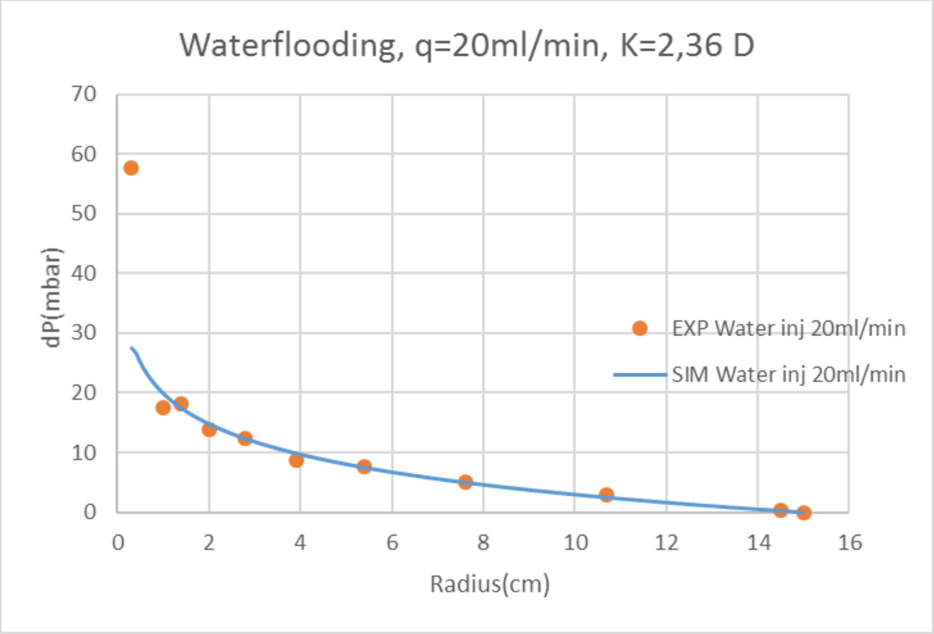

Figure (A.3). History match for q=20ml/min with an average analytical determined permeability, K=2,36D.

40ml/min

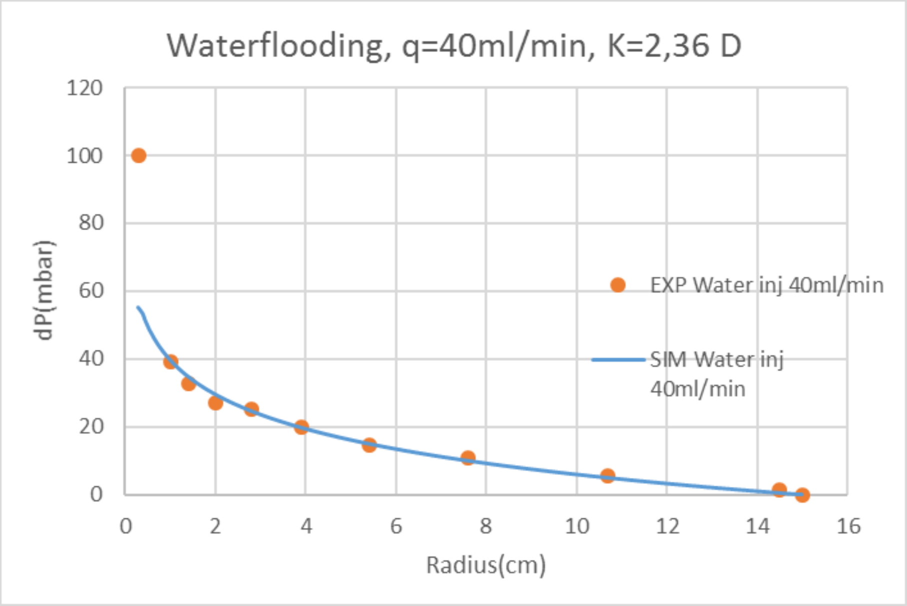

Figure (A.4). History match for q=40ml/min with an average analytical determined permeability. K=2,36D.

A.1.2 Heterogenous permeability

15ml/min

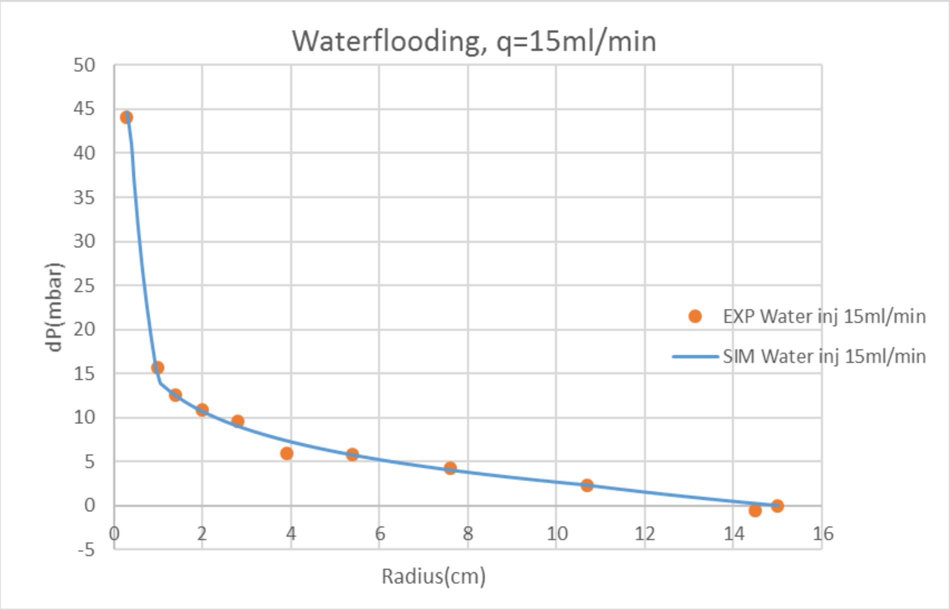

Figure (A.5). History match of waterflooding with q=15ml/min.

20ml/min

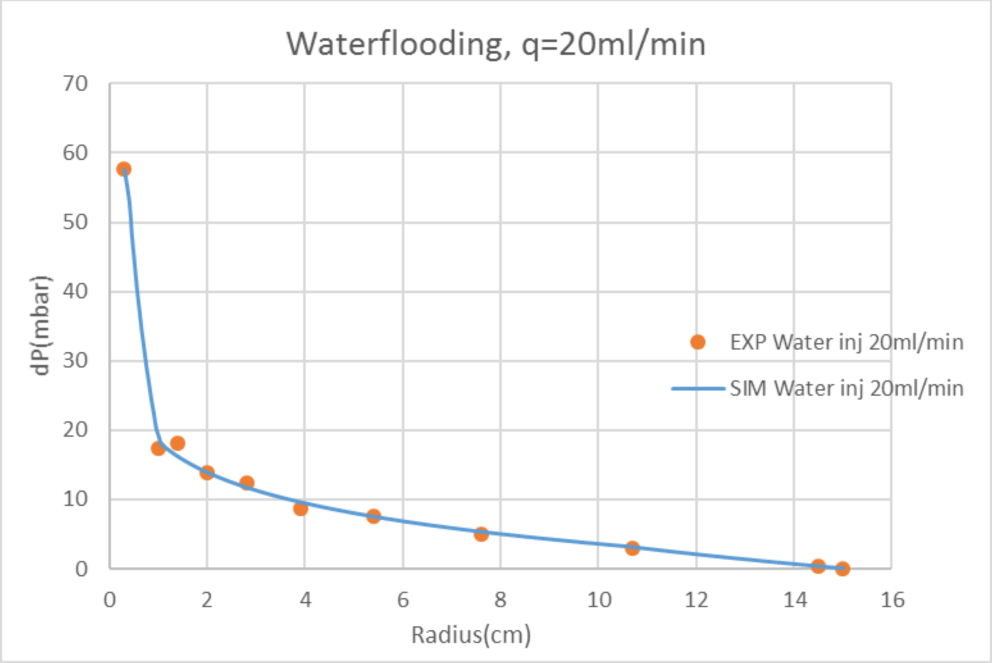

Figure (A.6). History match of waterflooding with q=20ml/min.

30ml/min

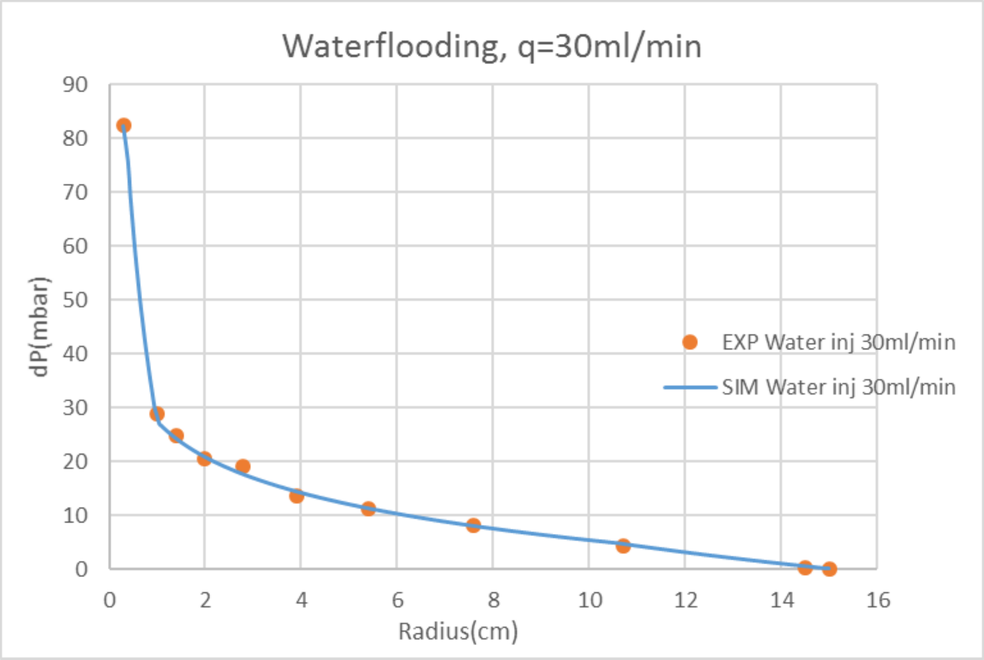

Figure (A.7). History match of waterflooding with q=30ml/min.

40ml/min

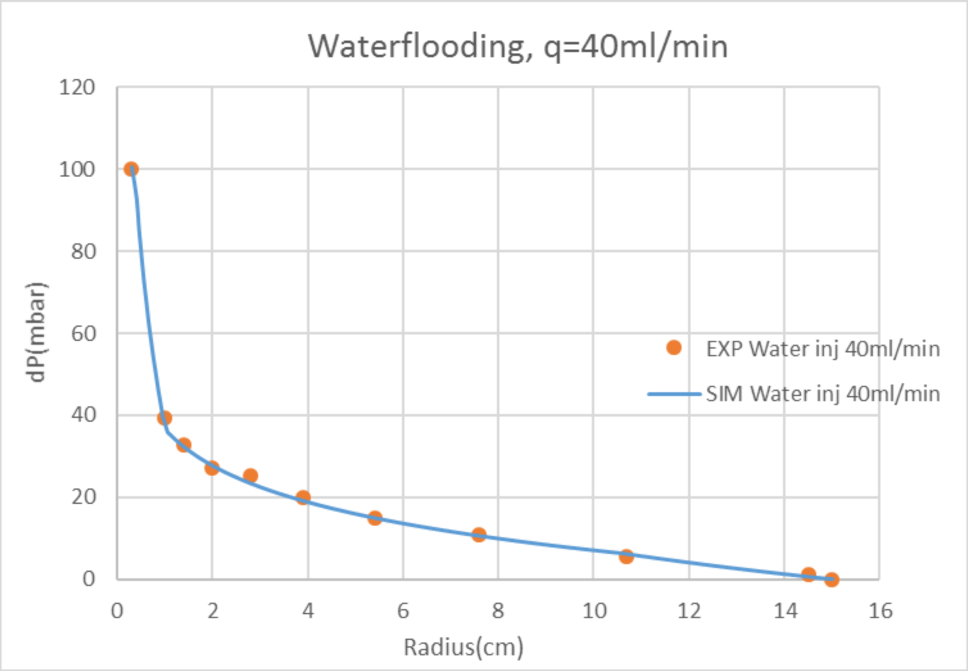

Figure (A.8). History match of waterflooding with q=40ml/min.

A.1.3 Constant permeability

15ml/min

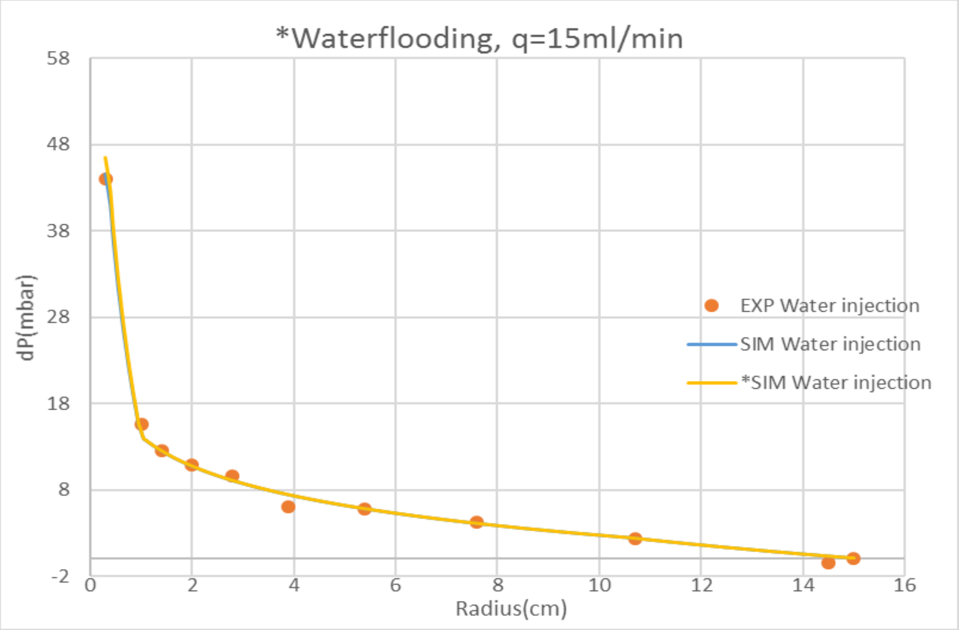

Figure (A.9). History match of a waterflooding with q=15ml/min with the permeability field from history match of q=10ml/min.

30ml/min

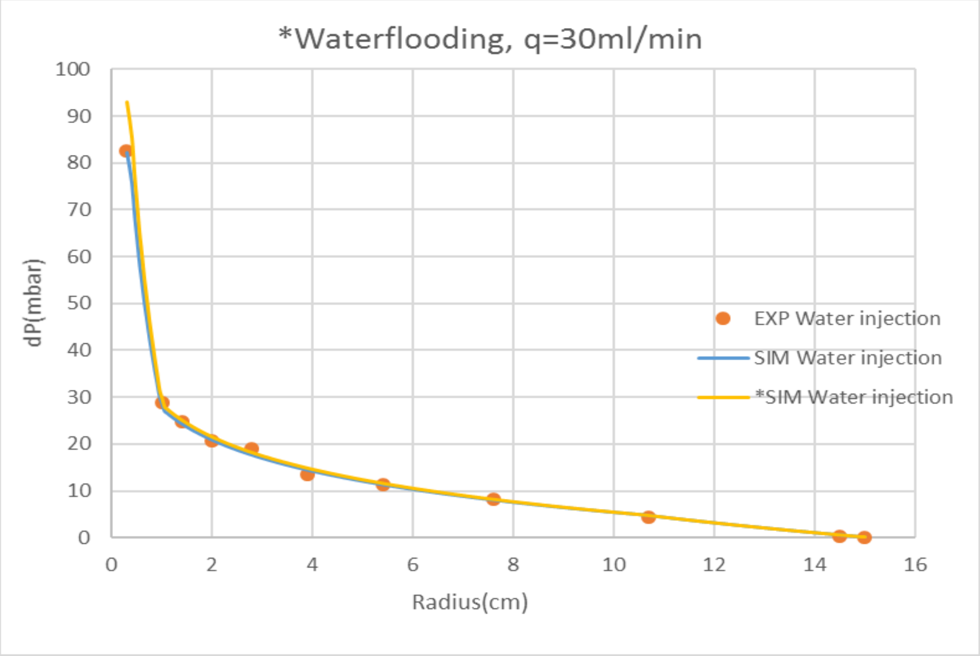

Figure (A.10). History match of a water injection with q=30ml/min with the permeability field found from the history match of q=10ml/min.

40ml/min

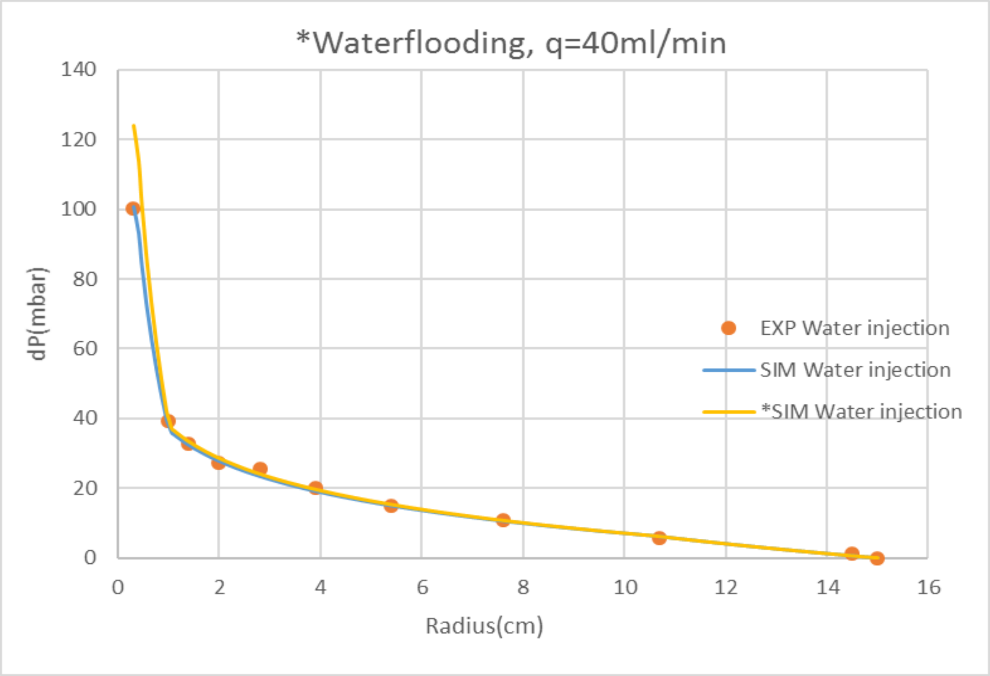

Figure (A.11). History match of a waterflooding with q=40ml/min with the permeability field found from the history match of q=10ml/min.

A.2 MRST – Waterflooding

A.2.1 Heterogenous permeability

5ml/min

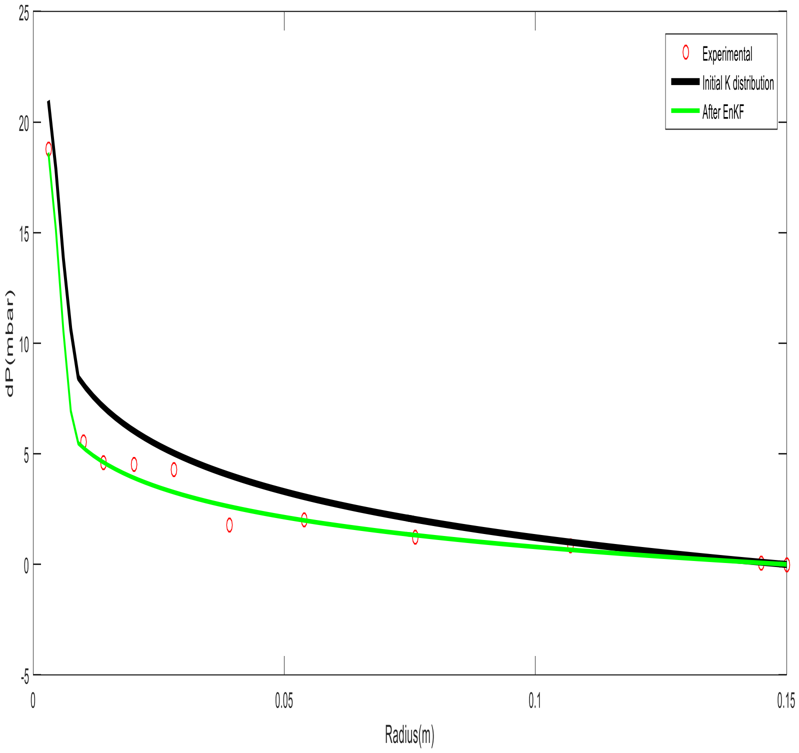

Figure (A.12). History match, waterflooding, q=5ml/min. Differential pressure (mbar) versus radius (m).

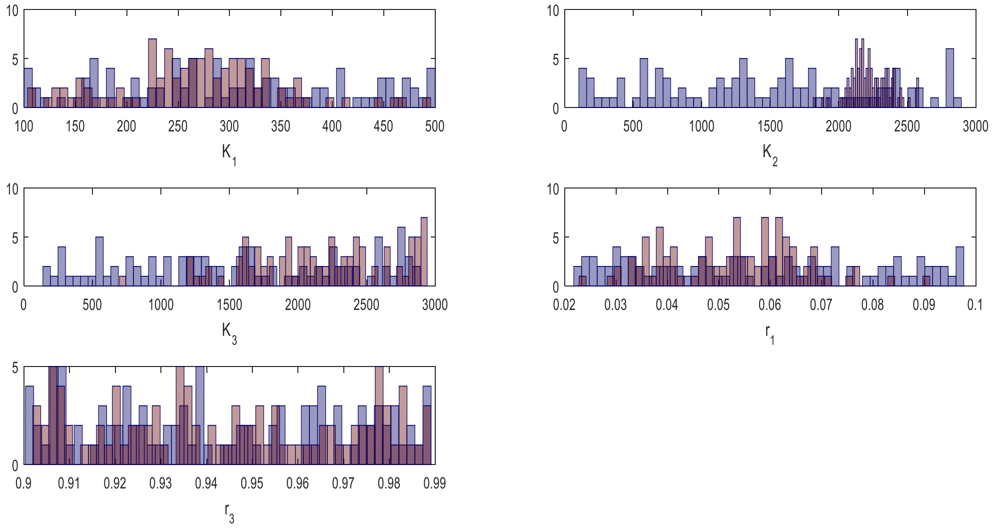

Figure (A.13). Distribution chart for waterflooding, q=5ml/min.

15ml/min

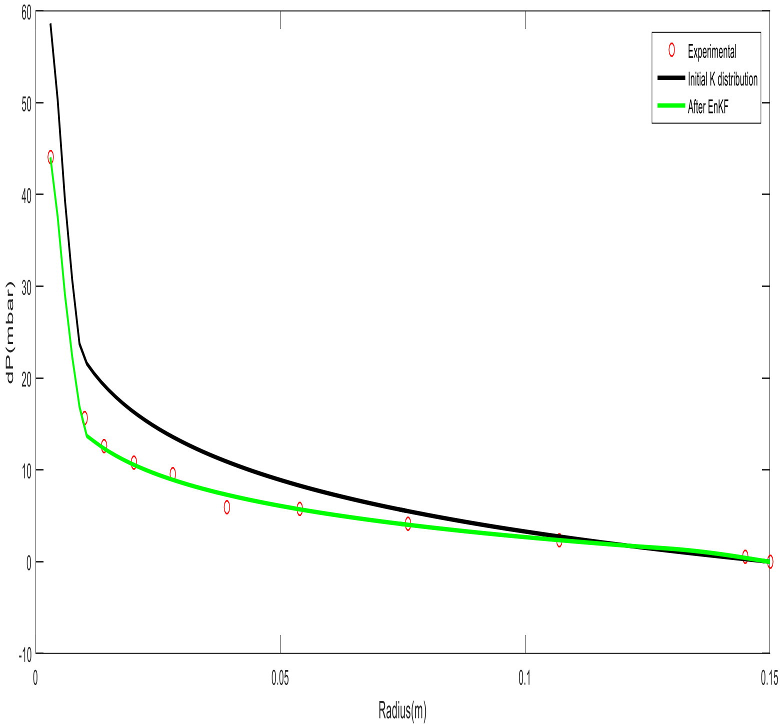

Figure (A.14). History match, waterflooding, q=15ml/min. Differential pressure (mbar) versus radius(m).

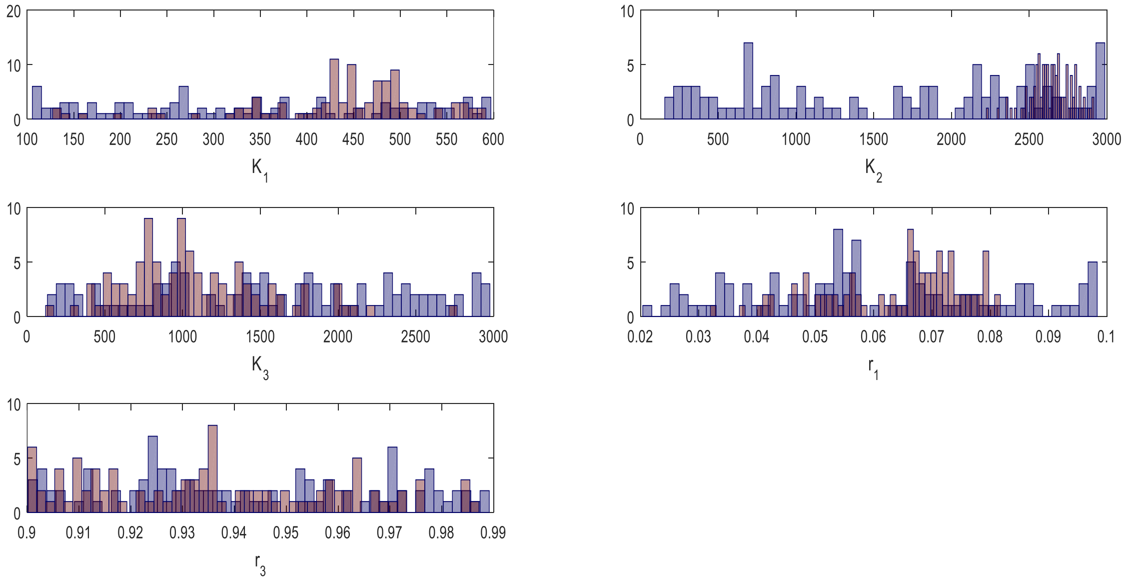

Figure (A.15). Distribution chart for waterflooding, q=15ml/min.

20ml/min

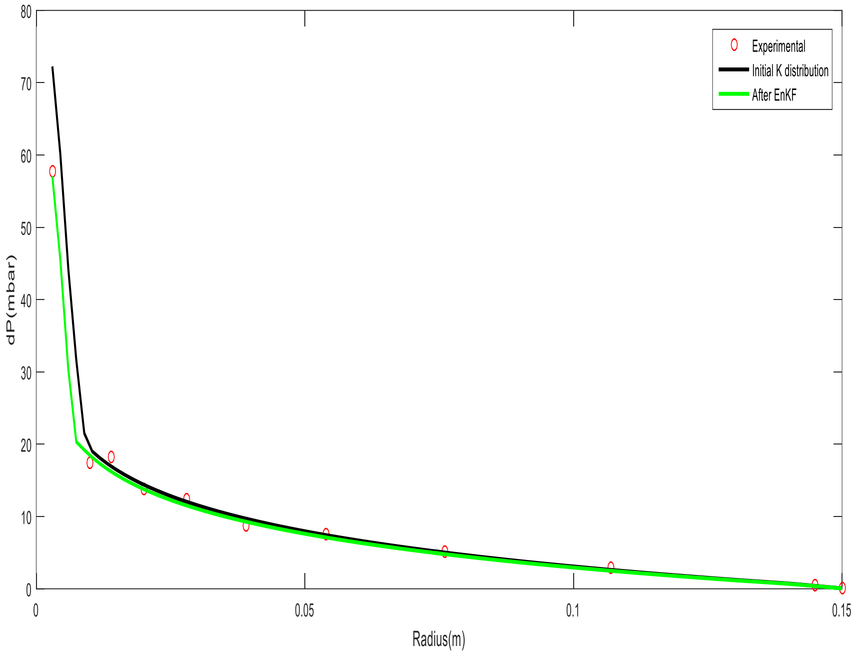

Figure (A.16). History match, waterflooding, q=20ml/min. Differential pressure (mbar) versus radius(m).

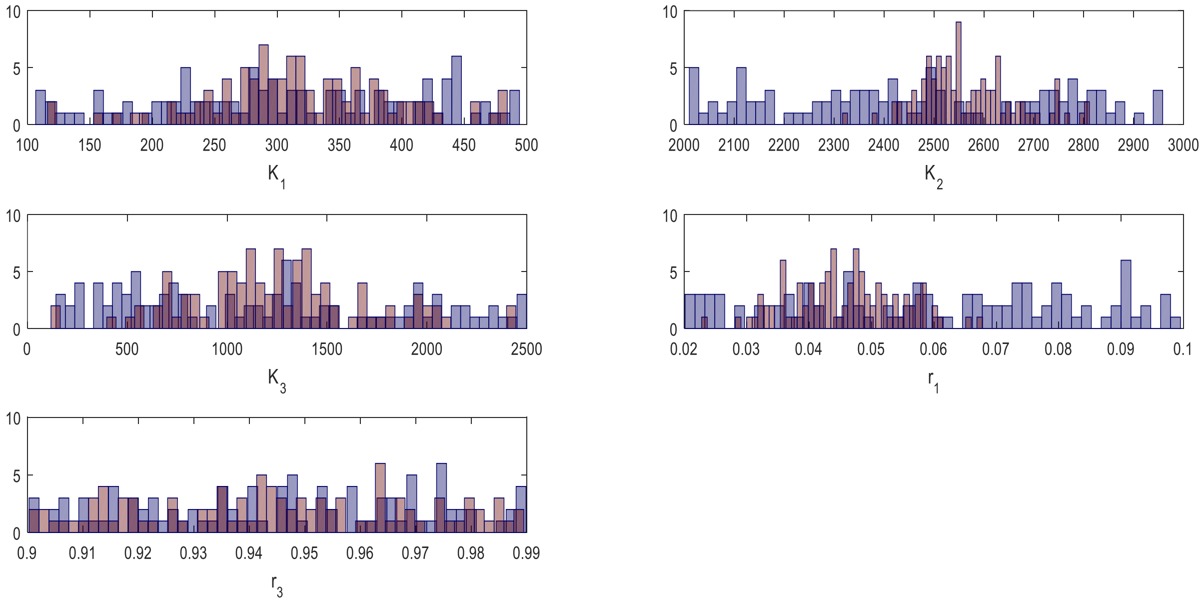

Figure (A.17). Distribution chart for waterflooding, q=20ml/min.

30ml/min

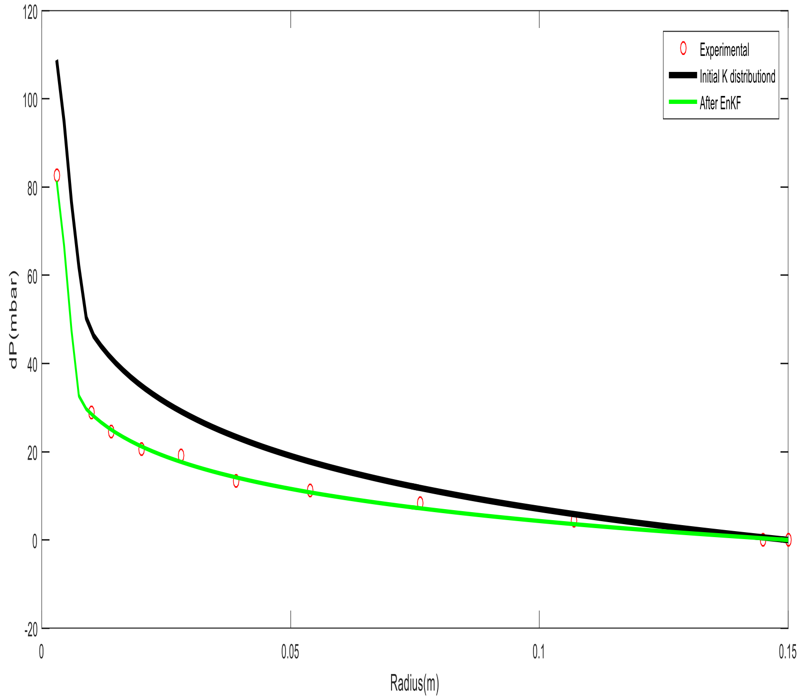

Figure (A.18). History match for waterflooding, q=30ml/min. Differential pressure(mbar) versus radius(m).

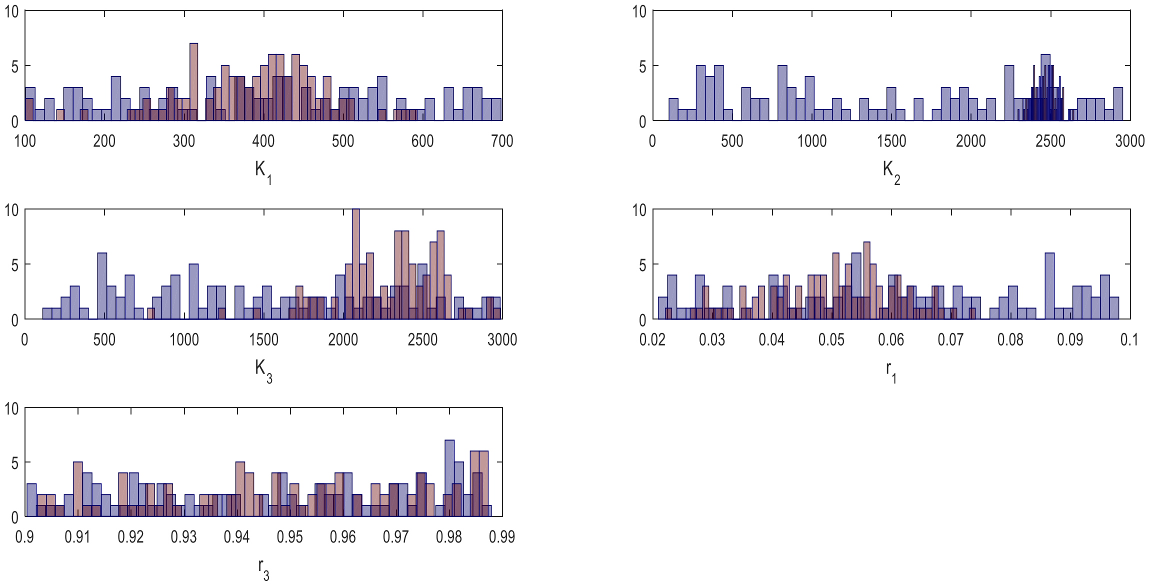

Figure (A.19). Distribution chart for waterflooding, q=30ml/min.

40ml/min

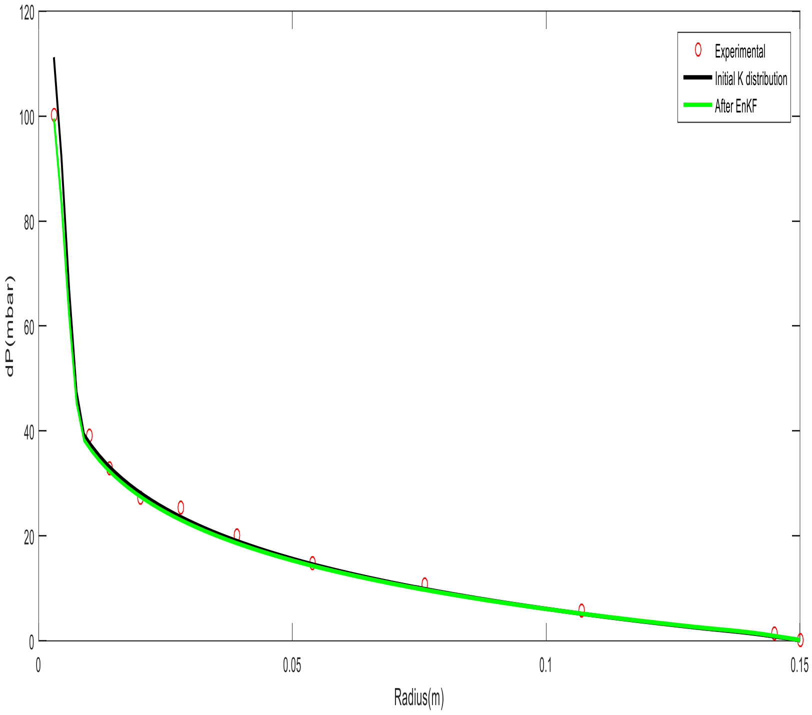

Figure (A.20). History match for waterflooding, q=40ml/min. Differential pressure(mbar) versus radius(m).

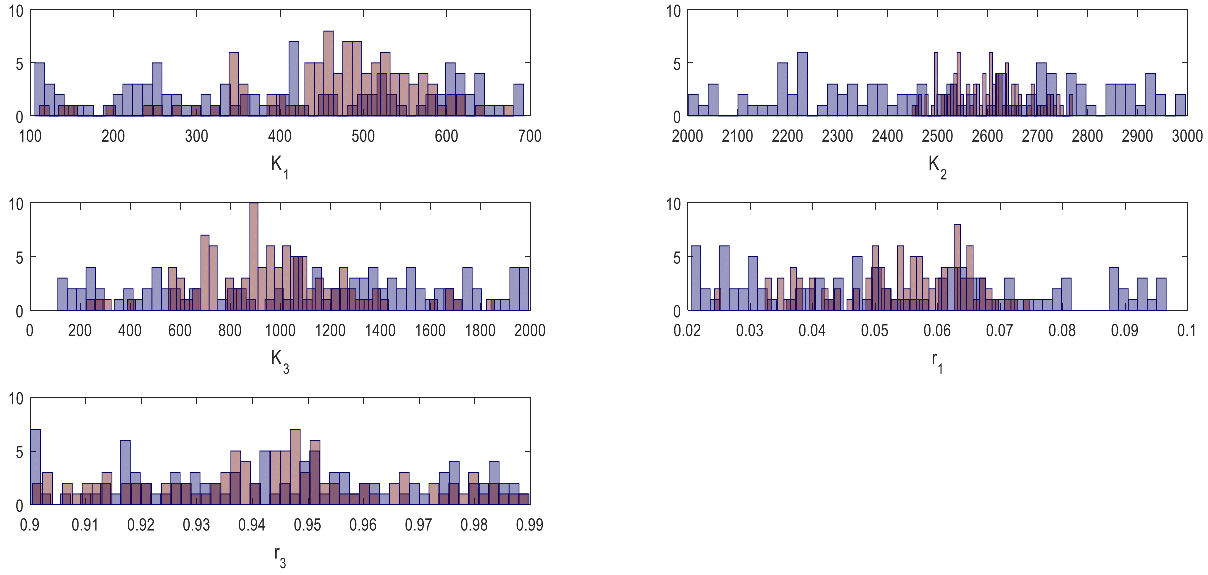

Figure (A.21). Distribution chart for waterflooding, q=40ml/min.

A.2.2 Constant permeability

5ml/min

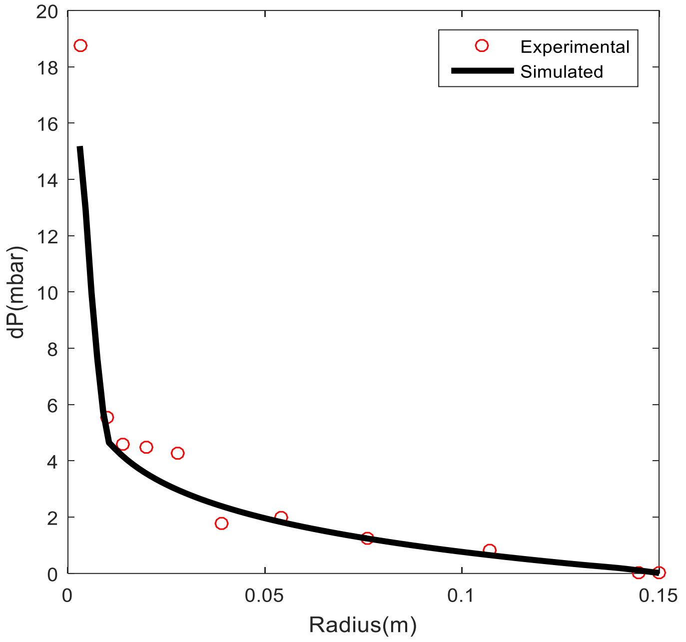

Figure (A.22). History match of a waterflooding with q=5ml/min when using the history matched permeability field found for q=10ml/min.

15ml/min

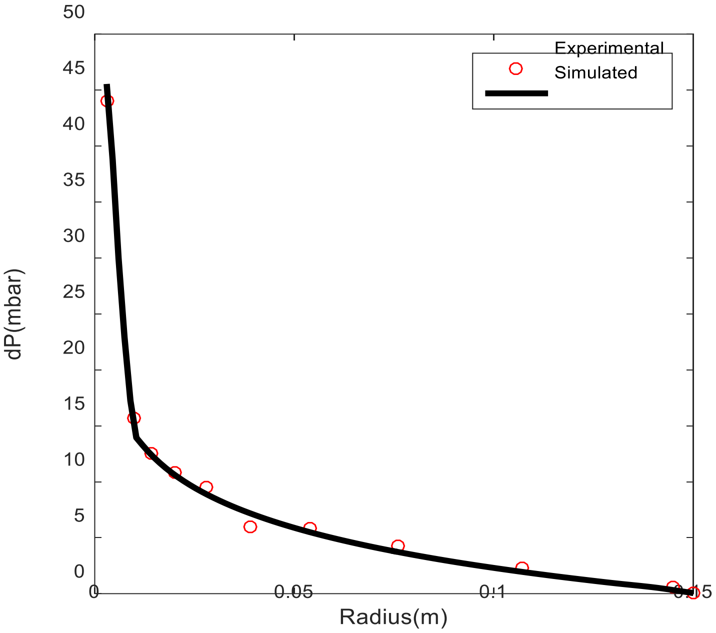

Figure (A.23). History match of a waterflooding with q=15ml/min when using the history matched permeability found for q=10ml/min.

20ml/min

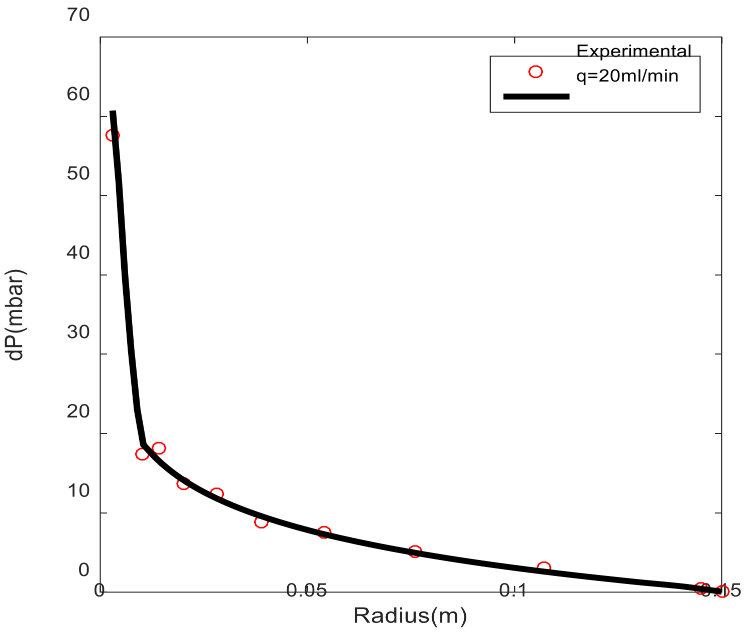

Figure (A.24). History match of a waterflooding with q=20ml/min when using the history matched permeability field found for q=10ml/min.

30ml/min

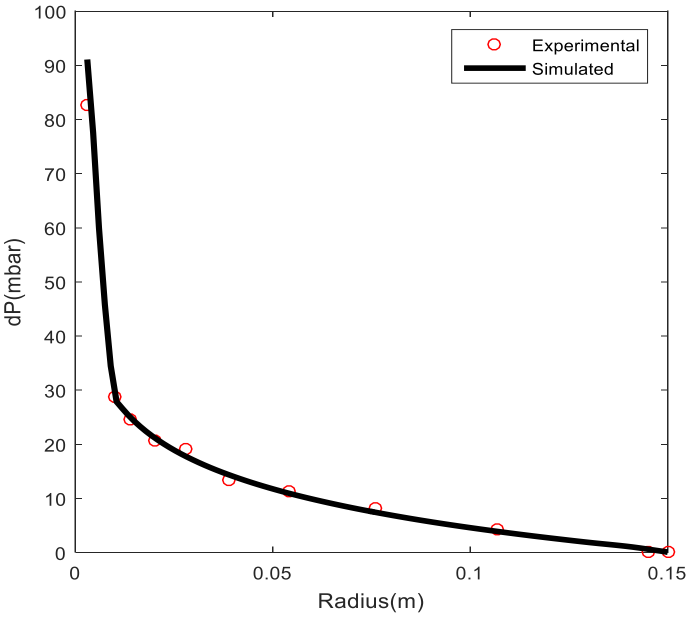

Figure (A.25). History match of a waterflooding with q=30ml/min when using the history matched permeability field found for q=10ml/min.

40ml/min

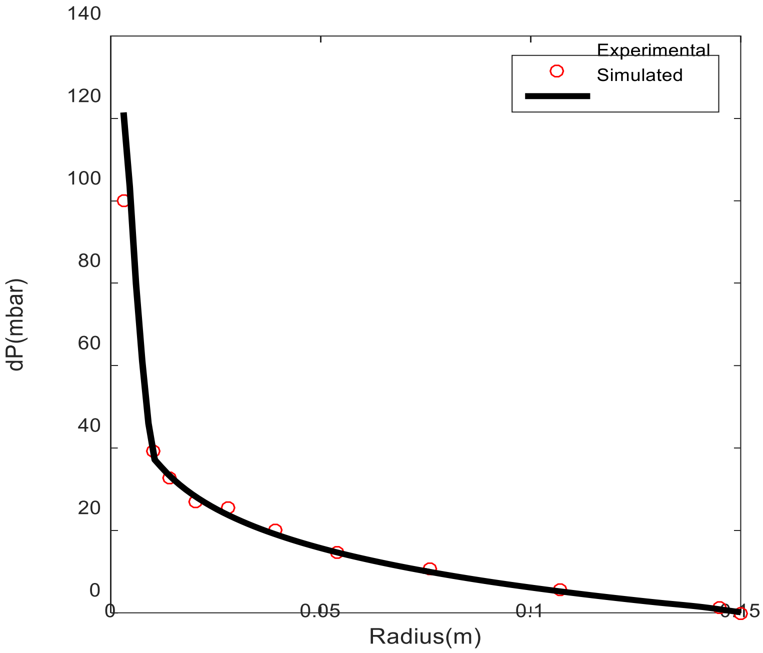

Figure (A.26). History match of a waterflooding with q=40ml/min when using the history matched permeability field found for q=10ml/min.

A.3 STARS – Polymer flooding

16ml/min

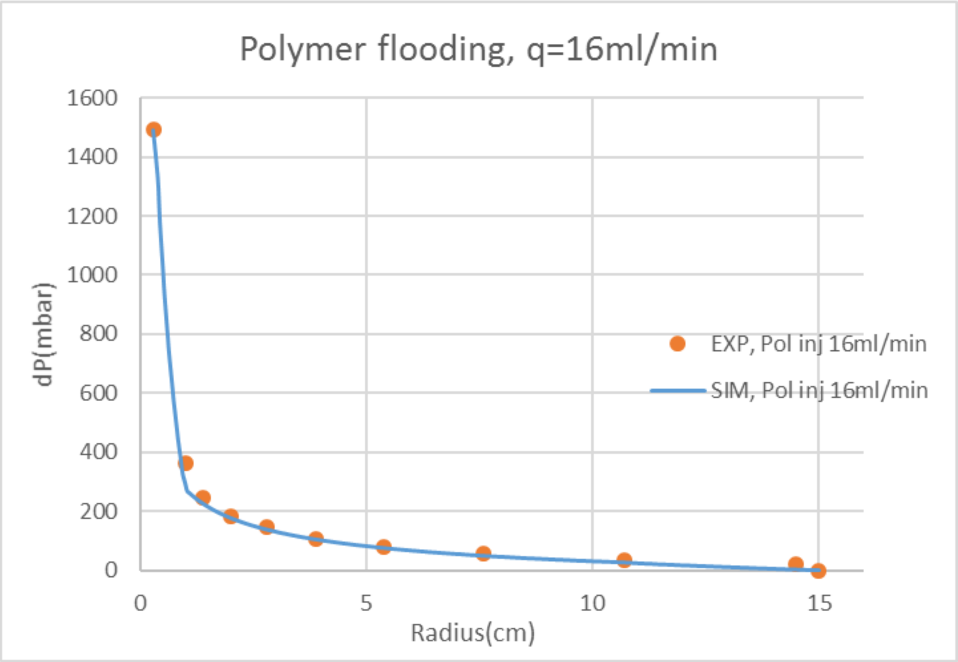

Figure (A.27). History match for polymer flooding, q=16ml/min.

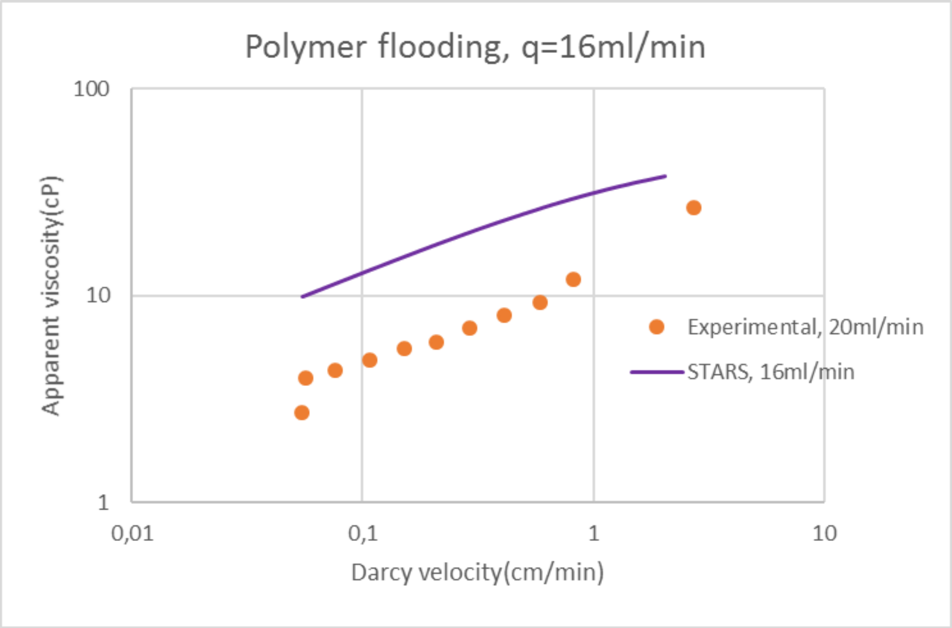

Figure (A.28). Viscosity output data from STARS and the calculated R_F from the experimental data for q=16ml/min.

12ml/min

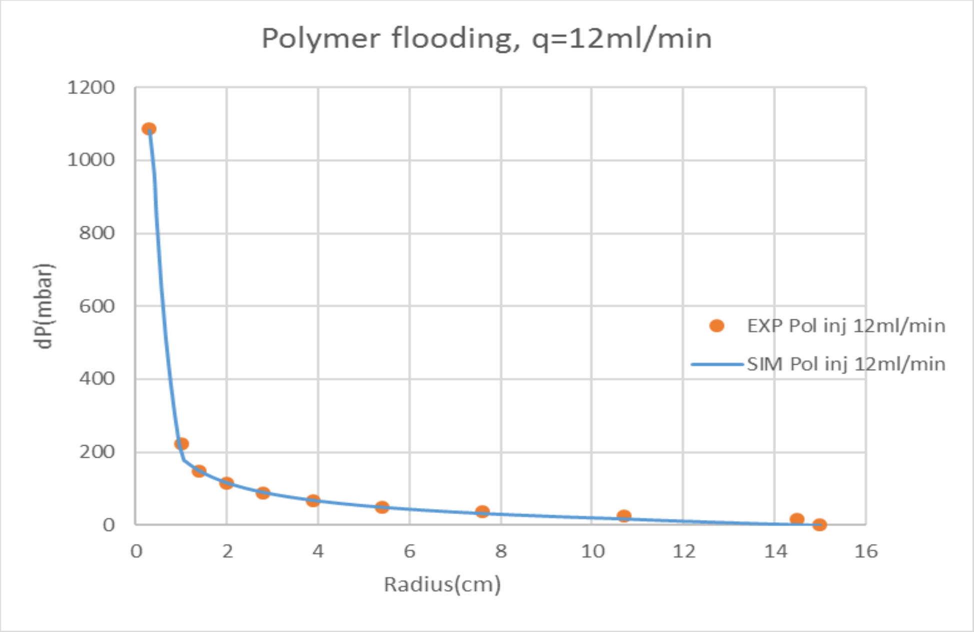

Figure (A.29). History match for polymer flooding, q=12ml/min.

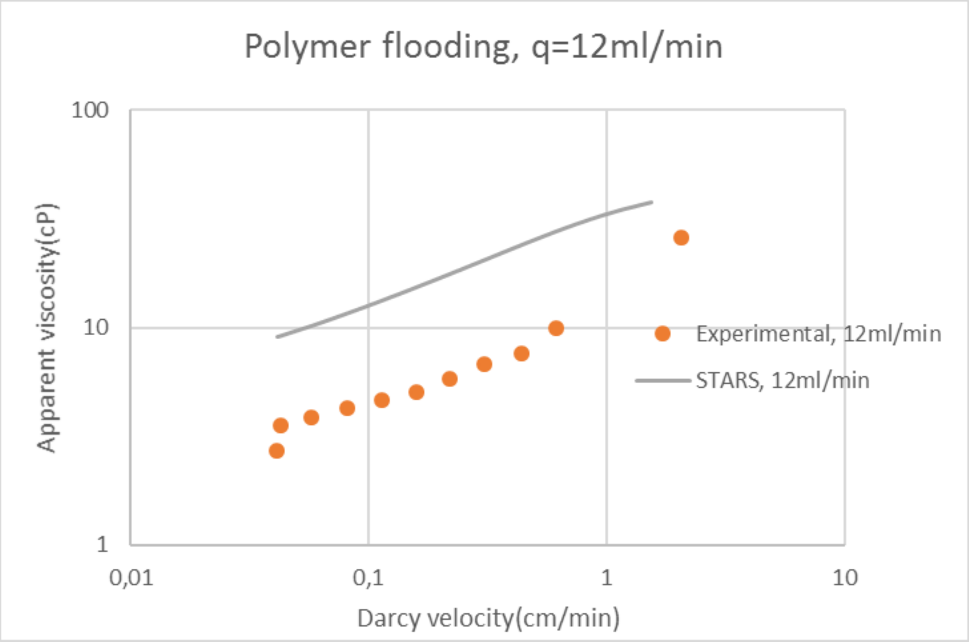

Figure (A.30). Viscosity output data from STARS and the calculated R_F from the experimental data for q=12ml/min.

10ml/min

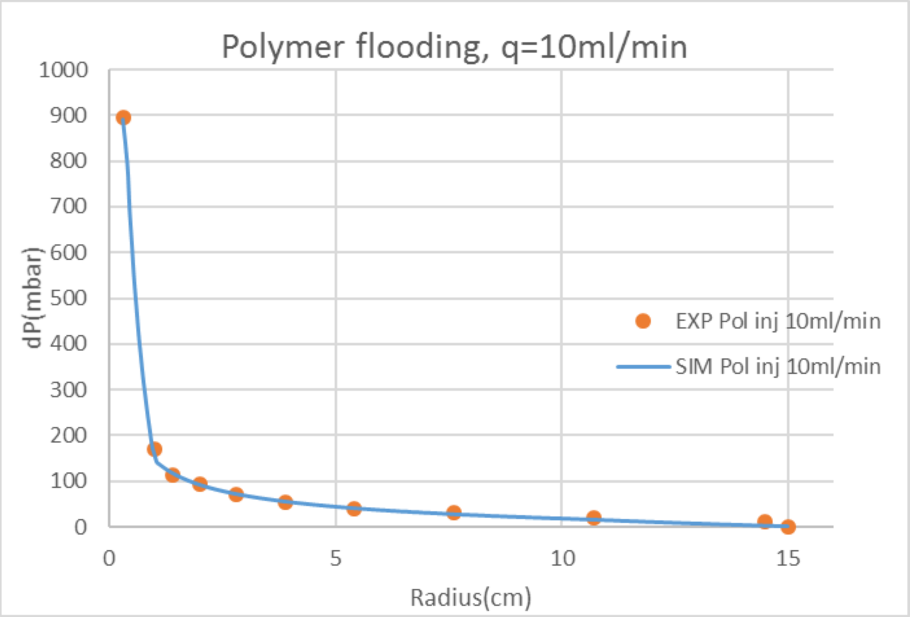

Figure (A.31). History match for polymer flooding, q=10ml/min.

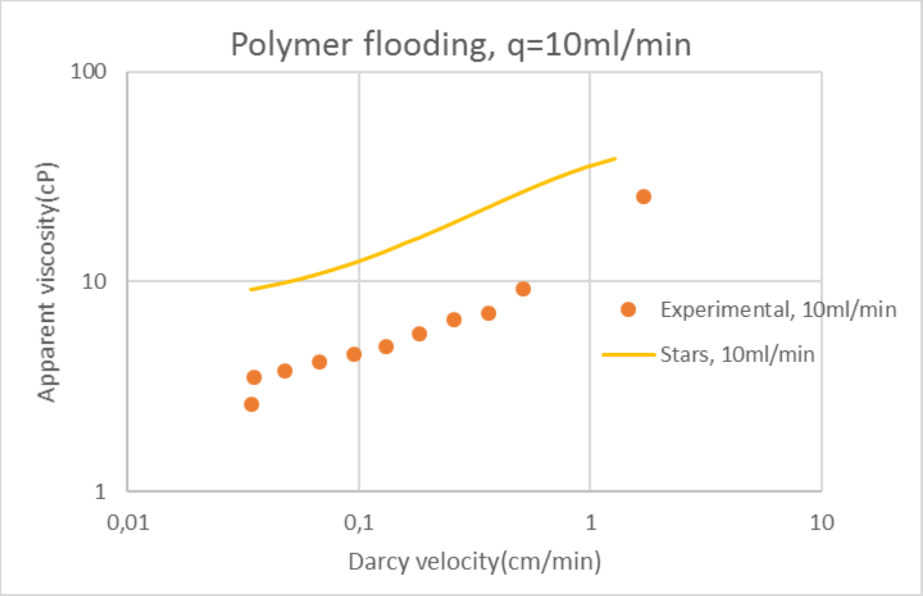

Figure (A.32). Viscosity output data from STARS and the calculated R_F from the experimental data for q=10ml/min.

8ml/min(2)

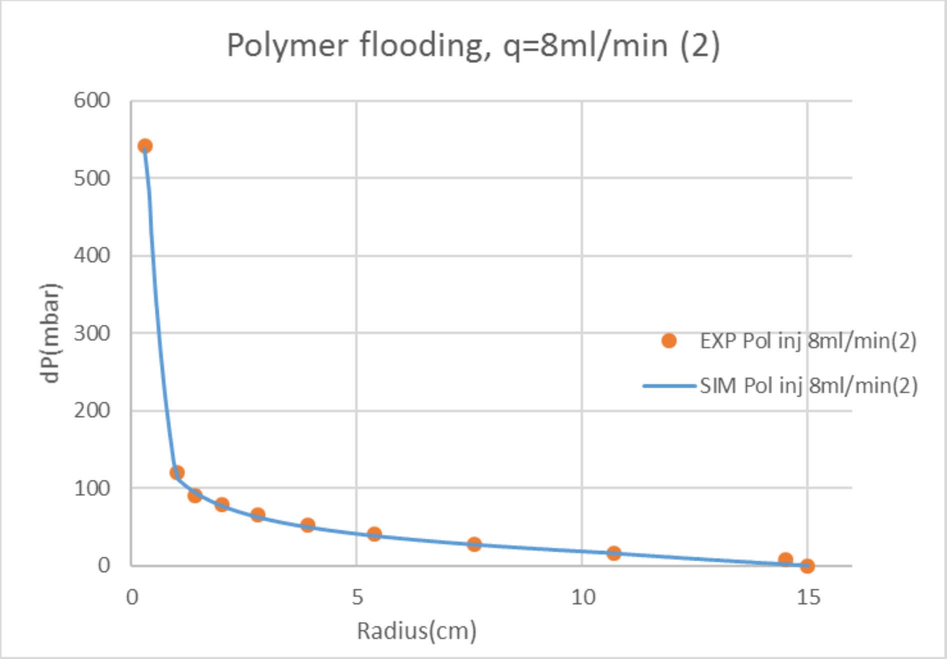

Figure (A.33). History match for polymer flooding, q=8ml/min(2).

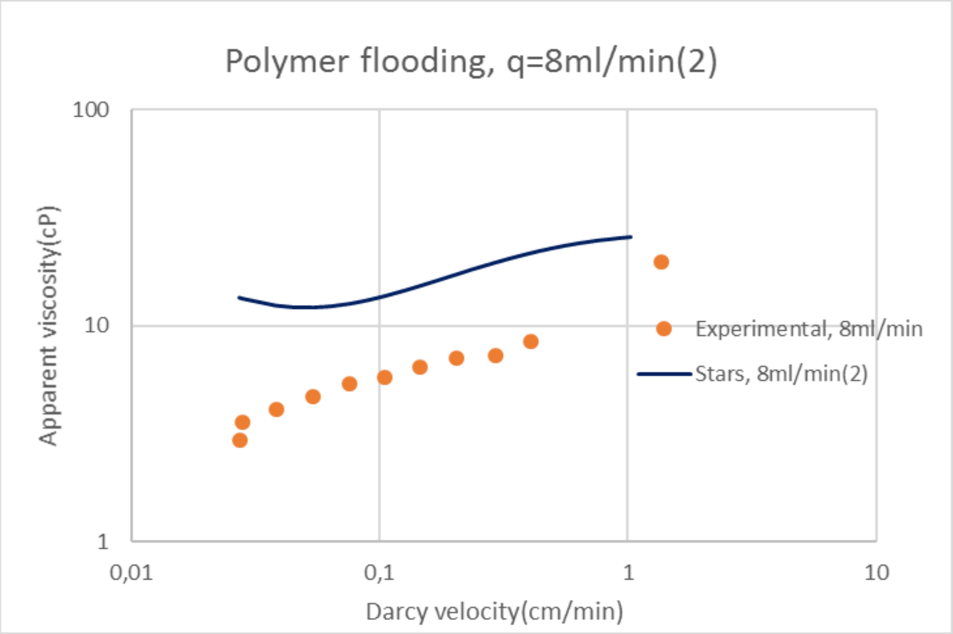

Figure (A.34). Viscosity output data from STARS and the calculated R_F from the experimental data for q=8ml/min(2).

5ml/min

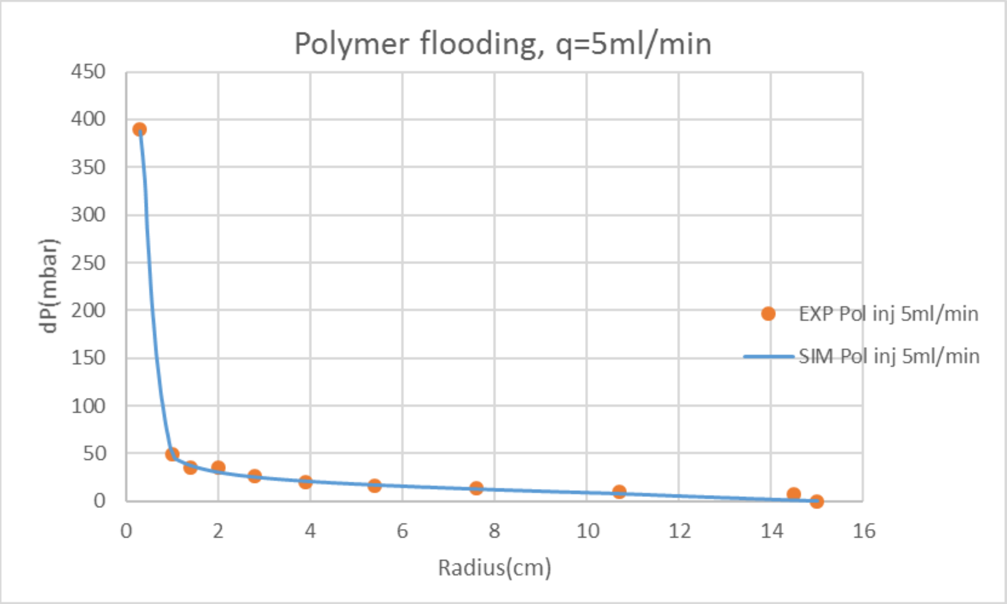

Figure (A.35). History match for polymer flooding, q=5ml/min.

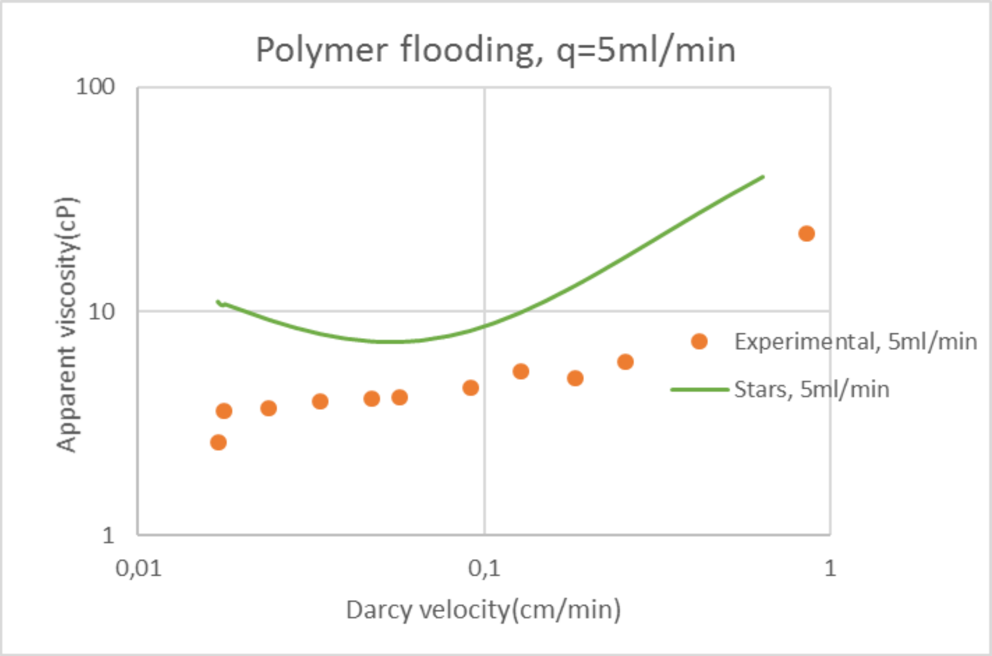

Figure (A.36). Viscosity output data from STARS and the calculated R_F from the experimental dataset for q=5ml/min.

*5ml/min**

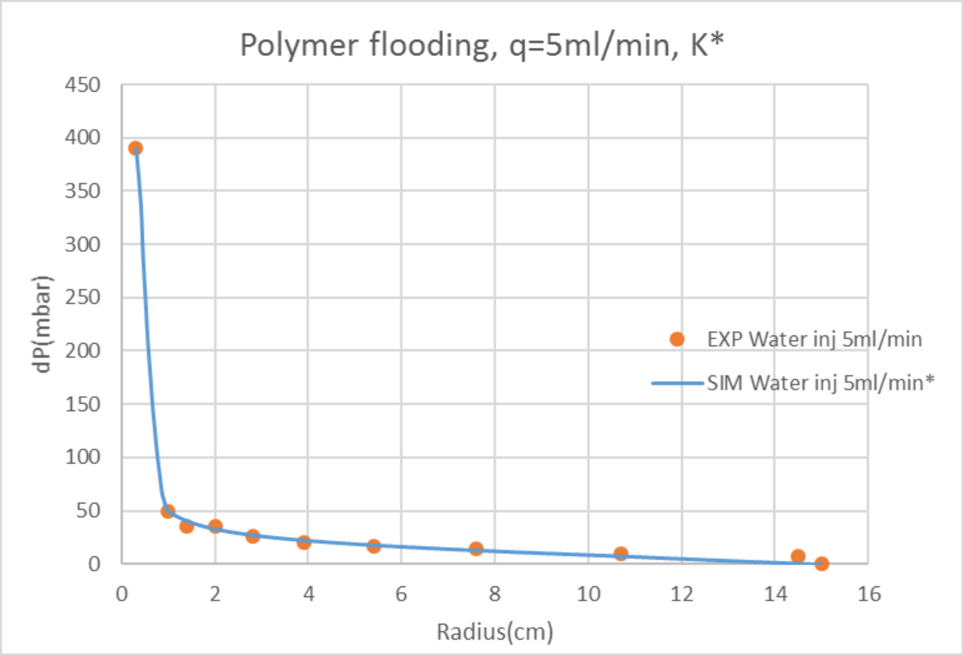

Figure (A.37). History match of polymer flooding, q=5ml/min when using the history matched rate dependent permeability field found for the corresponding rate.

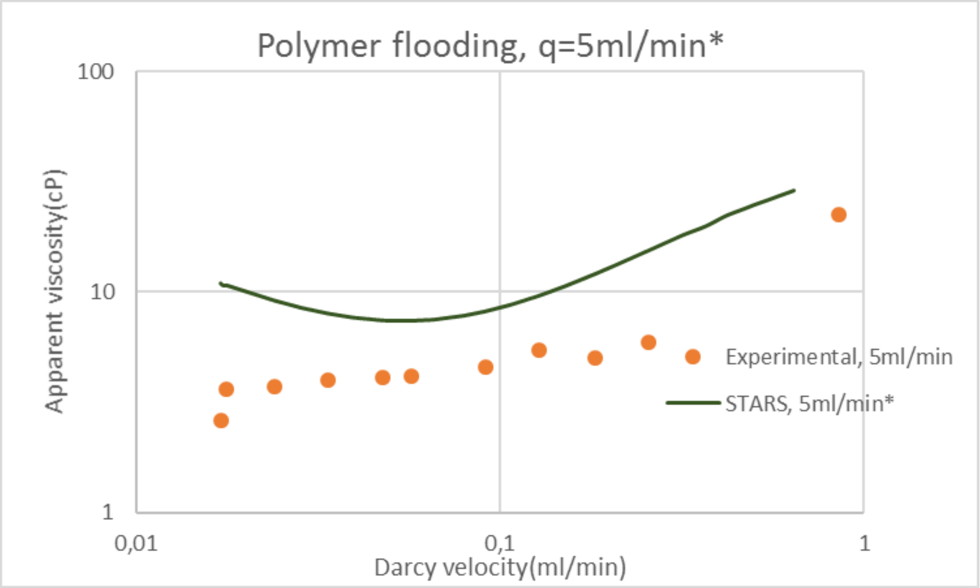

Figure (A.38). The viscosity output data from STARS when using the history matched rate-dependent permeability field found for 5ml/min and the calculated R_F from the experimental data for q=5ml/min.

1ml/min

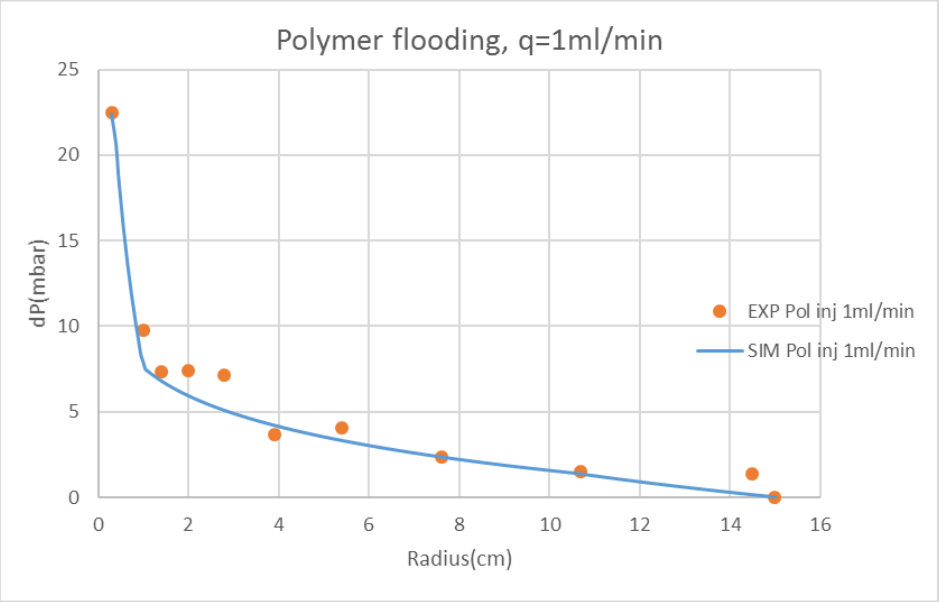

Figure (A.39). History match, polymer flooding q=1ml/min.

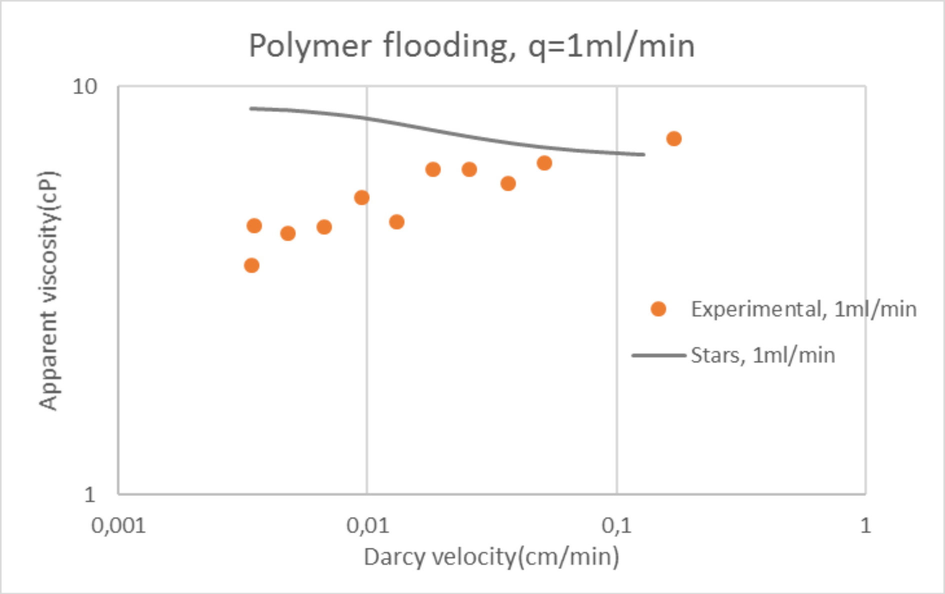

Figure (A.40). The viscosity output data from STARS and the calculated R_F from the experimental dataset for q=1ml/min.

0,5ml/min

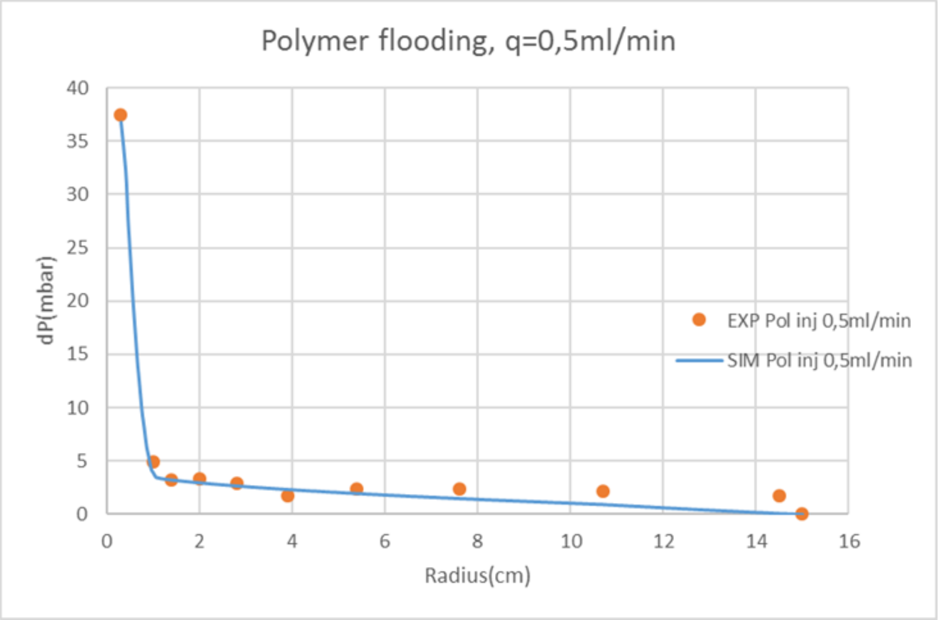

Figure (A.41). History match, polymer flooding, q=0,5ml/min.

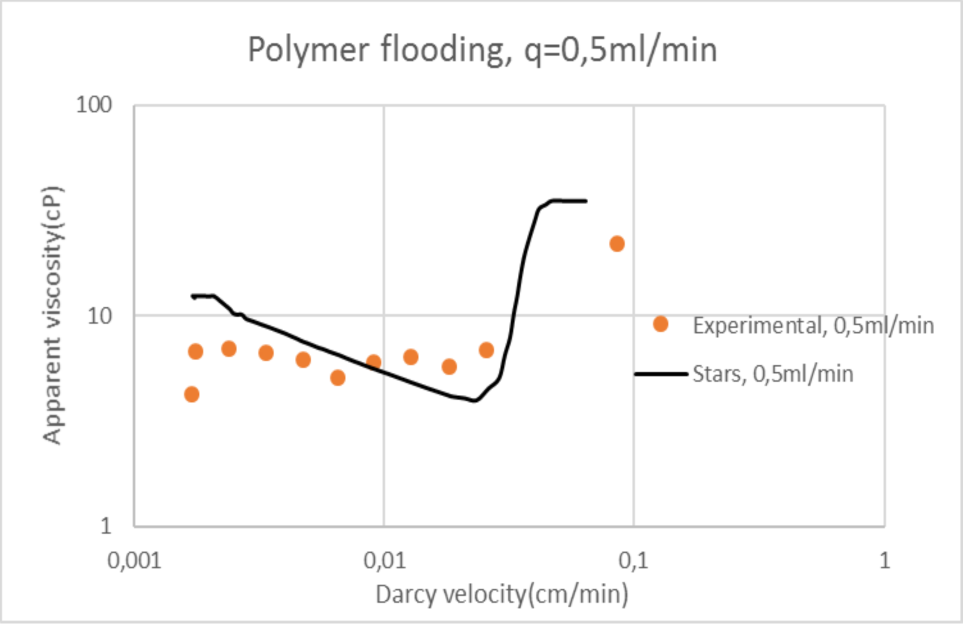

Figure (A.42). The viscosity output data from STARS and the calculated R_F from the experimental dataset from q=0,5ml/min.

STARS seemed to experience some issues during the simulation of the lowest injection rate and the pressure struggled with stabilization as the shear tab apparent viscosities input was not followed accordingly. Several measures were tested to try to solve the problem, including extending the shear tab, changing the permeability from heterogenous to homogenous and decreasing the time steps. The issue of pressure stabilization and struggles with the apparent viscosity input data was not encountered during the sensitivity analysis, where the injection rate was higher. The effect was in the end attributed to the large apparent viscosity changes, from 38 to 7cp at low flow rates, which might be physically incorrect and an effect of the rate-independent permeability and an overestimated permeability in the wellbore region. When utilizing the rheology obtained in MRST and using it as apparent viscosity input data in STARS, the same issue was not encountered, although the history match was poor. The issues of pressure stabilization when performed manual history matching in STARS at low flow rates can therefore be attributed to the user.

Table A.1. The obtained extended Carreau parameters for the polymer flooding simulated in STARS.

	Extended Carreau parameters					
q(ml/min)	**n_1**	**n_2**	**λ_1**	**λ_2**	**η_0**	**η_{max}**
20	0,020	1,58	10876364	11374	3,33	39,83
20*	0,022	1,57	1783785	6969	7,10	48,39
16	0,022	1,56	2305525	6947	2,63	46,13
12	0,022	1,81	30564	8907	4,96	42,56
10	0,023	2,03	15167	8821	7,39	41,55
8	0,033	1,88	15047350	8059	480,12	49,76
8(2)	0,010	1,80	772755	25758	31,00	25,5
5	0,203	2,22	4220333	6645	69,14	78,97
5*	0,213	2,14	14164350	10887	168,97	39,01
3	0,332	2,78	35030749	24793	158,81	37,63
1	0,010	1,01	540138	21923	3,44	8,67
0,5	0,458	12,80	1689523	160484	8,72	32,54

A.4 MRST – Polymer flooding

A.4.1 MRST – History matches

20ml/min

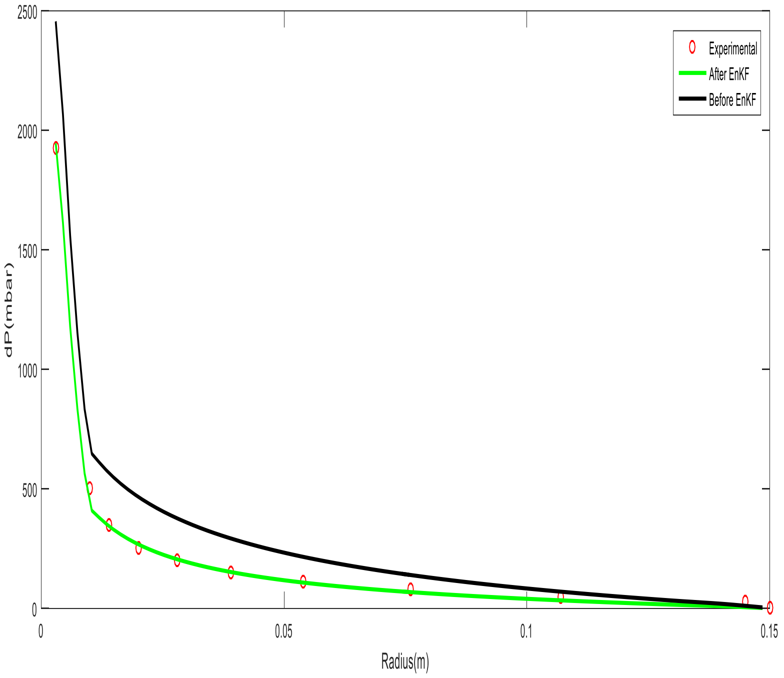

Figure (A.43). History match, q=20ml/min.

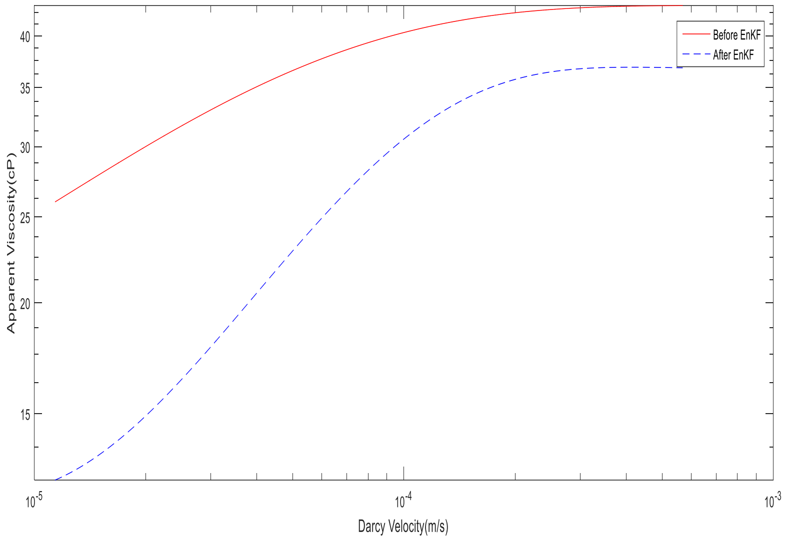

Figure (A.44). The apparent viscosity, q=20ml/min.

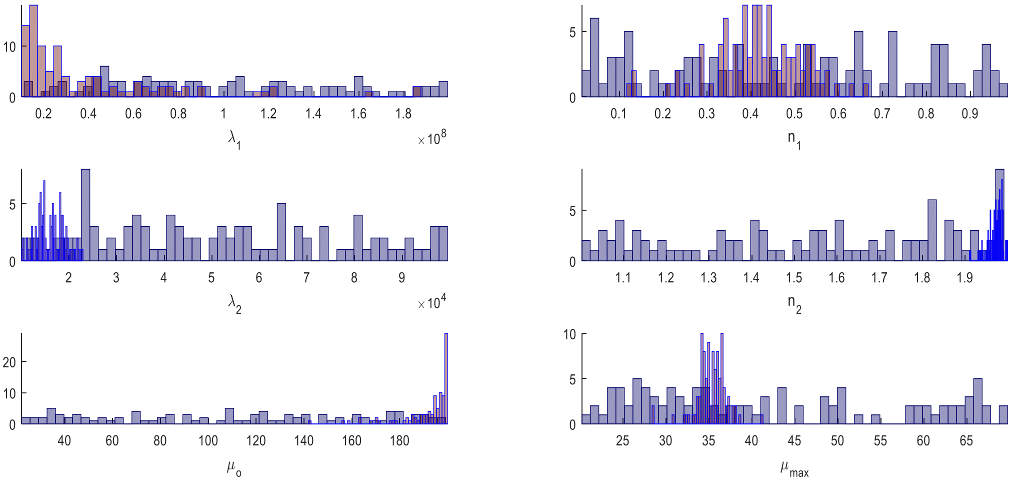

Figure (A.45). Distribution chart, q=20ml/min.

16ml/min

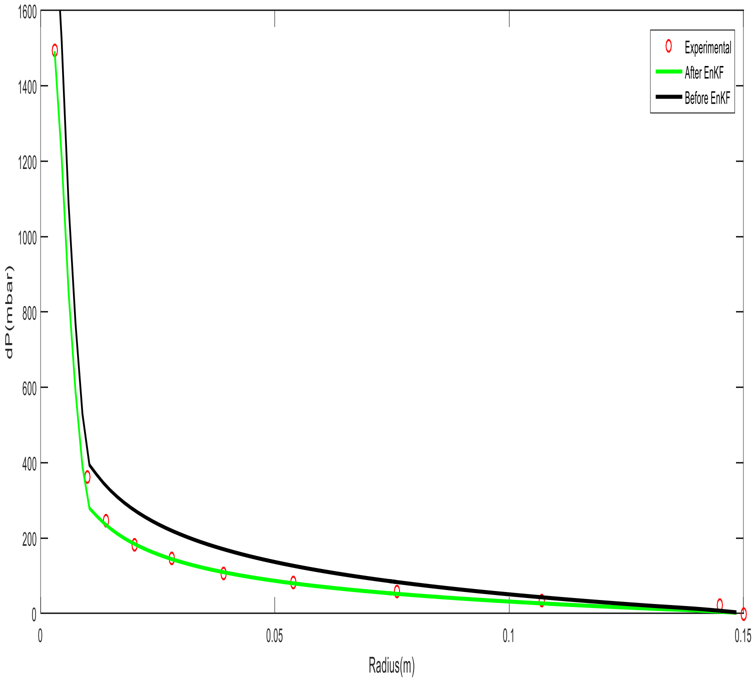

Figure (A.46). History match, q=16ml/min.

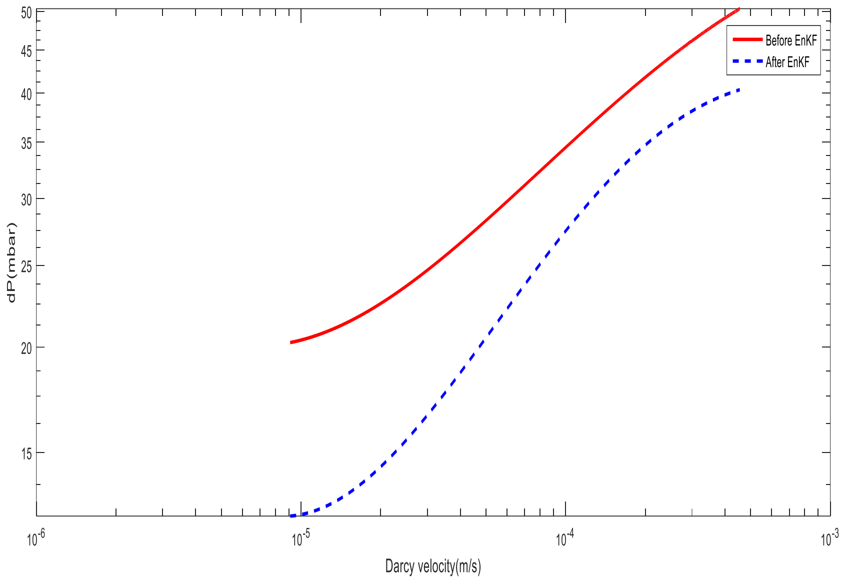

Figure (A.47). The apparent viscosity, q=16ml/min.

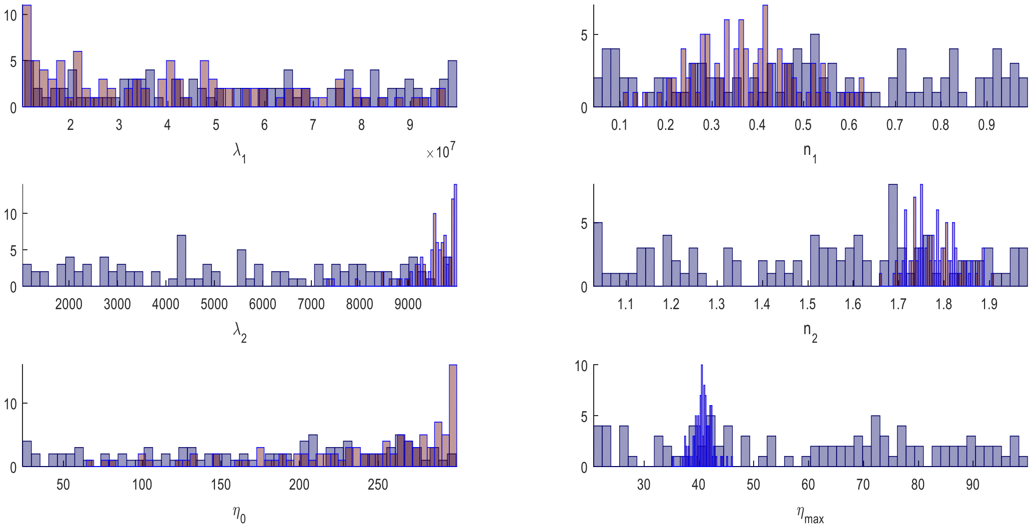

Figure (A.48). Distribution chart, q=16ml/min.

12ml/min

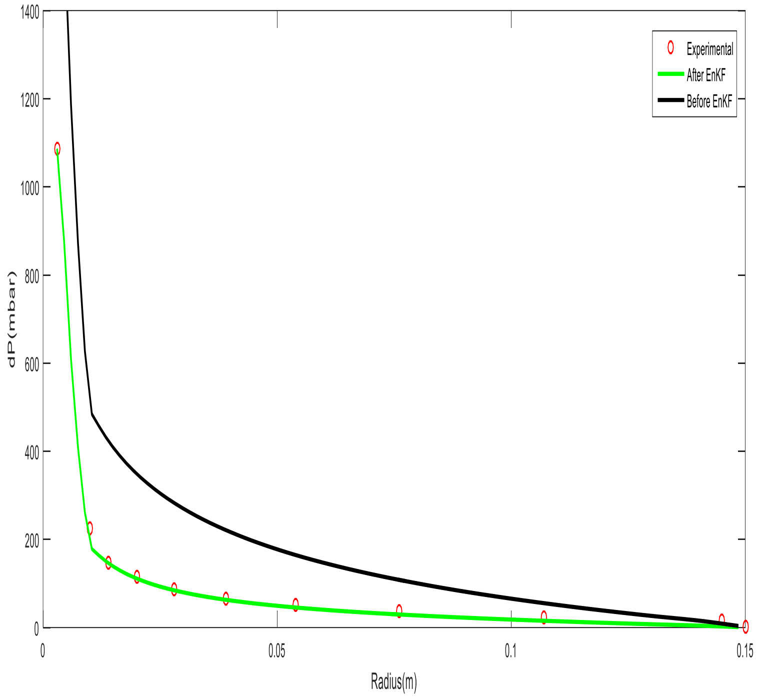

Figure (A.49). History match, q=12ml/min.

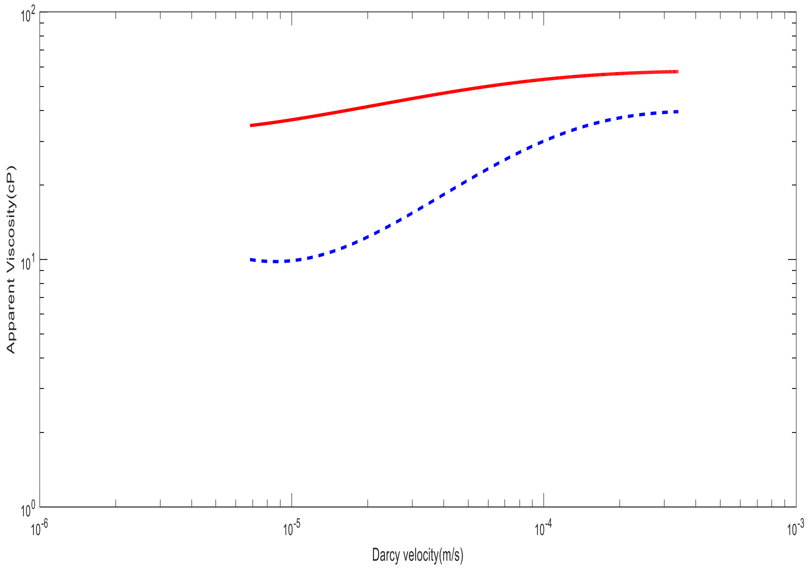

Figure (A.50). The apparent viscosity, q=12ml/min.

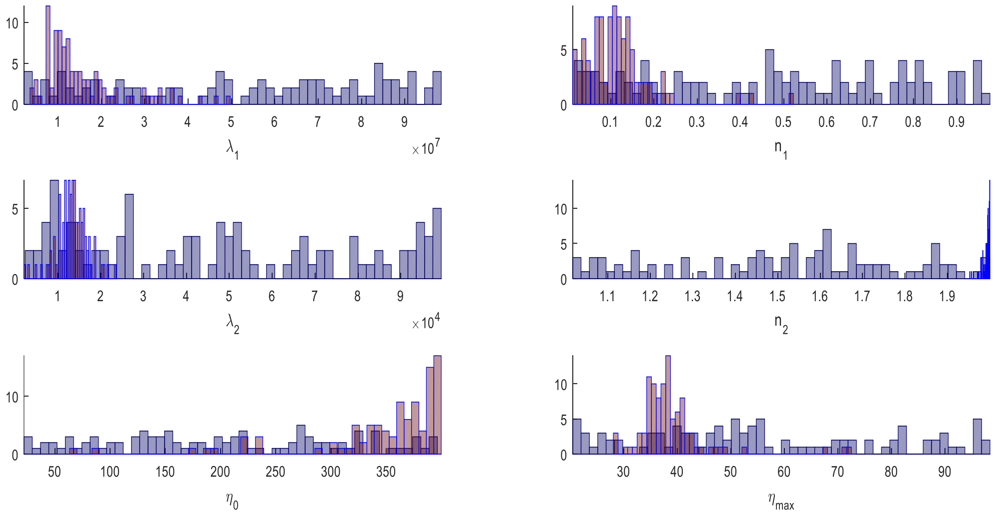

Figure (A.51). Distribution chart, q=12ml/min.

10ml/min

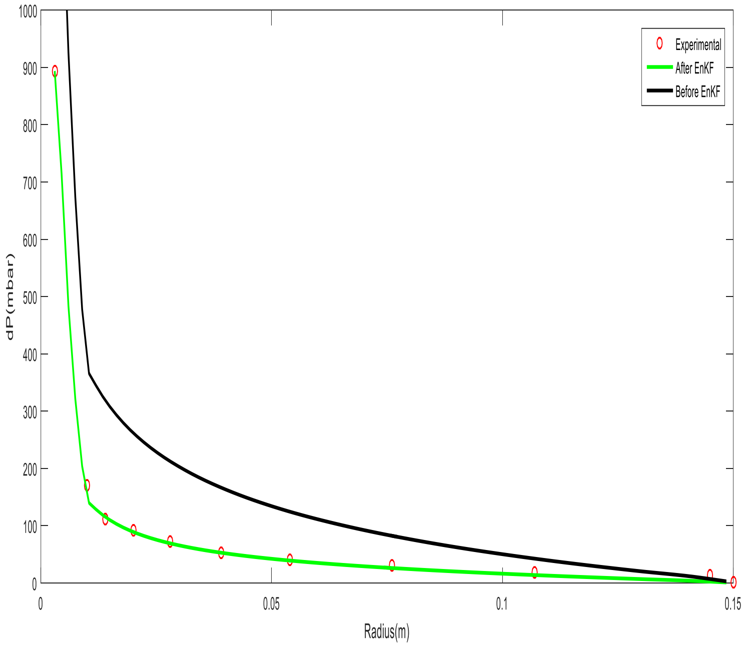

Figure (A.52). History match, q=10ml/min.

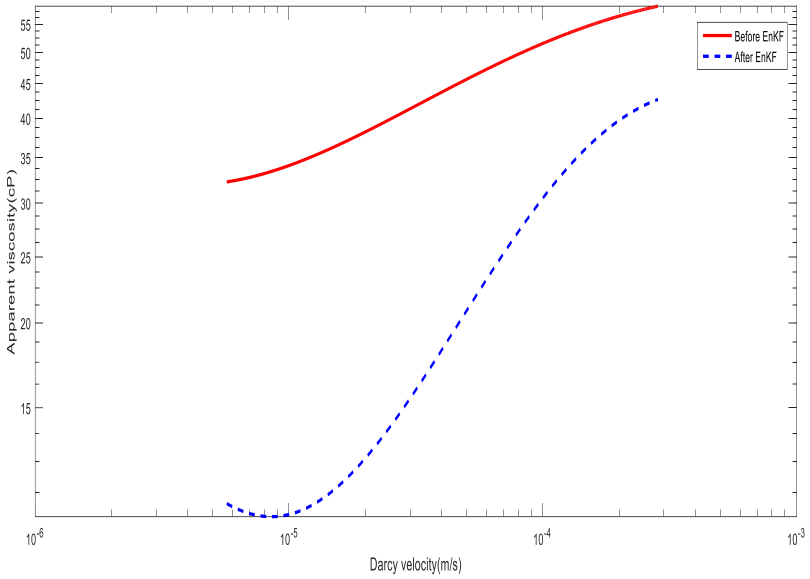

Figure (A.53). The apparent viscosity, q=10ml/min.

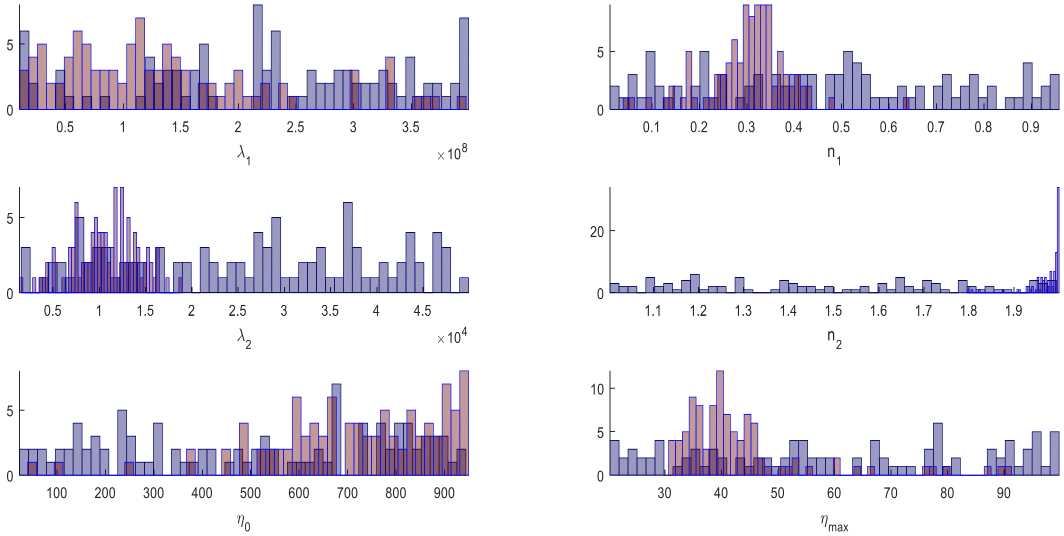

Figure (A.54). Distribution chart, q=10ml/min.

8ml/min

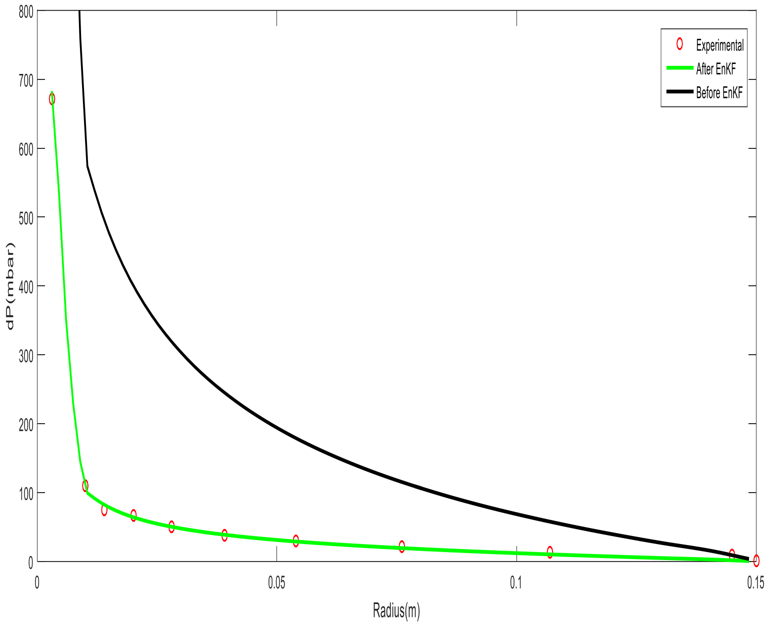

Figure (A.55). History match, q=8ml/min.

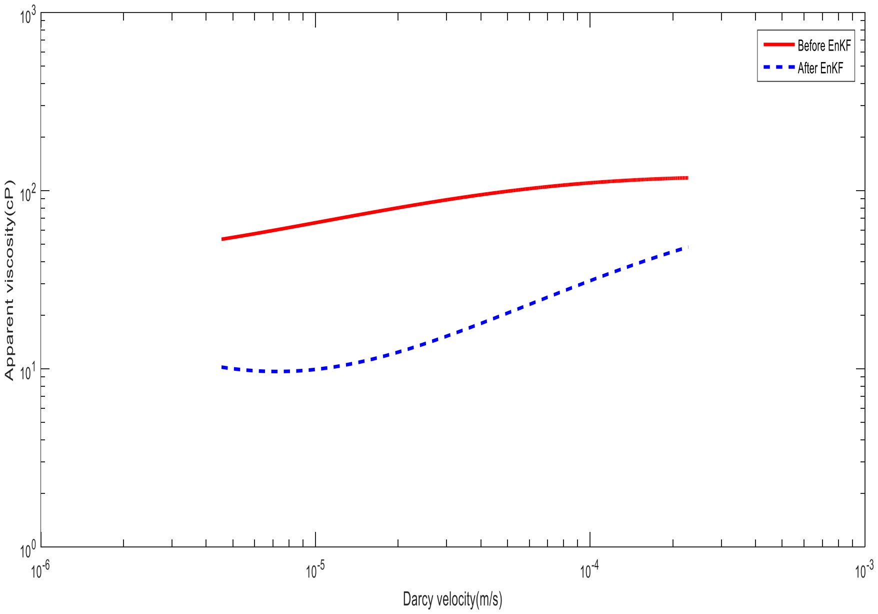

Figure (A.56). The apparent viscosity, q=8ml/min.

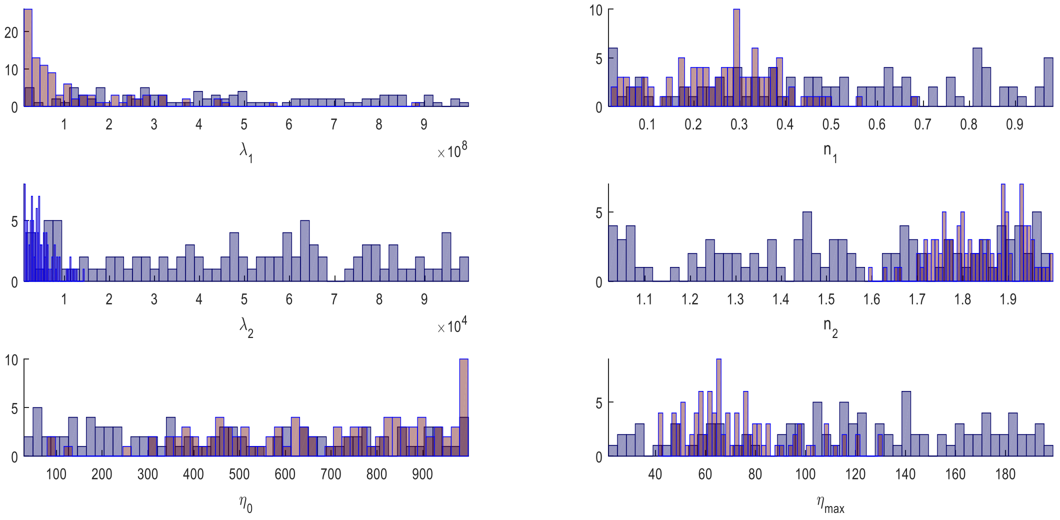

Figure (A.57). Distribution chart, q=8ml/min.

8ml/min(2)

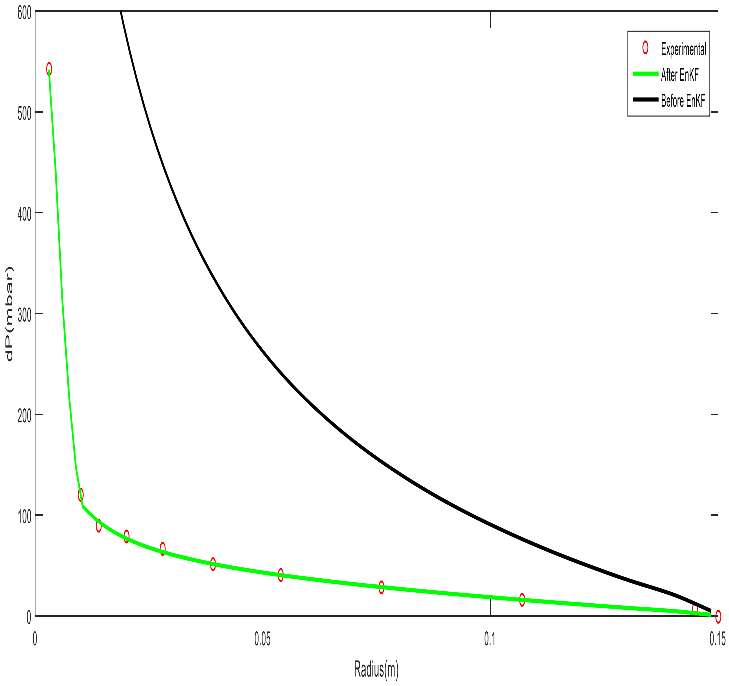

Figure (A.58). History match, q=8ml/min(2).

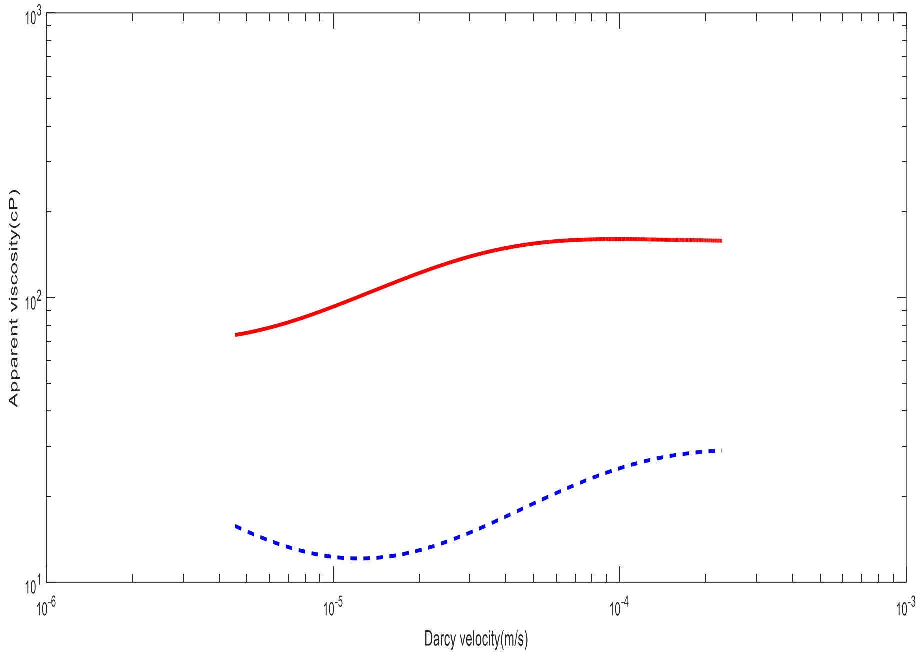

Figure (A.59). The apparent viscosity, q=8ml/min(2).

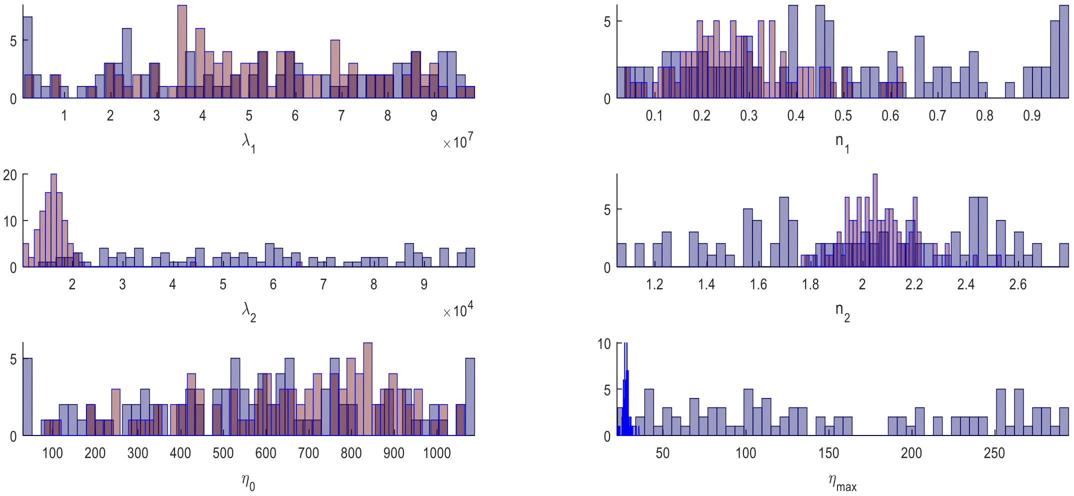

Figure (A.60). Distribution chart, q=8ml/min(2).

5ml/min

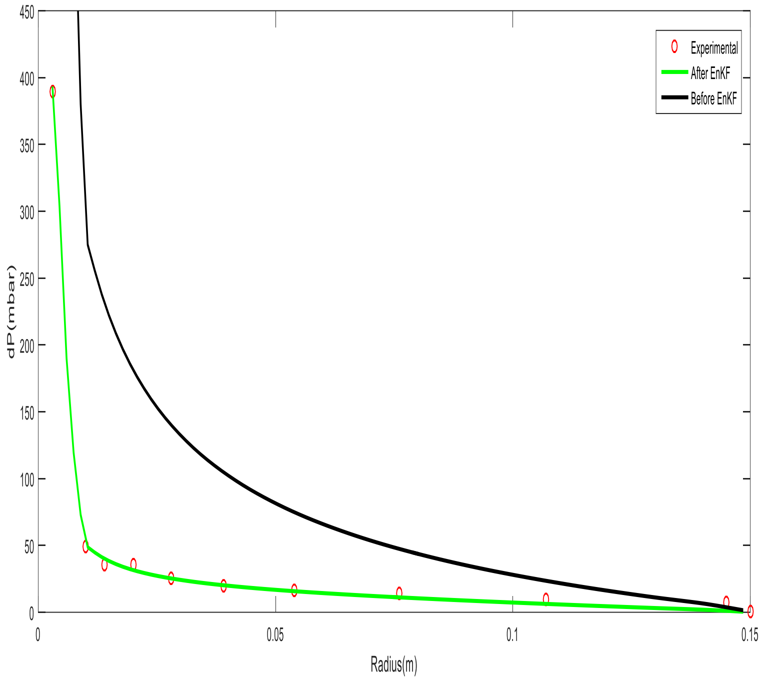

Figure (A.61). History match, q=5ml/min.

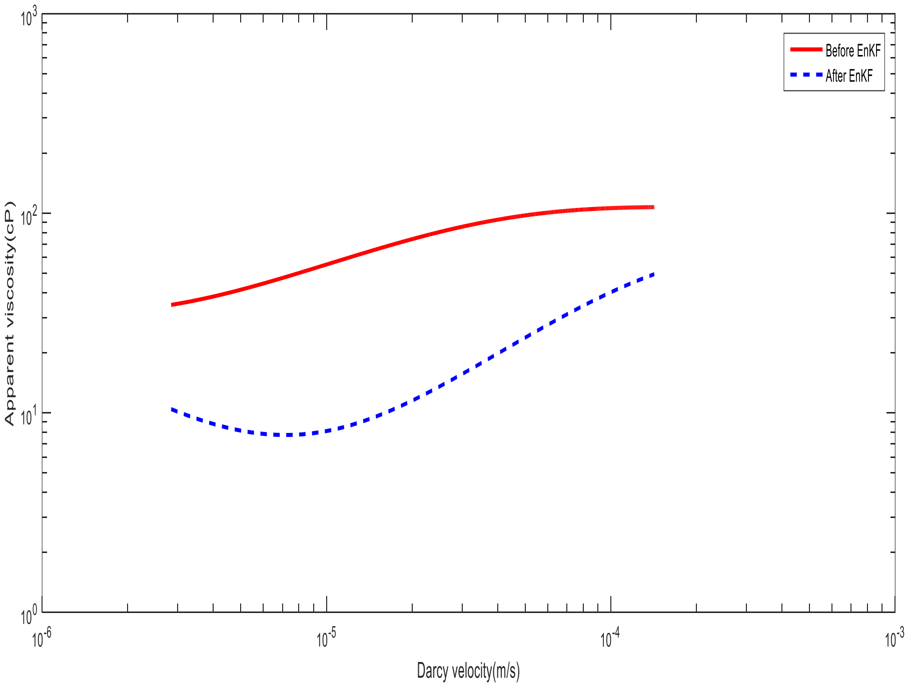

Figure (A.62). The apparent viscosity, q=5ml/min.

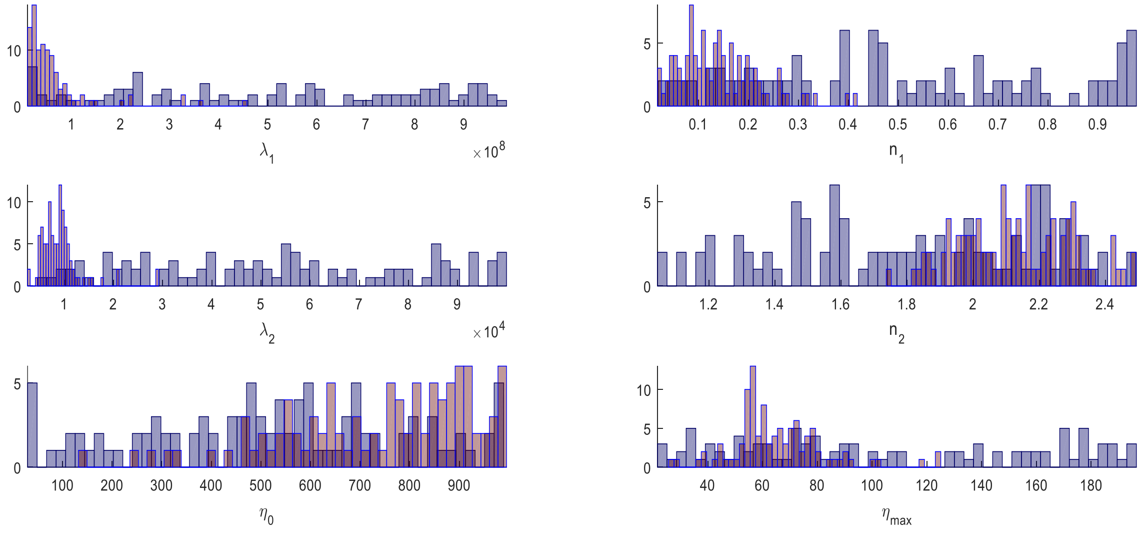

Figure (A.63). Distribution chart, q=5ml/min.

3ml/min

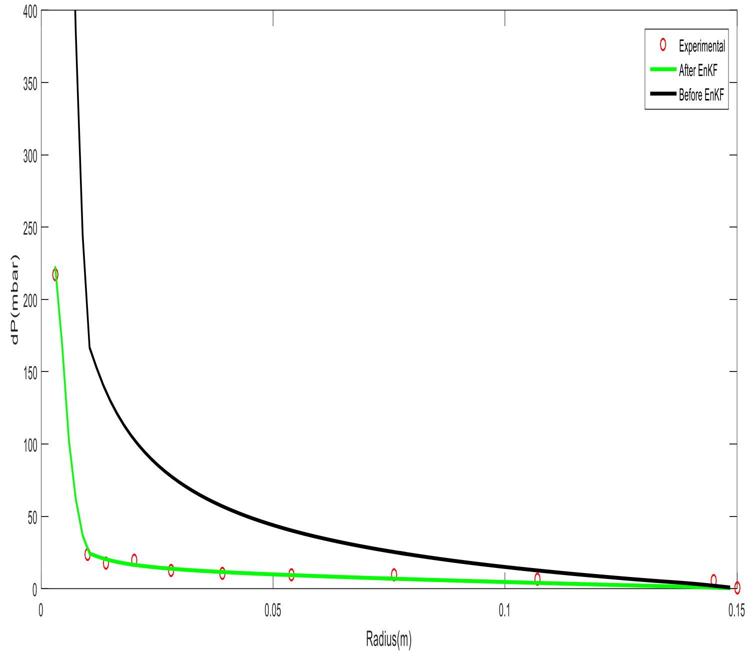

Figure (A.64). History match , q=3ml/min.

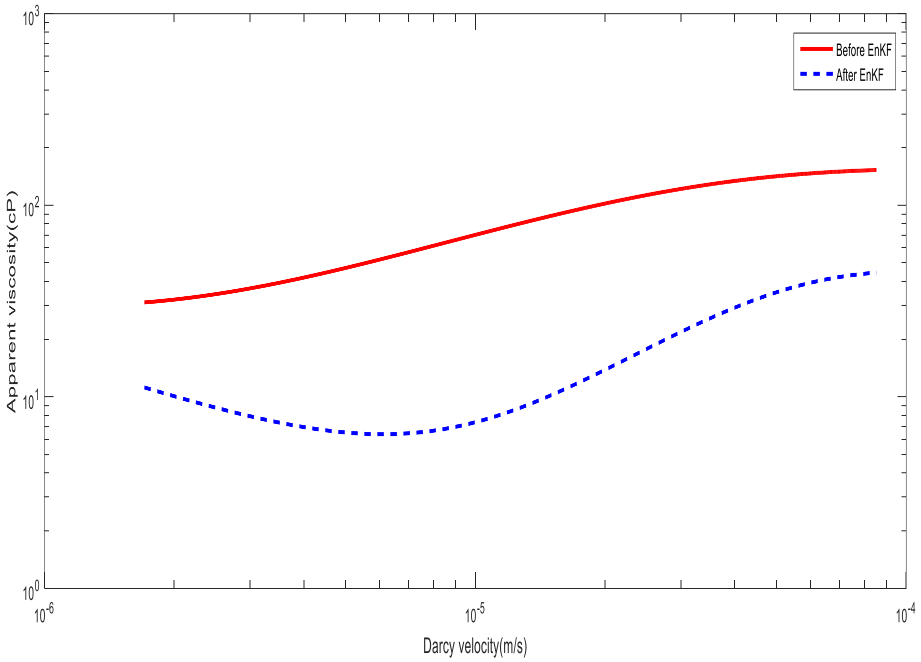

Figure (A.65). The apparent viscosity, q=3ml/min.

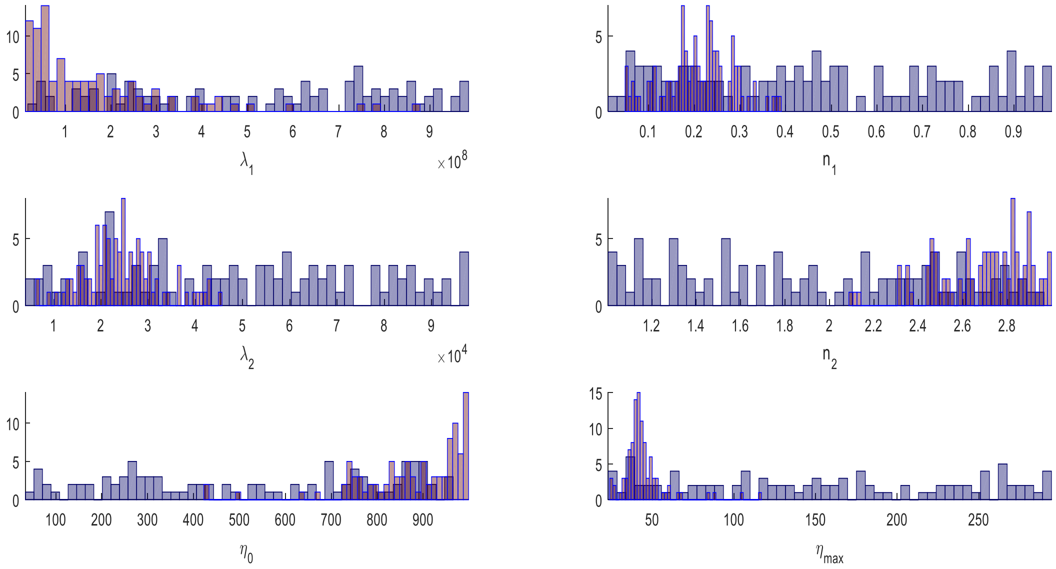

Figure (A.66). Distribution chart, q=3ml/min.

1ml/min

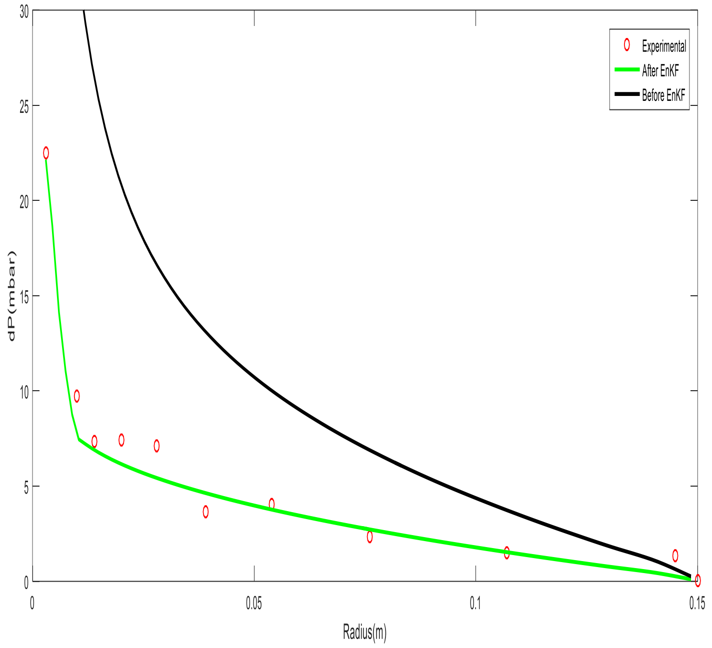

Figure (A.67). History match, q=1ml/min.

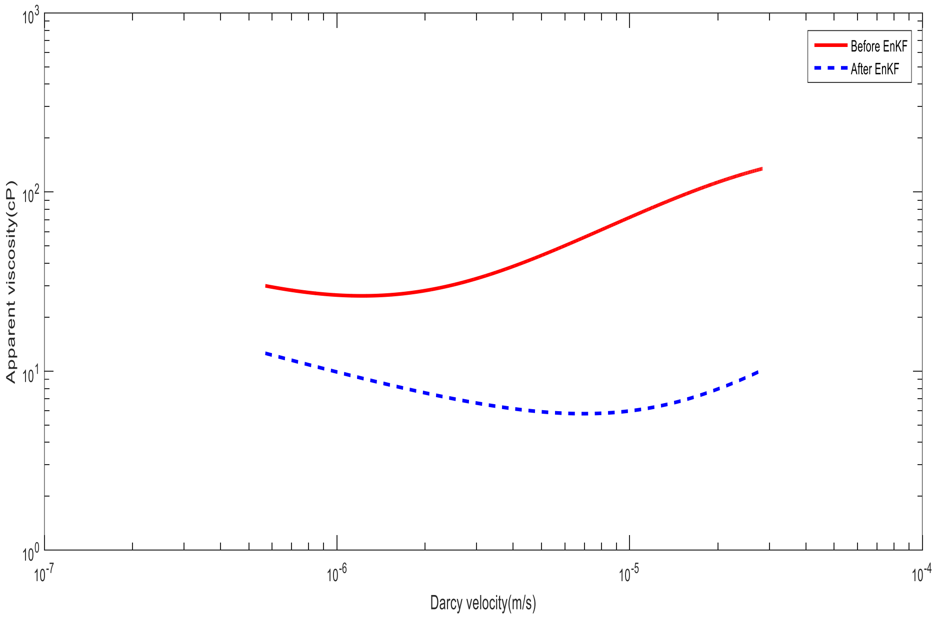

Figure (A.68). The apparent viscosity, q=1ml/min.

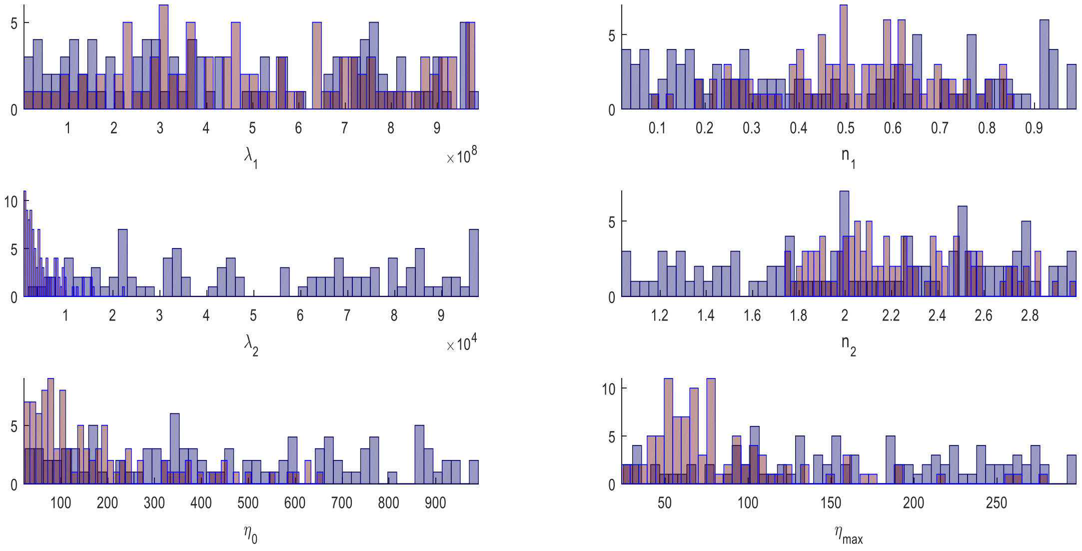

Figure (A.69). Distribution chart, q=1ml/min.

0,5ml/min

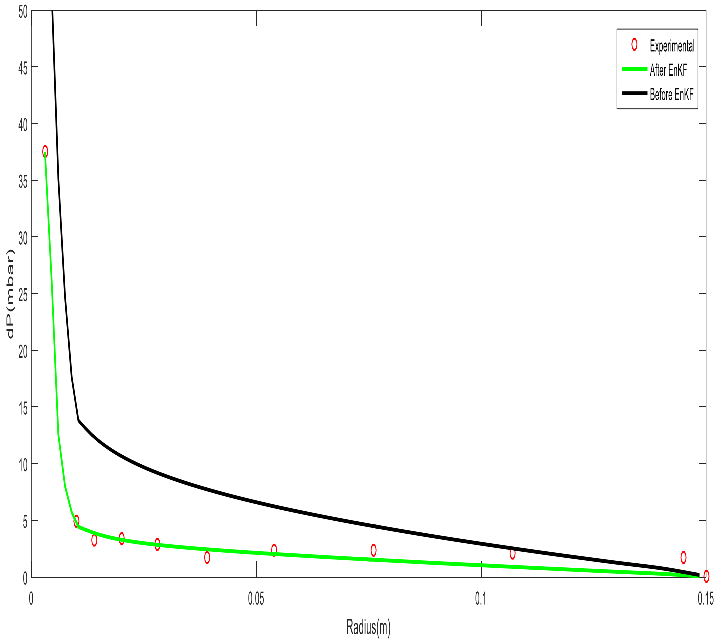

Figure (A.70). History match, q=0,5ml/min.

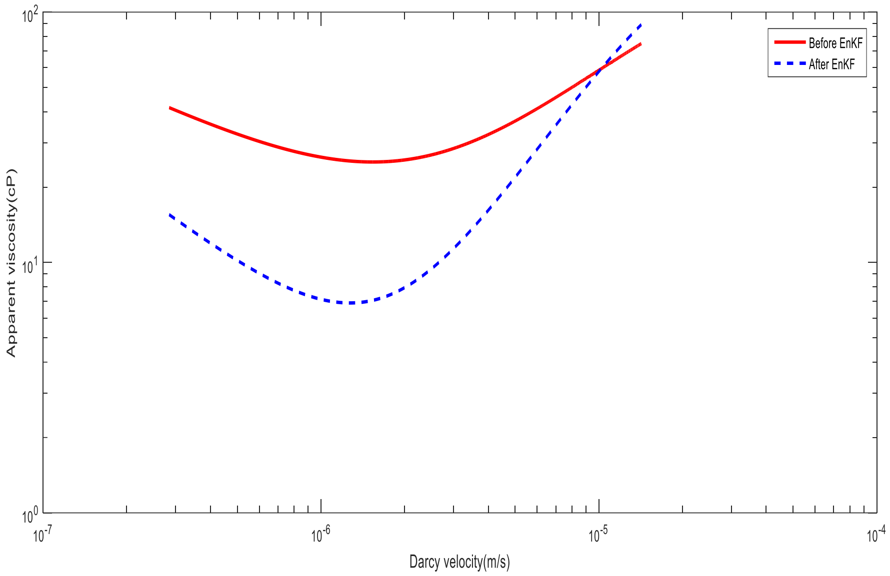

Figure (A.71). The apparent viscosity, q=0,5ml/min.

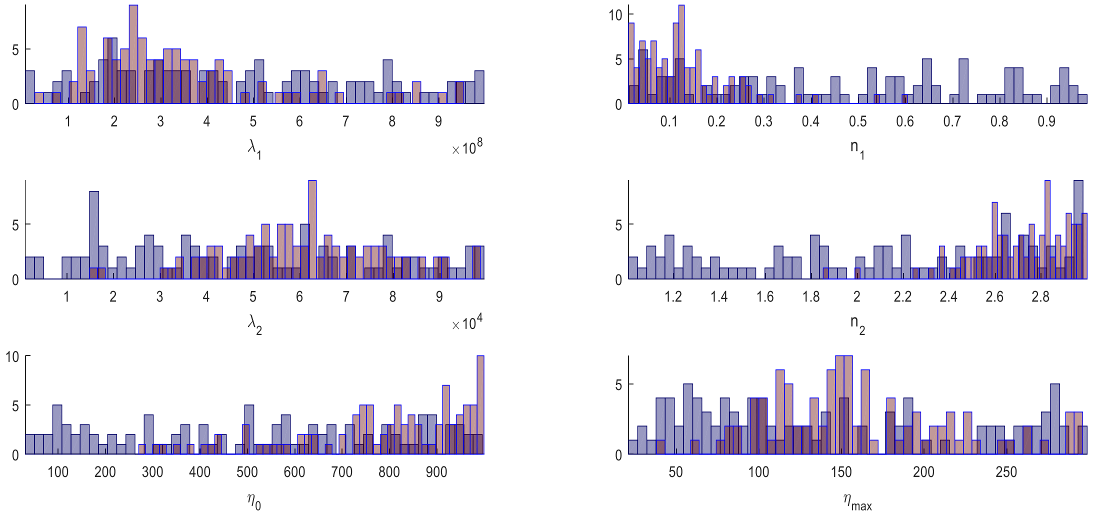

Figure (A.72). Distribution chart, q=0,5ml/min.

Table A.2. The obtained extended Carreau parameters for the polymer flooding simulated in MRST.

	Extended Carreau parameters					
q(ml/min)	**n_1**	**n_2**	**λ_1**	**λ_2**	**η_0**	**η_{max}**
20	0,418	1,97	39700128	16103	191,87	35,26
20*	0,444	1,90	54498212	9984	383,64	38,64
16	0,375	1,78	39394284	9521	237,93	40,64
12	0,116	1,99	15737459	13359	347,17	38,77
10	0,304	1,97	132818499	10735	716,76	43,43
8	0,261	1,84	120844868	4638	679,61	72,35
8(2)	0,285	2,06	52828956	16673	654,96	27,68
5	0,141	2,13	64407254	9121	737,87	65,26
5*	0,069	1,95	39536841	3999	815,86	80,90
3	0,208	2,69	166957341	25328	877,73	44,51
1	0,515	2,23	512397897	4983	181,39	85,41
0,5	0,129	2,72	345428776	60982	783,51	161,55

A.4.2 STARS vs. MRST

16ml/min

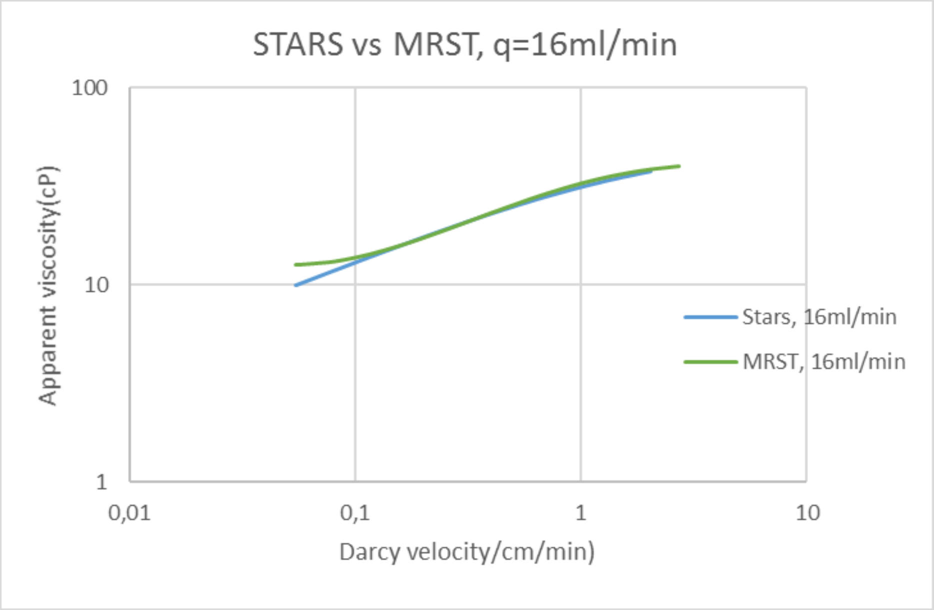

Figure (A.73). STARS vs. MRST rheology, q=16ml/min.

12ml/min

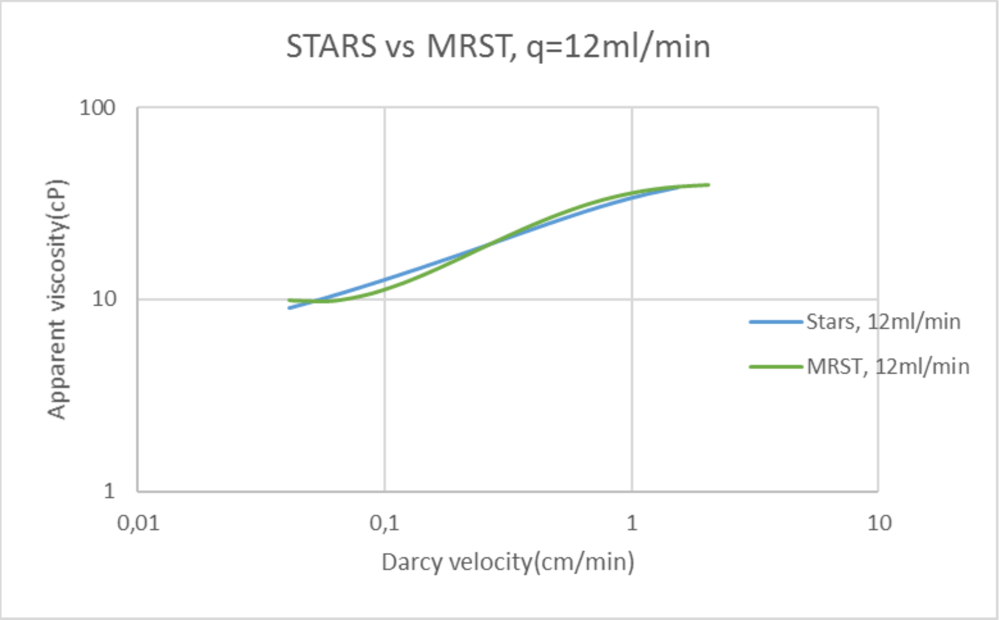

Figure (A.74). STARS vs. MRST rheology, q=12ml/min.

10ml/min

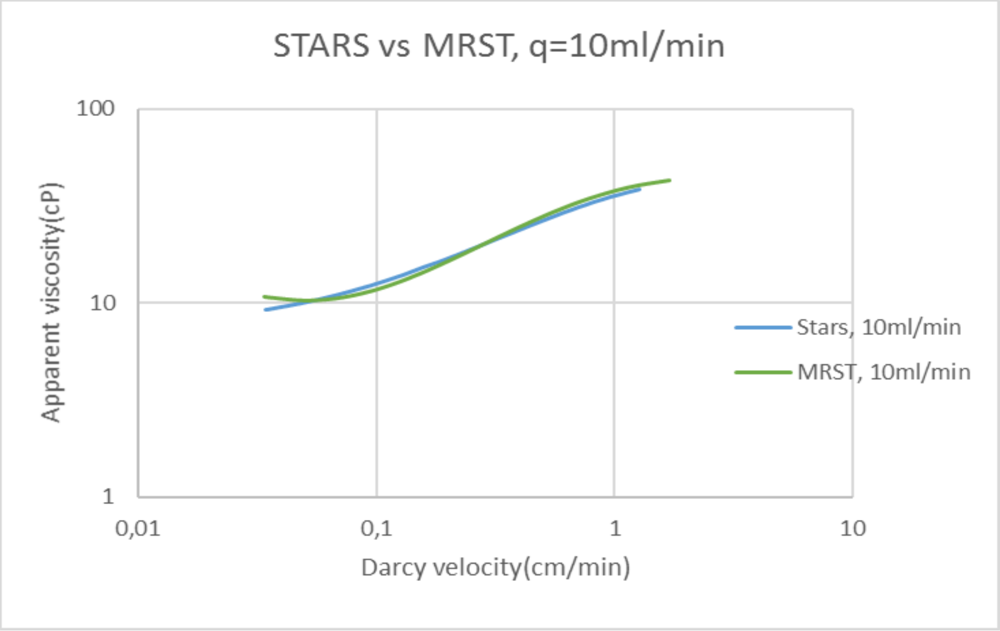

Figure (A.75). STARS vs. MRST rheology, q=10ml/min.

5ml/min

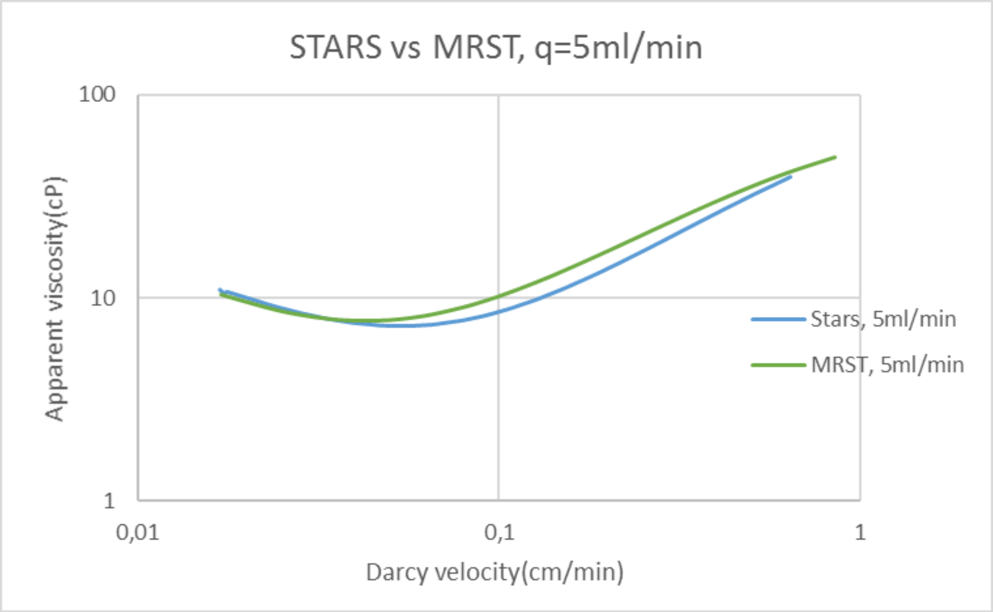

Figure (A.76). STARS vs. MRST, q=5ml/min.

0,5ml/min

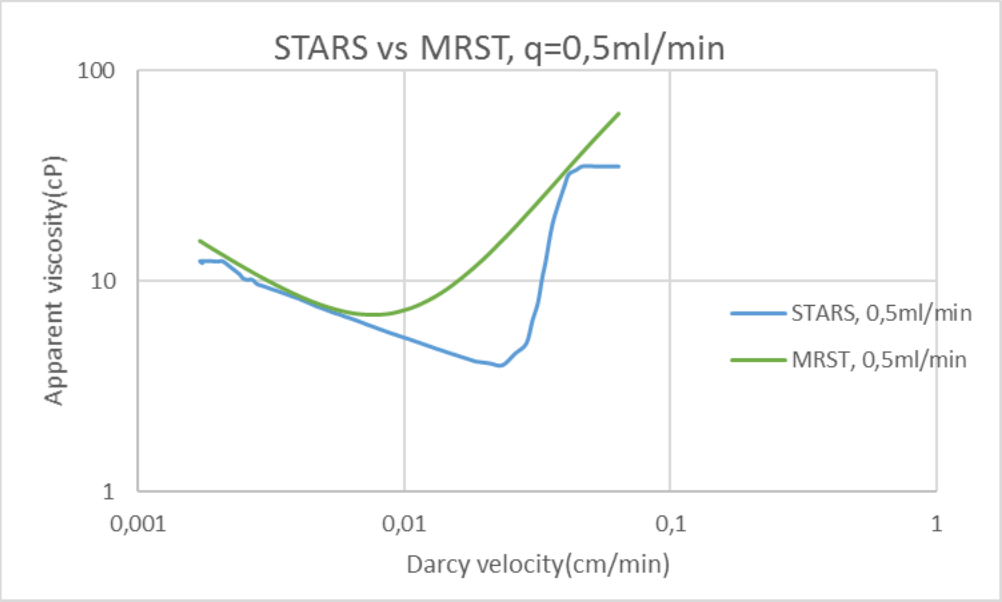

Figure (A.77). STARS vs. MRST rheology, q=0,5ml/min.

A.5 The effect of polymer rheology on injectivity

Table (A.3). The extended Carreau parameters used when extending the rheology curves used when examining injectivity.

	Extended Carreau parameters used when examining the injectivity					
	n_1	**n_2**	**λ_1**	**λ_2**	**η_0**	**η_{max}**
Shear thickening	0,022	1,56	2305525	6946,67	2,53	46,13
Shear thickening + shear thinning(1)	0,203	2,22	4220333	6645,17	69,14	78,97
Shear thickening + shear thinning(2)	0,213	2,14	14164350	10886,58	168,97	39,01
Shear thinning	0,7	1,08	100000	1000	22	1

B. Appendix B – STARS data-file

B.1 Waterflooding

```
** ============== INPUT/OUTPUT CONTROL ==========================

TITLE1 'Radial 1-phase Model'

INUNIT          LAB
OUTUNIT LAB
SHEAREFFEC SHV

WPRN             GRID TIME
OUTPRN GRID PRES SW W X VISW
OUTPRN WELL ALL

WPRN             ITER TIME
OUTPRN ITER NEWTON

WSRF            WELL 1
WSRF            GRID TIME
**WSRF          SECTOR 1
OUTSRF GRID MASS ADSORP MOLE ADSORP PPM ADSPCMP KRO KRW KRW
MASDENW MOLDENW
PRES RFW SHEARW
        SW VISCVELW VISW W X Y
OUTSRF WELL MOLE COMPONENT ALL
OUTSRF SPECIAL BLOCKVAR PRES 3,1,1
                 BLOCKVAR PRES 10,1,1
                    BLOCKVAR PRES 14,1,1
                    BLOCKVAR PRES 20,1,1
                    BLOCKVAR PRES 28,1,1
                    BLOCKVAR PRES 39,1,1
                    BLOCKVAR PRES 54,1,1
                    BLOCKVAR PRES 76,1,1
                    BLOCKVAR PRES 107,1,1
```

```
                BLOCKVAR PRES 145,1,1
                BLOCKVAR PRES 150,1,1

**$  Distance units: cm
**RESULTS XOFFSET         0.0000
**RESULTS YOFFSET          0.0000
**RESULTS ROTATION       0.0000  **$  (DEGREES)
**RESULTS AXES-DIRECTIONS 1.0 -1.0 1.0

** ========= RESERVOIR DESCRIPTION
====================================

GRID  RADIAL        148 1 1                    RW 0.3           **Cylindrical grid

KDIR  DOWN
DI    IVAR 147*0.1 0.3
DJ    CON 360
DK    CON 3.11

DTOP  148*1

NULL CON 1
POR ALL
147*0.239  0.99

PERMI ALL
7*420 96*2600 44*1900 1000000
PERMJ EQUALSI
PERMK EQUALSI
**  0 = pinched block, 1 = active block
PINCHOUTARRAY CON           1

END-GRID

** ============= COMPONENT PROPERTIES
==================================

MODEL 2 2 2 2
COMPNAME 'Water' 'Polymer'
```

```
CMM
0.018 18
PCRIT
0 0
TCRIT
0 0
PRSR 101
PSURF 101
MASSDEN
0.001 0.001
CP
0 0
AVISC
1 0
BVISC
0 0

VSMIXCOMP 'Polymer'
VSMIXENDP 0 1.80144e-006
VSMIXFUNC 0 0.1 0.2 0.3 0.4 0.5 0.6 0.7 0.8 0.9 1
**      velocity  viscosity
** Use the following keywords for a smooth shear effect that fits the data in SHEARTAB:
SHEARTHIN 0.97285  4.535e-008

SHEARTAB
        0.001     1
        0.1       1
        **    0.0214    30.0001
        **    0.0241    28.0001
        **    0.0276    29.0001
        **    0.0322    26.0001
        **    0.0362    25.0001
        **    0.0413    23.0001
        **    0.0482    20.0001
        **    0.0579        14
```

```
          **    0.0723        13
          **    0.0956        10
          **    0.1447        11
          **    0.1929        15
          **    0.2394    21.0001
          **    0.5787    30.0001
          **    1.9292    110.001


** ================ ROCK-FLUID PROPERTIES
========================

ROCKFLUID
RPT 1

SWT
0       0       1
0.1     0.1     0.9
0.2     0.2     0.8
0.3     0.3     0.7
0.4     0.4     0.6
0.5     0.5     0.5
0.6     0.6     0.4
0.7     0.7     0.3
0.8     0.8     0.2
0.9     0.9     0.1
1       1       0

**ADSCOMP 'Polymer' WATER
**ADSPHBLK W
**ADSTABLE
**    Mole Fraction  Adsorbed moles per unit pore volume
**    Mole Fraction  Adsorbed moles per unit pore volume
**              0                          0
**    4.508997705e-006              9.969376504e-008
**ADMAXT 9.96938e-008
```

```
**ADRT 2.49234e-009
**PORFT 1
**RRFT 1

** ============== INITIALIZATION =================================

INITIAL
VERTICAL OFF

INITREGION 1

PRES  CON 101.1
TEMP CON 22
SW CON 1
MFRAC_WAT 'Water' CON            1

** ============  NUMERICAL CONTROL ================================

NUMERICAL

TFORM ZT
ISOTHERMAL
MAXSTEPS 50000

RUN

** ============  RECURRENT DATA  =================================

TIME 0
DTWELL 1e-4
DTMIN 1e-8
DTMAX 0.01

WELL 'Injector'
INJECTOR MOBWEIGHT EXPLICIT 'Injector'
INCOMP  WATER  1  0
TINJW  22.0
PINJW  101.1
OPERATE  MAX  STW  10.0  CONT REPEAT
```

```
**         rad  geofac  wfrac  skin
GEOMETRY  K  0.3  0.2  1.0  0.0
PERF  GEO  'Injector'
** UBA     ff   Status  Connection
          1 1 1  1.0  OPEN    FLOW-FROM  'SURFACE'

WELL  'Producer1'
PRODUCER 'Producer1'
OPERATE  MIN  BHP  101.1  CONT REPEAT
**         rad  geofac  wfrac  skin
GEOMETRY  K  0.075  0.2  1.0  0.0
PERF  GEO  'Producer1'
** UBA       ff   Status  Connection
          148 1 1  1.0  OPEN    FLOW-TO  'SURFACE'

TIME 2
TIME 5
TIME 10
**WSRF        GRID 1
TIME 20
TIME 40
TIME 60
TIME 80
TIME 100
TIME 120
TIME 200
TIME 300
TIME 350

STOP
```

B.2 Polymer flooding

```
** ============== INPUT/OUTPUT CONTROL ========================

TITLE1 'Radial 1-phase Model'

INUNIT      LAB
OUTUNIT LAB
SHEAREFFEC SHV

WPRN        GRID TIME
OUTPRN      GRID PRES SW W X VISW
OUTPRN      WELL ALL

WPRN        ITER TIME
OUTPRN      ITER NEWTON

WSRF        WELL 1
WSRF        GRID TIME
**WSRF      SECTOR 1
OUTSRF GRID MASS ADSORP MOLE ADSORP PPM ADSPCMP KRO KRW KRW
MASDENW MOLDENW PRES RFW SHEARW SW VISCVELW VISW W X Y
OUTSRF WELL MOLE COMPONENT ALL
OUTSRF SPECIAL BLOCKVAR PRES 3,1,1
            BLOCKVAR PRES 10,1,1
            BLOCKVAR PRES 14,1,1
            BLOCKVAR PRES 20,1,1
            BLOCKVAR PRES 28,1,1
            BLOCKVAR PRES 39,1,1
            BLOCKVAR PRES 54,1,1
            BLOCKVAR PRES 76,1,1
            BLOCKVAR PRES 107,1,1
            BLOCKVAR PRES 145,1,1
            BLOCKVAR PRES 150,1,1

**$  Distance units: cm
**RESULTS XOFFSET       0.0000
**RESULTS YOFFSET       0.0000
```

```
**RESULTS ROTATION          0.0000  **$  (DEGREES)
**RESULTS AXES-DIRECTIONS 1.0 -1.0 1.0

** ========= RESERVOIR DESCRIPTION
========================================

GRID  RADIAL        148 1 1          RW 0.3          **Cylindrical grid

KDIR  DOWN
DI      IVAR 147*0.1 0.3
DJ      CON 360
DK      CON 3.11

DTOP  148*1

NULL CON 1
POR ALL
147*0.239  0.99

PERMI ALL
7*420 96*2600 44*1900 1000000
PERMJ EQUALSI
PERMK EQUALSI
**  0 = pinched block, 1 = active block
PINCHOUTARRAY CON           1

END-GRID

** ============= COMPONENT PROPERTIES
======================================

MODEL 2 2 2 2
COMPNAME 'Water' 'Polymer'
CMM
0.018 18
PCRIT
0 0
TCRIT
```

```
0 0
PRSR 101
PSURF 101
MASSDEN
0.001 0.001
CP
0 0
AVISC
1 9.21
BVISC
0 0

VSMIXCOMP 'Polymer'
VSMIXENDP 0 1.000844444e-006
VSMIXFUNC 0 0.1 0.2 0.3 0.4 0.5 0.6 0.7 0.8 0.9 1

**      velocity  viscosity
** Use the following keywords for a smooth shear effect that fits the data in SHEARTAB:
SHEARTHIN 0.97285  4.535e-008
SHEARTAB
        0.0341          9.21
        0.0353          9.27
        0.0478          9.93
        0.0569          10.40
        0.0673          10.94
        0.0787          11.51
        0.0948          12.29
        0.1024          12.66
        0.1137          13.20
        0.1312          14.00
        0.1599          15.37
        0.1828          16.23
        0.2132          17.45
        0.2558          19.06
        0.3655          22.73
```

```
          0.4265          24.52
          0.5117          26.78
          0.5686          28.14
          0.6397          29.70
          0.7311          31.49
          0.8529          33.54
          1.0235          35.87
          1.2794          38.40
          1.7058          40.91


** ================ ROCK-FLUID
PROPERTIES=========================

ROCKFLUID
RPT 1

SWT
0       0       1
0.1     0.1     0.9
0.2     0.2     0.8
0.3     0.3     0.7
0.4     0.4     0.6
0.5     0.5     0.5
0.6     0.6     0.4
0.7     0.7     0.3
0.8     0.8     0.2
0.9     0.9     0.1
1       1       0


ADSCOMP 'Polymer' WATER
ADSPHBLK W
ADSTABLE
**    Mole Fraction  Adsorbed moles per unit pore volume
```

```
**     Mole Fraction  Adsorbed moles per unit pore volume
           0                                0
 1.000844444e-006                  7.361214076e-009
ADMAXT 7.361214076e-009
ADRT 7.361214076e-009
PORFT 1
RRFT 1

** ============== INITIALIZATION =================================

INITIAL
VERTICAL OFF

INITREGION 1

PRES  CON 101.1
TEMP CON 22
SW CON 1
MFRAC_WAT 'Water' CON            1

** ============  NUMERICAL CONTROL ================================

NUMERICAL

TFORM ZT
ISOTHERMAL
MAXSTEPS 5000000

RUN

** ============  RECURRENT DATA  ================================

TIME 0
DTWELL 1e-4
DTMIN 1e-8
DTMAX 0.01

WELL 'Injector'
INJECTOR MOBWEIGHT EXPLICIT 'Injector'
```

```
INCOMP  WATER  0.9999989992  1.000844444e-006
TINJW  22.0
PINJW  101.1
OPERATE  MAX  STW  10.0  CONT REPEAT
**          rad  geofac  wfrac  skin
GEOMETRY  K  0.3  0.2  1.0  0.0
PERF  GEO  'Injector'
** UBA     ff   Status  Connection
1 1 1  1.0  OPEN    FLOW-FROM  'SURFACE'

WELL  'Producer1'
PRODUCER 'Producer1'
OPERATE  MIN  BHP  101.1  CONT REPEAT
**          rad  geofac  wfrac  skin
GEOMETRY  K  0.075  0.2  1.0  0.0
PERF  GEO  'Producer1'
** UBA       ff   Status  Connection
148 1 1  1.0  OPEN    FLOW-TO  'SURFACE'

TIME 2
TIME 5
TIME 10
**WSRF        GRID 1
TIME 20
TIME 40
TIME 60
TIME 80
TIME 100
TIME 120
TIME 200
TIME 300
TIME 350
TIME 400
TIME 500
TIME 550
```

```
TIME 600
TIME 700
TIME 750
TIME 800
TIME 850
TIME 900

STOP
```